On vortex rings impacting a sharply-stratified interface

Jason Peter Olsthoorn

Department of Applied Mathematics and Theoretical Physics
University of Cambridge

This dissertation is submitted for the degree of
Doctor of Philosophy

Hughes Hall May 2017

Table of contents

Dedicated to my Lou-Bear.

Declaration

I hereby declare that, except where specific reference is made to the work of others, the contents of this dissertation are original and have not been submitted in whole or in part for consideration for any other degree or qualification in this, or any other university. This dissertation is my own work and contains nothing which is the outcome of work done in collaboration with others, except as specified in the text and Acknowledgements.

Jason Peter Olsthoorn
May 2017

Acknowledgements

I would like to thank my supervisor Professor Stuart Dalziel. Without his support and encouragement, this thesis could not have been completed. When Newton spoke of “shoulders of giants”, he was speaking of Stuart.

Additional thanks is given to Professor Paul Linden, Professor Colm-cille Caulfield and Dr. John Taylor for their helpful discussions throughout my doctoral work.

Finally, I would like to thank the laboratory technicians: David Page-Croft, Colin Hitch, Paul Mitton, Andrew Denson, and John Milton. Without their faithful help constructing the various pieces of equipment used in this thesis, this work would not have been possible. I would also like to thank Mark Hallworth for his assistance.

Financial support for this work was provided by the Natural Sciences and Engineering Research Council of Canada (NSERC) and through the Engineering and Physical Sciences Research Council (EPSRC) grant number EP/L504920/1. Additional support has been provided by the EPSRC Mathematical Underpinnings of Stratified Turbulence grant EP/K034529/1. I would also like to thank Hughes Hall, The Cambridge Philosophical Society and the Lundgren Fund.

Jason Peter Olsthoorn
On vortex rings impacting a sharply-stratified interface
Summary

This thesis presents an investigation into the dynamics of vortex rings impacting a sharply-stratified density interface. This problem has a long history and is important for understanding how individual eddies in stratified turbulence mix the density field. We tackle this problem using a combination of experimental, numerical and modelling techniques to understand the flow instability and subsequent mixing induced by the impinging vortex ring. Our findings demonstrate that there exists a critical Richardson number, corresponding to a mixing transition, beyond which the mixing efficiency is constant.

Using a novel Stereo Particle Image Velocimetry (Stereo-PIV) technique, we analyze a series of vortex ring experiments. By amalgamating an ensemble of these experiments, we measure the full, time-resolved, three-dimensional velocity field of the vortex-ring interaction. These measurements capture the instability that is produced on the baroclinically generated vorticity field. This instability is identified as a Crow-like instability. At low Richardson numbers, the timescale of the interface rebound is faster than that of the instability. As a result, there exists a critical Richardson number below which the Crow-like instability will not have sufficient time to grow to large amplitude.

By generating a large number of vortex-ring interactions, we measure the incremental change to the stratification. After an initialization period, there is strong evidence to suggest that the mixing due to each vortex ring becomes constant over a moderate range of Richardson numbers. We suggest that the mixing efficiency of the vortex rings does drop at low Richardson numbers (below unity) in agreement with the analysis of the Stereo-PIV measurements. A model of the system accurately predicts the dependence of the mixing rate on the Richardson number.

Based upon our study of the vortex-ring system, we construct a one-dimensional turbulence model that includes the energy advection from the vortex rings. This model is validated with both physical experiments and numerical simulations of repeated vortex-ring generations. The constant mixing efficiency regime is recovered in all three methodologies.

Through examining the detailed dynamics of the flow, this work suggests that there exists a critical Richardson number corresponding to a transition between mixing regimes, and that this critical Richardson number is a result of the growth of a Crow-like instability. We have highlighted how to improve current mixing-models to capture this physics. New avenues of future research are currently underway to study the mixing produced by a stratified mixing-box experiment in light of these new developments.

Chapter 1

Introduction

> If I have seen further it is by standing on the shoulders of Giants.
>
> —Isaac Newton

Vortex rings have been studied in nearly every domain of fluid mechanics, from J.J. Thomson's treatise on the vortex atom theory of gases (Thomson, 1883), to the creation of knotted vortex rings (Kleckner & Irvine, 2013). Vortex rings are a classical fluid structure with azimuthal symmetry, allowing for their simplified (though by no means simple) analytic analysis. We contribute to this body of literature by studying vortex rings as they impact a stratified interface. Figure 1.1 presents an example of such a vortex-ring impact. As we will show below, by studying the breakdown of vortex rings in a stratified environment, we make progress in understanding stratified turbulent mixing.

In this thesis, mixing is defined as the irreversible increase in the gravitational potential energy of the system that results from an input of energy. We will follow the approach of Winters *et al.* (1995). Stratified turbulent mixing is an important problem with a broad range of applications, from designing combustion engines to solar corona heating in astrophysics. In order to quantify this mixing, significant research has been focused on determining the amount of energy that, when made available to drive mixing, will result in a change to the gravitational potential energy of the system. As an everyday example, consider milk poured into a cup of coffee. How much of the mechanical energy used to stir the liquid actually mixes the milk into the coffee? This problem has direct relevance to modern global climate models, where the estimated vertical fluxes do not close the energy budget (Ivey *et al.*, 2008). Quantifying mixing has proven to be a very challenging task, with seemingly contradictory results (Fernando, 1991; Linden, 1979; Shrinivas & Hunt, 2015). As such, we differentiate between types of stratified turbulence, and clarify where the present experiments are applicable.

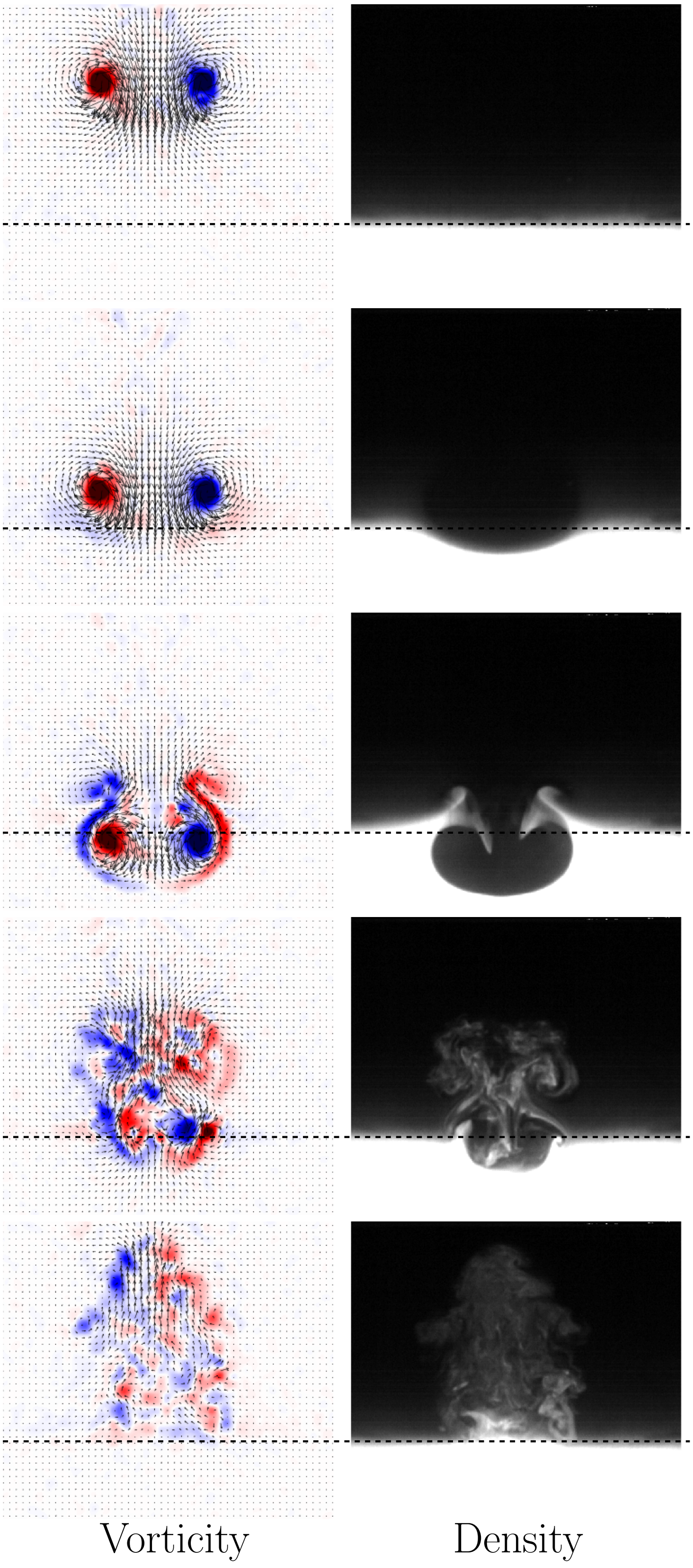

Fig. 1.1 An example of the evolution of a vortex ring impacting a density interface. This plot presents the computed vorticity field and the evolution of the density field within a vertical light sheet. See Chapter 4 for a complete description of the dynamics.

Turner (1979) distinguished between internally and externally forced stratified mixing. In his definition, *internal mixing* is defined as the mixing that occurs when the energy used to mix a stratification is produced at the location of the mixing. For example, Turner would define the mixing produced by a stratified shear instability to be an example of internal mixing. In contrast, Turner defined *external mixing* as the mixing that occurs when the energy is produced external to the mixing location. This heuristic definition can be made more precise by refering to the turbulent kinetic energy equation. We do not pursure that here. Turner's mixing box experiment, where an oscillating grid produces turbulence in a stratified tank, is an example of external mixing. This distinction is similar to one introduced by Tailleux (2009). In this thesis, we will generate vortex rings at the top of a water-filled tank, which will then propagate downwards (away from its generation point) and subsequently mix the stratification. In Turner's conceptualization, this problem would be an external-mixing problem. We are considering a mixing process where the only source of input energy is kinetic energy, as opposed to an input of potential energy, such as a Rayleigh-Taylor mixing experiment. As an additional constraint, we will only consider mixing in a potential-energy-dominated system (i.e. $\mathrm{Ri} \gtrsim 1$). We return to this in the conclusions. However, it should be noted that while we interpret the Richardson number a ratio of the potential energy to kinetic energy of the system, there are other interpretations. Another interpretation of the Richardson number is the balance of buoyant to advective timescales in the system.

Recent developments in the stratified turbulence community have suggested that, in the context of stratified shear flows, the buoyancy Reynolds number ($\mathrm{Re}_b = \frac{\varepsilon}{\mu N^2}$, the ratio of viscous dissipation to the product of viscosity and the strength of the stratification. Here, ε is the viscous dissipation rate, ν is the molecular viscosity and N is the buoyancy frequency) is a dynamically relevant parameter for the strength of the stratified turbulence (see Bartello & Tobias (2013) and others). The buoyancy Reynolds number can be thought of as the scaled ratio of the Ozmidov scale (L_O), the length scale where stratification affects vertical momentum transport, to the dissipation length-scale (L_k), $Re_b = \left(\frac{L_O}{L_k}\right)^{\frac{4}{3}}$. Thus, in order for there to be an appropriate separation of length scales corresponding to fully-developed stratified turbulent mixing, $\mathrm{Re}_b \gg 1$. The peak buoyancy Reynolds number of the vortex-ring experiments presented here is O(10), and not necessarily much greater than 1. Here, the buoyancy Reynold number is estimated from the propagation speed of the vortex ring ($U \approx 0.04$ m/s, the diameter of the vortex tube ($D \approx 0.04$ m), assuming a reduced gravity of 0.1 and a density interface thickness of 1mm.

While the we typically refer to grid generated turbulent mixing as a motivation for this study, this work as relevance to zero-mean shear turbulent mixing in geophysical applications. For example, this has application to understanding the formation and persistence of the upper mixed layer in the ocean (Kraus & Turner (1967),Mcdougall (1979)). As we will discuss below, turbulent layer formation remains elusive.

The use of vortex rings to study stratified turbulent mixing has its origins in the study of grid-generated turbulence. In the 1960s, Turner (1968) set up an experiment to measure the mixing produced by a vertically-oscillating grid within a stratified tank. He observed three key features to the flow: first, the turbulence appeared to create and maintain a sharp interface between the mixed fluid and the unperturbed stratification. Second, there were identifiable length-scales to the interface deformations, associated with the turbulent eddies. Third, it was the largest of these eddies that did the majority of the fluid mixing. Additional analysis (Turner, 1968) demonstrated that these large-scale mixing events appear to be independent of one another. This work prompted Linden (1973) to investigate vortex rings impacting a sharply-stratified density-interface, in analogy to these turbulent eddies. Linden's analysis of the vortex-ring-induced mixing has had a significant influence on the stratified turbulent literature. In this thesis, we will expand upon the work of Linden (1973) in order to compare its applicability to recent advancements in the stratified turbulence literature. Over the intervening 40 years, significant advancements have been made to experimental fluid mechanics. As such, this thesis implements several modern methods to investigate the mixing produced by vortex rings in a stratified environment.

In this thesis, we will use a combination of experimental, numerical, and modelling techniques to study the evolution of the fluid system when a vortex ring impacts a sharply stratified density interface. In particular, we want to understand the mechanics and dynamics of vortex rings as they interact with a two-layer stratification in order to predict how the density stratification will evolve.

Mixing occurs through the combination of stirring and diffusion. When a fluid is stirred, the total density gradient (i.e. $\int_V |\nabla\rho|^2 \, dV$, for the density field ρ) within the domain is increased, amplifying the diffusion-rate of the density field, and increasing the gravitational potential energy of the system. As such, axisymmetric vortex rings are ineffective mixers as they have (in an idealized sense) closed streamlines. In a stratified environment, the streamlines associated with the secondary vorticity, produced through the baroclinic torque, will not be closed, though the total density gradient will still be limited by axisymmetry. In order to produce significant mixing, the vortex-ring system must exhibit an instability in order to generate turbulence, and stir the density field. In an unstratified fluid, the work of Widnall & Sullivan (1973) and Widnall *et al.* (1974) demonstrated that a thin (inviscid) vortex ring of constant vorticity will always be unstable. It has been shown that an elliptical instability (second bending mode, known as a Widnall instability) will be the dominant instability mechanism, rather than a simple displacement mode (or Crow (1970) instability).

Recent experimental (Ponitz *et al.*, 2015) and numerical methods (Archer *et al.*, 2008, 2009) have demonstrated that both of these instability mechanisms do occur for a propagating unstratified vortex ring. However, the author is unaware of any theoretical analysis of the instability for non-thin vortex rings (vortex rings that have a vortex core diameter comparable with the ring diameter).

In a stratified environment, it is known that the stratification will expedite the instability of the vortex rings (Atta & Hopfinger, 1989; Maxworthy, 1977; Scase, 2003; Turner, 1957). Recent numerical simulations of vortex dipoles have started to identify the stratification-modified-instability mechanism (Nomura *et al.*, 2006; Ortiz *et al.*, 2015), which will likely relate to the stratification-enhanced-instability mechanism of vortex rings. However, both of these studies have focused on relatively low stratification strengths (Ri<O(1)). Chapter 4 identifies the initial vortex-ring instability that occurs for a vortex ring impacting a sharp, strongly-stratified density interface. We observe that the dynamics of this instability relate to those of a vortex dipole impacting a solid wall (see Bristol *et al.* (2004); Harris & Williamson (2012)). Chapter 4 further investigates the timescale of this instability growth and suggests that, due to its Richardson number dependence, this instability will not be observed at low Richardson numbers.

As we have noted above, Turner (1968) demonstrated that grid-generated turbulence produces sharp interfaces. In fact, the formation of layers has been observed in a number of other turbulent contexts (Fernando, 1991; Holford & Linden, 1999). In Chapter 5, we will argue that, similar to turbulent mixing experiments, the repeated generation of vortex rings will produce sharp interfaces. By studying how vortex rings produce sharp interfaces, we hope to shed light on the turbulent layer formation process. Using the experimental velocity-field measurements of Chapter 4, we use a numerical scheme to compute the vertical buoyancy throughout the vortex-ring interaction in Chapter 5. This work highlights how vortex rings are able to sharpen density interfaces.

Once the mechanics of the vortex-ring interaction have been clarified, we return to the turbulent analogy of vortex rings. In a stratified turbulence experiment, many turbulent eddies will impact a density interface and entrain a certain amount of fluid. As mentioned above, Linden (1973) used a model of vortex rings to predict a scaling for this entrainment rate (measured through an entrainment velocity u_e). However, as noted in Fernando (1991), this scaling has been contested. An alternative measure of the mixing is the mixing efficiency (η), which is the ratio of mixing to the sum of mixing and viscous dissipation (see Chapter 2 for a complete description). A canonical value of this mixing efficiency is often given as $\eta \approx 0.2$. Linden's scaling predicts a non-constant mixing efficiency. Indeed, mixing efficiencies $\eta \approx O(1)$ have been reported (Davies Wykes & Dalziel, 2014; Gayen *et al.*, 2013). In Chapter 6, we repetitively generate vortex rings in a stratified fluid, which is allowed to continuously evolve. For comparison, we measure both the vortex-ring-induced entrainment rate and mixing efficiency. We will show that, for moderate Richardson numbers, the density profile tends to a self-similar form, where the mixing efficiency is constant, in contrast to the theory of Linden (1973). Importantly, the value of the mixing efficiency is very high ($\eta \sim 0.42$), which was unexpected.

In order to study the dynamics of a stratified turbulent system, Balmforth *et al.* (1998) created a one-dimensional turbulence model that coupled the turbulent kinetic energy with the evolution of the density field. Using our knowledge of the vortex-ring mechanics and dynamics, we augment this model to create a simplified model of the vortex-ring-induced mixing system in Chapter 7. This model demonstrates that the constant mixing efficiency regime is recovered for a wide range of Reynolds, Richardson, and Schmidt numbers. These model results are supplemented with numerical simulations. All three methodologies (experimental, numerical, model) predict a similar evolution of the system.

This thesis has been organized into seven subsequent chapters. We start, in Chapters 2 and 3, with an introduction to the theory and experimental techniques used in the subsequent discussions. Next, Chapters 4 and 5 focus on the mechanics of the flow produced by vortex rings as they impact a stratified interface. Investigating the dynamics of the flow, Chapter 6 computes the mixing efficiency of vortex rings over a large number of vortex-ring generations. In order to model the vortex-ring-induced mixing, Chapter 7 presents a one-dimensional turbulence model for the system. Finally, we discuss these findings and conclude in Chapter 8.

A modified and extended version of each of the following chapters has been submitted for publication:

- Chapter 4 - OLSTHOORN, J. & DALZIEL, S. B. 2017*a* Three-dimensional visualization of the interaction of a vortex ring with a stratified interface. *Journal of Fluid Mechanics, Accepted*

- Chapter 5 - OLSTHOORN, J. & DALZIEL, S. B. 2016 Three-dimensional visualization of the interaction between a vortex ring and a stratified interface: The evolution of the density field. *Proceedings of the* VIII$^{\text{th}}$ *Int. Symp. on Stratified Flows*

- Chapter 6 - OLSTHOORN, J. & DALZIEL, S. B. 2015 Vortex-ring-induced stratified mixing. *Journal of Fluid Mechanics* **781**, 113–126

- Chapter 7 - OLSTHOORN, J. & DALZIEL, S. B. 2017*b* Vortex-ring-induced stratified mixing: Mixing model. *Journal of Fluid Mechanics, Under Review*

As such, each chapter is largely self-contained and, where appropriate, will review and extend the relevant theory, presented in Chapter 2, and experimental methods, presented in Chapter 3. The conclusions (Chapter 8) will provide the context of this thesis as a whole, and emphasize the major contributions of this work to the stratified turbulence literature.

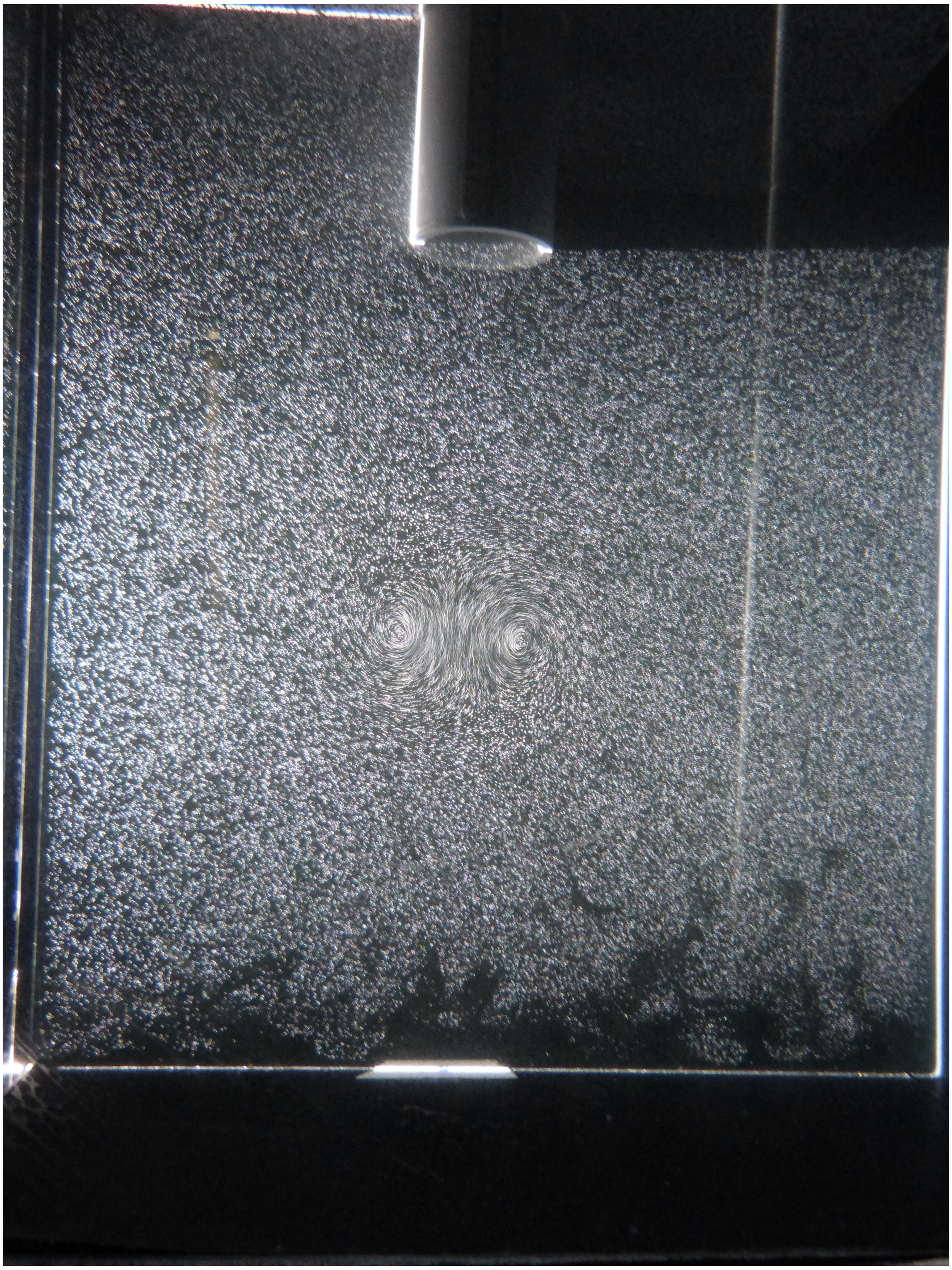

Plate 1: Photograph of a vortex ring propagating vertically downwards within an unstratified tank.

Chapter 2

Theoretical underpinnings

> and though I could not understand it, I was
> fascinated by its subject matter [...]
>
> —G I Taylor, in reference to Horace Lamb's Hydrodynamics.

Chapter 1 provided the historical context for the work performed in this thesis. This chapter supplements the introduction by providing the mathematical foundation for the statements made previously. These foundations will be referenced later in this thesis. This chapter is organized in a similar manner to Chapter 1. As such, we will begin with a discussion, in section 2.1, of the essential historical results related to fluid mixing and the associated application of vortex rings. We will discuss the theoretical formulation of vortex rings in section 2.2. We continue, in section 2.3, with a discussion of the instability mechanisms of unstratified vortex rings. Finally, section 2.4 concludes with a discussion of vortex rings impacting a solid wall.

2.1 Mixing theory

Historically, the mixing of a fluid was defined as the change in the gravitational potential energy of the system that results from the rate of energy input ($\mathbb{P}$). This definition excludes stirring of a homogeneous fluid, which is the displacement of Lagrangian fluid 'particles' without change to the gravitational potential energy of the system. It also excludes the change in gravitational potential energy in the system from purely thermodynamic diffusion. In this thesis, we will not explicitly consider any other source of potential energy in the system, other than gravitational potential energy. As such, unless otherwise noted, potential energy will refer to gravitational potential energy for the remainder of this thesis.

In order to compute the potential energy of the system, we must know the density of the fluid everywhere in the domain of interest. The density of a fluid (ρ) is a function of many variables, including the concentration of dissolved solutes ($\mathbb{S}_i$), temperature ($\mathbb{T}$), and pressure (P), amongst others. That is,

$$\rho\left(\mathbb{S}_1,\mathbb{S}_2,\ldots,\mathbb{T},P,\ldots\right).$$

In this thesis, we will only be considering the mixing of water solutions, where the dissolved solutes will typically be salts. As the maximum depth of our water tank is 60cm (with fluid velocities much slower than the speed of sound), variations in the density of the fluid as a result of pressure variations will be negligible. We will further make the assumption that, as the concentrations of the dissolved materials ($\mathbb{S}_i$) are low, that the density varies linearly with $\mathbb{S}$ and $\mathbb{T}$,

$$\rho=\rho_0+\alpha_0\left(\mathbb{T}-\mathbb{T}_0\right)+\Sigma_{i=1}\alpha_i\mathbb{S}, \tag{2.1}$$

for some constants $\{\alpha_i\}$ and reference temperature $\mathbb{T}_0$. The heat capacity is also assumed constant. For each of the physical experiments performed in this thesis, the temperature of the water was kept in near thermal equilibrium with the surrounding lab, and thus the temperature of the fluid was near uniform within the domain. These assumptions are implicit in the following chapters. Additionally, we will typically assume that the fluid is Boussinesq. These assumptions substantively simplify the analysis of the mixing. In particular, we do not need to consider variations in the internal energy of the system (see below). It is worth noting that we do not make these assumptions (of small density variations and constant temperature) when analyzing the experimental results of Chapter 6.

Under these assumptions, mixing has been quantified (using the above definition) according to the flux Richardson number (Ri_f), which is defined

$$\mathrm{Ri}_f=\frac{\mathbb{B}}{\mathbb{P}},$$

where $\mathbb{B}=<g\rho'w>$ is the volume-integrated vertical buoyancy flux computed from the acceleration due to gravity g, the density perturbation $\rho'=\rho-\rho_0$ and vertical velocity w. Typically, $\mathbb{B}$ is averaged over some appropriate time interval. Linden (1979) reviewed a number of previously published mixing experiments, which measured the mixing across a well-defined density interface, and computed their associated flux Richardson number. Figure 2.1, duplicated from Linden (1979), plots the set of flux Richardson numbers versus

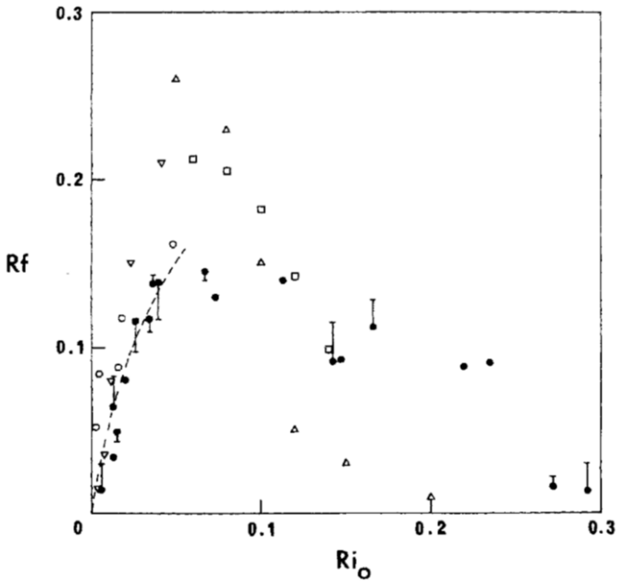

Fig. 2.1 Plot of the flux Richardson number as a function of overall Richardson number taken from Linden (1979). Data points with different symbols correspond to different experimental setups.

their corresponding bulk Richardson numbers,

$$\mathrm{Ri}_0 = \frac{g\Delta\rho}{\rho_0}\frac{L}{U^2},$$

which is a well defined quantity when there exists two homogeneous fluid layers separated by a sharp interface. Here, $\Delta\rho$ is the density jump across the interface relative to the reference density ρ_0. Characteristic length (L) and velocity (U) scales are defined for each experiment. This curve supports the conclusion that the buoyancy flux is not a monotonic function of the Richardson number. Results are plotted for a wide range of experimental setups (see Linden (1979) for a complete description).

However, this definition of mixing is somewhat poorly defined as it also includes the reversible changes in the potential energy of the system. For example, linear internal waves may instantaneously produce a change in the potential energy of the system before dissipating and reverting the system back to its previous state, with minimal mixing of the stratification. This ambiguity led Winters *et al.* (1995) to define mixing as the irreversible change in the potential energy of the system that results from an input of energy. We will use this definition here.

In order to distinguish between irreversible and reversible changes to the potential energy of the system, Winters *et al.* (1995) divided the potential energy (PE) into available potential energy (APE), and the background potential energy (BPE), where PE $=$ APE $+$ BPE. BPE is defined as the potential energy of the system once the density field has been adiabatically-sorted. APE encapsulates the remainder of the potential energy produced within the system. As such, changes to the BPE of the system are irreversible, and thus, BPE cannot decrease in time. Thermodynamic diffusion is perpetually increasing the BPE of the system. Conversely, the APE encapsulates all reversible (time-dependent) increases of the potential energy of the system. Peltier & Caulfield (2003) defined the generic pathway of kinetic energy (KE), APE and BPE as

$$\begin{aligned}\frac{d}{dt}\mathrm{KE} &= \mathbb{H} + \varepsilon,\\ \frac{d}{dt}\mathrm{APE} &= -\mathbb{H} - \mathbb{M},\\ \frac{d}{dt}\mathrm{BPE} &= \mathbb{M} + D_\rho.\end{aligned}$$

That is, the buoyancy flux ($\mathbb{H}$) is the transfer of energy from the kinetic to available potential energy. Note that $\mathbb{H}$ can be both positive or negative indicating that APE may generate KE and vice versa. Conversely, mixing ($\mathbb{M}$) is the transfer of available potential energy to background potential energy, and quantifies the rate of increase of BPE that results from fluid motion. Mixing is irreversible. As noted above, the background potential energy is continuously increasing (for a stratified fluid) as a result of background diffusion (D_ρ). This formulation ensures that any source of kinetic energy will eventually be dissipated (at rate ε[1]) or result in mixing of the background stratification. This leads naturally to the definition of the mixing efficiency η as

$$\eta = \frac{\mathbb{M}}{\varepsilon + \mathbb{M}}. \tag{2.2}$$

It is important to mention that, as noted by Tailleux (2009), this view of mixing is not always appropriate. Tailleux (2009) clarifies that it is unnecessary to construct a new mixing mechanism $\mathbb{M}$ for BPE production. Rather, the increase in BPE of the system that results from the conversion of internal energy (already accounted for through D_ρ) is the true mixing mechanism. Mixing, then, is simply the production of internal energy, which will subsequently increase BPE. Under our assumption of a Boussinesq fluid with constant α_i, this view is identical to that of Winters *et al.* (1995)[2]. However, if the fluid is not Boussinesq, or if the $\{\alpha_i\}$ are not constant, this distinction becomes important. For example, this distinction is clearly important for the case of nonlinear mixing. We will only consider mixing in the

---

[1] The dissipation rate is computed: $\varepsilon = \tau_{ij}e_{ij}$, for stress tensor τ_{ij} and strain tensor e_{ij}.

[2] We also implicitly assume that the heat capacity of the fluid is constant

context of Winters *et al.* (1995) and Peltier & Caulfield (2003), but we note the important assumptions that implicitly go into this model.

In this thesis, we will use a modified version of the mixing efficiency (2.2). The fundamental basis for both definitions is the same. Here, we compute a time integrated mixing efficiency

$$\eta = \frac{\int_0^T \mathbb{M}(t')\,dt'}{\int_0^T \mathbb{P}\,dt'} \approx \frac{\int_0^T \mathbb{M}(t')\,dt'}{\int_0^T \mathbb{M}(t') + \varepsilon(t')\,dt'}, \tag{2.3}$$

for some time interval T, long compared to the dissipation/mixing timescale of the system. This was denoted at η_c is Peltier & Caulfield (2003). As we will see, $\int_0^T \mathbb{P}\,dt'$ will be defined as the kinetic energy of the input vortex ring. This definition of the mixing efficiency defines the change in BPE for a given input of available energy (KE+APE). We return to this definition in Chapter 6.

In order to compute the background potential energy of a Boussinesq system from a given density dataset, it is necessary to compute the potential energy of the adiabatically sorted density field. That is, given a density field $\rho(x,y,z)$, one can sort ρ to find a sorted field $\rho_s(z)$ which depends only on the vertical coordinate z. The BPE is then computed (for a finite volume) as:

$$\text{BPE} = \int g\rho_s z\; dxdydz.$$

In practice, it is often convenient to numerically compute BPE from the probability density function (pdf), $P(\rho)$, of density ρ, as was originally proposed by Tseng & Ferziger (2001). In this formulation, it is possible to compute the vertical position z^* that each parcle of fluid would have if it were adiabatically rearranged. That is,

$$z^*(\rho) = \frac{V}{A}\int_\rho^{\rho_M} P(\rho)d\rho,$$

provided the maximum density (ρ_M) within a domain of volume (V) and cross sectional area (A) is know. Then thee BPE is simply computed

$$\text{BPE} = \int g\rho(z^*)z^*\; dxdydz.$$

However, in this thesis, we explicitly sort the density field when we compute the background potential energy. The available potential energy can then be appropriately computed as:

$$\text{APE} = \text{PE} - \text{PE}_B = \int g\rho z\; dxdydz - \int g\rho_s z\; dxdydz.$$

It is worth noting that once all of the kinetic energy in the system has dissipated and APE $= 0$, then PE $=$ BPE.

Under this mixing paradigm, we continue with a discussion of a mixing box experiment. Turner's investigation into the mixing produced by a vertically oscillating mixing grid motivated the use of vortex rings to study turbulent mixing.

2.1.1 Turner's mixing box experiment

In this thesis, we will focus on externally-forced mixing experiments, where the kinetic energy is produced external to the mixing location. As an example of such an experiment, Turner's mixing box (Turner, 1968) is setup with a vertically oscillating grid within a stratified fluid. Figure 2.2 is a photograph of a similar mixing box experiment. The turbulence from the oscillating grid mixes the stratification, producing a nearly homogeneous fluid layer surrounding the grid. It is observed that the grid generated turbulence often produces a sharp interface between the homogeneously mixed layer and the unperturbed stratification. The traditional version of this experiment is initialized with a two-layer stratification such that the system evolves in a self-similar manner; the system maintains two homogeneous layers with a sharp interface. Turner's experiment extracted fluid from the mixed layer in order to keep the interface between the two fluid layers stationary. Measuring the rate of fluid extraction, normalized by the tank plan area (A), provided a measure of the mixing through an entrainment velocity (u_e). Figure 2.3 is a copy of the mixing rate (entrainment velocity) plot presented in Turner (1968). Both salt (open dots) and heat (solid dots) experiments were performed. Turner concluded that the entrainment rate of heat experiments scales as $u_e \sim \mathrm{Ri}^{-1}$ and $u_e \sim \mathrm{Ri}^{-\frac{3}{2}}$ for the salt experiments for $Ri \gtrsim 1$.

In this experiment, the density interface is sharp and, as the interface deformations are small compared to the height of the two fluid layers, the entrainment velocity provides an estimate for the change in BPE of the system. If we also make the assumption that diffusion of the background density profile is negligible (that is, $\frac{D_\rho}{\mathbb{M}} \ll 1$) ,a fairly crude approximation in the case of heat experiments, we can write that

$$\mathbb{M} \sim g\Delta\rho L_z u_e A,$$

where L_z is the depth of the mixed layer. If we further assume that the system has reached an equilibrium such that there is no build up of kinetic energy at the interface, then we can establish that

$$\mathbb{P} \approx \mathbb{M} + \varepsilon \sim \frac{\left(\rho_0 U^2\right)\left(a^3\right)}{\frac{a}{U}},$$

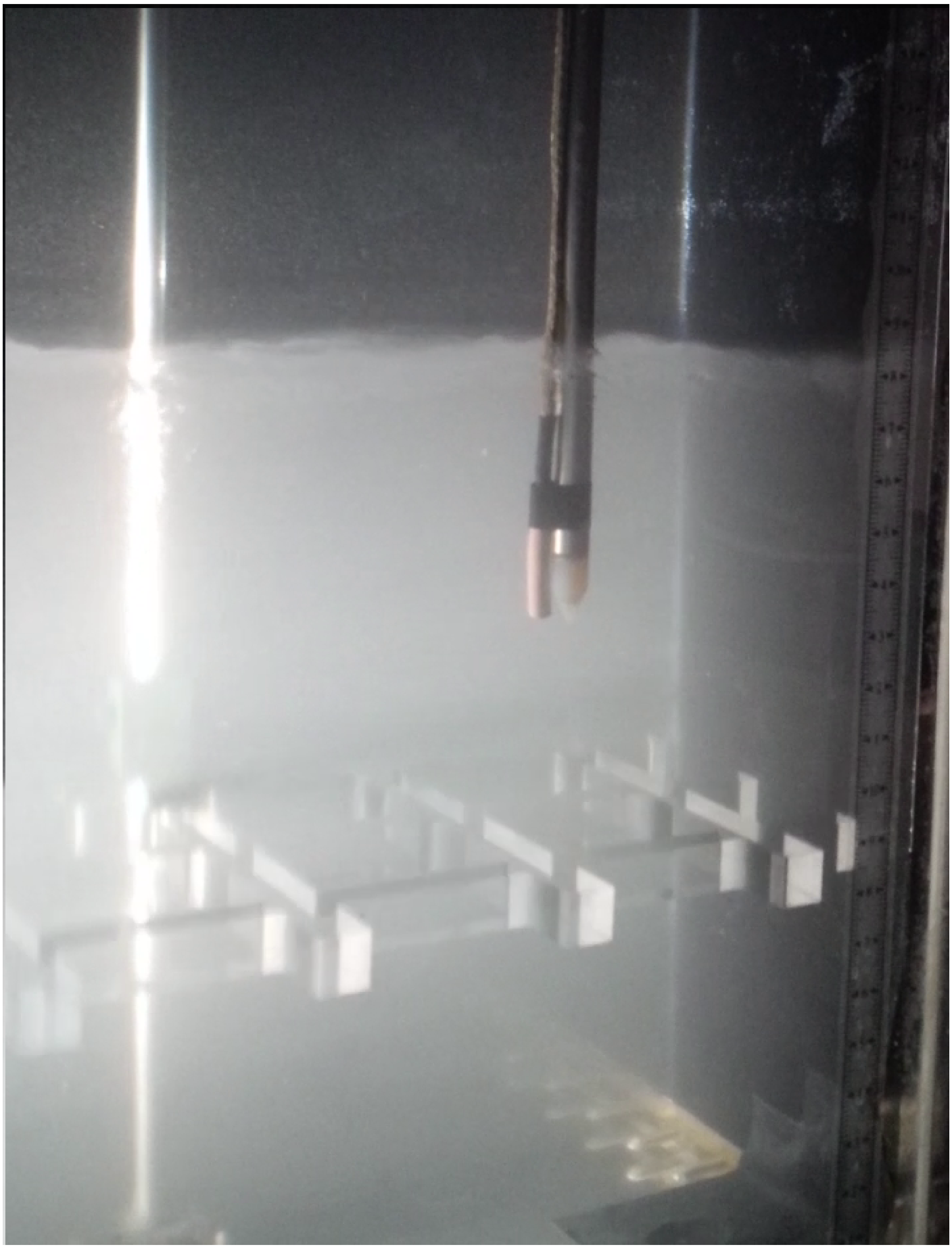

Fig. 2.2 Photograph of a mixing box experiment, similar to the one performed by Turner (1968). This experiment was conducted in collaboration with Nicole Lindsay.

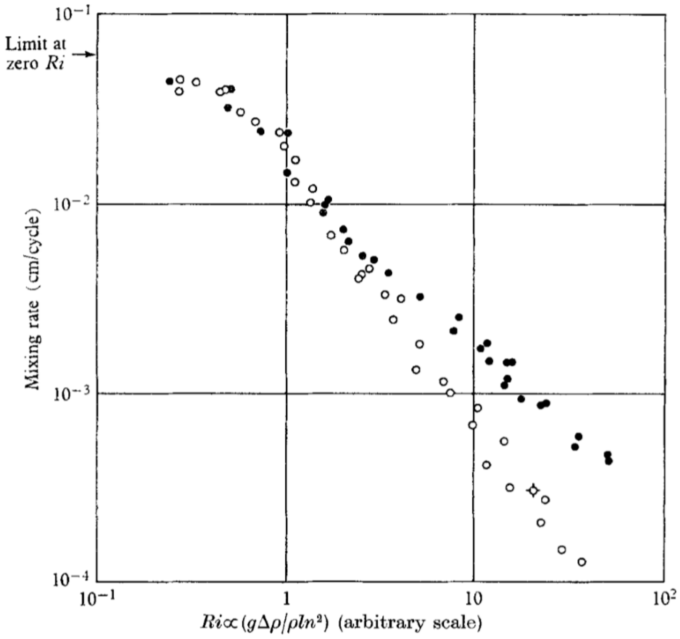

Fig. 2.3 Figure of the mixing rate in Turner's mixing box experiment, copied from Turner (1968). Here, the mixing rate for salt is given by the open dots and heat is denoted by the solid black dots. The frequency of the grid oscillations is denoted (here only) as n.

for some characteristic velocity U and length scale a, typically estimated from the turbulent eddies at the interface height. We will assume that $a \ll L_z$. The rate at which the turbulent kinetic energy is supplied to the interface is given as $\mathbb{P}$. The (time-dependent) mixing efficiency is then estimated as

$$\eta \approx \frac{g\Delta\rho L_z u_e}{(\rho_0 U^2)(U a^2)} \sim \frac{u_e}{U}\mathrm{Ri}, \qquad \mathrm{Ri} = \frac{g\Delta\rho}{\rho_0}\frac{a}{U^2}, \tag{2.4}$$

where $\frac{a}{L_z}$ is fixed. The data from figure 2.3 suggests that, for a fixed stratifying agent, the entrainment law has the form

$$\frac{u_e}{U} \sim \mathrm{Ri}^{-n}, \tag{2.5}$$

over some range of Richardson numbers. By accurately predicting the entrainment coefficient n, the mixing efficiency is then identically determined. As noted by Fernando (1991), many experiments have been performed to determine n, without a clear consensus on its precise value. Typical values are within $1 \le n \le \frac{3}{2}$.

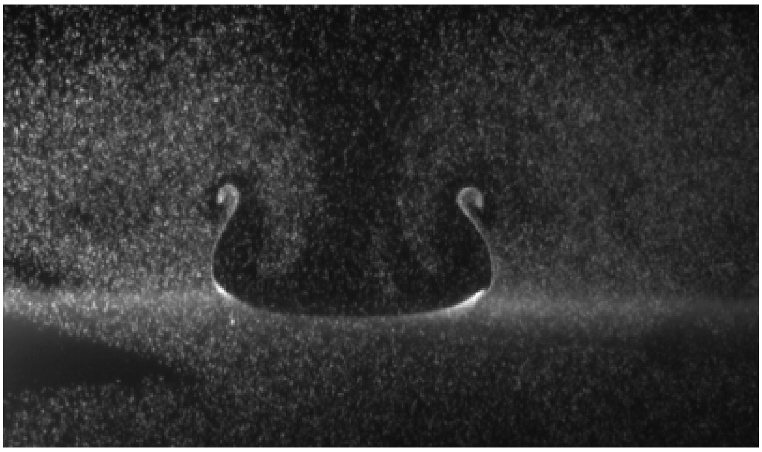

Fig. 2.4 Photograph of a vortex ring as it reaches its point of maximum penetration.

2.1.2 Linden's vortex ring mixing argument

Linden (1973) proposed a model for the entrainment coefficient (see equation (2.5)) by investigating vortex rings impacting a stratified interface. Linden's argument relies on the balance between the rate at which the turbulent kinetic energy is supplied to the interface and the rate at which the potential energy of the system is increased. For high Richardson numbers, which were considered by Linden, the vortex rings will expand as they approach the density interface. Linden's argument begins by determining a scaling law for the effective area of the vortex rings as they expand, and then proceeds to predict the entrainment coefficient.

Linden considered a vortex ring when it reached its point of maximum penetration, such that its vertical propagation speed was instantaneously zero. Figure 2.4 is a picture taken of a vortex ring near its point of maximum penetration. We denote the maximum penetrative depth of the vortex ring into the lower layer as h. Outside of the vortex ring core, the flow is assumed irrotational, which enables us to use potential theory where $(u_r, w) = (\partial_r \phi, \partial_z \phi)$ in cylindrical coordinates, defined below. At this instant, Bernouilli's equation, evaluated along the interface (streamline) under the impinging vortex ring, is

$$g\Delta\rho h = \frac{1}{2}\rho_0 U^2 - \rho_0 \dot{\phi}, \tag{2.6}$$

for velocity potential ϕ. Here, U is the propagation speed of the freely propagating vortex ring (in an unstratified fluid). One can then show that $\dot{\phi} = \frac{d}{dt}\int_{z(t=0)}^{z(t)} \dot{w}dz' = \int_0^t \dot{w}wdt' = \frac{1}{2}w^2 \sim U^2$. Thus, equation (2.6) can be rearranged to show that

$$\frac{h}{a} \sim \frac{1}{\mathrm{Ri}}. \tag{2.7}$$

In the context of vortex rings, the characteristic length scale a is defined as the vortex ring diameter.

As mentioned above, as the vortex ring impacts the stratification, it will also expand due to its interaction with its image ring. This is similar to a vortex ring impacting a free-slip wall, which we will discuss in greater detail in section 2.4. If we assume that no mixing has occurred during the initial impingement (which we will justify later in this thesis), the volume of the vortex ring remains unchanged but it will have a new effective radius, r_e, such that

$$a^3 \sim h r_e^2.$$

From equation (2.7) we can show that

$$\frac{r_e^2}{a^2} \sim \mathrm{Ri}. \tag{2.8}$$

With this scaling in hand, we can now determine the entrainment rate dependence on the Richardson number.

As the vortex ring impacts the interface, most of its kinetic energy (KE$\sim \rho_0 a^3 U^2$) will be converted into potential energy. Linden argued that the rate at which the turbulent kinetic energy will be made available during the rebound of the interface, averaged over the area of the interaction, is then given as $\sim \rho_0 a^3 U^2/\tau/r_e^2$. Here, τ is the timescale of the interface rebound. During the rebound, potential energy of the system (averaged over the tank plan area) will increase by $\sim g\Delta\rho u_e d$ for the interface rebound height d. By equating the rate of turbulent kinetic energy production with the rate of potential energy increase, we find that

$$\frac{\rho_0 a^3 U^2}{\tau r_e^2} \sim g\Delta\rho d u_e, \implies u_e \sim \frac{1}{\tau}\frac{1}{\mathrm{Ri}}\frac{\rho_0}{g\Delta\rho}\frac{aU^2}{d}, \tag{2.9}$$

Here, the idea is to average over many such vortex ring events such that u_e is a well defined quantity.

With reference to figure 2.4, it is seen that during the impact, the lower layer fluid is raised to a height comparable with the ring diameter a. As vortex rings are known to maintain sharp interfaces, it is argued that $d \sim a$. The last unknown of the problem is the interface rebound timescale τ. Linden (1973) assumed that the recoil of the interface is a purely buoyancy driven response, which implies that

$$\tau \sim \sqrt{\frac{\rho_0 d}{g\Delta\rho}}.$$

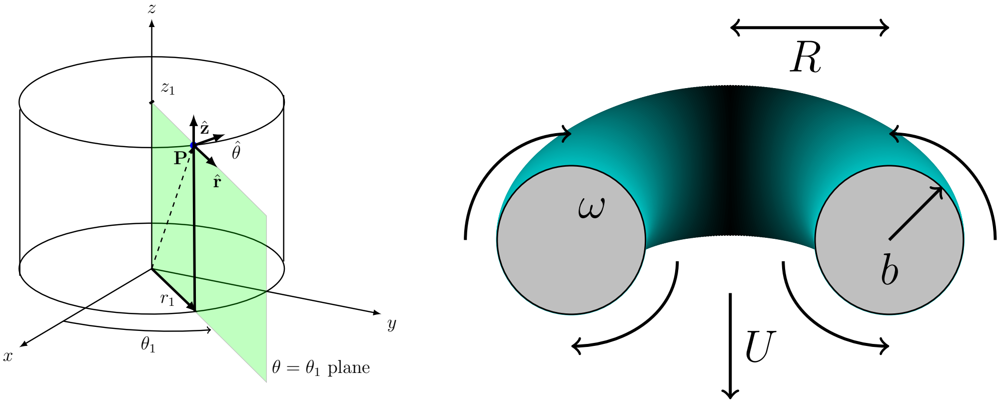

(a) (b)

Fig. 2.5 A diagram of the cylindrical coordinate system (a), along with a cartoon of a vortex ring (b).

With this result, equation (2.9) can be re-written as

$$\frac{u_e}{U} = C\,\mathrm{Ri}^{\frac{-3}{2}},$$

for some constant C. Thus, Linden (1973) predicts an entrainment coefficient of $n = \frac{3}{2}$. This result appears to agree well with the published data from the salt stratified experiments found in Turner (1968). However, there still exists a dispute over the accuracy of this prediction (see Fernando (1991)).

It is worth noting, at this point, that Linden (1973) was considering the average mixing of the vortex ring over time. In this thesis, we will investigate the total mixing produced per unit event, as defined in equation (2.3). That is, we consider the aggregate mixing produced by each vortex ring.

2.2 Theoretical formulation of vortex rings

In order to fully understand the vortex-ring-induced dynamics and associated mixing, this chapter continues with a discussion of the essential mathematical results for unstratified vortex rings. We begin with a definition: vortex rings are toroidal fluid-structures of azimuthal vorticity that propagate under their self-induced velocity field. The azimuthal symmetry of these structures has allowed for their study in a broad range of contexts. Much of the following discussion on the theoretical formulation of vortex rings can be found in Akhmetov (2009), Saffman (1995) and Lamb (1945). For this discussion, we introduce cylindrical (r, θ, z) coordinates. Figure 2.5(a) presents a sketch of this coordinate system. Figure 2.5(b) plots a cartoon of a vortex ring, where only half the ring is shown in order to aid the visualization. Note that the vortex ring is symmetric about the z-axis. For an inviscid, uniform-density fluid for which the flow field is azimuthally symmetric (as for the unperturbed vortex ring), then the equations for the velocity field $\mathbf{u}$, the streamfunction (ψ) in the rz-plane, and vorticity (ω) are written as

$$\boldsymbol{\omega} = \nabla \times \mathbf{u}, \qquad u_r = -\frac{1}{r}\frac{\partial \psi}{\partial z}, \qquad u_z = \frac{1}{r}\frac{\partial \psi}{\partial r}, \qquad \frac{D\boldsymbol{\omega}}{Dt} = \boldsymbol{\omega} \cdot \nabla \mathbf{u}. \tag{2.10}$$

Here, $\frac{D}{Dt} = \partial_t + \mathbf{u} \cdot \nabla$ is the material derivative, and u_r, u_z are the radial and vertical components of velocity, respectively. Boldface variables denote vector quantities. By construction, we will define $\boldsymbol{\omega} = \omega \hat{\boldsymbol{\theta}}$, such that the vorticity vector is entirely in the azimuthal ($\hat{\boldsymbol{\theta}}$) direction. We highlight that figure 2.5(a) depicts the direction of $\hat{\boldsymbol{\theta}}$. As a consequence, we can simplify the azimuthal vorticity equation,

$$\frac{D}{Dt}\omega = \frac{u_r \omega}{r}, \implies \frac{D}{Dt}\left(\frac{\omega}{r}\right) = 0, \tag{2.11}$$

which implies that

$$\frac{\omega}{r} = f(\psi). \tag{2.12}$$

That is, the quantity $\frac{\omega}{r}$ is constant along streamlines. As we will see, it is typically assumed in the theoretical analysis that, within the core, $f(\psi) = A$, where A is a constant.

We note that this result is directly related to Kelvin's circulation theorem, which states that for an inviscid, uniform density fluid, the total circulation around any closed Lagrangian curve is constant. We do not continue this discussion, but reference the interested reader to Batchelor (2000) for more information.

2.2.1 Streamfunction

Provided that the vorticity distribution is known, we can use the well known Biot-Savart law to solve for the Stokes streamfunction in cylindrical coordinates:

$$\nabla^2\left(\frac{\psi}{r}\hat{\boldsymbol{\theta}}\right) = -\omega\hat{\boldsymbol{\theta}} \implies \psi(\mathbf{x}) = \frac{-1}{4\pi}\int \frac{r\omega(\mathbf{x}')}{|\mathbf{x} - \mathbf{x}'|}\, dV', \tag{2.13}$$

The above integral is integrated over all space. If we determine ψ in any (r,z) plane, symmetry then ensures that we know ψ at all points within the domain. By evaluating ψ on the $\theta = 0$ plane (see figure 2.5(a) for an example of such a constant θ plane), the streamfunction ψ is determined[3]

$$\psi(r,z) = \frac{-1}{4\pi}\int_{x',z'}\left(\int_0^{2\pi}\frac{\cos\theta' d\theta'}{r^2+r'^2-2r'r\cos\theta'+(z-z')^2}\right) r\omega(\mathbf{x}')r'dr'dz'. \tag{2.14}$$

With reference to Lamb (1945), by defining $k^2 = \frac{4rr'}{(r+r')^2+(z-z')^2}$, we can then write

$$I = \left(\int_0^{2\pi}\frac{\cos\theta'\, d\theta'}{r^2+r'^2-2r'r\cos\theta'+(z-z')^2}\right) = \frac{2}{(rr')^{\frac{1}{2}}}\left[\left(\frac{2}{k}-k\right)F(k)-\frac{2}{k}E(k)\right],$$

in terms of the complete elliptic integrals of the first (F) and second (E) kind. The stream function is then given as

$$\psi = \frac{-1}{2\pi}\int_{r',z'}(rr')^{\frac{1}{2}}\left[\left(\frac{2}{k}-k\right)F(k)-\frac{2}{k}E(k)\right]\omega(\mathbf{x}')\, dr'dz'. \tag{2.15}$$

2.2.2 Thin vortex rings - Lamb's solution

Under the framework described above, Lamb (1945) considered vortex rings with a circular core of finite radius b inside of which $f(\psi) = A$, a non-zero constant. The approach we take here follows that of Saffman (1995). The diameter of these rings is $2R$. The aspect ratio of the vortex ring ($\frac{b}{R}$) is assumed to be small. As such, we will defined a core-centred coordinate system (s,ϕ,θ),

$$r = R + s\sin\phi, \qquad z = s\cos\phi, \qquad r' = R + s'\sin\phi', \qquad z' = s'\cos\phi', \tag{2.16}$$

where s, s' denotes the distance from the centre of the vortex core.Thus, assuming a circular core (it can be shown by expanding s in powers of $\frac{b}{R}$ that, to leading order, the core is indeed circular), the vorticity of the vortex ring is given,

$$\omega(\mathbf{x}') = \begin{cases} \omega_0\left(1+\frac{s'}{R}\sin\phi'\right), & s<b \\ 0, & s>b \end{cases},$$

---

[3] We note that in Cartesian coordinates (x,y,z):

$$\omega(\mathbf{x}')\cdot\hat{x} = -\omega\sin\theta, \qquad \omega(\mathbf{x}')\cdot\hat{y} = \omega\cos\theta.$$

where $\omega_0 = AR$. The small aspect ratio assumption drastically simplifies expression (2.15). Here, the small aspect ratio assumption allows us to approximate the elliptic integrals within the core,

$$\left(\frac{2}{k}-k\right)F(k)-\frac{2}{k}E(k)=\ln\frac{4}{k'}-2+O(k'^2\ln k'), \qquad k'^2=1-k^2.$$

Substituting for the core centred coordinates (see equation (2.16)), we determine that,

$$\begin{aligned}
\psi &= \frac{-1}{2\pi}\int_{r',z'}\omega(\mathbf{x}')\left(r'r\right)^{\frac{1}{2}}\left(\ln\frac{8R}{\left((r-r')^2+(z-z')^2\right)^{\frac{1}{2}}}-2\right)dr'dz', \\
&= \frac{-1}{2\pi}\int_{s',\phi'}\omega_0\left(1+\frac{s'}{R}\sin\phi'\right) \\
&\qquad \left[R\left(1+\frac{s\sin\phi+s'\sin\phi'}{2R}+O\left(\frac{ss'}{R^2}\right)\right)\right] \\
&\qquad \left(\ln\left[\frac{8R}{(s'^2+s^2-2s's\cos\phi-\phi')^{\frac{1}{2}}}\left(1+\frac{s}{2R}\sin\phi+\frac{s'}{2R}\sin\phi'+O\left(\frac{s^2}{R^2}\right)\right)\right]-2\right) \\
&\qquad s'\,ds'd\phi'. \qquad (2.17)
\end{aligned}$$

Equation (2.17) can be integrated to determine ψ within the ring core (see Fraenkel (1969) for the details)[4]:

$$\psi=\frac{-\omega_0 Rb^2}{2}\left(\ln\frac{8R}{b}-\frac{3}{2}-\frac{s^2}{2b^2}+\frac{s}{2R}\sin\phi\left(\ln\frac{8R}{b}+1-\frac{5s^2}{4b^2}\right)+O\left(\frac{b^2}{R^2}\ln\frac{R}{b}\right)\right).$$

As the core is circular, within the core $s\in[0,b]$. Outside of the core, the flow field is given by potential theory. In principle, with ψ known, all other properties of the vortex ring can be determined. In particular, we can compute the speed of the vortex ring (U). First, we will

---

[4] We use the integral identities

$$\int_0^{2\pi}\ln\left(s'^2+s^2-2s's\cos\phi-\phi'\right)^{\frac{1}{2}}d\phi'=\begin{cases}2\pi\ln s', & s'>s\\ 2\pi\ln s, & s>s'\end{cases},$$

and

$$\int_0^{2\pi}\cos\left(\phi-\phi'\right)\ln\left(s'^2+s^2-2s's\cos\phi-\phi'\right)^{\frac{1}{2}}d\phi'=\begin{cases}-\pi\ln\frac{s}{s'}, & s'>s\\ -\pi\ln\frac{s'}{s}, & s>s'\end{cases}.$$

define the circulation

$$\Gamma = \int \omega \, dr' dz' = \pi \omega_0 b^2.$$

Provided that there exists a constant propagation speed (U) for this vortex ring, we can define a ring-centred coordinate system. That is, in the reference frame of the vortex ring, the Stokes streamfunction is given

$$\Psi = -\frac{1}{2} U r^2 + \psi.$$

If we evaluate Ψ along the circular boundary of the vortex ring ($s = b$), we then find (substituting in for Γ),

$$\begin{aligned} \Psi(s = b) = -\frac{1}{2} U R^2 + \frac{-\Gamma R}{2\pi} \left(\ln \frac{8R}{b} - \frac{3}{4} \right) \\ + \sin\phi \left(URb + \frac{-\Gamma b}{4\pi} \left(\ln \frac{8R}{a} - \frac{1}{4} \right) \right) + O\left(\frac{b^2}{R^2} \ln \frac{R}{b} \right). \end{aligned} \tag{2.18}$$

As the vortex core boundary is a streamline, Ψ must be constant along $s = b$. That is, the coefficient of $\sin\phi$ must be zero. Thus, to leading order, we recover the propagation velocity for a thin vortex with a circular core of constant vorticity as

$$U = \frac{\Gamma}{4\pi R} \left(\ln \left(\frac{8R}{b} \right) - \frac{1}{4} \right).$$

It is worth noting that Saffman (1995) has shown that a ring with a Gaussian core (non-constant vorticity) will propagate slower as

$$U = \frac{\Gamma}{4\pi R} \left(\ln \left(\frac{8R}{b_e} \right) - 0.558 \right),$$

for an effective core radius $b_e = \sqrt{4\nu t}$, where ν is the molecular viscosity of the fluid and time t.

2.2.3 Hill's vortex

At the other end of the spectrum, the simplifications that allowed for the computation of the streamfunction of the thin-core vortex rings can no longer be applied for large aspect ratios ($\frac{b}{R} \sim 1$). Thankfully, there exists an exact solution for a spherical vortex of constant $f(\psi)$, known as a Hill's spherical vortex. Starting with equations (2.10), we use the conservation relation (2.12) to write down

$$\partial_r^2 \psi - \frac{1}{r}\partial_r \psi + \partial_z^2 \psi = -r^2 f(\psi). \tag{2.19}$$

Let us make the assumption that $f(\psi) = A$ is constant inside of a sphere of radius R, and zero outside. This equation has an exact solution if we prescribe that $\psi = 0$ on the surface of the sphere,

$$\psi = \frac{1}{10} A r^2 \left(a^2 - z^2 - r^2\right), \quad r < R.$$

The outer flow is then prescribed by the potential flow around a sphere with translating velocity U,

$$\psi = -\frac{Ur^2}{2}\left[1 - \frac{R^3}{(r^2+z^2)^{\frac{3}{2}}}\right], \quad r > R.$$

Imposing continuity of the velocity field (derivatives of ψ) across the boundary at $r = R$ determines $A = \frac{15U}{2R^2}$. Thus, one can write down an explicit form of the velocity field for a spherical vortex

$$u_r = \begin{cases} \frac{3}{2} U \frac{zr}{R^2}, & r \le R \\ \frac{3}{2} U \frac{zr}{R^2} \left(\frac{R^2}{z^2+r^2}\right)^{\frac{5}{2}}, & r > R \end{cases}, \qquad u_z = \begin{cases} \frac{3}{2} U \left(1 - \frac{2r^2+z^2}{R^2}\right), & r \le R \\ U\left[\left(\frac{R^2}{r^2+z^2}\right)^{\frac{5}{2}} \left(\frac{2z^2-r^2}{2R^2}\right) - 1\right], & r > R \end{cases}. \tag{2.20}$$

This analytic solution to the Euler equations makes a Hill's vortex simple to implement numerically. However, it should be noted that there is a discontinuity in the vorticity field across the boundary $r = R$ and, as such, a Hill's vortex is not a solution to the Navier-Stokes equations, which have a non-zero viscosity.

2.2.4 Norbury rings

Between a Hill's spherical vortex, and Lamb's model of a thin vortex ring, Norbury (1973) determined a family of vortex rings with varying aspect ratio. Similar to the Hill's vortex, Norbury rings have the distribution

$$f(\psi) = \begin{cases} A, & \mathbf{x} \in \mathbb{D}, \\ 0, & \text{elsewhere}, \end{cases}$$

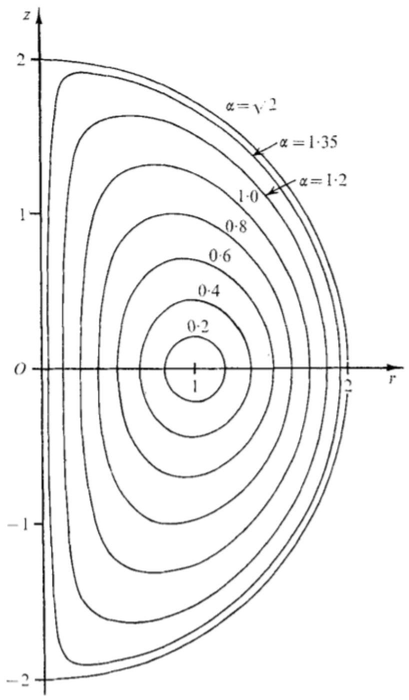

Fig. 2.6 Plot of the shape of the Norbury vortex rings for increasing α. This image has been duplicated from Norbury (1973).

for some core region $\mathbb{D}$ with perimeter $\partial\mathbb{D}$ and area D. Norbury found a family of vortex rings that depend on a single parameter $\alpha \in [0, \sqrt{2}]$ defined as $\alpha = \frac{D}{\pi R^2}$, where R is the distance from the vortex ring axis to the centre of $\mathbb{D}$. Figure 2.6 plots $\partial\mathbb{D}$ for increasing α, duplicated from Norbury (1973). Norbury rings provide a useful class of inviscid solutions to compare with experimentally generated vortex rings. For more details on Norbury rings, see Norbury (1973).

2.3 Vortex-ring stability

As noted in Chapter 1, vortex rings are unstable. This was originally demonstrated by Widnall & Sullivan (1973), based upon the work of Crow (1970) who performed the stability analysis of vortex filaments. Indeed, the study of the stability of vortex rings has proven to be very fruitful. This investigation started by considering the stability of anti-parallel vortex filaments, the three-dimensional extension of a vortex dipole (see Crow (1970) and Tsai & Widnall (1976)). It has been shown that vortex filaments demonstrate many of the instabilities commonly found in vortex rings. In particular, Crow (1970) determined that vortex pairs will go unstable to a long wavelength instability. This instability, now called

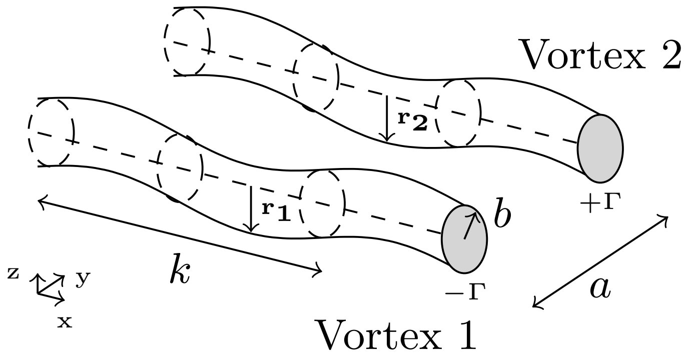

Fig. 2.7 Diagram of the perturbed vortex filaments.

a Crow instability, fundamentally depends on the coupling of perturbations to each vortex filament. Later Widnall *et al.* (1974) demonstrated that a second instability (corresponding to a second bending mode) of a vortex pair is the dominant instability mode. In this section, we discuss the stability of vortex filaments due to their much simpler mathematical analysis. We focus on the two instabilities listed above. We will conclude this section by discussing how the curvature of the rings modify the instability. This work will have direct relevance to Chapter 4 when we investigate the instability of vortex rings in a stratified environment.

2.3.1 Stability of vortex filaments

Consider two, straight, thin vortex tubes of opposite signed, but equal circulation Γ. The unperturbed vortex tubes are anti-parallel, located at positions $y = +\frac{a}{2}$ and $y = -\frac{a}{2}$ respectively. As a simplification, we will assume that the vortex tubes have constant vorticity inside of their core radius (b), and zero elsewhere. In this work, "thin" refers to vortex pairs with $a \gg b$. Here, we write out the well known Biot-Savart law relating the vorticity ω to the velocity field $\mathbf{u}$,

$$\begin{aligned} \mathbf{u}(\mathbf{x}) &= \frac{1}{2\pi}\int_{V_{2D}} \frac{(\mathbf{x}-\mathbf{x}')\wedge\omega(\mathbf{x}')}{|\mathbf{x}-\mathbf{x}'|^2}\, dV' \qquad \text{2D}, \\ \mathbf{u}(\mathbf{x}) &= \frac{-1}{4\pi}\int_{V_{3D}} \frac{(\mathbf{x}-\mathbf{x}')\wedge\omega(\mathbf{x}')}{|\mathbf{x}-\mathbf{x}'|^3}\, dV' \qquad \text{3D}. \end{aligned} \tag{2.21}$$

For unperturbed line vortices (a 2D vortex dipole), one can show that a vortex pair will translate with a constant speed equal to $\frac{\Gamma}{2\pi a}$. We recall that Γ is the circulation of the vortex core. Let us now additionally assume that there exists small wave-like perturbations $\mathbf{r}_1 = b + \hat{\mathbf{r}}_1(y,z)\exp[\alpha t - ikx]$ and $\mathbf{r}_2 = b + \hat{\mathbf{r}}_2(y,z)\exp[\alpha t - ikx]$ on the first and second vortices respectively, where we are implicitly taking the real part of the perturbation. Figure 2.7 plots a diagram of the physical setup. In a frame of reference moving with the vortex pair, we consider the velocity induced by the vortex perturbations. Without loss of generality, we consider the velocity field at the centre of vortex 2, where one can decompose the velocity field as

$$\mathbf{u}_2 = \mathbf{u}_{1,0} + \mathbf{u}_{1,\varepsilon} + \mathbf{u}_{2,\varepsilon}.$$

That is, the velocity field at the core of vortex 2 ($\mathbf{u}_2$) is given by the combination of the straining field produced by the unperturbed vortex 1 ($\mathbf{u}_{1,0}$), the perturbation velocity field produced by the perturbed vortex 1 ($u_{1,\varepsilon}$), and the self-induced rotation of the perturbation to vortex 2 ($\mathbf{u}_{2,\varepsilon}$). We will assume that there is no streamwise flow along the filaments (i.e. $u_i = 0$, see below). Far from the vortex centre, the vortices can be considered to be point vortices, and as such the Biot-Savart law (equation (2.21)) can be used to solve for the velocity components $\mathbf{u}_{1,0}$ and $\mathbf{u}_{1,\varepsilon}$, written as

$$\begin{aligned}
v_{1,0} &= \frac{\Gamma}{2\pi a^2} z_2, \\
w_{1,0} &= \frac{\Gamma}{2\pi a^2} y_2, \\
v_{1,\varepsilon} &= -\frac{\Gamma}{2\pi a^2}\Big((ka)^2 K_0(ka) + (ka) K_1(ka)\Big) z_1, \\
w_{1,\varepsilon} &= -\frac{\Gamma}{2\pi a^2}\left(kaK_1(ka)\right) y_1.
\end{aligned}$$

Here, we have explicitly written $\mathbf{u}_i = (u_i, v_i, w_i)$ with perturbation $\hat{\mathbf{r}}_i = (x_i, y_i, z_i)$. The functions K_0, K_1 are modified Bessel functions of the first kind. As $u_{2,\varepsilon}$ is the self-induced rotation as a result of the vortex perturbation, it necessarily has the form

$$v_{2,\varepsilon} = \omega_s' z_2, \qquad w_{2,\varepsilon} = -\omega_s' y_2.$$

In the absence of any viscous or body forces, the vorticity will simply be advected by the flow and hence

$$\frac{D}{Dt}\hat{r}_i = \mathbf{u}_i \Big|_{\hat{r}_i}.$$

Thus, for small perturbations, this problem becomes an eigenvalue problem for the non-dimensional growth-rate $\bar{\alpha}$, written

$$\bar{\alpha}\begin{bmatrix}\hat{y}_1\\ \hat{z}_1\\ \hat{y}_2\\ \hat{z}_2\end{bmatrix}=\begin{bmatrix}0 & -1+\omega_s & 0 & \chi\\ -1-\omega_s & 0 & \psi & 0\\ 0 & -\chi & 0 & 1+\omega_s\\ -\psi & 0 & 1-\omega_s & 0\end{bmatrix}\begin{bmatrix}\hat{y}_1\\ \hat{z}_1\\ \hat{y}_2\\ \hat{z}_2\end{bmatrix}, \tag{2.22}$$

$$\chi=(ka)^2K_0(ka)+(ka)K_1(ka), \tag{2.23}$$

$$\psi=(ka)K_1(ka). \tag{2.24}$$

Here, we have non-dimensionalized the problem according to the advection timescale $\frac{2\pi a^2}{\Gamma}$. That is, $\bar{\alpha}=\alpha\frac{2\pi a^2}{\Gamma}$. Thus, given the functional form of ω_s, one can solve the linear stability problem of the vortex dipole. A great deal of effort has been spent trying to determine the functional form of ω_s. Crow (1970) implemented a cutoff parameter method to solve for ω_s. We simply write down a result from Kelvin for a vortex filament of constant vorticity, which is recorded (see Saffman (1995)) as

$$\frac{(\omega_s'+m\Omega)^2}{4\Omega^2-g^2}\left[\frac{\beta bJ'_{|m|}(\beta b)}{J_{|m|}(\beta b)}+\frac{2\Omega m}{g}\right]=-b|k|\frac{K'_{|m|}(|k|b)}{K_{|m|}(|k|b)}, \tag{2.25}$$

$$g=\omega_s'+m\Omega, \qquad \beta^2=k^2\frac{(4\Omega^2-g^2)}{g^2}. \tag{2.26}$$

Here, J_m is the Bessel function of order m and Ω is the solid body rotation of the vortex. The variable, g, is then a weighted total rotation of the filament, with β parameterizing the relative strength of the self-induced rotation rate. The parameter m denotes the mode of deformation for the vortex core, given $\mathbf{r}_i=b+c\exp\left[i\left(kx+m\theta-\alpha t\right)\right]$. It is instructive to visualize these wave modes. Figure 2.8 plots the first six wave modes; this plot is similar to one found in Tsai (1976). In general, an instability will occur for any two perturbation modes m_1, m_2 provided $|m_1-m_2|=2$ (Kerswell, 2002). Based upon this figure, one might intuit that the $m=\pm1$ waves, the bending modes, will be the most unstable as they are the only modes where the centre of mass of the core is perturbed. For a uniform vortex, it can be shown that $m=\pm1$ will result in the fastest growing instability, which we consider here. By symmetry, as $\omega(k,m)=-\omega(-k,-m)$, we consider only the $m=1$ case.

At this point, we introduce the scaled rotation parameter κ and non-dimensional wavenumber ζ of the perturbation as

$$\kappa=\beta b, \qquad \zeta=kb.$$

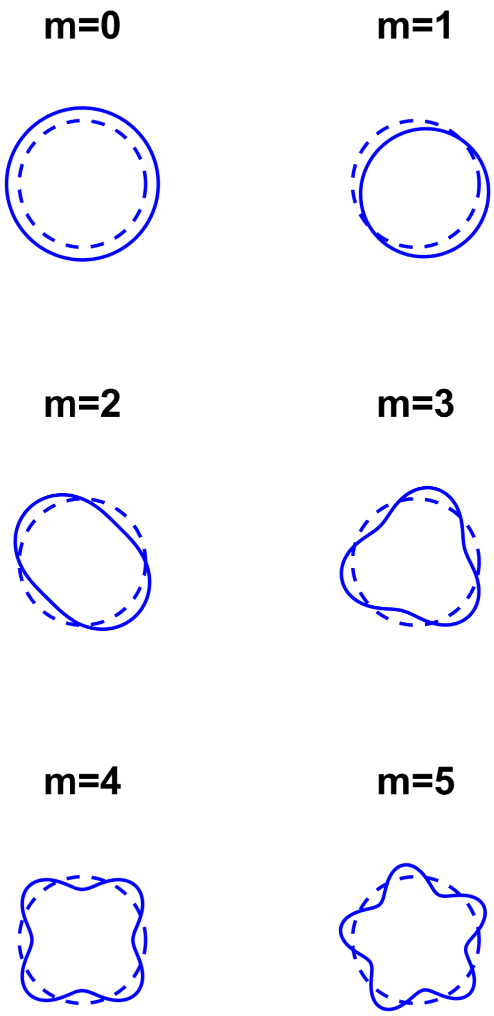

Fig. 2.8 Plot of the first six vortex-core perturbation modes (solid lines) with the unperturbed core plotted as a dashed line.

By restricting the mode-number to $m = 1$, the dispersion relation (2.25) can be simplified to the following:

$$\omega_s = \left(\frac{b}{a}\right)^2 \frac{\left(2s\zeta - \sqrt{\kappa^2+\zeta^2}\right)}{\sqrt{\kappa^2+\zeta^2}}, \tag{2.27}$$

$$\frac{\zeta^2}{\kappa}\frac{J_1'(\kappa)}{J_1(\kappa)} = -s\zeta\frac{\sqrt{\kappa^2+\zeta^2}}{\kappa^2} - \zeta\frac{K_1'(|\zeta|)}{K_1(|\zeta|)}. \tag{2.28}$$

Here, the constant $s = \pm 1$ accounts for the retrograde or prograde motion of ω_s.

Figure 2.9 plots the right hand side (RHS) and left hand side (LHS) of equation (2.28) with $\zeta = 1$. We see that for a given ζ, there exist multiple roots κ_n for which equation (2.28) has a solution. This series of roots are ordered $n = 0, 1, 2, ...$ with solution dependent on the sign of s. Note that there exists only a single root at $n = 0$ corresponding to the $s = 1$, or retrograde, motion. Each of these roots correspond to a different instability. That is, the $n = 0$ root corresponds to a Crow instability, which is the first bending mode. The $n = 1$ root is the Widnall instability, which is the second bending mode. The higher order bending-mode instabilities are not named.

For a given aspect ratio $\frac{b}{a}$, we solve for the roots κ_n which determine ω_s. Figure 2.10 plots ω_s as a function of ζ for $\frac{b}{a} = 0.25$. Here, three modes ($n = 0$ (black), $n = 1$ (blue), $n = 2$ (red)) are plotted. The $s = -1$ modes are plotted as dashed lines. If the angular frequency ω_s drops to (near) zero, the vortex will diverge due to the action of the imposed straining field. Thus, for each mode there exists a characteristic wavenumber for which the vortex will go unstable. Figure 2.11 plots the computed growth-rate for each mode ($n = \{0, 1, 2\}$) as a function of ζ. This plot underscores the conclusion that for each mode, there exists a characteristic wavenumber which will grow most rapidly. In particular, note that it is the short-wave Widnall instability ($n = 1$, blue) rather than the long-wave Crow instability ($n = 0$, black) that has the higher growth-rate, demonstrating why it is the dominant instability. Also note that the $n = 2$ instability has a similar growth rate to the Widnall instability. However, viscosity (not included in this analysis) will damp the higher wavenumbers more strongly.

Understanding these instability mechanisms will be important when we discuss the stratification induced vortex-ring instability observed in Chapter 4. We continue, here, with a discussion of the effects of curvature on the instabilities described above.

2.3.2 The effect of curvature

Until now, we have focused on vortex filaments. However, straight vortex filaments do not possess curvature, whereas vortex rings do. The stability of vortex filaments has been

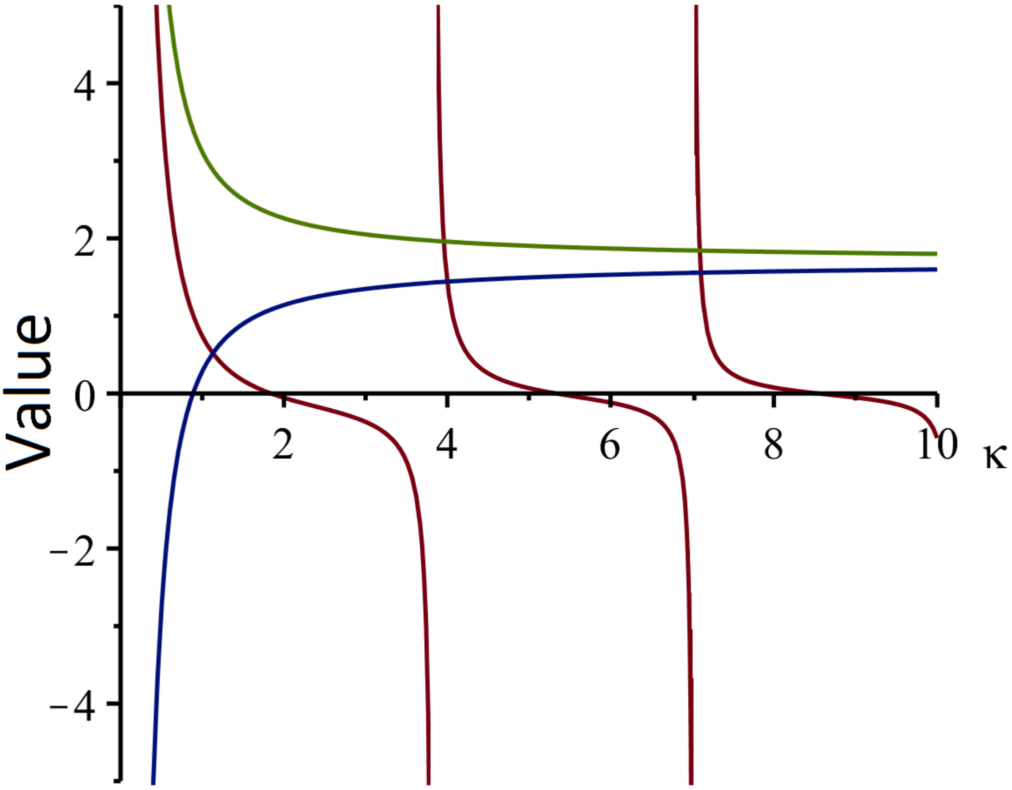

Fig. 2.9 Plot of the solutions to equation (2.28) for $\zeta = 1$. The LHS of equation (2.28) is plotted in red, the RHS with $s = 1$ is plotted in blue and the RHS with $s = -1$ is plotted in green.

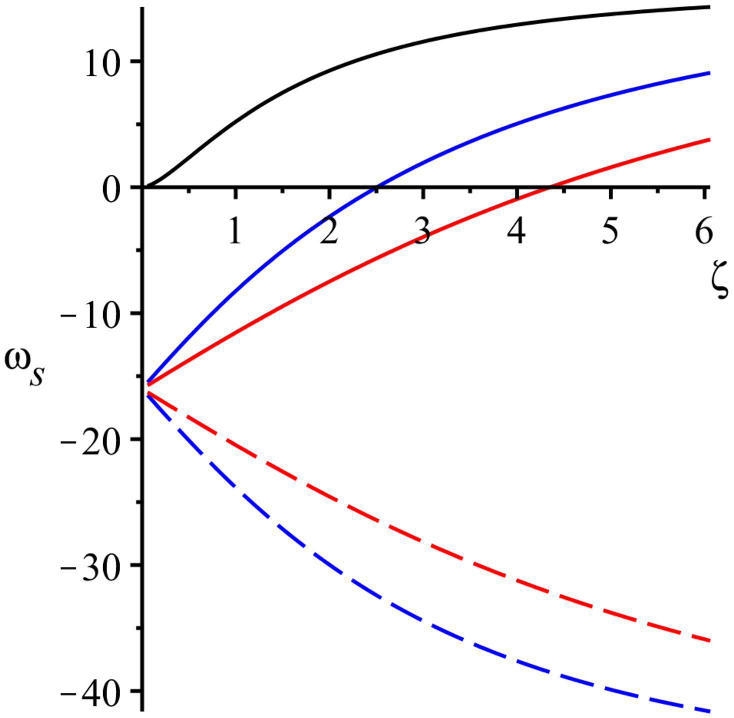

Fig. 2.10 Plot of ω_s as a function of ζ. Roots are plotted for $n = 0$ (black), $n = 1$ (blue) and $n = 2$ (red). Solid (dashed) lines correspond to the $s = 1$ ($s = -1$) roots.

presented as it is the historical approach to the problem. Under the assumption that the radius of curvature (R) of the vortex ring is much larger than the core radius ($\frac{b}{R} \ll 1$), then we might consider the analogy of the vortex filament and estimate the most unstable wavenumber of the vortex ring instability as

$$k \approx \frac{2.5}{b}.$$

(See figure 2.11, $\zeta_{\max} = kb \approx 2.5$.) For a vortex ring, the wavenumbers are restricted to integer mode numbers in order for the unstable mode to 'fit' onto the ring. This approach, originally presented by Widnall & Sullivan (1973), agrees well with observations of unstable vortex rings.

Widnall & Tsai (1977) solved for the linear instability of vortex rings, including the effects of curvature. Specifically, Widnall & Tsai (1977) considered thin vortex rings with constant vorticity. Expanding in terms of the vortex-ring aspect ratio $\varepsilon = \frac{b}{R}$, an asymptotic series for the flow field was determined, up to $O(\varepsilon^2)$. It can be shown that, again, it is the bending modes ($m = \pm 1$) that will be the most unstable. The analysis is also similar to that presented above, in that the instability is expected to occur when $\omega_s \approx 0$, with an identical parameter κ_n to the vortex filament (Widnall & Tsai (1977) estimated $\kappa_n \approx \{2.504, 4.35, \ldots\}$). The amplification rates of the vortex-ring instability are modified from the vortex filament,

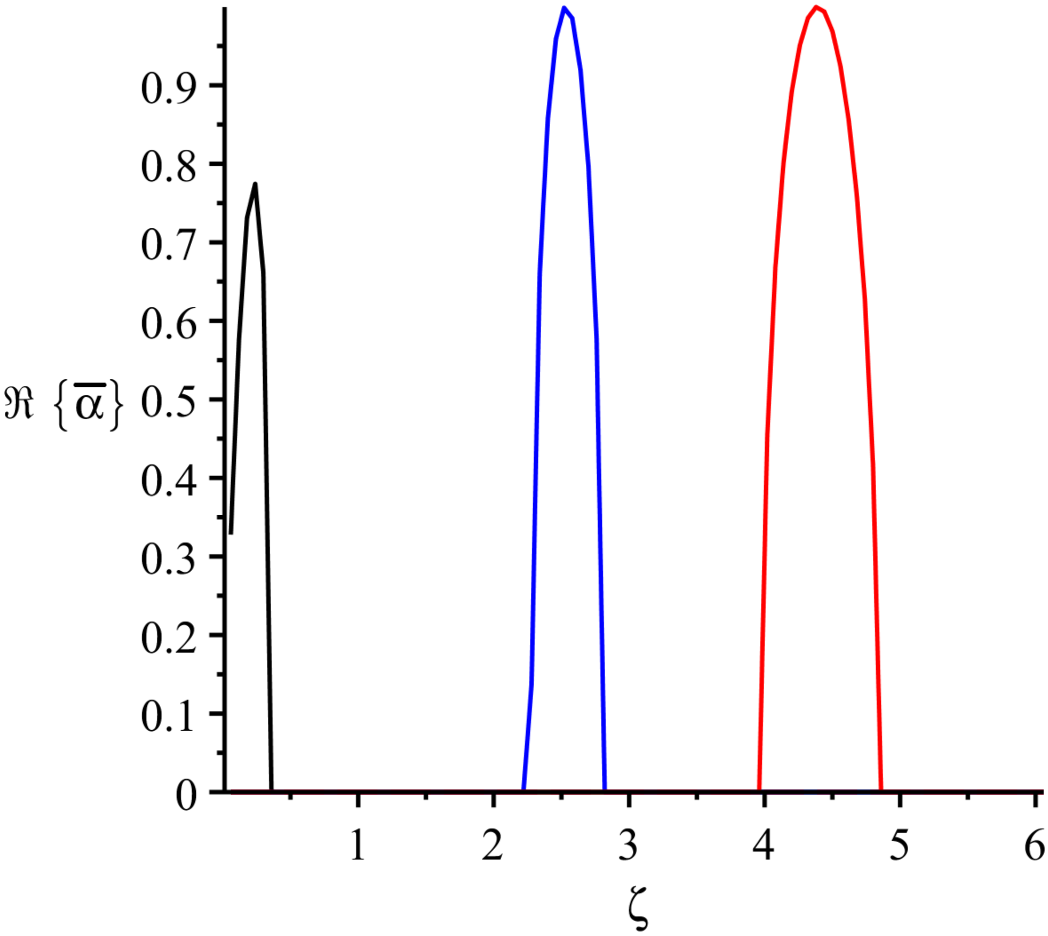

Fig. 2.11 Growth rates of the instability at non-dimensionalized wavenumbers corresponding to the different instability mechanisms. Colours represent the first three bending modes: $n = 0$ (black), $n = 1$ (blue), $n = 2$ (red).

and can be written down, for $\kappa = 2.5$, as

$$\bar{\alpha} \approx 2\left[\left(0.856\ln\frac{8}{\varepsilon} - 0.9102\right)^2 - 0.1138\right]^{\frac{1}{2}}, \tag{2.29}$$

assuming the same non-dimensionalization used previously.

Harris & Williamson (2012) investigated an instability observed for vortex filaments impacting a solid wall. They argued that, based upon the work of Bristol *et al.* (2004), the observed instability was a Crow instability that resulted from the interaction of the vortex filament with the secondary vorticity shed from the wall. The Crow instability may be the dominant instability for two vortex filaments of uneven circulation, provided the circulation ratio is sufficiently low ($\frac{\Gamma_1}{\Gamma_2} \lesssim 0.1$). We will argue, in Chapter 4, that we observe a similar Crow-like instability between the vortex ring, and the secondary vorticity. In that case, the secondary vorticity has been produced through a baroclinic torque. As the unstratified instability mechanisms are similar for the vortex pair and the vortex ring, we are confident that this Crow-like instability is indeed the correct interpretation for the observed instability. Indeed, for thin vortex rings with a large radius of curvature, this analogy should be even more robust, as the primary and secondary vorticity field are concentric. See Chapter 4 for more details.

2.4 Impacting a solid wall

We conclude Chapter 2 with a discussion of the vortex ring-wall collision. As we will see, this has relevance to the problem of a vortex ring impacting a stratified interface. We will return to this, in Chapter 4, for our discussion for vortex rings impacting a stratified interface.

Let us consider an inviscid fluid in which a vortex ring approaches a free-slip wall. Using the method of images, as a vortex ring propagates towards a wall, its image vortex ring will simultaneously draw near to this wall. As these two vortex rings approach, their mutual interaction will cause them to expand. Now, as a result of Kelvin's circulation theorem (see Batchelor (2000)), as the vortex ring expands, the total circulation will remain constant. This will result in a shrinking of the core radius, and an acceleration of the radial propagation (see Bethke (2009)). Figure 2.12 is a cartoon of the expansion of the vortex ring as it approaches a free-slip wall. If the wall were truly free-slip, the ring would continue to expand as it approaches (but never reaches) the wall. Indeed, Archer *et al.* (2009) performed a numerical simulation of this event where he observed a Widnall instability occurring on the vortex ring, prior to the development of a Crow instability.

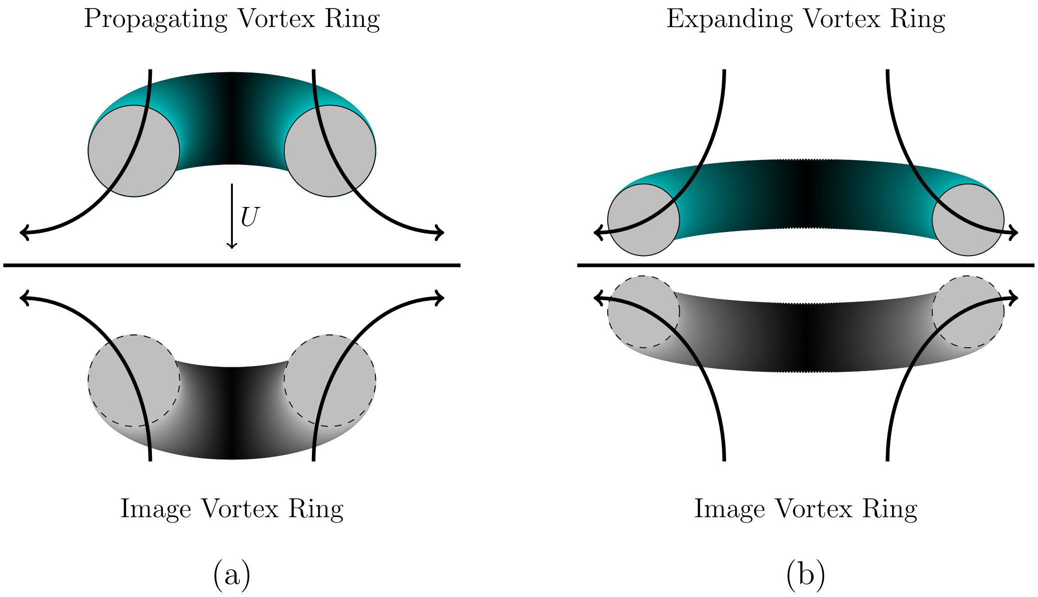

Fig. 2.12 A cartoon of the expansion of a vortex ring as it approaches a free-slip wall.

The effect of viscosity will limit this expansion. The associated no-slip boundary condition on the wall will induce the generation of vorticity within a boundary layer, which will eventually separate and surround the impinging vortex ring. This secondary vorticity field, of opposite sign to the approaching vortex ring, will interact with the primary vortex ring, reducing its propagation speed and constraining the extent to which the vortex ring can expand. Depending on the Reynolds number of the impinging vortex ring, a vortex ring formed from the secondary vorticity field can escape back into the water column.

A density interface does not represent a no-slip rigid-boundary condition. A sharp interface will deform in the presence of the vortex ring. In addition, velocity and shear must be continuous across the interface. Buoyancy will resist the penetration of the vortex ring through the density interface. Similar to the no-slip wall, stratification allows for the generation of vorticity through a baroclinic torque. We will see, in Chapter 4, that the vortex-ring produced secondary vorticity will again restrict the expansion of the vortex ring.

In this thesis, we will use novel experimental techniques to measure the kinematics of the flow produced by vortex rings impacting a stratified interface. The evolution of such a system has characteristic features similar to the vortex ring-wall collision. We continue with a discussion of some of these experimental techniques.

Plate 2: Photograph of the bike pump setup used to generate vortex rings within a stratified tank.

Chapter 3

Experimental setup

> In theory, there is no difference between theory and practice. In practice, there is.
>
> —Yogi Berra

In this chapter, we describe the essential setup for the vortex ring experiments, starting with an empty tank. Section 3.1 begins with a description of how the tank is initially stratified. Then, section 3.2 describes the refractive index matching methodology, which was essential to the results produced in Chapter 4. Once the tank has been filled, vortex rings are generated, as described in section 3.3. In order to quantify the velocity field associated with these vortex rings, we perform Particle Image Velocimetry (PIV), as will be described in section 3.4. This experimental setup was used in both Chapters 4 and 6. Finally, we provide details on the conductivity probe, used in Chapter 6, to measure a vertical profile of the stratification. Where necessary, the details of the setup described in this chapter will be reiterated and clarified in the subsequent chapters.

3.1 Filling the Tank

In this thesis, we study the effect of vortex rings impacting a sharp interface. Here, we describe how the experimental tank is initially filled to produce a sharp density stratification. Starting with an empty water tank, we first prescribe the maximum height of the water column, along with the depth of the lower fluid layer. By specifying these two heights, the volume of both the upper and lower layers are known. The empty tank is then partially filled with the upper layer fluid of the appropriate volume. Typically, the upper layer was simply fresh water, but as we will see below, it was occasionally filled with a salt-water solution (Sodium Chloride) in order to match refractive indices of the upper and lower fluid layers.

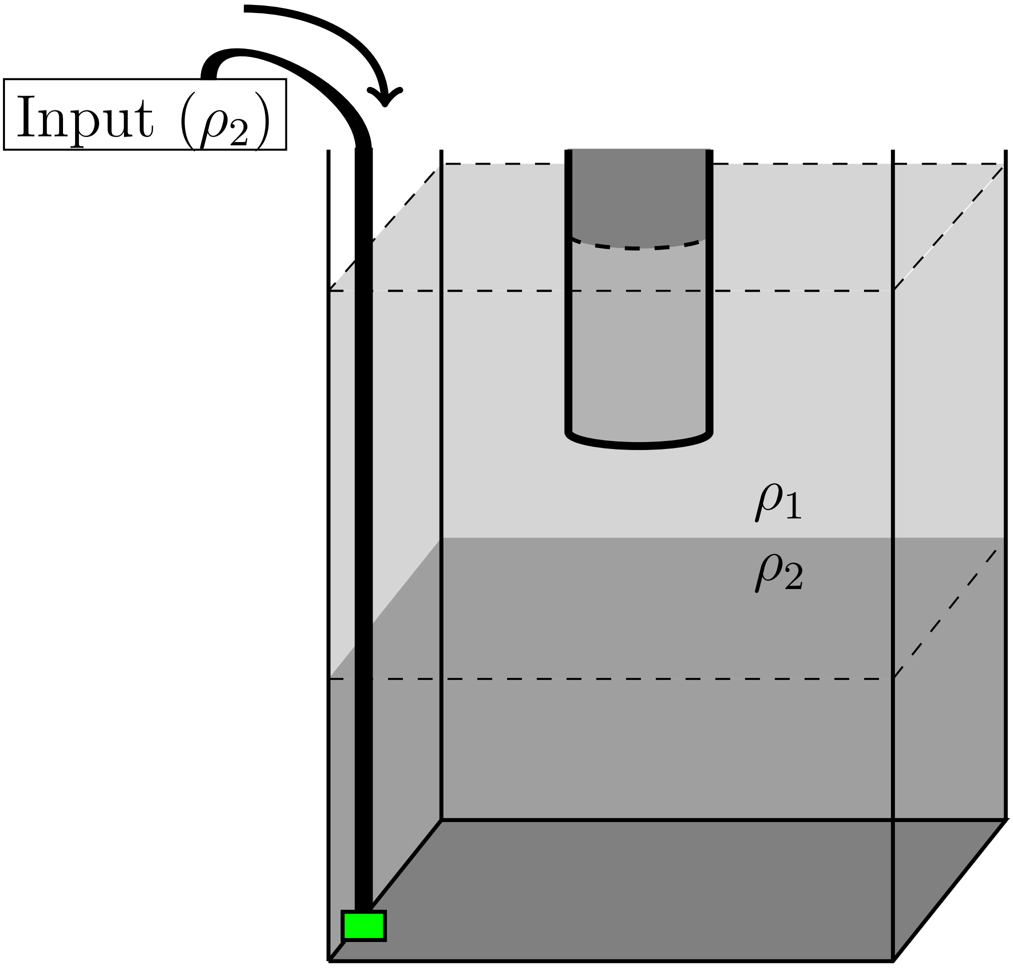

Fig. 3.1 Diagram of the basic tank filling methodology.

The fluid which will form the lower-layer was prepared by mixing a nearly-saturated salt-water solution with fresh water from the mains. These fluids are mixed to form a reservoir of lower-layer fluid. The density of this fluid is then measured using a density meter (Anton Paar DMA 5000). Once the tank has been partially filled, the fluid that will form the lower layer is slowly injected at the base of the tank via a long hollow rod. Figure 3.1 draws a diagram of this setup. At the base of this filling rod, a small sponge (here highlighted in green) was used to remove as much of the kinetic energy from the input fluid as possible. By slowly injecting fluid at the base of the tank, a lower density layer is generated with a sharp interface, as we will see in Chapter 6. Once the water column has reached its prescribed maximum height, the fluid injection is stopped.

Two methods were used to inject fluid at the base of the tank. The first is a simple gravity feed. In this method, the lower-layer fluid was siphoned through the filling rod to the tank base, and the injection rate of the lower-layer fluid was simply controlled by gravity. This was the primary filling method used in Chapter 6. This method was subsequently replaced by a second method that used a peristaltic pump. The peristaltic pump is preferable as it allows for a more precise control of the injection rate at the base of the tank. In both cases, the flow-rate was set to be initially slow, in an attempt to keep the interface sharp. As the lower-layer filled, the flow-rate was increased in order to speed up the filling time. The filling time with both methods ranged from 1-2 hours. The flow rate was not explicitly quantified. Using either method resulted in a variable initial density-interface thickness, however, typical values were much smaller than the vortex tube diameter.

3.2 Sodium Nitrate

When table salt (sodium chloride) is added to water, it changes the refractive index of the solution. As a result, a light ray passing through a stratified fluid will be deflected towards the direction of the density gradient. This can be useful if one is trying to identify the location of a density interface. However, when trying to capture the motion of tracer particles within a flow, erratic refractive index variations will prohibit the velocity field computation due to the spurious shifts to the particle positions within a camera recording. Thus, it is necessary to find a method of minimizing refractive index variations within a stratification. The solution used in this thesis relies on the refractive index of a solution of sodium nitrate ($NaNO_3$) to have a different scaling with concentration than a solution of sodium chloride. That is,

$$\left.\frac{\partial \rho}{\partial n}\right|_{NaNO_3} > \left.\frac{\partial \rho}{\partial n}\right|_{NaCl}.$$

Figure 3.2 plots the density of both salt solutions versus its refractive index (n). In order for the refractive index of both layers to match, the salt concentrations, and hence the densities, will necessarily be different. We use this phenomenon to generate stratifications of a single refractive index. In principle, the refractive index of each layer will depend on its respective salt concentration, in addition to the temperature of the two layers and the wavelength of the incident light. In practice, for a near uniform temperature profile within the tank, and single wavelength light source, these additional dependencies are negligible in the experiments presented here. This salt-solution methodology is similar to that employed by McDougall (1979) for studying plumes.

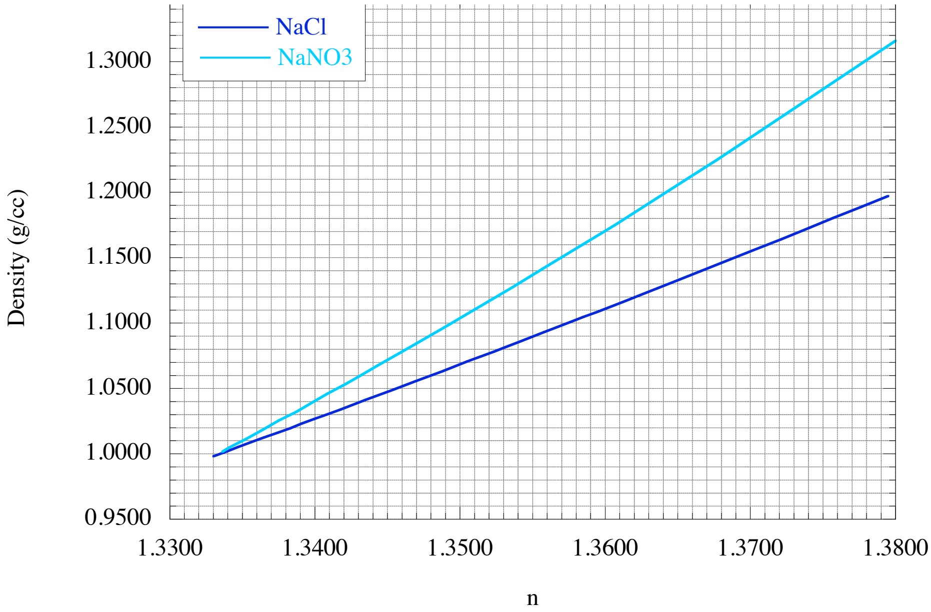

Fig. 3.2 Plot of the density of both salt (NaCl or $NaNO_3$) solutions versus the refractive index (n). Figure courtesy of Dr. Mark Hallworth. Data from Haynes (2012).

It should be noted that, as of writing this document, it is still unclear to what extent the refractive index is linear with mixing of solutes. That is, a mixture of refractive index matched NaCl and $NaNO_3$ solutions may not be matched to the two separate solutions. However, as we limit ourselves to low density differences between the salt solutions for practical purposes, this did not become an issue in this work.

For each refractive index matched experiment, we plot the density of the NaCl (ρ_{NaCl}) solution versus the density of the $NaNO_3$ (ρ_{NaNO3}) solution with the same refractive index in figure 3.3. We find a linear fit to this data. While refractometer measurements were always performed to ensure refractive index matching, this figure provides a quick estimate of the relative densities required. A fit to the data is given:

$$(\rho_{NaNO3} - \rho_0) = 1.48 \times (\rho_{NaCl} - \rho_0)\,.$$

This is consistent with the results of figure 3.2. For reference, the molar mass of Sodium Chloride is 58.44 g/mol and the molar mass of Sodium Nitrate is 84.99 g/mol. The ratio of molar masses for the sodium nitrate solution to the sodium chloride solution is 1.44 suggesting that the balance of refractive indices may be related to the balance of molecular concentrations.

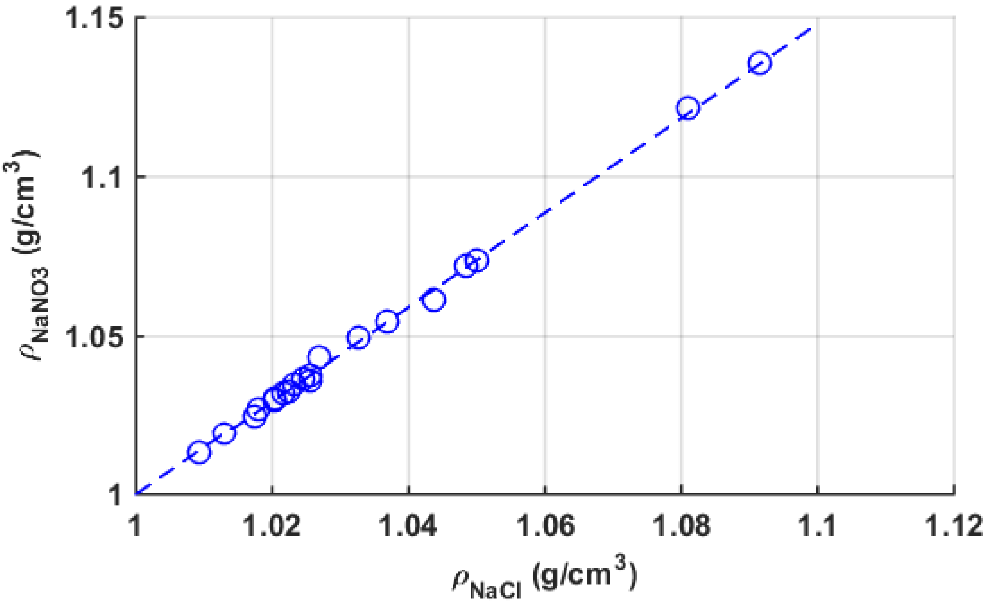

Fig. 3.3 Plot of the density of NaCl versus $NaNO_3$ for a number of the experiments performed.

Ion	Diffusivity (10^{-9} m^2/s)
Cl^-	2.032
Na^+	1.334
NO_3^-	1.902

Table 3.1 Table of the diffusivities of the various ionic species found in our experiments. Diffusivities can be found in Haynes (2012).

We briefly make note of the cross-diffusivities of the two different salt solutions. The diffusion rates of either salt should not be substantially different due to their similar molecular mass. For reference, the diffusion rates of each ion present in solution is found in the Handbook of Chemistry and Physics (Haynes, 2012), and presented in table 3.1. Note that the difference in the coefficient of diffusivity of each ion is within a factor of two. In order to maintain a charge balance within the stratification, ions of different charge must remain paired. Hence, we note that as the difference between the ionic diffusivity of Chlorine and Nitrate is an order of magnitude lower than either constituent, we are confident that double diffusion will not play a role. We note that the maximum duration of the refractive-index-matched experiments was very fast (about six hours) compared to the diffusion timescale of the system. We did not pursue this further in this thesis.

Elsewhere, other approaches have been used to match the refractive indices of two fluid layers. One common approach is to use ethanol as a solute, rather than sodium nitrate, as used by the Coriolis platform at LEGI[1] Grenoble (Venaille *et al.*, 2014). Ethanol has the advantage of decreasing the density of its solvent. However, large quantities of ethanol pose a potential safety concern as it is highly flammable. Isopropyl alcohol has also been used to match refractive indices in Dalziel (1993). It is also worth noting that the mixing of alcohol in water is not linear, i.e. the volume of an ethanol/water solution is not the sum of the volume of its constituents. This would prove challenging for any direct mixing measurements. Another common approach is to use glycerol as the solute (Alahyari & Longmire, 1994). However, glycerol spills are challenging to clean. We chose to use sodium nitrate as it is easily disposable, of minimal safety concern and is cost effective.

3.3 Vortex Ring Generation

Once the experimental tank has been filled, we now need to generate a vortex ring within the stratification. In all of the experiments performed in this thesis, vortex rings were generated using a computer controlled traverse, attached to a bicycle-pump (0.029 m internal diameter). This bike pump was connected to a partially submerged hollow cylindrical tube (internal diameter $D = 0.039$ m). The pump, and the connected tubing, is filled with air. The actuation of the bike pump will result in a pressure pulse within the tube, displacing the contained fluid. This fluid ‘slug’ motion will produce a vortex ring at the base of the tube, which will propagate along the tube’s axis. Figure 3.4 presents a basic schematic of the experimental pump setup. Using a UEI card (PDL-ML, United Electronics Industries INC.), the computer sent a series of ‘ticks’ (a ± 5V signal) to an in-house built control box. For each ‘tick’ sent, the stepper motor attached to the pump traverse will rotate by a fixed angle, which corresponds to a fixed linear translation of the traverse. The sign of each ‘tick’ controls the direction of its translation. Thus, by controlling the number of ‘ticks’ sent from the computer, this will drive the traverse a fixed distance. By controlling the rate at which these ‘ticks’ are sent, this controls the speed of the traverse. Tuning the distance and speed of the traverse, we generate reproducible vortex rings. See Chapter 6 for an evaluation of the pump methodology.

In order to effectively drive the pump, an acceleration and deceleration phase of the piston motion allowed for a greater maximum pumping speed. These “ramps” also increase the reproducibility of the vortex rings. Figure 3.5 draws the characteristic pump displacement as a function of non-dimensional time. The functional form of the pump signal is piecewise defined with a constant pump speed between constant acceleration and deceleration phases. The acceleration and deceleration phases each correspond to 15% of the total signal.

---

[1] Laboratoire des Écoulements Géophysiques et Industriels

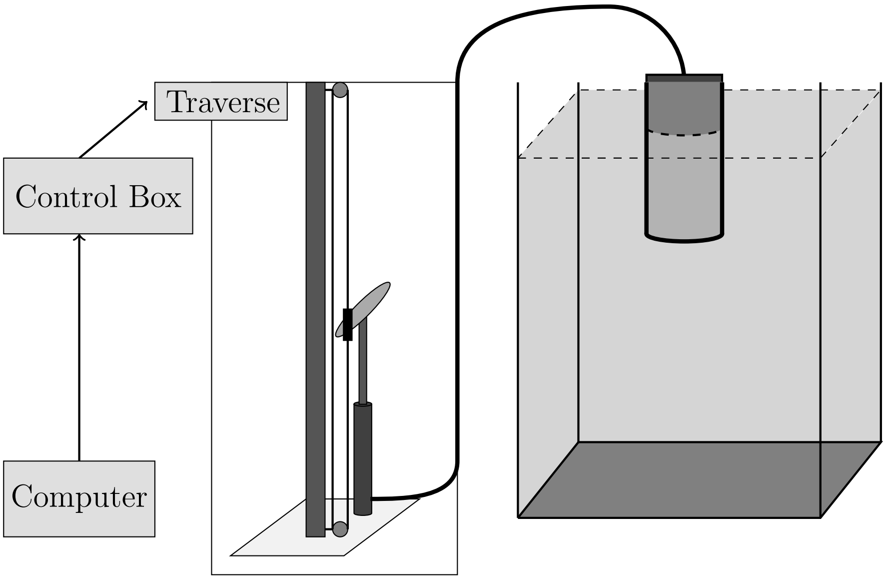

Fig. 3.4 Schematic of the digitally controlled bike pump.

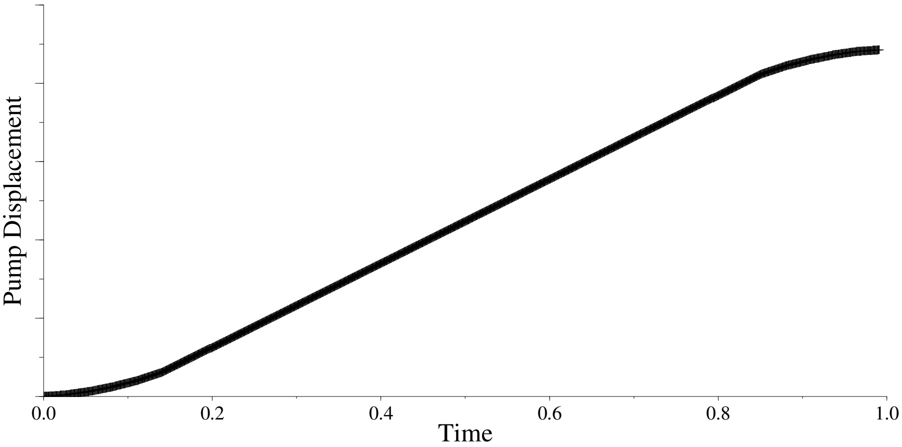

Fig. 3.5 Plot of the functional form of the pump displacement as a function of non-dimensional time.

The generation methodology used in this thesis is similar to that of Linden (1973), who generated vortex rings by ‘striking’ a rubber diaphragm attached to a partially submerged chamber. Importantly, the generation methodology used in this thesis produces no net volume flux into system. This allows for the sequential generation of vortex rings. The work of Munro *et al.* (2009); Scase (2003) and Bethke & Dalziel (2012) also used a bicycle pump apparatus to produce vortex rings. This approach does not follow the piston approach of Gharib *et al.* (1998); Maxworthy (1972, 1977); Sullivan *et al.* (2008). In all of the experiments performed in this thesis, we restrict ourselves to the case where only a single vortex ring was generated from the pump actuation.

The formation of vortex rings results from the separation of boundary layer vorticity, generated within the vortex tube, into the outer flow. Figure 3.6 plots the vorticity evolution of a forming vortex ring. Here, the vorticity is plotted in colour with the velocity vectors superimposed on top. The initial boundary layer separation produces a ring of vorticity into the outer flow (figure 3.6(a)). Subsequently separated vorticity wraps around the seeded vortex ring (figure 3.6(b)-(c)). The vortex ring then propagates away from the vortex tube (figure 3.6(d)). In this thesis, we generate a single vortex ring, as shown in figure 3.6(e). However, as demonstrated by Gharib *et al.* (1998), depending on the formation time of the vortex ring, it is possible to generate a series of overlapping vortex rings. We do not exceed this critical formation time. Assuming a “slug model” (Shariff & Leonard, 1992), we can show that given a uniform velocity within the vortex tube, U_p, the vorticity flux into the outer fluid is

$$\frac{d\Gamma}{dt} = \int \omega_\theta u_z \, dr \approx \int -\frac{\partial u_z}{\partial r} u_z \, dr \approx \frac{1}{2} U_p^2.$$

Here, Γ is the fluid circulation. This model does fairly well at predicting the circulation of the generated vortex rings,

$$\Gamma \approx \frac{1}{2} \int_t U_p^2 \, dt',$$

as shown by Maxworthy (1977) and Shariff & Leonard (1992). As we are interested in the dynamics of the vortex rings after they have been generated, we do not continue this discussion.

3.4 PIV Methodology

Finally, now that we are able to produce vortex rings, we want to be able to quantify the flow field of their induced dynamics. In order to do so, we use particle image velocimetry (PIV). PIV is an experimental technique for computing the velocity field from a camera recording of the flow. In our approach, tracer particles are initially seeded into the stratification, prior

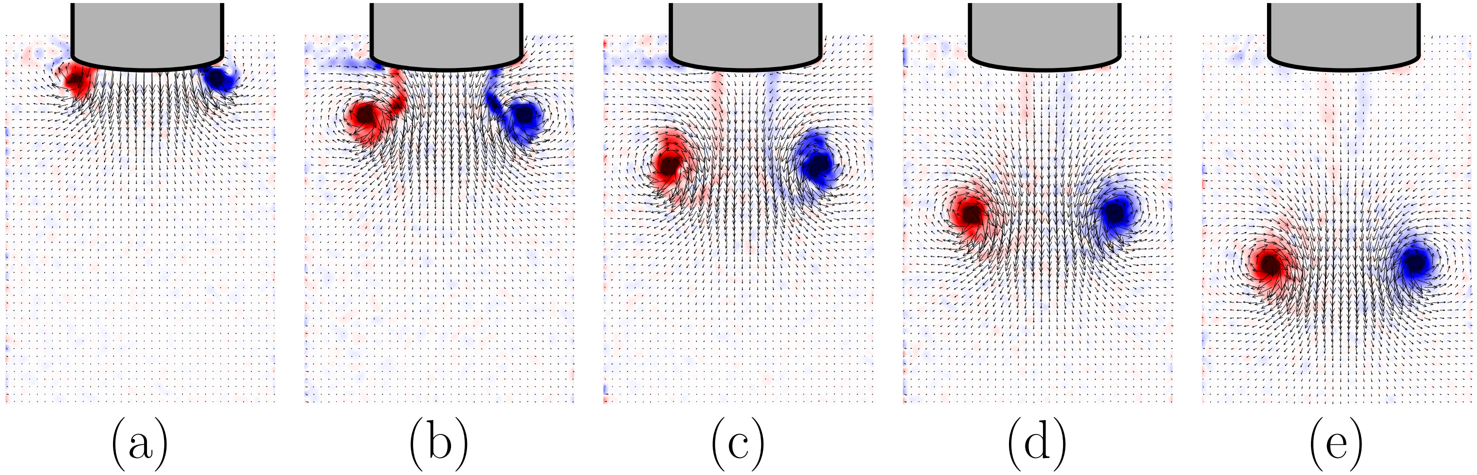

Fig. 3.6 Plot of the vorticity for a forming vortex ring. Velocity vectors are overlayed. Panels are ploted every 0.33s. A cartoon of the vortex tube has been overlayed.

to an experiment. The cameras then record the motion of these tracer particles within a thin light sheet. With the cameras focused on this light sheet, a series of snapshots are taken of the flow, with a precise timestep (Δt) between the images. By measuring the distance the tracer particles have moved between snapshots, and knowing the precise inter-image timestep Δt, the velocity field within the fluid can be computed. The light sheet was illuminated with two different technologies. In Chapter 4, we used a pulsed-laser system with which it is possible to precisely correlate the triggering of the laser pulse with the camera frame capture. In contrast, Chapter 6 used two 300 watt arc lamps that continuously illuminate the light sheet. These will be discussed more thoroughly in their respective chapters.

All of the PIV computations performed in this thesis will use DigiFlow^{tm} (Dalziel Research Partners), a software developed by Professor Stuart Dalziel. A comprehensive document on the inner workings of Digiflow can be found in Dalziel (2012). We present an elementary description of DigiFlow's PIV algorithm as follows: Two images (p^1, p^2) with a known temporal spacing (Δt) are specified for which the velocity field is to be computed. Each image, p is then divided into a grid $p_{i,j}$. For each grid element (i, j), an interrogation window of $nx \times ny$ pixels is used to limit the optimization region over which the displacements will be computed. Then, the optimal shift between $p^1_{i,j}$ and $p^2_{i,j}$ (accounting for translations and distortions) is computed. The optimal shift is defined as that which minimizes the absolute difference between the distorted windows $p^{1,*}_{i,j}$ and $p^{2,*}_{i,j}$. That is,

$$\text{error}_{i,j} = \sum_{k,l}^{nx,ny} |p^{1*}_{i,j} - p^{2,*}_{i,j}|_{k,l},$$

is minimized. Figure 3.7 plots a cartoon of the PIV methodology to find the optimal displacement vector between image pairs. Note that numerically, DigiFlow uses a multi-grid method to find the optimal shifts. Knowing the optimal displacements, and the time step between the two images, DigiFlow uses a central difference scheme to compute the velocity field at intermediate time $t + \frac{\Delta t}{2}$.

The use of Digiflow^{tm} to compute the velocity field of vortex rings has been used in a variety of contexts. Both Bethke (2009) and Munro *et al.* (2009) used Digiflow^{tm} to study the dynamics of a vortex ring impacting a solid wall. Scase (2003) similarly used Digiflow^{tm} to analyze the flow evolution of vortex rings that were generated in a linear stratification. Typical vortex ring propagation velocities used in the previous experiments were much greater than those found here. This present work builds upon these previous vortex ring experiments by studying vortex rings impacting a sharply stratified interface. In addition, as we will see in Chapter 4, we extend the two-dimensional PIV methodology to a stereo-PIV

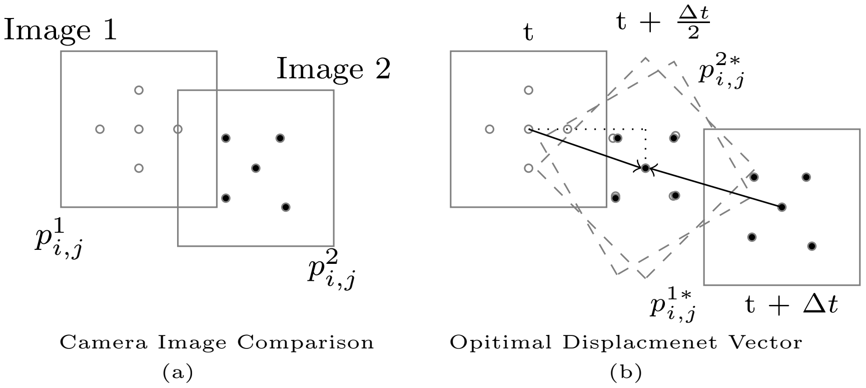

Fig. 3.7 A cartoon of the PIV algorithm. Two images are compared (a) and subsequently, the optimal displacement vector is computed.

system, which is capable of computing the three components of the flow velocity within a single plane.

3.5 Conductivity Probe

We use an aspirating conductivity probe to measure the stratification within a water-filled tank. This probe is attached to a digitally driven traverse that controls the vertical position of the density measurement, enabling the operator to measure a vertical profile of the density stratification. We additionally attach a thermistor near to the sampling point of the probe to correct for temperature fluctuations within the fluid. The underlying principle of the conductivity probe is that the resistance of a measured volume of fluid is proportional to the amount of ionized material within that volume[2]. When using the conductivity probe, we will use a table salt (NaCl) solution, which contains disassociated sodium and chlorine ions, changing the resistance of the fluid. In principle, any conducting solute could be used. By measuring the change in resistivity of the fluid, we can then calibrate the probe to provide a measure of the salinity of the fluid, and thus, assuming a single solute, its density.

The probe is constructed from a long conductive cylinder connected to a ~1cm long conical probe head. The probe head itself has a small (0.3mm diameter) hole by which the surrounding fluid can enter. Within the body of the conductivity probe, there is an inner conductive cylinder separated from the outer cylinder by an insulating material. An electrical circuit is then established between the inner and outer cylinders through the ambient fluid.

---

[2] Note that Conductivity $= \frac{1}{\text{Resistivity}}$

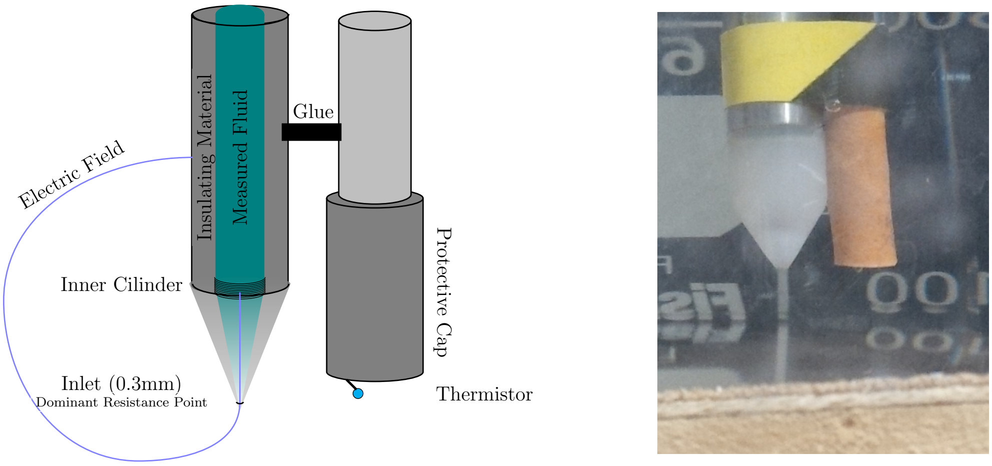

(a) (b)

Fig. 3.8 Diagram (a) of the conductivity probe with the attached thermistor along with a picture (b) of the experimental device.

During measurement, the fluid surrounding the tip of the probe is driven through the head and subsequently expelled from the system, aspirating at $\sim$ 1mL/s. Due to the small radius of the hole in the probe head, the resistance of the circuit is dominated by the conductivity of the fluid at the probe tip. This fluid parcel moves quickly through the head at O(1m/s), thus allowing for a very quick response to a change in salinity. Figure 3.8(a) presents a diagram of the conductivity probe with the attached thermistor along with a picture (Figure 3.8(b)) of the experimental device. The probe head slowly expands with the absorption of water and hence, must be stored in water when not in use in order to ensure consistency of the calibration. This probe design was originally designed in DAMTP around 1995, which was subsequently modified to its current form, as used by Holford & Linden (1999).

The conductivity of salt water is also temperature dependent. In order to control for this variability, we additionally attach a thermistor (P25 NTC type, General Electric) to the edge of the probe tip. This approach was originally implemented by Davies Wykes & Dalziel (2014). The thermistor was encased in glass ensuring a stable calibration over a long time period. The response time of this thermistor in water is 23ms (Davies Wykes, 2014). Using water of a given salinity, we vary its temperature and record the corresponding change in probe voltage. From this, we can correct for the variation of the probe output as a result of temperature variations and reduce the drift of the calibration curve. See Appendix A for details on the calibration procedure.

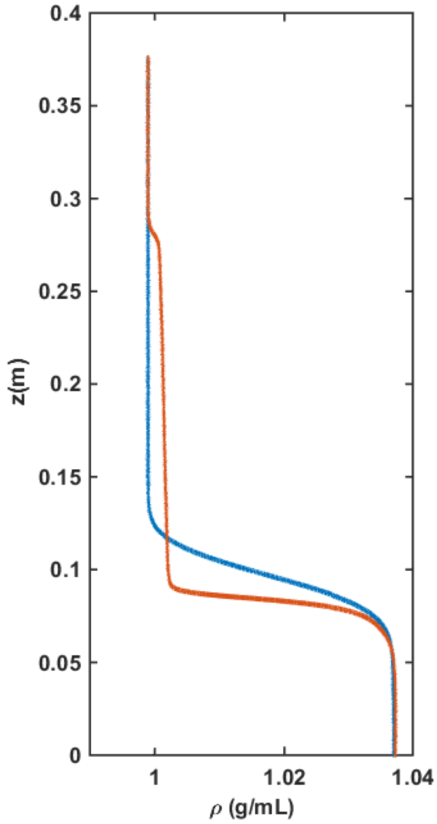

Fig. 3.9 Plot of the initial density stratification (blue) determined by the conductivity probe. The density profile after 300 vortex ring generations (red) has also been plotted.

Figure 3.9 plots an example of the initial stratification (blue, prior to the generation of any vortex rings) determined by the conductivity probe. After 300 vortex rings were sequentially generated within the stratification (allowing for the kinetic energy to dissipate between subsequent vortex-ring generations), a subsequent density profile (red) has been plotted. We see that the interface sharpens significantly. We will fully discuss the dynamics of such a system in Chapter 6. However, we will start, in Chapter 4, by discussing the mechanics of vortex rings as they impact a stratified interface. It is worthwhile to keep this picture in mind when considering the following chapters.

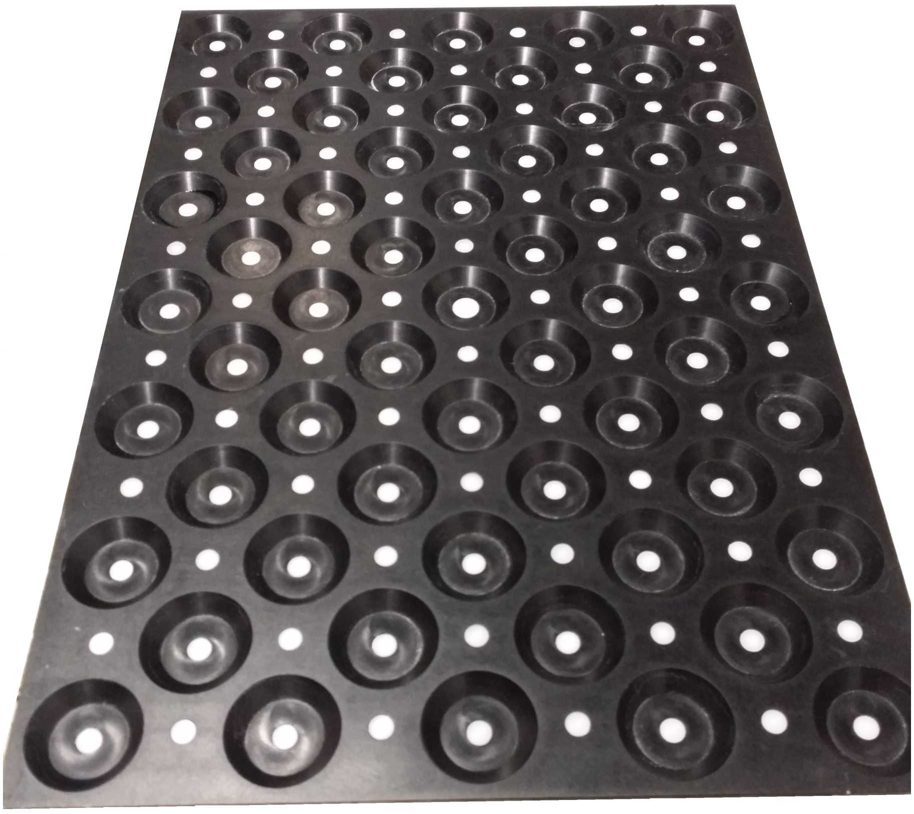

Plate 3: Photograph of the 3D calibration grid used for the Stereo-PIV.

Chapter 4

Three-dimensional visualization of the interaction of a vortex ring with a stratified interface

> The earliest theoretical treatments of isolated vortex ring kinematics and dynamics predate quantitative experimental observations of the same phenomena by a half-century [...]
>
> —Dabiri and Gharib, JFM, (2008)

As we have seen in Chapter 2, the study of vortex-ring-induced stratified mixing has long played a key role in understanding externally-forced, stratified turbulent mixing. The aim of this chapter is to understand the mechanics of vortex-rings-induced mixing of the density field. As discussed in the introduction, we will study how the vortex-ring propagation is modified in the presence of a stratification. This chapter presents an experimental investigation of the kinematic evolution of these vortex rings, including the stratification-modified three-dimensional instability. We will build upon this work when we discuss a model for the vortex-ring-induced mixing in Chapter 7.

We begin with a discussion of the Reynolds and Richardson number dependence of the vortex-ring interaction using two-dimensional particle image velocimetry measurements. Then, through the use of modern imaging techniques, we reconstruct the full, three-dimensional, time-resolved velocity field of a vortex ring interacting with a stratified interface. This work agrees with many of the previous two-dimensional experimental studies, while providing insight into the three-dimensional instabilities of the system. Observations indicate that the three-dimensional instability has a similar wavenumber to the unstratified vortex-ring instability (Widnall instability) at later times. The structure of the underlying instability is a simple displacement mode of the vorticity field and we identify it as a Crow-like instability. We determine that the timescale associated with this instability growth has an inverse Richardson number dependence. Thus, the timescale associated with the instability is different from the timescale of the buoyancy driven interface recovery (see Chapter 2). As such, this suggests that there exists a critical Richardson number below which the instability does not have sufficient time to grow before the interface recovers.

4.1 Introduction

The study of vortex rings has a long history extending back to the 19th-century (for example, Helmholtz (1858)). Since that time, the study of vortex rings has been integrated into nearly every domain of fluid dynamics (see Shariff & Leonard (1992), and the examples therein). This chapter investigates the three-dimensional mechanics of vortex rings interacting with a stratified interface. For clarity, the complete dynamics that result from the interaction of the vortex ring with a density stratification will be simply denoted as the "vortex-ring interaction" in what follows.

At the start of the twentieth century, it was uncertain whether vortex rings were stable fluid structures. Crow (1970) demonstrated that a vortex dipole of constant vorticity was unstable to coupled long-wavelength perturbations. Widnall & Sullivan (1973) applied Crow's argument to the case of a vortex ring with a large radius of curvature, demonstrating that (nearly) all vortex rings with a finite core size are unstable. However, the wavelength of the experimentally observed perturbations was short with respect to the core diameter, in violation of the long wavelength analysis. Subsequent analysis (see Widnall *et al.* (1974),Moore & Saffman (1975),Tsai & Widnall (1976),Widnall & Tsai (1977)) has shown that the fastest growing instability for both a dipole, and the vortex ring, is an example of an elliptic instability. Bayly (1986) and Pierrehumbert (1986) demonstrated this instability in a broad class of straining flows; see Kerswell (2002) for a review of elliptic instabilities. We have discussed the mathematical formulation of these instabilities in Chapter 2. Experimentally, the instability of vortex rings has been observed in Krutzsch *et al.* (1939) and more recently in Maxworthy (1977). A recent publication (Ponitz *et al.*, 2015) has presented a full three-dimensional experimental visualization of the elliptic vortex-ring instability observed in an unstratified environment, which compares well with the numerical work of Archer *et al.* (2008). In this discussion, we investigate vortex rings that are modified in the presence of a stratification.

The impact of vortex rings on a solid wall has also been studied in the literature (Munro *et al.*, 2009; Orlandi & Verzicco, 1993; Swearingen *et al.*, 1995). We have discussed the characteristic features of this flow in section 2.4. As was noted there, the vortex ring expands as it approaches the wall, and, due to the no-slip boundary condition, secondary vorticity is produced. The interaction of the primary vortex ring with the secondary vorticity results in an instability on the secondary vorticity surface. Both Swearingen *et al.* (1995) and Orlandi & Verzicco (1993) interpreted this instability as a result of the straining field produced by the primary vortex ring. More recently, Harris & Williamson (2012) investigated the impact of a vortex dipole on a solid wall and argued that the resultant instability in the secondary vorticity field is primarily due to a Crow instability, though it is often misinterpreted as an elliptic instability due to the similarity in the instability wavenumber. We will see that this earlier work has direct applicability to the case of a vortex ring impacting a stratified interface. For a vortex ring impacting a free-slip surface, there is no secondary production of vorticity and thus the vortex ring continues to expand in the presence of its image ring (using the Method of Images). As demonstrated by Archer *et al.* (2009), the interaction of the vortex ring with its image will result in an Widnall instability followed by a Crow instability.

While topologically distinct, understanding the dynamics of dipoles has played a key role in understanding the dynamics of vortex rings and vice versa. (See Leweke *et al.* (2016) for a review of the dipole instabilities). The work of Nomura *et al.* (2006) and Ortiz *et al.* (2015) both highlight the role of stratification on the instability of vortex dipoles. In both of these studies, the stratification was chosen to be linear and the Richardson number (defined below) was restricted to be no greater than unity. As the dipoles propagate, stratification is observed to significantly enhance the instability as the two vortices are pushed together, resulting in an enhanced straining field, and hence a rapid growth of an elliptic instability. For a Richardson number much less than one, the instability grows in essentially the same manner as the unstratified case. For a Richardson number equal to one, Ortiz *et al.* (2015) used a linear adjoint-loop optimization technique to find the initial perturbation to the vortex dipole that will result in the largest gain in energy over some finite time, and showed that the wavenumber of maximum growth occurred for an antisymmetric perturbation (identified as an elliptic instability) with a growth rate greater than twice the unstratified case.

Similarly, the evolution of vortex rings is modified in a stratified environment (see Atta & Hopfinger (1989); Scase & Dalziel (2006); Turner (1957)). To our knowledge, no analytic theory currently exists that explicitly investigates the linear stability of vortex rings in a stratified environment. Early work on the interaction between a vortex ring and a two-layer stratification is found in Linden (1973) who investigated the bulk mixing of the density field as a result of the vortex-ring breakdown. The work of Dahm *et al.* (1989) presents two-dimensional images of a dyed vortex ring impacting upon a sharply stratified interface. Numerical investigation of vortex-ring interactions with a stratification has become increasingly popular in recent years due to the increase in computational resources available. Stock *et al.* (2008) numerically simulated the inviscid vortex-ring interaction and observe some small-amplitude three-dimensionalization, though they do not characterize the instability. Camassa *et al.* (2013) also investigated (using both experimental and numerical techniques) the interaction of dense vortex rings with an interface and observed a parameter space division between trapped and escaping vortex rings.

This chapter presents an experimental investigation of the stability of vortex rings in a stratified environment. We begin with an analysis of the two-dimensional dynamics of the vortex rings as they impact a density interface. In order to analyze the three-dimensional dynamics, we reconstruct the full, three-dimensional velocity field of a vortex ring vertically impacting onto a stratified interface. We achieve this reconstruction through the use of a stereo-PIV (Stereoscopic Particle Image Velocimetry) setup, which determines the three components of velocity on a single horizontal plane. By moving the height of this horizontal plane relative to the density interface, we determine the three components of velocity for a range of level heights. By combining these results, we reconstruct a three-dimensional dataset of the interaction of the vortex ring with the density stratification. The limitations of this methodology, including a verification of its validity, will be discussed below. Experimental and theoretical evidence suggest strong qualitative and quantitative agreement between the reconstructed velocity field and the true interaction.

The remainder of this chapter is organized as follows. Section §4.2 provides two-dimensional simultaneous PIV/LIF[1] measurements of a vortex-ring interacting with a stratified interface, for a range of Reynolds and Richardson numbers. Section §4.3 details the experimental setup, image capture and processing methodology for the three-dimensional visualization, followed by §4.4, which presents a detailed analysis of the evolution of the velocity field. Finally, §4.5 summarizes the present work.

4.2 Vertical-slice observations

In a water-filled tank ($0.20 \times 0.40 \times 0.50$ m^3), we produced vortex rings that propagate vertically downwards towards the base of the tank. Vortex rings were generated by driving a computer-controlled linearly actuated bicycle-pump (0.029 m internal diameter) that was connected to a partially submerged hollow cylindrical tube (internal diameter $D = 0.039$ m). The vortex tube was inserted to an approximate depth of 0.13 m. The tank setup and stratification procedure has been documented in Chapter 3. In both the vertical-slice measurements found here and the horizontal-slice measurements found below, the base of

---

[1] Laser Induced Fluorescence

the vortex tube was always positioned at least two vortex diameters away from the density interface. This criterion ensures that the density interface does not affect the formation of the vortex ring.

A vertical light sheet was produced within the tank, oriented so that each vortex ring's axis was coplanar with the laser sheet. This laser sheet was generated by a frequency-doubled, double-pulsed Neodynium-Yag (Nd:YAG) laser (Litron Lasers). Each 532 nm beam was fired at a rate of 99 Hz. Two cameras (Teledyne DALSA, Falcon2 4M180) equipped with 60mm (f/2.8) Nikon lenses, were positioned facing the tank. The fluid within the tank was seeded with 20μm polyamid particles ($\rho_p \sim 1.02$ g/mL), which have a settling velocity[2] on the order of 0.005% of the vortex ring propagation speed. The cameras recorded the motion of the particles within the light-sheet at 99 frames per second. Both the laser and cameras were triggered via the connected computer system allowing for precise laser-pulse/camera-frame triggering and synchronization. The PIV methodology used to compute the fluid velocity within the vertical light sheet has been described previously, in section 3.4. Figure 4.1 presents a diagram of the experimental tank setup. The vertical laser sheet has been positioned to bisect the vortex tube. The two cameras were oriented such that their plane of focus is coplanar with the laser sheet. A florescent dye was also added to the lower layer. We return to this later.

For both the vertical-slice results presented here, and the three-dimensional results presented later, we initialize the experimental tank with a two-layer stratification. As discussed in Chapter 3, the stratification was generated using a peristaltic pump to slowly inject the denser fluid (ρ_2) beneath a layer of less dense fluid (ρ_1). As we will show in Chapter 6, this methodology produces sharp interfaces. Typically, these two fluid layers would have different refractive indices, which distort the camera images. In this chapter we will use the refractive index matching methodology described in section 3.2. For the vertical-slice experiments performed, we additionally add a small concentration of rhodamine 6G to the denser fluid (ρ_2, sodium nitrate layer), which is fluorescent when illuminated by the 532 nm laser. The concentration of Rhodamine was on the order of 5×10^{-6} wt% compared to 0.01 wt% of salt in solution and as such, does not have a measureable effect on the density. A 575nm low-pass filter was then added to one of the DALSA cameras to filter out any light from the PIV particles within the tank. The other DALSA camera was fitted with a 3 nm wide notch filter so that only the particles were visible.

Three two-layer stratifications were produced with different top-to-bottom density jumps $\triangle\rho$. The refractive index of the stratification was matched in all cases. For each density

---

[2] The settling velocity u_s is computed as $u_s = \frac{gd^2(\rho_p - \rho_m)}{18\mu}$ where g is the acceleration due to gravity, d is the particle diameter, ρ_m is the density of the medium and μ is the dynamics viscosity of the fluid.

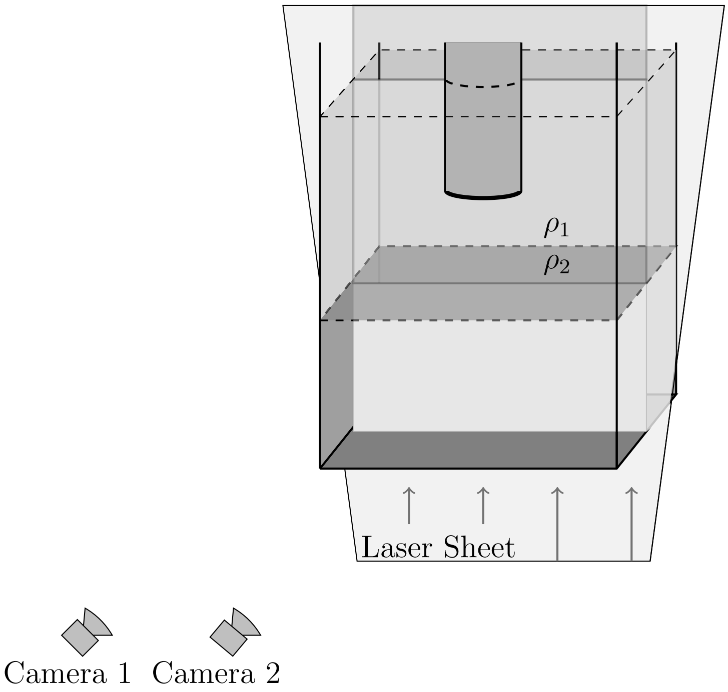

Fig. 4.1 Diagram of the tank setup for a vertical laser sheet. Note that the laser sheet is positioned such that it bisects the vortex tube.

Case	$\Delta\rho$ (10^{-3} kg m^{-3})	U (m/s)	Re	Ri
(a)	0.008	0.040	1600	1.9
(b)	0.008	0.050	2000	1.2
(c)	0.008	0.061	2400	0.8
(d)	0.008	0.071	2800	0.6
(e)	0.017	0.040	1600	4.1
(f)	0.017	0.050	1000	2.6
(g)	0.017	0.061	2400	1.8
(h)	0.017	0.071	2800	1.3
(i)	0.041	0.040	1600	9.8
(j)	0.041	0.050	2000	6.3
(k)	0.041	0.061	2400	4.2
(l)	0.041	0.071	2800	3.1

Table 4.1 Table of the parameter values associated with the twelve vertical-slice vortex-ring-interaction cases.

stratification, vortex rings with four different parameter sets were generated within the tank. This set of twelve cases allows us to evaluate the vortex-ring interaction for a suite a parameter values. Table 4.1 presents these twelve parameter cases along with their corresponding Reynolds (Re) and Richardson (Ri) numbers defined as:

$$\mathrm{Re} = \frac{DU}{\nu}, \qquad \mathrm{Ri} = \frac{g\triangle\rho}{\rho_0}\frac{D}{U^2}.$$

Here, U is the propagation speed of the vortex ring, g is the acceleration due to gravity, ν is the molecular viscosity of the fluid and ρ_0 is a reference density, taken to be $\rho_0 = 1 \times 10^3$ kg m^{-3}. The length scale was selected to be the diameter of the vortex tube D. An alternative length scale would be the vortex ring's diameter (a), however, Maxworthy (1977) demonstrated a weak parameter dependence on the ratio $\frac{a}{D}$. Due to the difficulty of perfectly aligning the light sheet with the propagation axis of the vortex rings, and thus a precise determination of a, we select the length scale to be that of the tube diameter but note the ratio $\frac{a}{D} \approx 1.25$ (shown below), as observed previously by Maxworthy (1977). Indeed, in Chapters 6 and 7, we will define the Richardson number with the vortex ring diameter, as it is an important parameter to define the kinetic energy of the vortex rings. However, the two definitions of the Richardson number are related through this ratio $\frac{a}{D}$.

A single frame from each of the twelve cases is plotted in figure 4.2. The slices were selected just prior to the breakdown of the vortex-ring interaction. The "breakdown" of the vortex-ring interaction refers to the generation of turbulent/chaotic motion, which is not precisely reproducible. For each case, the density field is visualized in the upper panel while the simultaneous vorticity measurements (saturated to ± 25 /s) are plotted in the bottom panel. The velocity field (vectors) is overlayed on top of the vorticity plots. The view windows measure 80 mm x 91 mm. While similar plots have been made previously (e.g. Dahm *et al.* (1989); Stock *et al.* (2008)), we believe we are the first to present simultaneous Laser Induced Fluorescence (LIF) /PIV measurements of the vortex-ring interaction with a stratified interface. This data will be compared with the three-dimensional results found later in this chapter. Due to the low number of generated vortex rings, it is assumed that the density stratification does not change significantly over the course of these experiments, in agreement with the results of Chapter 6.

These plots demonstrate two key features of the vortex-ring interaction. First, that the evolution of the system is largely dominated by the Richardson number, which is related to the ratio of the potential energy of the stratification to the kinetic energy of the vortex ring. Note the strong similarity between figure 4.2(b) and figure 4.2(h) with similar Richardson numbers but at very different Reynolds numbers. Second, that the transport of the lower layer fluid, ρ_2, into the upper layer tracks with the generation of secondary vorticity by the baroclinic shear. That is, the primary vorticity in the system is that of the vortex ring that, through interaction with the stratification, produces a secondary vorticity that entrains the lower layer fluid. For the purposes of this paper, we will define the process of generating secondary vorticity as the baroclinic vorticity transfer, or BVT. Here, BVT occurs at the location of the deformed interface, where the density gradient is largest. The secondary vorticity then rolls up the density interface as it transports lower layer fluid into the upper layer.

It is worth noting that due to the finite light-sheet thickness ($\sim$2mm), many of the density field images demonstrate a weak background signal resulting from the three-dimensionality of the flow. In particular, the instability of the vortex ring is visible in the bright/dark fringes within the density field image (particularly noticeable in figure 4.2(l) located just below the '$\times$'). We will refer back to this in §4.4 when discussing the "phase-locking" discovered in the three-dimensional ensembles.

It is important to understand how the depth of penetration of the vortex rings changes with the Richardson number. Figure 4.3 plots the location of the Re=2000 vortex ring's peak vorticity as a function of time. In this figure, z_ρ is the height of the unperturbed density interface and the vortex ring's diameter, a, is defined as the distance between vorticity centroids. In each of the cases presented, length has been non-dimensionalized by the vortex tube diameter (D), and time has been non-dimensionalized by the advective timescale ($t^* = D/U$). The time $t = 0$ has been specified when the vortex ring is a distance D from

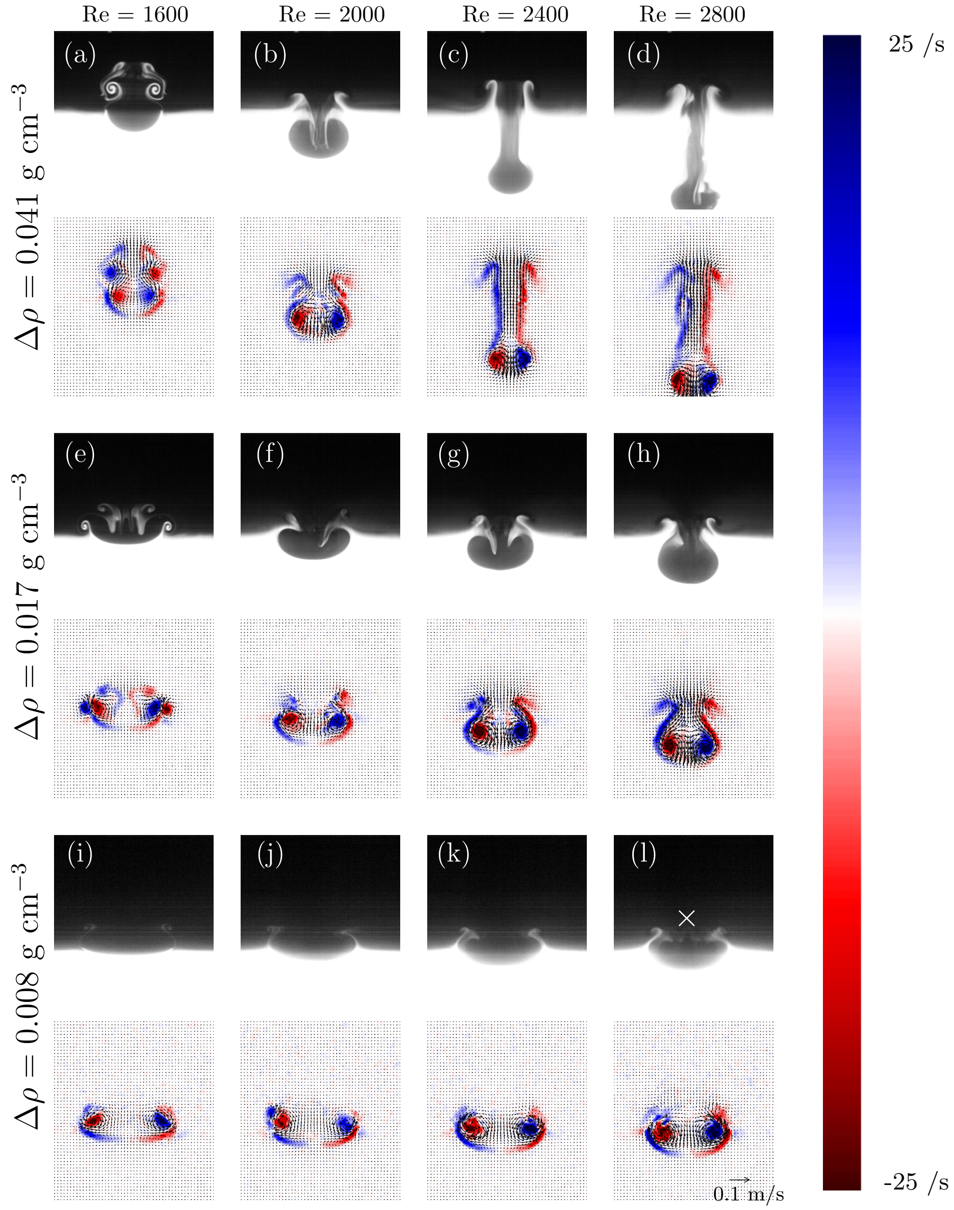

Fig. 4.2 Plot of characteristic snapshots of vortex rings interacting with a stratified interface. Images were selected just prior to the breakdown of the vortex-ring interaction. Each panel has a plot of the density (top) and the corresponding vorticity field (bottom) with the velocity field overlayed. Vorticity values have been saturated to ±25 (s^{-1}). Each column corresponds to a specific Reynolds number as indicated at the top of each column. Each row corresponds to a particular density difference as indicated on the left. The same view window was used for all panels measuring 80 mm x 91 mm. A small '×' highlights the fringes identified in the text.

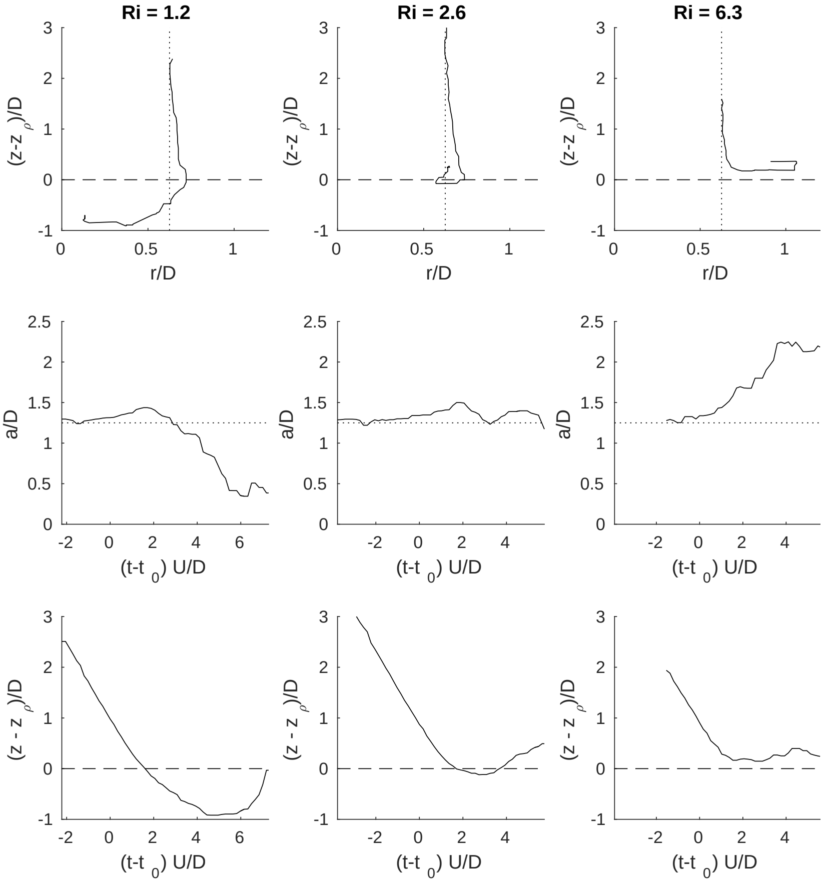

Fig. 4.3 Plot of the evolution of the vortex ring centre for Re=2000 demonstrating the penetrative, partially penetrative and non-penetrative regimes (from left to right respectively). All axes have been appropriately non-dimensionalized by the vortex tube diameter and the advective timescale. A dashed line has been plotted at $z = z_\rho$. A dotted line has also been plotted at $a/D = 1.25$.

the unperturbed density interface. In this analysis, the vertical position of the vortex ring is defined as the mean vertical position of the two vorticity centroids of the vortex ring in the plane of the laser sheet. This definition provides a simple measure for the vortex ring penetration depth over a significant portion of the interaction, but clearly loses its meaning once the flow becomes sufficiently turbulent. In figure 4.3, we observe two different stratification regimes: a penetrative regime where the vortex rings are capable of penetrating into the lower-layer, and a non-penetrative (wall-like) regime where they are not. From left to right, figure 4.3 plots typical examples of the penetrative, partially penetrative (boundary case), and non-penetrative regimes. We observe that in all cases, as the vortex ring approaches the lower layer, the vortex ring's diameter expands, even within the penetrative regime. This is true even for the lowest Richardson number cases. This expansion, which will result in vortex-stretching, has the potential to produce instabilities on the vortex-ring. Tracking of the vortex ring's core terminates once the vortex-ring interaction becomes sufficiently chaotic that the vortex ring becomes masked by the turbulent vorticity.

It is clear in figure 4.3 that the timescale of the interface rebound decreases with an increase in the Richardson number. The trajectory of the vortex-ring rebound is not quadratic as would be expected for a purely buoyancy-driven response of the interface. If the vortex ring penetrates into the lower layer, the ring diameter will contract until it has been "unwound" by the BVT mechanism. In contrast, if the vortex ring is unable to penetrate into the lower layer, the vortex ring diameter will expand, similar to the results of Bethke & Dalziel (2012). Many similarities exist between the present high Richardson number vortex-ring interactions and the interaction of a vortex ring with a solid wall. In both cases, there is a production of secondary vorticity under the impinging vortex ring in combination with the ring expansion. However, the mechanism of the vorticity production is different between the two cases. In the vortex ring-wall interaction, the secondary vorticity is produced through the viscous boundary layer as a result of the no-slip wall condition. The interface boundary condition for a vortex ring impinging on a two-layer stratification does not lead to this viscous boundary layer formation directly, rather, the secondary vorticity is generated via the BVT. In both cases, the secondary vorticity is "rolled up" around the primary vortex, which results in the vortex-breakdown.

Figure 4.4 plots the maximum penetration depth of the vortex ring's core for all cases. We expect to find (as in Linden (1973)) that the penetration depth is given by a balance of the kinetic energy of the vortex ring and the potential energy of the displaced density field. Specifically, we expect the penetration depth to scale as 1/Ri. A piecewise linear fit to the data (plotted as a solid line in figure 4.4) is given:

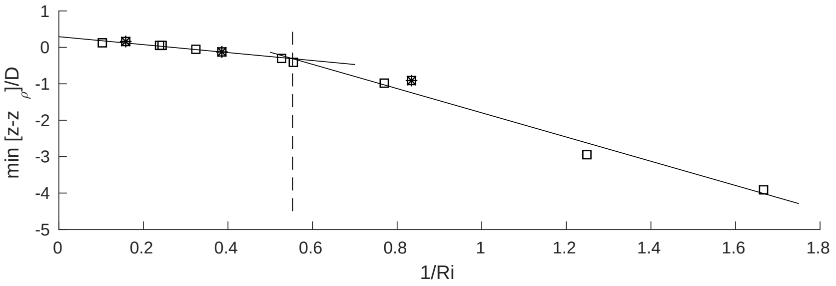

Fig. 4.4 Plot of the minimum vertical position achieved by a vortex ring for all cases. Stars (*) represent the cases presented in figure 4.3. A dashed line has been plotted to denote the boundary between penetrative and non-penetrative regimes.

$$\frac{\min[z - z_\rho]}{D} = \begin{cases} (-1.09 \pm 0.29)\ \mathrm{Ri}^{-1} + 0.07 & \mathrm{Ri} \leq 1.81, \\ (-3.38 \pm 1.53)\ \mathrm{Ri}^{-1} + 0.24 & \mathrm{Ri} > 1.81. \end{cases} \tag{4.1}$$

Note that due to the low number of data points, the error in the fit slopes is large. However, there is a clear division between the penetrative and non-penetrative regimes. Here, we expect the division to occur when there is a balance of potential and kinetic energy in the system, Ri=O(1). The experimental division point is estimated as Ri=1.81, though we suggest that there should be a smooth transition between regimes about this point. In the discussion of the three-dimensional vortex-ring visualizations below, we present a case within the penetrative regime (Ri=0.98), a case near the division point (Ri=1.7), and a case in the non-penetrative regime (Ri=2.4). This separation between regimes is reminiscent of the work of Camassa *et al.* (2013) who investigated the trapping/penetration of dense vortex rings into the lower layer of a two-layer stratification. More work is needed to expand upon the comparison between such negatively buoyant rings and our present scenario.

Linden (1973) argued that the rebound timescale of the vortex-ring interaction scales as a purely buoyancy driven response, i.e. $\mathrm{Ri}^{-\frac{1}{2}}$. Here, we investigate the timescale associated with the production of secondary azimuthal vorticity generated by the BVT. We argue that this is a better measure of the rebound timescale. This secondary vorticity generated by the BVT has an azimuthal component of opposite sign to the impinging vortex ring. We determine the timescale by plotting the total (volume integrated) secondary vorticity as a function of time. The exact functional form of the baroclinic production is unknown but a Gaussian function provides a good fit to the growth of secondary vorticity. The Gaussian fit then provides a timescale for the baroclinic production. Figure 4.5(a) explicitly denotes

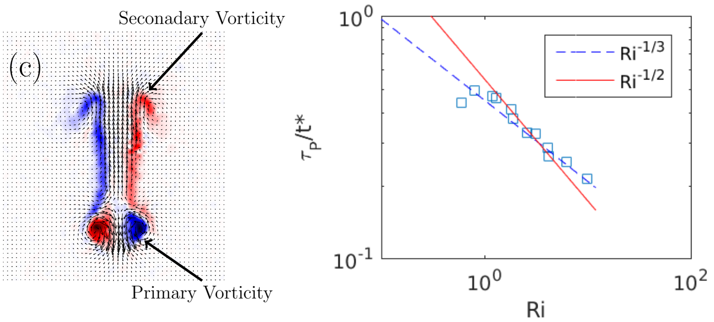

(a) (b)

Fig. 4.5 Plot of the (a) Vorticity field extracted from figure 4.2 denoting the primary and secondary vorticity and (b) the timescale associated with the baroclinic production of vorticity as a function of Ri.

the difference between the primary and secondary (BVT generated) vorticity. Figure 4.5(b) plots the timescale of secondary vorticity production non-dimensionalized by the advective timescale (t^*) vs. Richardson number. We observe that the production timescale appears to scale as $\mathrm{Ri}^{-\frac{1}{3}}$. If the baroclinic production and interface rebound occur on the same timescale, this will directly affect the Linden (1973) estimate for the entrainment rate. As the primary aim of this chapter is to investigate the three-dimensionality of the interaction, we do not discuss this further but we note that the power-law exponent for the timescale of the interface rebound, in either methodology, is less than one. We return to this in the Chapter 8 of this thesis.

4.3 Three-dimensional methods

For the remainder of this chapter, we will consider vortex rings generated in a large tank ($0.45 \times 0.45 \times 0.60$ m^3), with a horizontal light-sheet produced by the pulsed lasers. The horizontal light sheet was positioned normal to the vertically propagating vortex rings. Each laser was triggered at a rate of 75 Hz. Two cameras (Allied Vision Technologies, Bonito CMC-4000 4MP), equipped with 60mm (f/2.8) Nikon lenses, were positioned on opposite sides of the tank, looking down at the laser sheet at an angle of approximately 45 degrees to the vertical. The cameras were set to record at 150 frames per second. In order to increase the temporal resolution of the image pairs, the two laser-pulses were staggered (with a pulse separation of 2ms) about the camera frame separation. Here, 75 pairs of laser pulses were produced each second. We are able to achieve much higher temporal resolution image pairs

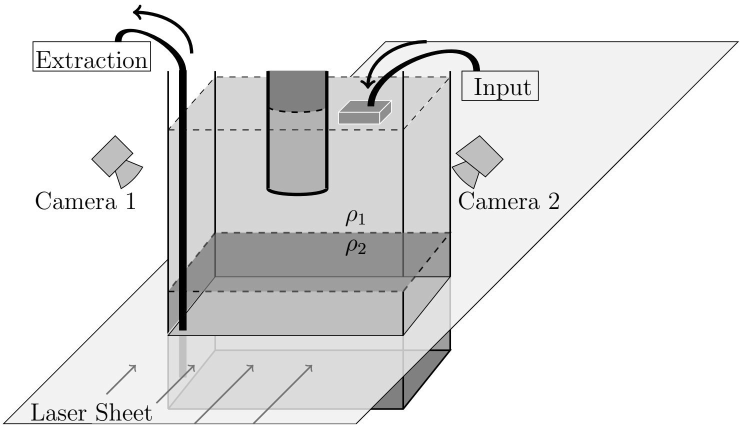

Fig. 4.6 Diagram of the tank setup for the horizontal laser sheet, highlighting the discharge of fluid from the tank base, and the addition of fresh water to the top of the water column.

than with an evenly spaced laser triggering. However, as a consequence of the precise laser triggering, only one velocity field can be computed for each pair of laser pulses. Thus, each second the cameras record 150 images, which results in 75 image pairs used to determine the velocity field within the flow. Both laser and cameras were triggered via the connected computer system allowing for precise laser-pulse and camera-frame triggering. The cameras were additionally equipped with Scheimpflug adapters (Dantec Dynamics), which allow both cameras to be focused onto the laser sheet within the tank. The fluid within the tank was again seeded with 20μm polyamid particles. Figure 4.6 shows a diagram of the experimental setup.

It is worth noting that there are several stark differences between the work presented here and the vertical-slice cases presented in §4.2. Primarily, the laser sheet is now horizontal with the two cameras positioned at an angle to the plane normal. The cameras were positioned facing the lateral sides of the tank to avoid the vortex tube framework. The incident angle of the cameras was low enough such that the tank walls did not substantially obscure the particle images. The incident angle is limited by the internal angle of reflection of the tank walls. As both available cameras were used for the StereoPIV, no density information is available. The second camera used for PIV enables the three-dimensional reconstruction of the velocity field, which was not previously available. As the only light reaching the cameras was that scattered from the particles within the light sheet, no filters were necessary.

4.3.1 Stereo-PIV methodology

It should be noted here that the Stereo-PIV methodology described here was created and implemented by Professor Stuart Dalziel. This implementation was incorporated into DigiFlow^{tm}. The paper associated with this chapter was the first to publish results using this methodology.

Each PIV camera provided a two-dimensional projection of the particles visible within the laser sheet. As a first step, the image sequence from each camera was used to compute a two-dimensional pixel-displacement field in that camera's natural pixel coordinate system. Three coordinate systems are then needed to project this information onto the three components of velocity within the plane of the laser sheet.

The coordinate systems were constructed using a two-level calibration grid of a known geometry, placed within the focal plane window of both cameras at a known real-world position. Using this information, mappings between the pixel and world coordinates could be established. Here, we determined the two-dimensional world coordinate mapping for each camera along with a three-dimensional world coordinate system projecting the four pixel coordinates (two per camera) into three-dimensional space. Each coordinate system was constructed using a least squares procedure from polynomial basis functions. The individual two-dimensional systems were registered to the plane of the laser sheet through an iterative process that included cross-correlating the PIV images from one camera with those from the other. A coordinate refinement step was also added in order to correct for a mis-alignement between the laser sheet and the calibration grid.

The individual two-dimensional coordinate systems were then used to map the pixel-displacement field from the pixel coordinates of each camera onto the common $x-y$ coordinates of the laser sheet so that four pixel-displacement components are known for every location in the $x-y$ plane. Finally, the Jacobian derivative matrix of the three-dimensional coordinate system mapping was used to project these four pixel-displacements into the three components of the velocity field.

To verify this process, we also back-projected the three components of the velocity in the world coordinate system onto pixel-displacements in the pixel-coordinates of the individual cameras. Comparing these back-projected fields with the original pixel-displacement fields from the two-dimensional PIV allowed the performance of the processing to be assessed and optimized.

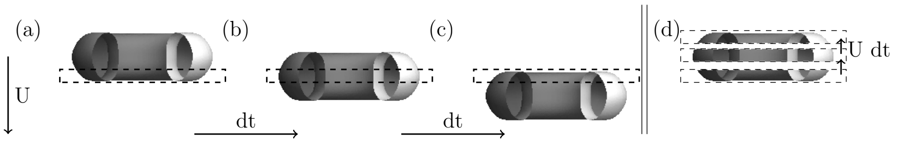

Fig. 4.7 Diagram of the reconstruction algorithm from a series of horizontal slices taken with a temporal spacing dt.

4.3.2 Vortex ring reconstruction

As an initial test of the stereo-PIV system, we produce vortex rings in an unstratified tank. In order to reconstruct the velocity field of the vortex ring in the homogeneous fluid, the vortex ring is assumed to be purely advected according to its propagation speed (in this case, U = 0.040 m/s). The advective assumption states that as the vortex ring propagates, the velocity field recorded within a fixed plane normal to the direction of propagation is equivalent to the instantaneous velocity of the vortex ring in all three spatial dimensions. Under this assumption, the virtual level spacing between each frame of a camera recording is simply given by $dz = Udt$. That is, the vertical spacing (dz) is the product of the vortex-ring propagation speed (U) and the time between velocity snapshots (dt). Figure 4.7 provides a diagram of this reconstruction process. For these unstratified experiments, the camera capture rate was limited to 100 frames per second, resulting in 50 image pairs per second used to reconstruct the velocity field. The vertically discretized reconstruction R is thus computed from the velocity field slices I. The slices I are computed from images of the physical vortex ring flow field F at the fixed laser-sheet height z_0 and the varying frame time t_f, written

$$R(x,y,Ut_f - z_0) = I(x,y,z_0,t_f) = \int F(x,y,z,t)\delta_z(z - z_0)\delta_t(t' - t_f)dzdt'.$$

This is an idealization where δ_z and δ_t are Dirac delta functions. In practice, R is constructed from finite width intervals where δ_z is the laser sheet thickness ($\approx$1mm) and δ_t is the duration of the laser pulse ($\approx$10ns). The physical coordinates are given as x, y, z. An alternative method would be to reposition the light sheet and reconstruct the vortex ring over an ensemble of experiments by appropriately time-correlating the image frames to a fixed time t_0, relative to the generation time. That is, for repositioned laser-sheet height z_E,

$$R(x,y,Ut_f - z_0) \sim \tilde{R}(x,y,z_E) = \int F(x,y,z,t)\delta_z(z - z_E)\delta_t(t' - t_0)dzdt'.$$

The $(\tilde{\cdot})$ denotes a reconstruction assembled from an ensemble of experiments. This ensemble approach projects the data into the space of reproducible velocity field measurements. That

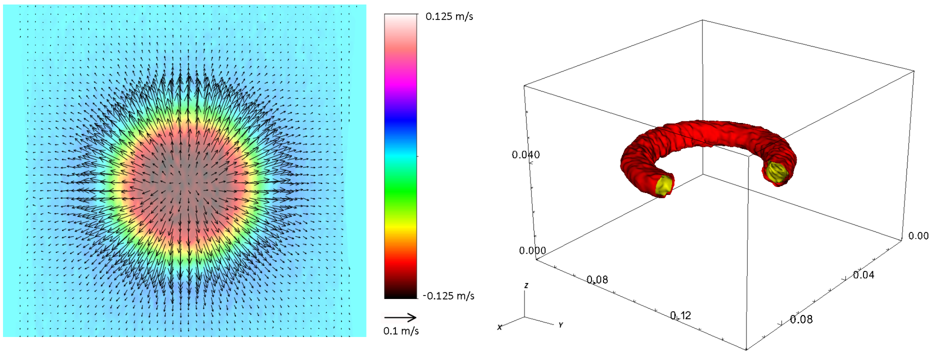

(a) (b)

Fig. 4.8 Three-dimensional reconstruction of a vortex ring within a homogeneous fluid. Panel (a) plots the three components of velocity within a single frame. Colour represents the vertical velocity (out of the page) and arrows indicate the planar velocity field. Panel (b) plots isocontours of vorticity magnitude at 40% (yellow) and 25% (red) of the maximum value of vorticity for the smoothed data set. The axis dimensions are in metres.

is, chaotic or turbulent motions will manifest as noise using this ensemble methodology. The two methods are asymptotically similar in the limit of small inter-frame spacing and level heights, provided that the motion is perfectly repeatable between realizations.

Figure 4.8(a) plots a single frame of the reconstructed three components of velocity within a horizontal plane. Here, the vertical velocity (out of the page) is represented by the image colours, and the vectors represent the planar velocity field. Figure 4.8(b) then plots isosurfaces of the magnitude of the vorticity vector for the three-dimensional reconstruction. the isosurfaces are plotted at 40% (yellow) and 25% (red) of the maximum value of vorticity for the smoothed (using a median filter) data set. The axis dimensions are in metres. The spatial resolution of the ensemble was $dx \times dy \times dz = 0.172 \times 0.171 \times 0.779$ mm.

We find excellent agreement between the three-dimensional velocity data set R collected here and the velocity field collected from two-dimensional measurements in a vertical light sheet through the centre of a vortex ring. Figure 4.9 plots a comparison of the horizontal (figures 4.9(a) and (b)) and vertical (figure 4.9(c) and (d)) velocity fields determined using both a vertical light sheet (panels (a) and (c)), and a simulated virtual light sheet (panels (b) and (d)) derived from the vortex-ring reconstruction (i.e. $R(x, y_0, z)$ for fixed constant y_0, positioned at the centre of the vortex ring). Both the vertical light sheet and reconstructed planes are saturated to the same values. We find good agreement in the diameter of the ring and in the velocity values. The magnitudes of the velocity fields are slightly larger in the 3D case, and the width of the vertical velocity distribution is marginally greater. The differences

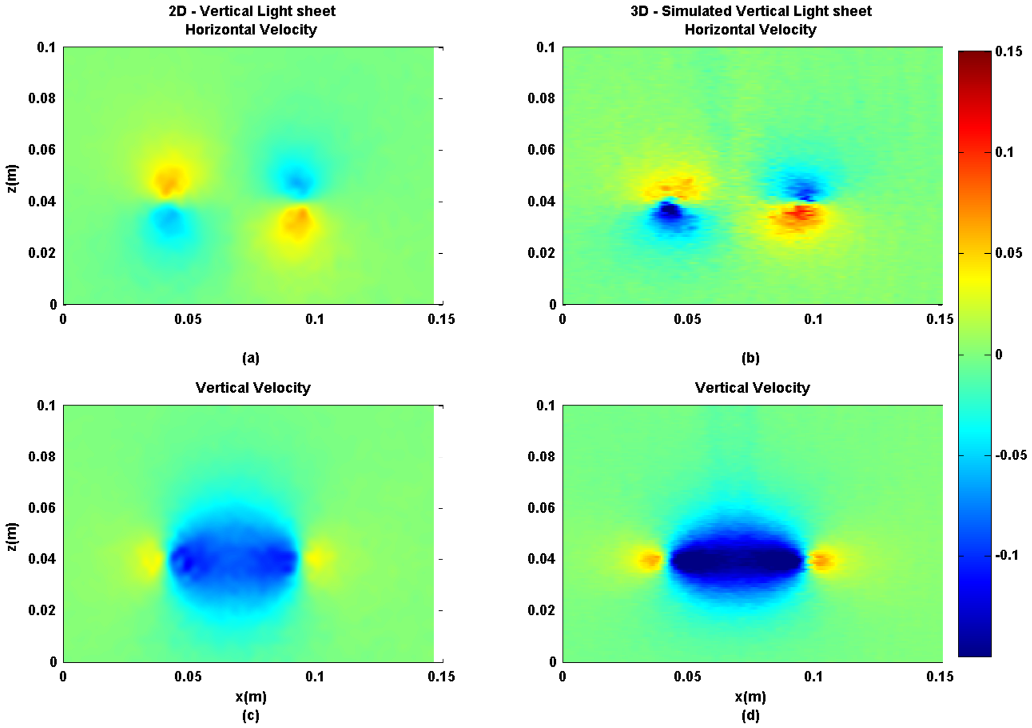

Fig. 4.9 Comparison of the computed horizontal (panels (a), (b)) and vertical (panels (c), (d)) velocity fields within a vertical plane. Panels (a), (c): Velocity field computed from a vertical light sheet. Panels (b), (d): Velocity field computed from the reconstruction using the layering methodology.

between the two planes can be largely explained by the vertical light sheet being slightly off-centre to the axis of the ring, which is an experimental inevitability. Additionally, we note that the change of experimental setups will also add to the discrepancy between velocity measurements. We believe that this comparison strongly supports the ensemble methodology.

Note that we do not observe any instability occurring on the ring. The Widnall *et al.* (1974) instability will eventually grow to large amplitude and cause the vortex ring to become visibly unstable. However, at the time at which the vortex ring reaches the height of the laser sheet, the instability has not had sufficient time to grow to finite amplitude. This has important implications for the work presented below.

4.3.3 3D field from multiple experiments

In §4.2, we observe that vortex-ring interactions with a stratified interface are surprisingly robust. We take advantage of this reproducibility here. In the following work, we fill the experimental tank with a two-layer stratification. The tank was stratified as described previously. As some of the lower-layer fluid will be extracted between subsequent experiments in order to “slice-through” the vortex-ring interaction, the initial depth of the lower fluid layer was estimated such that the maximal penetration of the vortex ring was just above the laser sheet. Typical initial lower layer depths were on the order of 0.25m, where the light sheet was position at a height of 0.19m above the base of the tank.

Once the stratification was established, the following experimental protocol was followed:

(i) - The laser system is activated and temporally synchronized with the cameras.

(ii) - A vortex ring is generated.

(iii) - The vortex-ring interaction is recorded.

(iv) - The cameras and laser system are turned off.

(v) - Using a peristaltic pump, a controlled volume of fluid is removed from the lower layer. Using a second peristaltic pump, fresh water was added at the top of the water column in order to conserve the total water-column height. The volume removed was 393($\pm$2) mL corresponding to an interface shift of 0.0019m.

(vi) - A 5-minute settling-period is implemented from the start of the previous experiment in order for any residual motions within the water tank to diffuse.

(vii) - The experiment is repeated.

By controlling the position of the interface through the use of two peristaltic pumps, the distance between the density interface and the laser sheet is changed. This allows us to control the relative height of each recorded experiment in order to “scan through” the vortex-ring interaction. Note that figure 4.6 includes the extraction and input of fluid through the system.

In contrast to the unstratified case, we cannot use the propagation speed of the vortex ring to determine the spacing between level heights of the ensemble. Here, each individual realization is now time dependent regardless of the frame of reference. By knowing the volume extracted between each vortex-ring interaction, we estimate the relative height between each experimental data plane (i.e. Δz_E). As we will see in Chapter 6, the vortex-ring-induced mixing of the interface produces an additional shift to the interface position. We account for this additional shift when computing Δz_E, which is approximately 5% of the total shift. We “stack” the individual experiments together, adjusting for the propagation speed of the vortex rings, in order to reconstruct the full, time-resolved, three-dimensional velocity field. Figure 4.10(a) plots a representation of this ensemble of different experiments.

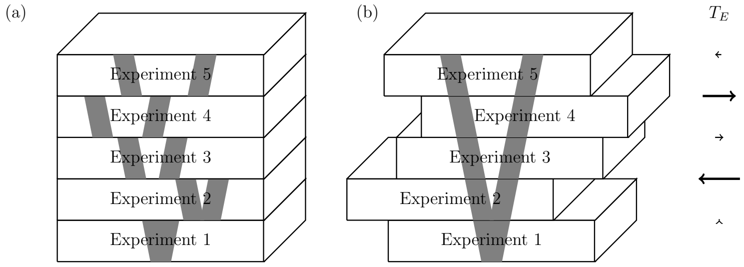

Fig. 4.10 Diagram of the three-dimensional velocity reconstruction from a series of vortex-ring interaction experiments. Panel (a) represents the "stacking" of individual experiments in order to capture the full, three-dimensional, dynamics. Panel (b) presents the ensemble once the experiments have been time-correlated according to their RMS values to produce a consistent data-set. The arrows on the right represent variations in the time synchronization T_E.

That is, the reconstruction $\tilde{R}$ is given

$$\tilde{R}(x,y,z_E,t-T_E) = \int F(x,y,z,t')\delta_z(z-z_E)\delta_t(t'-(t-T_E))dzdt'.$$

For the purposes of the ensemble, the first experiment is assigned a vertical height of $z_E = 0$. The time synchronization between individual experiments (T_E) must account for the additional time delay between the vortex-ring generation and when it reaches the laser sheet (the additional propagation time of the ring) as the vortex tube was fixed between experiments. In addition, T_E must account for signal delays between the start of the camera capture and the generation of the vortex ring. Although hardware synchronization was used between the lasers and the camera, ensuring consistency, the synchronization between the image capture and vortex generation was software based between laboratory computers. This introduced a small random offset between different experiments of the ensemble. In order to account for this variation, the root-mean-squared (RMS) value of the vertical velocity was computed over a range of frames (O(1000) frames). Then, T_E was computed as the temporal shift that provides the best correlation between subsequent experiments. Figure 4.10(b) plots a representation of a time-correlated ensemble. Typical T_E variations are ≈ 0.1s, consistent with the software delay between computers. Both the level height z_E and the time synchronization T_E are a function of the discrete vortex ring experiment number.

In this chapter, three ensembles are presented. Each ensemble was filtered using a spectral and smoothing filter. The parameters associated with these ensembles are presented in table 4.2. The advective timescale is given as t^*. Density differences are restricted to small values due to the difficulties of maintaining matched refractive indices at larger density differences.

Case	U (m/s)	$\Delta\rho$ (10^{-3} kg/ m^3)	Re	Ri	t^* (s)	$n_x \times n_y \times n_z$	$dx \times dy \times dz$ (10^{-3} m)
1	0.040	0.0044	1600	0.98	1.03	$256 \times 256 \times 59$	$0.526 \times 0.538 \times 2.11$
2	0.061	0.017	2400	1.7	1.56	$256 \times 256 \times 63$	$0.526 \times 0.538 \times 2.03$
3	0.040	0.010	1600	2.4	1.03	$256 \times 256 \times 45$	$0.526 \times 0.538 \times 2.00$

Table 4.2 Table of the three cases used for three-dimensional velocity field reconstruction of the vortex-ring interaction.

The quantities n_x, n_y, n_z and dx, dy, dz are the grid size and grid spacing respectively. Note that the last quantity n_z denotes the number of experiments used to construct each ensemble. The horizontal resolution was subsampled using a cubic spline in order to facilitate the computations.

4.3.4 Limitations of the methodology

A number of assumptions have been made when developing the current methodology. The primary assumption is that throughout these experiments, the vortex rings are highly reproducible. This assumption has been validated by looking at the propagation speed of vortex rings produced within a vertical light sheet. This assumption is also supported by the high degree of correlation between neighbouring members of each ensemble. We additionally attempt to control the variation of these parameters by ensuring that the water column height remains fixed when discharging the lower layer fluid. The second assumption is that the vortex-ring interaction dynamics are also reproducible. As we will show later in §4.4, not only are the dominant axisymmetric dynamics reproducible, but we capture the resultant instabilities of the interaction. Third, the change in stratification between vortex-ring interactions does not substantially change the dynamics. The correlation of the RMS values defined previously suggests that the dynamics are not substantially affected by the small perturbations to the density field. In addition, as will be shown in Chapter 6, the mixing rate associated with the vortex-ring interactions is near constant. Finally, and potentially the greatest source of error in this methodology, is the assumption that the stratification gradient is not the dominant control parameter to this problem. While the interface thickness is sharp, an exact density profile could not be determined due to the method used to match refractive indices. Here, we assume, again with reference to Chapter 6 for supporting evidence, that this does not have a dominant effect on the interaction. We did not find any evidence to suggest that the vortex rings generated first had different dynamics to those generated subsequently in the ensemble.

It should be reiterated that the methodology presented here will only produce a coherent ensemble when the vortex-ring interaction is sufficiently reproducible. Of course, the vortex-ring interaction will eventually breakdown into turbulent motions. This turbulent motion is similar to that of a plume/fountain but will not be studied here. As we will show below, the ensemble will eventually become incoherent once the turbulent motion dominates. However, as will also be shown below, the instability itself is remarkably robust and is clearly captured by the ensemble.

4.4 Results

From the experiments described above, the resultant ensembles are fully three-dimensional, time-resolved velocity field measurements for the evolution of the vortex-ring interactions. Unfortunately, due to the need for precise refractive-index matching of the density stratification, we do not have access to the evolution of the density field.

4.4.1 Case 1 - Penetrative - Re = 1600, Ri = 0.98

We begin with a discussion of Case 1 (Re = 1600, Ri = 0.98). Figure 4.11 plots three-dimensional projections of 10 evenly-spaced isosurfaces of vertical velocity, between w/U= ± 2.5 ($w = \pm 0.1$ m/s), over the evolution of the interaction. Here, the plots have been generated every one advective time-unit (t^*). Note that the arbitrary time origin of this data corresponds to the first plane presented. The data has been sliced through the centre of the vortex ring in order to visualize the core dynamics.

The Richardson number of Case 1 is well within the penetrative regime (see §4.2), and as such the penetration depth of the vortex ring into the lower layer is significant. We observe the incoming vortex ring in figure 4.11(b). Through the BVT, the vortex ring is slowly “unwound,” as seen in figure 4.11(c), where the vortex ring core slowly shrinks over time. The remaining panels, figure 4.11(d)-(f), plot the slow recovery of the interface. Note that the vortex ring penetrates slightly deeper than the visualization domain.

The parameters associated with this ensemble are similar to those of the vertical slice case presented in figure 4.2(f). Indeed, the vertical velocity in figure 4.2(f) is nearly identical to figure 4.11(e). Thus, the vertical slice results provide a validation of the layering methodology of the ensemble. We note that the ensemble has a lower signal-to-noise ratio than the vertical slice results. This error is partially a result of the inter-generational variation of the vortex rings. The experimental difficulties introduced by the non-normal camera angle and the imperfectly matched refractive indexes of the two fluid layers will produce additional sources

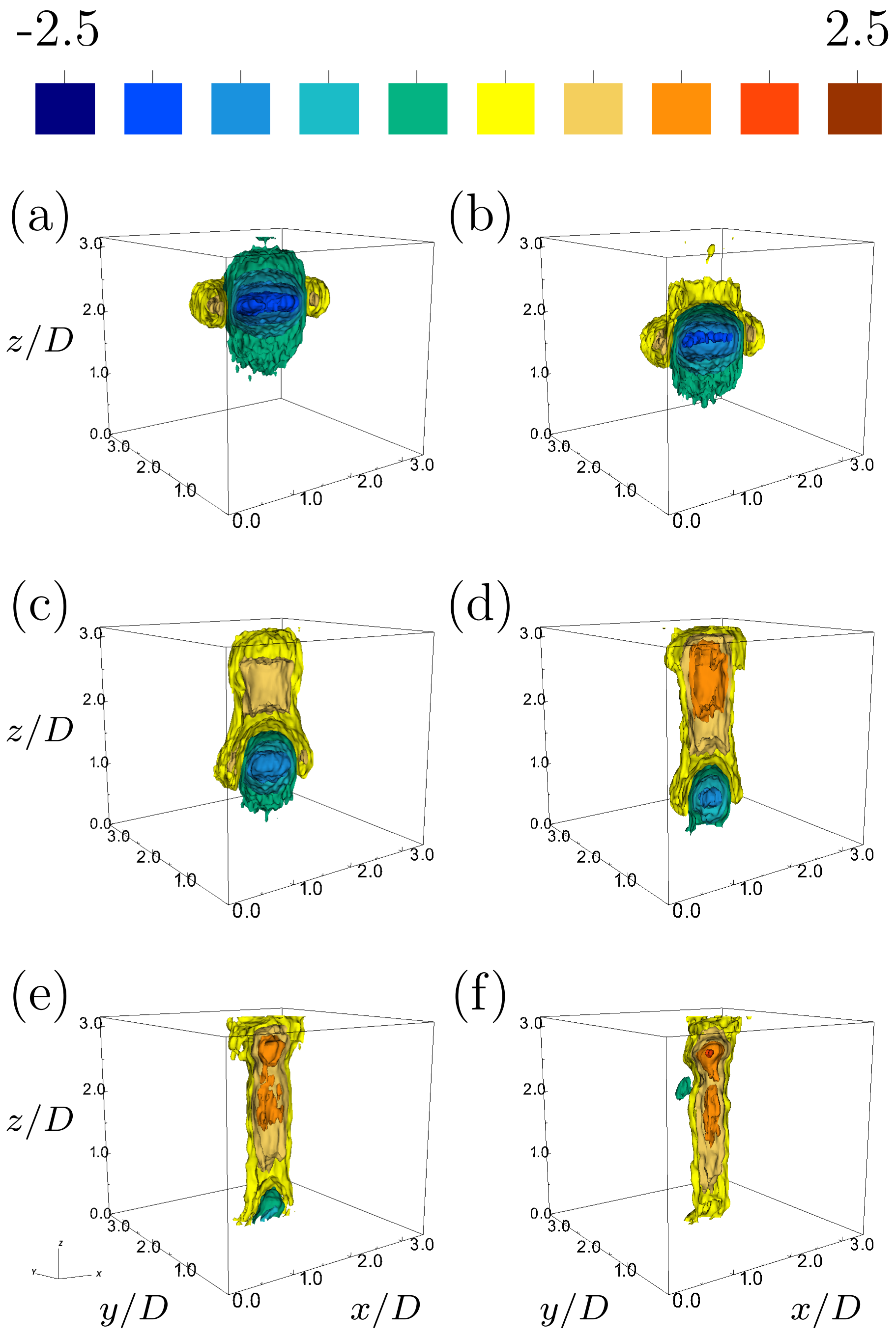

Fig. 4.11 Case 1: 10 isosurfaces of vertical velocity evenly spaced between w/U= $-2.5..2.5$ ($w = -0.1..0.1$ m/s). The contours are plotted every one advective time-unit ((a) $t/t^* = 0$, (b) $t/t^* = 1$, (c) $t/t^* = 2$, (d) $t/t^* = 3$, (e) $t/t^* = 4$, and (f) $t/t^* = 5$). The data has been cropped about the centre ($y/D = 1.8$) of the vortex ring in order to visualize the core dynamics.

of error. Thermal and other residual motion within the tank may also contribute to the noise in the ensemble. Lastly, as we mentioned above, once the vortex-ring interaction breaks down into turbulence, the image recordings will contain data that may be identified as noise in the ensemble. However, the velocity field remains surprisingly coherent until late times of the interaction, and is more than sufficient to analyze the growth of the three-dimensional instability of the flow.

4.4.2 Case 2 - Partially Penetrative - Re = 2400, Ri = 1.7

The parameters of Case 2 present both a higher Reynolds and Richardson number (Re = 2400, Ri = 1.7) than Case 1. Figure 4.12 plots 10 evenly-space isosurfaces of vertical velocity, in a similar manner to figure 4.11. The contours are plotted at every one advective time-unit. As for Case 1, we observe the incoming vortex ring in figure 4.12(b). The penetration of the vortex ring into the lower layer is increasingly restricted due to the significantly higher Richardson number. We observe the corresponding rebound of the interface in Figure 4.12(d-e). Figure 4.12(f) was selected to demonstrate that once the coherent nature of the vortex-ring dynamics break down into turbulent motions, the coherence of the visualizations also breaks down.

In this chapter, we primarily focus on the evolution of the vortex ring velocity field due to its smoothness. However, Figure 4.13 plots 10 isosurfaces of the azimuthal component of vorticity at $t/t^* = 3.2$ saturated at $\omega_\theta D/U = \pm 16$. Figure 4.13(a) plots the vorticity, which has been sliced through the ring centre in order to view the core dynamics and to make a comparison with the vertical slice experiments with similar parameter values (see, figure 4.2(g)). It is clear that the ensemble approach and the vertical slice images are in qualitative and quantitative agreement (the isosurfaces have been saturated to the same value as that of figure 4.2). Figure 4.13(b) plots the identical data without the mid-plane slicing such that the three-dimensionality of the interaction can be seen. There exists a clear modal instability in the azimuthal direction. Here, the vorticity generated by the BVT is plotted in red. A discussion of the instability is provided below. However, we note here that the instability is occurring on the baroclinically generated vorticity, which is of the same mode-number as would be observed in the primary vorticity of the unstratified vortex ring (there is no secondary vorticity in that case).

It is worth noting that the Richardson number of Case 2 is near the boundary between the penetrative and non-penetrative regimes discussed in §4.2.

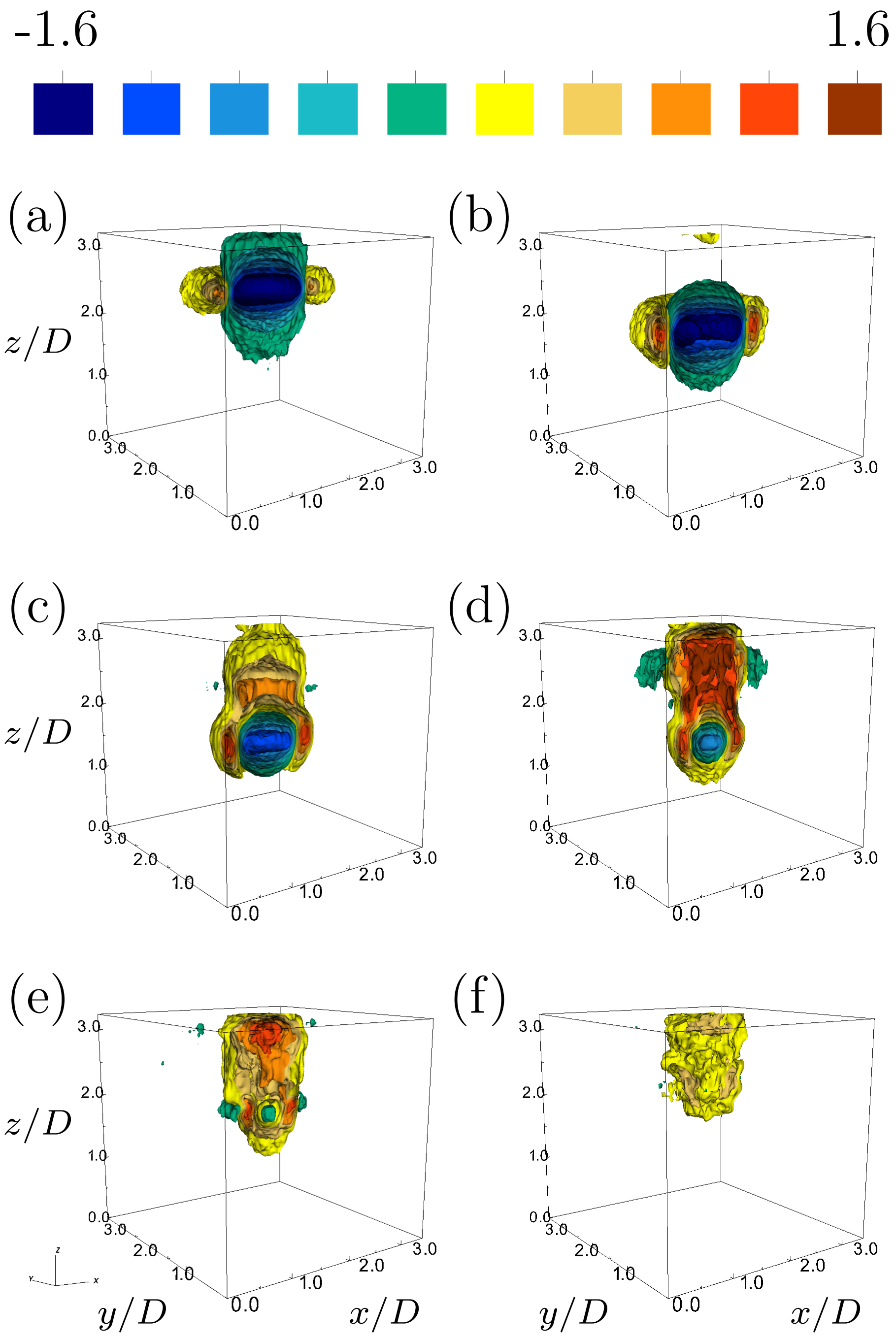

Fig. 4.12 Case 2: Plot of 10 isosurfaces of vertical velocity evenly spaced between w/U= $-1.6..1.6$ ($w = -0.1..0.1$ m/s). The contours are plotted every one advective time-unit ((a) $t/t^* = 0$, (b) $t/t^* = 1$, (c) $t/t^* = 2$, (d) $t/t^* = 3$, (e) $t/t^* = 4$, and (f) $t/t^* = 5$). The data has been cropped about the centre ($y/D = 1.8$) of the vortex ring in order to visualize the core dynamics.

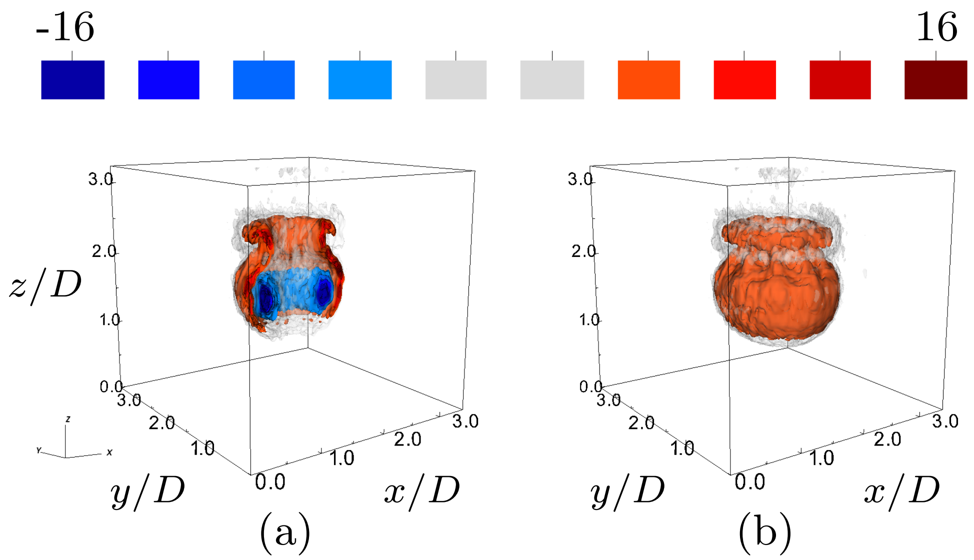

Fig. 4.13 Case 2: Plot of 10 isosurfaces of azimuthal vorticity, bounded by $\omega_\theta D/U = -16..16$. Contours are plotted at $t/t^* = 3.2$. (a) Plot of the vorticity sliced through the centre of the ring. (b) The identical vorticity plot without slicing.

4.4.3 Case 3 - Non-Penetrative - Re = 1600, Ri = 2.4

Case 3 has an identical Reynolds number to Case 1 but with a higher Richardson number (Re = 1600, Ri = 2.4). As with figures 4.11 and 4.12, figure 4.14 plots 10 evenly-spaced isosurfaces of vertical velocity, between w/U= ±2.5 ($w = \pm 0.1$ m/s), over the evolution of the interaction. The contours are plotted at intervals of 1 advective time unit. A similar evolution of the vortex ring is observed here as for the previous two cases.

The vertical slice case that most closely corresponds to the Richardson number of Case 3 is plotted in figure 4.2(f). As Case 3 is within the non-penetrative regime, we do not observe a shrinking of the vortex ring's diameter during the vortex-ring interaction but rather its expansion (see Figure 4.14(c)-(d)). Despite the much higher Richardson number, the mode of instability in the velocity field is identical for Case 1 and Case 3, which have the same Reynolds number. We return to this later.

It is remarkable that the vortex-ring interaction with a stratified interface is as repeatable as shown here. In the three cases presented above, the vortex ring dynamics are encapsulated by the ensemble until relatively late stages of the interaction despite the breakdown of the axisymmetry. Indeed, the ensemble captures the initial growth of the instability as well as the bulk dynamics of the flow. The instability itself appears to be phase-locked and does not require rotation of the individual realizations about the z-axis as was originally expected. This phase-locking, discussed below, may be a result of non-circular perturbations to the

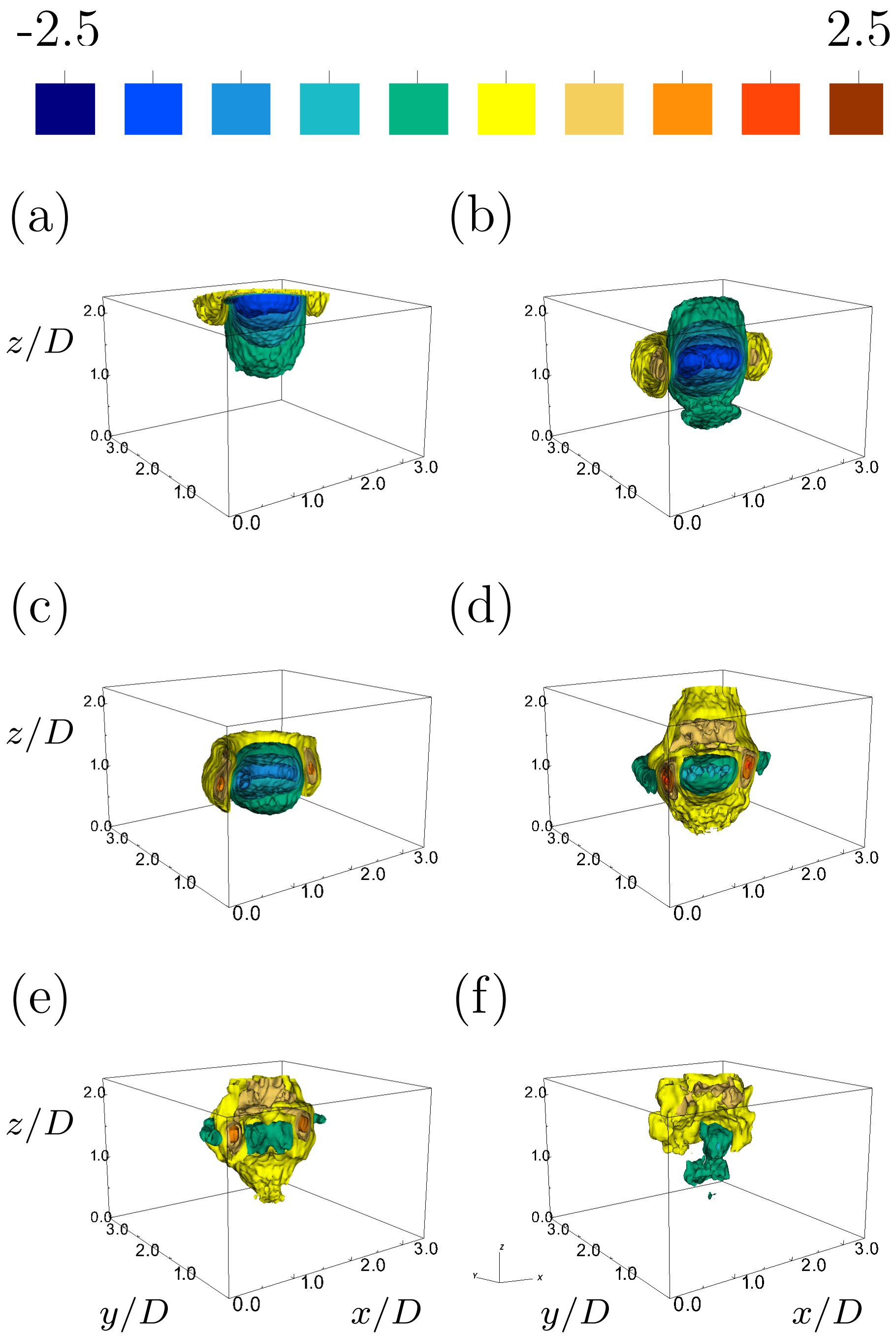

Fig. 4.14 Case 3: Plot of 10 isosurfaces of vertical velocity evenly spaced between w/U= $-2.5..2.5$ ($w = -0.1..0.1$ m/s). The contours are plotted every one non-dimensional time-unit ((a) $t/t^* = 0$, (b) $t/t^* = 1$, (c) $t/t^* = 2$, (d) $t/t^* = 3$, (e) $t/t^* = 4$, and (f) $t/t^* = 5$). The data has been cropped about the centre ($y = 1.8$) of the vortex ring in order to visualize the core dynamics.

base of the vortex tube (measured to be 0.64 ± 0.13 % of the vortex tube diameter), which are of sufficiently small amplitude that their effect is not visible in the homogeneous case. We suggest that the azimuthally anisotropic perturbation was sufficient to phase-lock the azimuthal instability without controlling the mode number of the instability. As we will continue to show below, the consistency of the vortex-ring interaction is surprising beyond any initial estimates.

4.4.4 Three-dimensional Instability

In the absence of stratification, Maxworthy (1977) noted the appearance of definitive peaks and troughs in the dye entrained by a vortex ring. He associated these modes with solitary waves forming on the surface of the vortex ring. It was then shown that the mode number of the vortex-ring waves depends on the Reynolds number alone, for low Reynolds numbers (Maxworthy, 1977; Saffman, 1978). We do not observe any evidence of this instability on a vortex ring within an unstratified fluid at the position of the laser sheet. However, for the stratified cases, figure 4.15 plots a $0.26D$ thick horizontal slice of six isosurfaces of vertical velocity for all three ensembles at: Case 1 at $t/t^* = 3.76$ ($z = 1.22..1.47$), Case 2 at $t/t^* = 4.18$ ($z = 1.67..1.92$), and Case 3 at $t/t^* = 3.76$ ($z = 1.41..1.67$). These slices were positioned just above the downward propagating vortex ring in order to demonstrate the dominant instability in the vertical velocity field. The mode number of the instability, for each case, can be identified as (a) Case 1 (Re=1600) - mode 8, (b) Case 2 (Re=2400) - mode 10, and (c) Case 3 (Re=1600) - mode 8. We see that the mode number of the instability is indeed dictated by the Reynolds number of the vortex ring. The mode number of the unstratified vortex-ring instability (Widnall *et al.*, 1974) is estimated as $n \approx 9$ in all three cases. This agrees well with the present observations in a stratified environment. We note that the instability is predominantly expressed in the secondary vorticity field generated through the BVT. We also point out that the uneven nature of the instability is viewed elsewhere for vortex rings traveling in an unstratified medium (Krutzsch *et al.*, 1939).

In addition to the mode number, figure 4.15 highlights that increasing the Richardson number of a vortex-ring interaction increases the maximum amplitude of the instability as well as the complexity (or structure) of the perturbations. In reference to figure 4.15[c], the structure of this instability is reminiscent of the numerical results found by Feng *et al.* (2009) and Archer *et al.* (2008) in the absence of stratification. Note that the instability appears to be all but absent in Stock *et al.* (2008) for the numerical simulation of a vortex ring impacting a stratified interface. The similarity of the results presented in this chapter with the numerical studies of unstratified vortex rings, along with the theoretical results of Widnall *et al.* (1974),Maxworthy (1977), and Saffman (1978), is suggestive that there is a

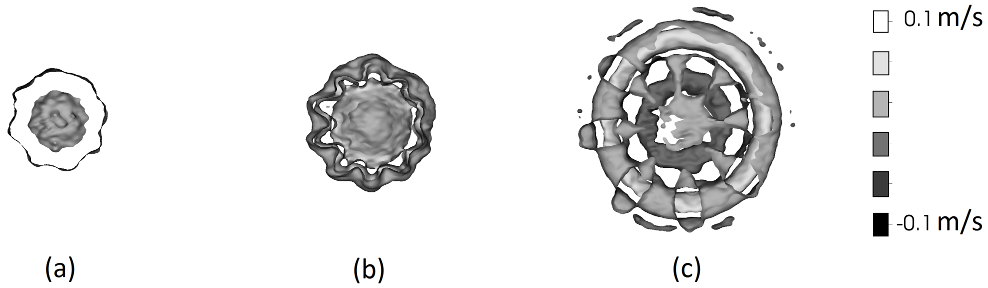

Fig. 4.15 Representative slices of vertical velocity are plotted to demonstrate the interaction instability. The time of each ensemble slices are given: (a) Case 1 at $t/t^* = 3.76$ ($z = 1.2..1.5$), (b) Case 2 at $t/t^* = 4.18$ ($z = 1.7..1.9$), and (c) Case 3 at $t/t^* = 3.76$ ($z = 1.4..1.7$).

strong correlation between the unstratified and stratified instability mechanism. However, it is clear that the stratification does affect the growth of the vortex-ring instability, catalyzing the growth of waves on the secondary vorticity surface. This stratification-enhanced growth is consistent with the work of Atta & Hopfinger (1989) who showed that vortex-ring instabilities occurred substantially earlier in a stratified environment than in the corresponding unstratified case.

In order to investigate the instability of the vortex-ring interaction, the azimuthal coordinate, θ, was divided into fifty bins, θ_i, from which the angular distribution of vertical velocity, $P(z,t)$ was computed

$$P_j(z,t) = \sqrt{\frac{\int_0^R \int_{\theta_j}^{\theta_j+\frac{2\pi}{100}} (w^2 - <w>^2)\, r dr d\theta}{\int_0^R \int_{\theta_j}^{\theta_j+\frac{2\pi}{100}} r dr d\theta}}.$$

The angled brackets denote the horizontal mean. The finite extent of the ensemble domain restricts the radial extent of the integration R, here selected to be $R = 0.05$m. Figure 4.16 is a waterfall plot of P_j vs θ for the same output times as figure 4.15. We observe the striking phenomena that in all three ensembles there exists a phase-locking of the instability between consecutive experiments of the ensemble. Specifically, the instability is rotationally aligned over many different experiments (each horizontal line is from a different experiment of the ensemble) of a particular parameter case. Evidence from the vertical laser-sheet experiments in §4.2, performed in a smaller tank, suggest that the phase-locking phenomena is not a result of the tank domain. It is possible that small non-circular perturbations on the inside of the tube used to generate the vortex rings may be the cause of the phase-locking. However, the orientation of the instability is not constant for different ensembles (see below). Regardless of how the phase-locking is occurring, the phase locking does not control the wavenumber of the instability.

Recent experimental measurements of unstratified vortex rings (Ponitz *et al.*, 2015) have demonstrated that the unstratified instability is stationary (i.e. no azimuthal propagation) at early-times. Indeed, this agrees with both the prediction of Widnall *et al.* (1974) and the numerical results of Archer *et al.* (2008). Thus, we suggest that the vortex-ring instability in the stratified environment should be similarly stationary. Indeed, we do not observe any azimuthal propagation of the wave structures in the ensembles.

In reference to the phase-locking, we observe the existence of a phase reversal of P (determined from the vertical velocity) at various heights. This phenomenon is observed for all three cases. As discussed above, this phase reversal is not a result of an angular phase speed of the instability. Figure 4.16[(d)-(f)] plots the associated three-dimensional structure of the vertical velocity, which demonstrates the phase reversal of the instability. Figure 4.13(b) also plots this phase-reversal in the secondary vorticity field. Note that we are only looking at one component of the velocity in P. The instability can rotate into u then back into w. This phase reversal is not entirely understood. One explanation is that as the instability of the secondary vorticity field grows, it is also being advected. This advection causes the sheet of secondary vorticity to 'roll up' on itself producing an apparent reversal. More work needs to be done to understand this phenomenon.

We observe that the dominant instability is of a single mode number. From the angular distribution of vertical velocity, which was sampled at points j, we compute the Fourier transform of each level height z_a as,

$$P_j(z_a,t) = \sum_k c_k(z_a,t) \exp\left[ik\theta_j\right].$$

For the dominant instability mode n, we write the corresponding complex Fourier coefficient in polar form, $c_n = Ae^{i\phi}$, for real coefficients A, ϕ. A median filter was applied to both coefficients. In order to distinguish between the phase-reversed instabilities, figure 4.17(a)-(c) plots $A(z)\cos\left[\phi(z)-\phi_0\right]$ as a function of time, for case-dependent constant ϕ_0. The parameter ϕ_0 was selected such that $\cos\left[\phi(z)-\phi_0\right] = 1$ where $A(z)$ is maximized. In the current coordinate system, the values of ϕ_0 are given by

$$\text{Case 1}: \frac{\phi_0}{\pi/2} = -0.44, \qquad \text{Case 2}: \frac{\phi_0}{\pi/2} = 0.56, \qquad \text{Case 3}: \frac{\phi_0}{\pi/2} = -0.34.$$

Figure 4.17(a)-(c) differentiates between the phase reversed instabilities. The two dominant instabilities are highlighted with white lines on the corresponding panels (a)-(c). The total

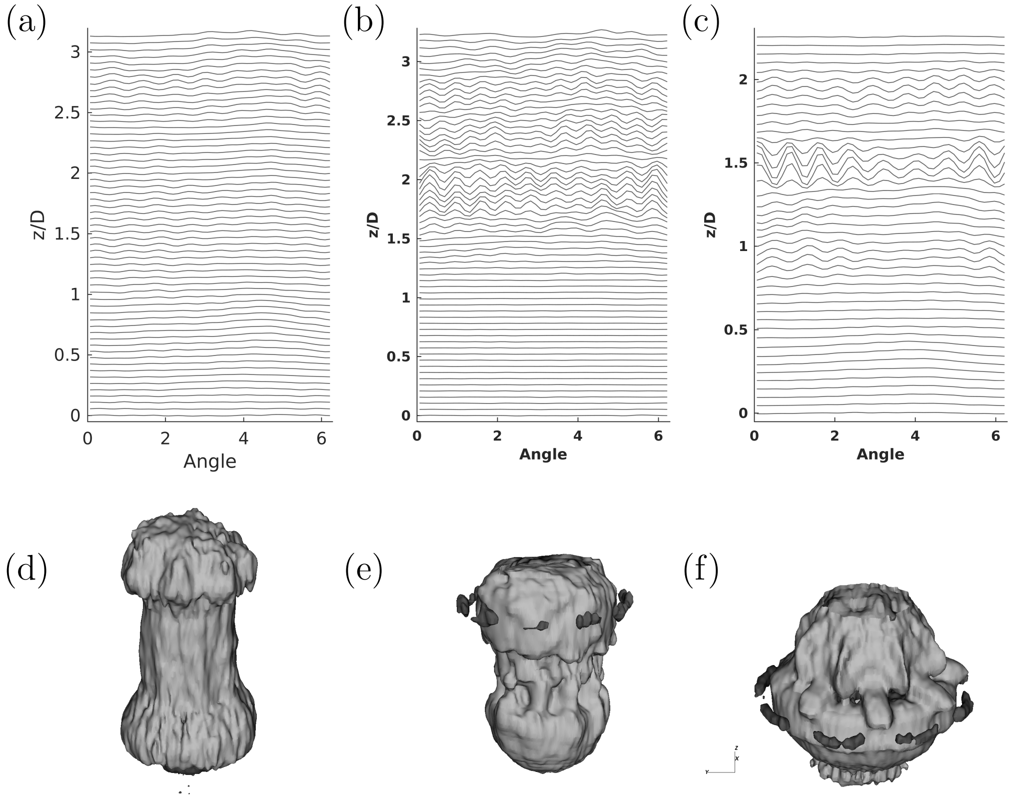

Fig. 4.16 Waterfall plots (a)-(c) of the angular distribution of vertical velocity by level height. Panels (d), (e), (f) plot two isosurfaces of the vertical velocity field, highlighting the three-dimensional structure. Note that the phase reversal is clearly visible in all three panels. From left to right the panels plot the ensembles corresponding to Case 1, Case 2 and Case 3. The time at which each plot is taken is identical to figure 4.15.

energy of the identified instability (i.e. $E = \int A^2\Phi_i(A)dz$, for weighted Heaviside filter function Φ_i) is then plotted in figure 4.17(d)-(f). These plots visualize the growth of the instability as a function of time. Linear stability theory suggests that at early times, the dominant instability should grow as an exponential. For each instability, E was fitted to an exponential, written as

$$L = \alpha \exp\left[\frac{t}{\tau}\right].$$

This method identifies a timescale (τ) associated with the instability growth. The fits are then overlaid onto the appropriate panels, with the solid line plotting the fit for the dominant instability and the dashed line plotting the fit for the phase-reversed instability (corresponding to the respective phases in panels (a)-(c)). All plots are normalized by their maximum value. We note that computing the timescale from the peak values of the mode instability energy, rather than the integrated measure, provides similar results.

As the stratification is modifying the growth of the instability, we suggest that the timescale of the instability growth should be a function of the Richardson number. Figure 4.17(g) plots τ for each case, non-dimensionalized by the advective time scale, and scaled by the Richardson number. Under this scaling, a constant line indicates an inverse Richardson number dependence, specifically

$$\frac{\tau}{t^*} \sim \frac{1}{Ri}.$$

The data agrees well with the plotted horizontal lines at a timescale value of 0.30 and 0.13. The dominant and phase-reversed instabilities have different total growth rates but they both have the same Richardson number dependence. While there are only six data points at three different parameter values, the good agreement between the data and the lines is highly suggestive. Indeed, this suggests that the growthrate of the instabaility scales as $\sigma = \frac{1}{\tau} \sim \frac{g\Delta\rho}{\rho_0}\frac{1}{U}$, indepdendent of an independent length scale, as we might expect. Linden (1973) argues that the timescale associated with the rebound of the vortex-ring interaction should scale as $\mathrm{Ri}^{-\frac{1}{2}}$. Figure 4.5 supports the conclusion that the timescale power-law coefficient is less than one. This work predicts that the vortex-ring instability will grow faster than the time required for the interface to rebound when Ri$> O(1)$, allowing for the development of non-axisymmetric waves on the vortex ring. When Ri$< O(1)$, the interface will rebound prior to the development of the vortex-ring instabilities. The weak instability amplitude of Case 1 (Ri=0.98) supports this conclusion. The damping of the vortex-ring instability, when Ri$< O(1)$, may explain the drop in mixing efficiency at low Ri suggested in Chapter 6.

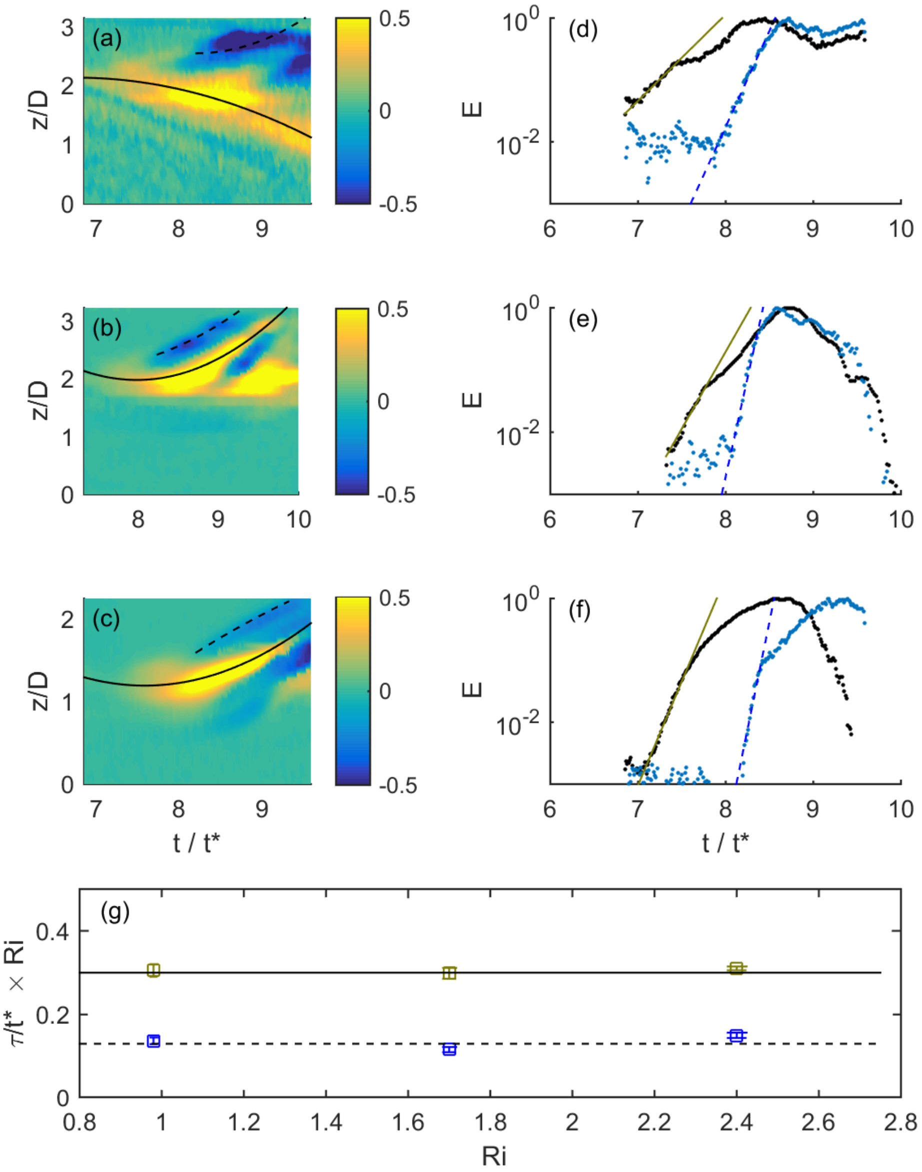

Fig. 4.17 Plots are presented for Case 1 (a),(d) isolating the mode-8 signal, Case 2 (b),(e) isolating the mode-10 signal, and Case 3 (c),(f) isolating the mode-8 signal. Panels (a)-(c) plot $A\cos[\phi - \phi_0]$ for a case specific constant ϕ_0, versus time. Panels (d)-(f) plot the energy associated with the two instabilities (identified by white lines) versus time. The scaled timescale associated with the instability growth are plotted versus the Richardson number in (g). Plots (b),(d), and (f) are normalized to unity.

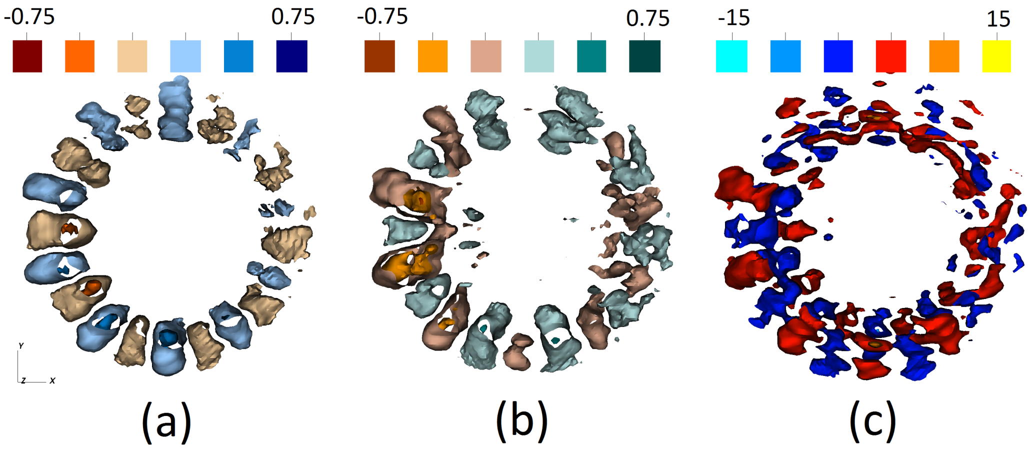

Fig. 4.18 Slices of the perturbations from axisymmetric for (a) vertical velocity (w/U), (b) radial velocity (u_r/U) and (c) azimuthal vorticity ($\omega_\theta D/U$) at $t/t^* = 3.2$ (see figure 4.13). Slices are taken from Case 2 are defined for $z/D \in [1.97, 2.10]$.

4.4.5 Linear stability

As the mode number of the observed instability is the same as the unstratified vortex-ring instability, it is tempting to assert that the instability mechanism is essentially a Widnall instability. However, for the case of a vortex dipole impacting a solid wall, Harris & Williamson (2012) have argued that the observed instability of the boundary-layer-produced vorticity is actually a Crow-like instability. A Crow instability produces a simple displacement mode of the vortex tube. The theoretical basis for this argument was derived from Bristol *et al.* (2004) who studied the stability of a vortex dipole of uneven circulation. The analysis shows that the Crow instability has a higher growth rate than the Widnall instability once the ratio of circulations becomes less than approximately 0.1. The wavenumber of the Crow instability is then comparable to the Widnall instability for a symmetric dipole. In addition, the instability grows more rapidly on the weaker vortex. For these reasons, Harris & Williamson (2012) concluded that the observed instability of the secondary vorticity field was Crow-like. It should be noted that the shape of the secondary vorticity distribution is in Harris & Williamson (2012) is different from the work of Bristol *et al.* (2004).

In the present scenario, the problem is further complicated by the effects of stratification and the curvature of the ring. As such, a more thorough investigation of the observed instability is warranted than will be presented here. However, in order to demonstrate the nature of the underlying instability, we investigate the structure of the non-axisymmetric flow field of the instability. By removing the azimuthally averaged value, figure 4.18 plots slices of the non-axisymmetric perturbations to the vertical velocity (figure 4.18(a)), the radial velocity (figure 4.18(b)), and the azimuthal vorticity (figure 4.18(c)). All data was taken from Case 2 at time $t/t^* = 3.2$ (see figure 4.13). We see that there is no strong azimuthal dependence to the radial structure to either the vertical or radial velocity perturbations. That is, the perturbation field ω_ε can be written as

$$\omega_\varepsilon = f(r,z)\cos(m\theta + \phi),$$

for azimuthal wavenumber m. In a manner similar to section 4.4.4, we can use a Fourier transform for the azimuthal vorticity to get the structural form of $f(r,z)$. Figure 4.19 plots $f(r,z)$ corresponding to the mode of the instability mechanism. We observe that the signal of this vortex-ring instability is much smaller than that of the secondary vorticity field generated by the BVT. The perturbations to the azimuthal component of the secondary vorticity field are characteristic of a simple displacement mode. Both the Crow instability and the instability observed here are characterized by a displacement mode. However, recent work on the interaction of vortex rings Deng *et al.* (2016, 2017) has demonstrated the growth of a different, though visually similar, instability that may relate to the present instability mechanism. Future work will further investigate the effect of the stratification on the instability mechanism, and subsequently, how the stratification modifies the growth rate.

4.5 Summary

This chapter presents fully three-dimensional, time resolved ensembles encapsulating the interaction of a vortex ring with a stratified interface. We present three of these ensembles. This work demonstrates the robust and repeatable nature of the evolution of the velocity field, including the development and growth of a three-dimensional instability. This methodology is consistent with the measured vertical-slice data.

The ensembles indicate that the mode number of the vortex-ring instability in the presence of a stratified interface is consistent with the unstratified vortex-ring instability. At early times where the unstratified case showed no finite amplitude instability, the presence of stratification amplifies and catalyzes the instability. The timescale of the instability growth decreases with increasing Richardson number. We suggest an inverse Richardson number dependence for the instability timescale. The structure of this instability has been characterized, and it corresponds to a displacement mode of the secondary vorticity field in a manner reminiscent of the Crow instability.

The methodology employed in this chapter reconstructs the reproducible component of the flow evolution from an ensemble vortex-ring experiments. This method does not capture

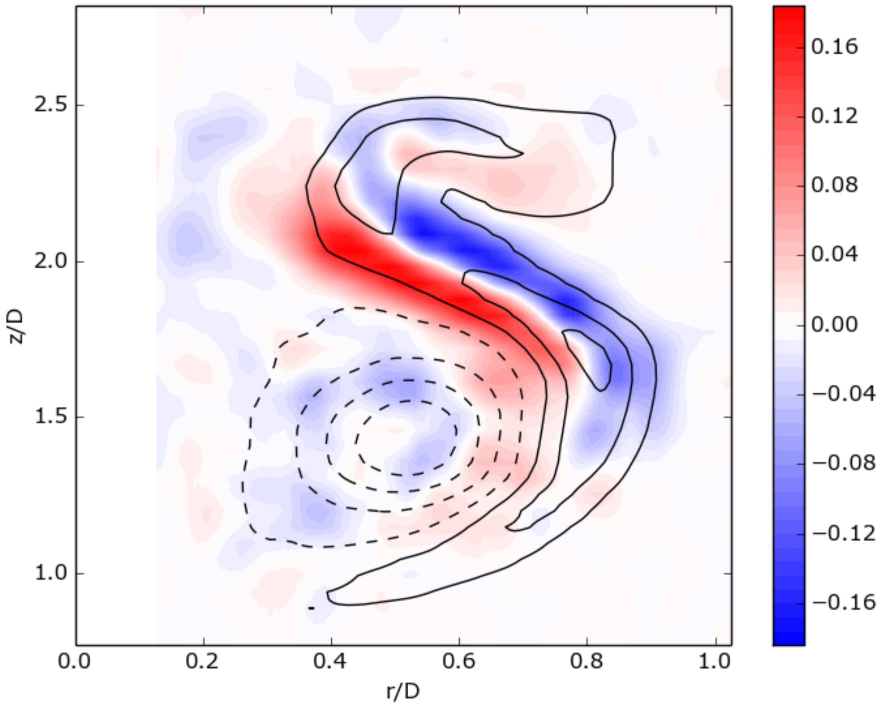

Fig. 4.19 Plot of the normalized perturbation structure $f(r,z)$ of the instability at $t/t^* = 3.2$. Ten evenly-spaced contours of the mean azimuthal vorticity field have been overlayed for comparison highlighting the primary vortex (dashed lines) and the secondary vorticity (solid lines) fields.

the turbulent motions that occur at late stages of the vortex-ring interaction. This work has highlighted that the vortex-ring generation procedure is highly reproducible. It is possible that this methodology could be applied to other unstable systems where the system is both highly reproducible and initially sufficiently laminar. One possible example would be an internal solitary that produces an instability in the bottom boundary layer. We were able to temporally resolve the evolution of the system down to $\Delta t = 0.013$s, with a vertical spatial resolution of ~ 2mm. Recently, a scanning laser device has been constructed by the GK Batchelor Laboratory. This technology has the potential to provide near-instantaneous three-dimensional flow measurements. However, at this point the spatial and temporal resolution of procedure is significantly lower than that found here.

The ability to achieve full three-dimensional time-resolved velocity field measurements for vortex-ring instabilities represents important progress in experimental fluid dynamics. Future work will see the integration of the present work with numerical methods to provide valuable insight into the mixing and dissipation rates of the vortex-ring evolution.

In this chapter, we were not able to measure the evolution of the density field during the vortex-ring interaction. However, it would be useful to understand how the fluid is stirred during the interaction. In the next chapter, we will discuss a numerical scheme used to reconstruct the density field evolution from the ensemble velocity field constructed here.

Note

Special thanks is given to Yonathan Achache for helping the author during the initial trials of this chapter.

Portions of the data associated with this chapter can be found in the repository: https://doi.org/10.17863/CAM.8284.

Plate 4: Picture of a dyed lower layer as the flow goes unstable due to a Crow-like instability. Image courtesy of Ben Jackson.

Chapter 5

Three-dimensional visualization of the interaction between a vortex ring and a stratified interface: the evolution of the density field

> One of the most striking phenomena that occurs in stratified turbulent fluids is the spontaneous formation of mixed layers separated by interfaces.
> —Balmforth *et al.*, JFM, (1998)

One of the characteristic features of stratified-turbulent mixing is the formation of layers (Oglethorpe *et al.*, 2013; Park *et al.*, 1994). In fact, Phillips (1972) has proposed one theoretical argument for the layer formation process based upon the bulk entrainment dynamics of the system. However, the mechanics of layer formation remains elusive. As with stratified turbulence, it was shown in Figure 3.9[1] that vortex rings sharpen density interfaces during their interaction. Understanding how vortex rings establish sharp layers may help highlight the mechanism of layer formation in stratified turbulence.

In the previous chapter, we used a novel experimental technique to visualize the three-dimensional evolution of a vortex-ring-induced mixing event. We demonstrated that there exists a linear instability that grows on the secondary vorticity field. The interaction rapidly becomes turbulent and will mix the density stratification. However, we were not able to measure the density field itself. In this chapter, we numerically compute the density field and its evolution using the previously constructed velocity ensemble. While the velocity

---

[1] This will also be shown in Chapter 6.

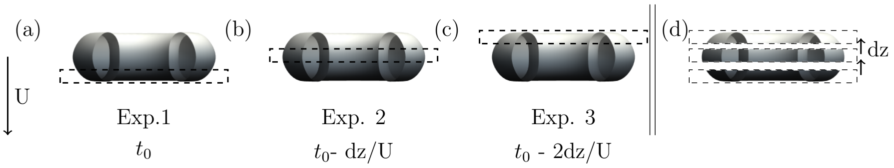

Fig. 5.1 Diagram of the velocity-reconstruction process, highlighting the change in the vertical position of the horizontal light sheet.

field ensemble will not accurately capture the late-time dynamics of the interaction, we have confidence that it does accurately encapsulate the reproducible features of the flow. In this chapter, we are interested in the evolution of the density field that results from the reproducible component of the velocity field associated with the vortex-ring interaction. We will show that there is a distinct asymmetric nature to the buoyancy flux produced by the vortex-ring interaction, which will result in the sharpening of the density interface.

As this chapter builds upon the work of Chapter 4, we briefly review the essential features of those experiments. That is, in a tank ($0.45 \times 0.45 \times 0.60$ m^3), a two-layer stratification was established. Within the tank, a vortex ring was generated at the top of the water column, which propagated vertically downward (parallel with the direction of gravity). Using a horizontal laser sheet, we measured the three-components of velocity of the vortex-ring interaction within a single plane. We vertically shifted the laser sheet relative to the density interface such that, by producing subsequent vortex rings, we computed velocity-field measurements of the vortex-ring interaction on a different horizontal plane. Iterating this procedure, we generated a sequence of velocity slices that, when appropriately time correlated and filtered, produced an ensemble capturing the reproducible components of the vortex-ring interaction. A diagram of this process is provided in figure 5.1.

In order to reconstruct the density field evolution during the vortex-ring interaction, we begin, in section 5.1, by describing a Lagrangian particle advector, used to estimate the position and thickness of the density interface. We use these estimates as initial conditions for the density field solver, as described in section 5.2. Once the evolution of the density field has been simulated, we compute the vertical buoyancy flux, in section 5.3, and discuss these findings.

5.1 Lagrangian particles

As a first attempt to understand how vortex rings mix the stratification, we simulate the advection of Lagrangian particles. Lagrangian particles are massless tracer particles that

Case	Ri	Re	μ (m)	σ (m)
1	0.98	1600	0.081	0.019
2	1.7	2400	0.060	0.0011
3	2.4	1600	0.036	0.0094

Table 5.1 Table of the estimated interface parameters associated with the three ensemble cases.

simply advect with the flow. The position of each particle ($\mathbf{p}_i$, $i = \{1...N_p\}$) is given:

$$\frac{d}{dt}\mathbf{p}_i = \mathbf{u}_\mathbf{p}, \qquad \mathbf{p}_i(t) = \mathbf{p}_i(t = t_0) + \int_{t_0}^{t} \mathbf{u}_\mathbf{p} dt, \tag{5.1}$$

where $\mathbf{u}_\mathbf{p} = \mathbf{u}(\mathbf{x} = \mathbf{p}(t), t)$ is the fluid velocity at the location of the particle. Boldfaced variables denote vector quantities. Unlike the velocity field measurements, the Lagrangian particles are not confined to a spatial grid (lattice). As such, we use a first-order spatial interpolation scheme between elements of the lattice to determine $\mathbf{u}_\mathbf{p}$. We then solve equation (5.1) using a second-order predictor-corrector method. See Appendix B for details on the numerical methods used in this chapter.

As the Lagrangian particles advect, some of them will reach the edge of the ensemble domain. We select the boundary conditions that we feel are most appropriate for the problem at hand. We impose horizontal no-flux boundary conditions such that particles cannot transport beyond the horizontal extent of the ensemble domain. The vertical boundary conditions are more nuanced. Both the top and bottom boundary conditions are “sticky.” That is, particles may not re-enter the fluid domain once they have impacted either vertical boundary. These particles are still counted when computing the histogram of vertical displacement (see below). The initial particle positions were randomly sampled from a uniform distribution. In the work presented here, $N_p = 100{,}000$ particles were advected within the flow.

For each ensemble case presented in Chapter 4, Lagrangian particles were initialized and advected over the entire measurement duration. A histogram of the final vertical displacement of all the particles was computed for each case. These histograms are plotted, in figure 5.2, for Case 1[figure 5.2(a)], Case 2[figure 5.2(b)] and Case 3[figure 5.2(c)]. In each case, there exist two peaks in the particle displacements. The primary peak corresponds to particles that, after the vortex-ring interaction, have not been significantly (vertically) displaced from their initial position. The second peak in the histogram indicates the vertical position where

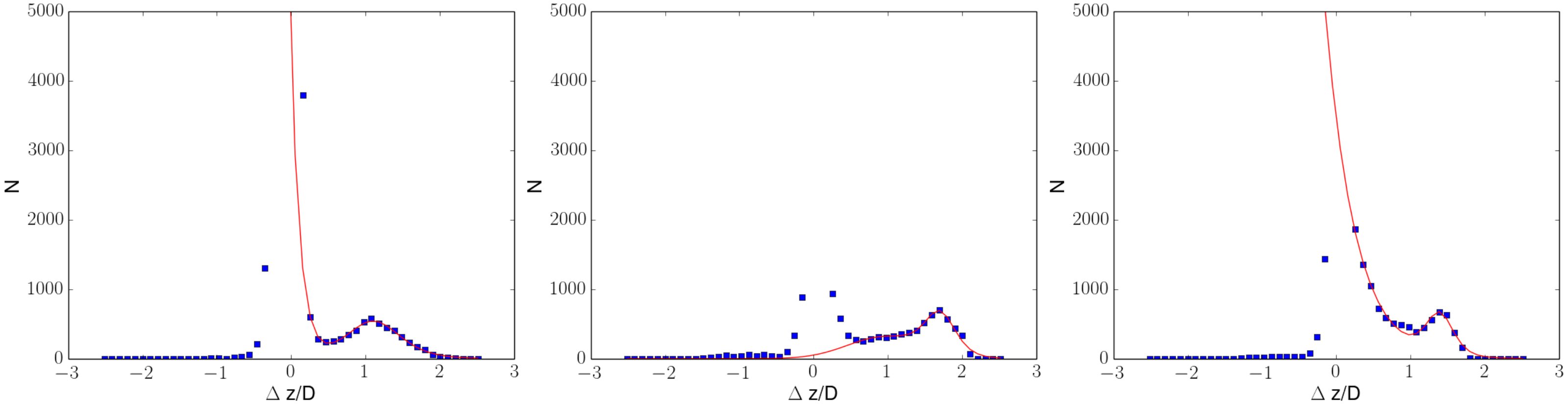

(a) (b) (c)

Fig. 5.2 Histogram of the final vertical displacement of particles from their initial position for Case 1(a), Case 2(b), and Case 3(c). The fit (solid line) captures the position and width of the secondary peak in particle displacement.

preferential vertical entrainment occurred. The histogram data was fit with

$$f_{fit} = A\exp\left[-\left(\frac{z-z_0}{\sigma_0}\right)^2\right] + B\mathrm{sech}^2\left(\frac{z-\mu}{\sigma}\right).$$

The sech^2 parameters, which are associated with the second peak, are provided in table 5.1. We associate the second peak with particles that have been entrained from the interface. We will use the fit parameters μ and σ to initialize the mean position and width of the density interface in section 5.2.[2]

In order to demonstrate the ability of this methodology to predict the position of the density interface, figure 5.3 plots the evolution of the Lagrangian particles. For each panel, a slice of the vorticity field has been plotted on the left. The rz-coordinates of all particles that were initially below the estimated density-interface position (μ), are plotted on the right. The columns of this figure correspond to Case 1(left), Case 2 (middle), and Case 3 (right) as defined in Chapter 4. Plots were given at 1 time unit spacing (non-dimensionalized by the advective timescale). We observe strong similarities between the evolution of the particles observed here, and the two-dimensional LIF results found in Chapter 4. In particular, note the similarity between figures 5.3(j) and 4.2(c), figures 5.3(h) and 4.2(g), and figures 5.3(i) and 4.2(f).

5.2 Density solver

By inputting the velocity field ensemble from Chapter 4 into an advection-diffusion-equation solver, we numerically compute the evolution of the density field. Specifically, given the velocity-field ensemble ($\mathbf{u}_E$), the density field is computed:

$$\partial_t\rho + \mathbf{u}_E\cdot\nabla\rho = \kappa\nabla^2\rho, \qquad \rho(t=0) = \frac{\Delta\rho}{2}\left(1+\tanh\left[\frac{z-\mu}{\sigma}\right]\right). \tag{5.2}$$

We set $\kappa = 1\times10^{-6}$ m^2/s. As the time step of the ensemble is not sufficient to meet the CFL condition[3] for the numerical solver, we use a weighted five-point least-squares method to temporally interpolate the ensemble velocity data onto a series of sub-steps. The stability requirements of the numerical solver require approximately 10 sub-steps between ensemble outputs. Pseudospectral spatial derivatives, computed with Fast Fourier Transforms (FFTs), were used due to their spectral accuracy. The advection-diffusion solver was then

---

[2] These values for the interface thickness are consistent with those of Chapter 6.

[3] Courant-Friedrichs-Lewy condition.

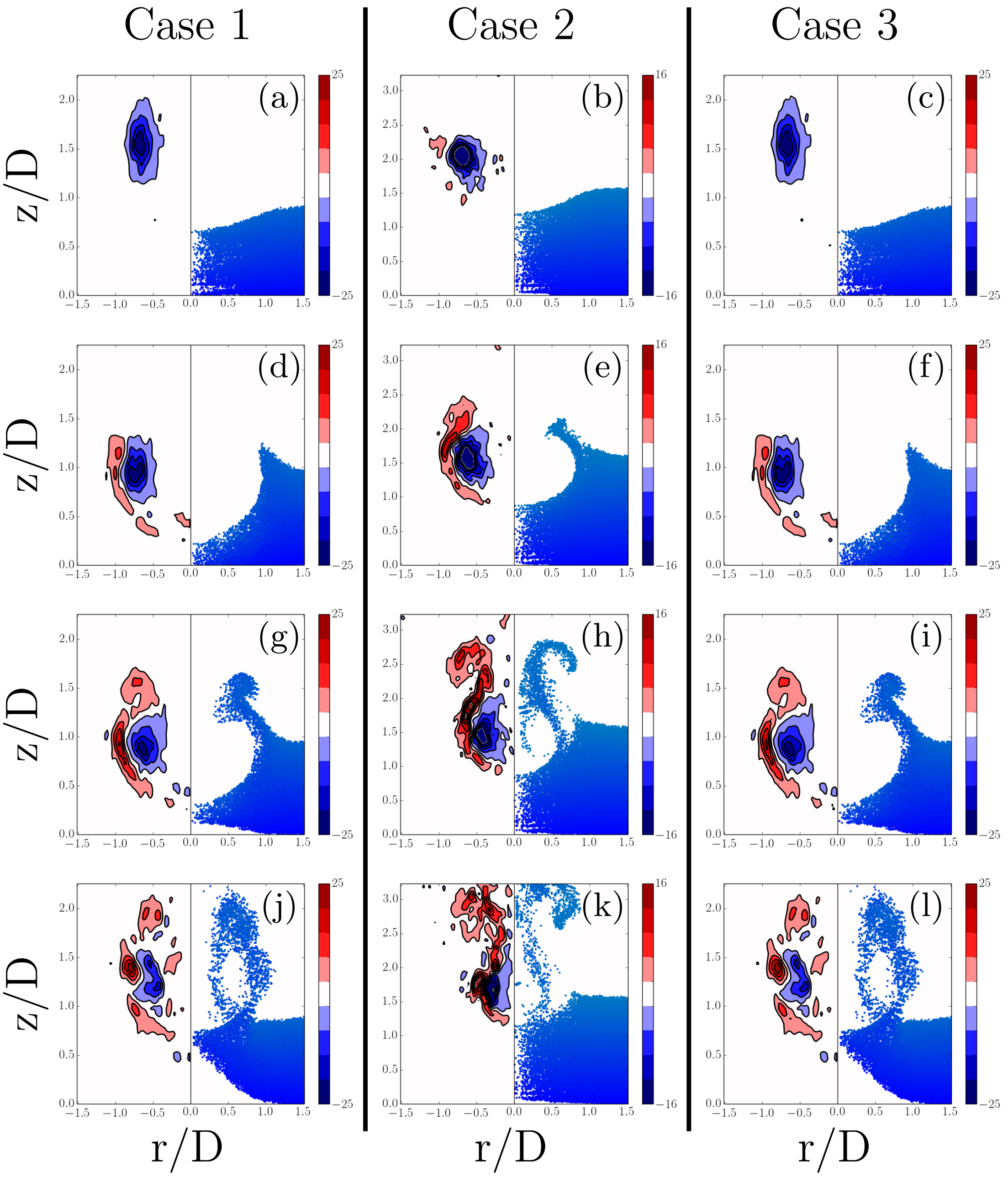

Fig. 5.3 Evolution of the Lagrangian particles below the estimated interface position. For each panel, the vorticity within a radial plane has been plotted on the left, and the *rz*-coordinate of all of the Lagrangian particles initially below the estimated interface position are plotted on the right. Panels have been plotted at 1 time unit spacing.

implemented using a third-order semi-implicit time-stepping method, incorporating the velocity field measurements from the temporally interpolated ensemble. See Appendix B for more details on the numerical implementation of the density solver. In order to efficiently use FFTs to compute the spatial derivatives, the vertical grid of each ensemble was interpolated, using a third-order spline, onto a $n_z = 64$ grid such that each dimension of the ensemble grid ($n_x \times n_y \times n_z = 256 \times 256 \times 64$) is a power of 2. Due to the limited spatial resolution of the velocity ensemble, we do not resolve down to the viscous or diffusive scales. We are not resolving all of the scales of interest. Finally, we note that the precise value of σ does not have a substantial effect on the discussion below.

For the vortex-ring interaction discussed in the next section, the velocity ensemble Case 2 from Chapter 4 was used. Here,

$$\mathrm{Re} = \frac{UD}{\nu} = 2400, \qquad \mathrm{Ri} = \frac{g\Delta\rho}{\rho_0}\frac{D}{U^2} = 1.7.$$

See Chapter 4 for the associated parameter values and appropriate nondimensionalization.

5.3 Results

Figure 5.4 plots the evolution of the vorticity and density field of the vortex-ring interaction at non-dimensional time $t = 2$ (a)-(b), $t = 3$ (c)-(d), $t = 4$ (e)-(f), and $t = 5$ (g)-(h). Note that the time of the first panel has been arbitrarily chosen to be $t = 2$. Both the vorticity and density field have been sliced through the vortex ring's centre in order to visualize the core dynamics. This figure plots the vortex ring as it approaches the density interface (panels (a)-(b)), where the interface depresses in the presence of the vortex ring's associated velocity field. As the density field is deformed, the baroclinic torque produces vorticity of the opposite sign (red) to the impinging vortex ring (blue) (panels (c)-(d)). As time progresses (panels (e)-(f)), this baroclinic vorticity transfer (BVT) 'unwinds' the vortex ring. The subsequent advection of BVT produced vorticity induces the transport of lower layer fluid into the upper layer where the mass diffusion necessary for mixing will occur. As this vortex ring has sufficient energy such that its centre penetrates below the equilibrium interface position, the lateral buoyancy gradient compresses the vortex ring (see panels (g)-(h)) until it has been sufficiently eroded, at which point the interface will rebound, further ejecting fluid into the upper layer.

In order to verify that the present methodology is consistent with the physical vortex-ring interactions, the three-dimensional ensemble generated using a horizontal light sheet was compared with the measurements of a vortex-ring interaction (Re$=$ 2400, Ri$=$ 1.8) obtained using a vertical light sheet (see Chapter 4). In contrast to a horizontal light sheet, a vertical

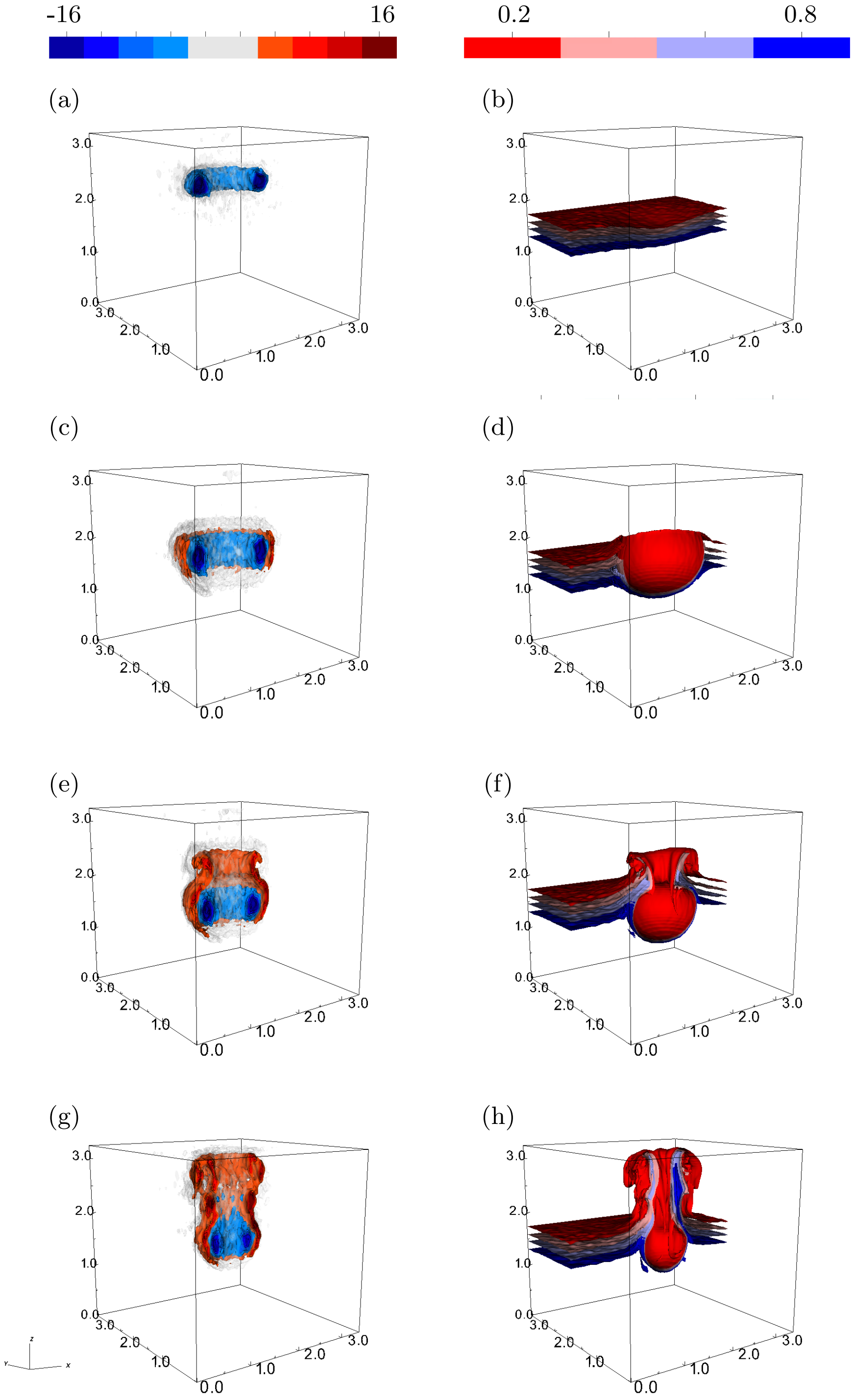

Fig. 5.4 Plot of the evolution of the vortex-ring interaction over time. Panels (a),(c),(e),(g) plot the azimuthal vorticity and panels (b),(d),(f),(h) plot the evolution of the computed density field. Panels have been plot at $t = 2$ (a)-(b), $t = 3$ (c)-(d), $t = 4$ (e)-(f), $t = 5$ (g)-(h). Both vorticity and density are presented in non-dimensional units.

light sheet provides us with density and velocity field measurements from a single experiment at the expense of the three-dimensional information of the interaction. Figure 5.5 compares the results of a vertical light sheet (panels (a)-(c)) with the computed three-dimensional density and velocity field (panels (b)-(d) respectively). We see that there is very good agreement between the directly observed density field (a) and the ensemble determined density field (b). There exists strong quantitative agreement between the vorticity field computed using a vertical light sheet (c), and the reconstructed vorticity field (d) (both plots have the same colour saturation). The agreement between these two approaches provides a validation of the current computational methodology.

Now that we have an accurate estimate of the density field evolution, we can start to answer questions about the advection of mass within the system. We are particularly interested in understanding the interface sharpening observed experimentally (see Figure 3.9). We will start by investigating the vertical transport of mass in the system, which corresponds to an increase in the potential energy within the system. One measure of the local increase in the potential energy of the system is the vertical buoyancy flux. We note that the instantaneous buoyancy flux is not a measure of true mixing of the system (the irreversible change in potential energy) as it includes the reversible change in the potential energy of the system; that is, the available potential energy. However, the vertical buoyancy flux does provide a measure for the 'stirring' of the stratification. Thus, figure 5.6 plots the horizontally-averaged vertical buoyancy flux as a function of time. The vertical buoyancy flux[4] (F)is computed as

$$F =< \rho w >_H,$$

where $< \cdot >_H$ denotes the non-dimensional horizontal average. The key feature-of-note in this plot is the location of the peak in vertical buoyancy flux, at $t \sim 5$. We observe that the dominant buoyancy flux occurs above the equilibrium height of the interface (plotted as a solid line). Indeed, this peak in buoyancy flux is approximately four times larger than the negative buoyancy flux produced during the impingement of the vortex ring. The asymmetry of the buoyancy flux about the interface was noted previously when discussing figure 5.4 but, figure 5.6 provides a quantified metric indicating that the vertical buoyancy flux is predominantly positive and above the density interface. This asymmetry in the vertical buoyancy flux explains why the interface sharpens over subsequent vortex-ring interactions, as the fluid above the interface will be preferentially vertically displaced.

We can further quantify the amount of vertical mass transport in the system by decomposing the vertical buoyancy flux into its positive and negative component. That is, we can

---

[4] The buoyancy flux F has been normalized by the acceleration due to gravity (g).

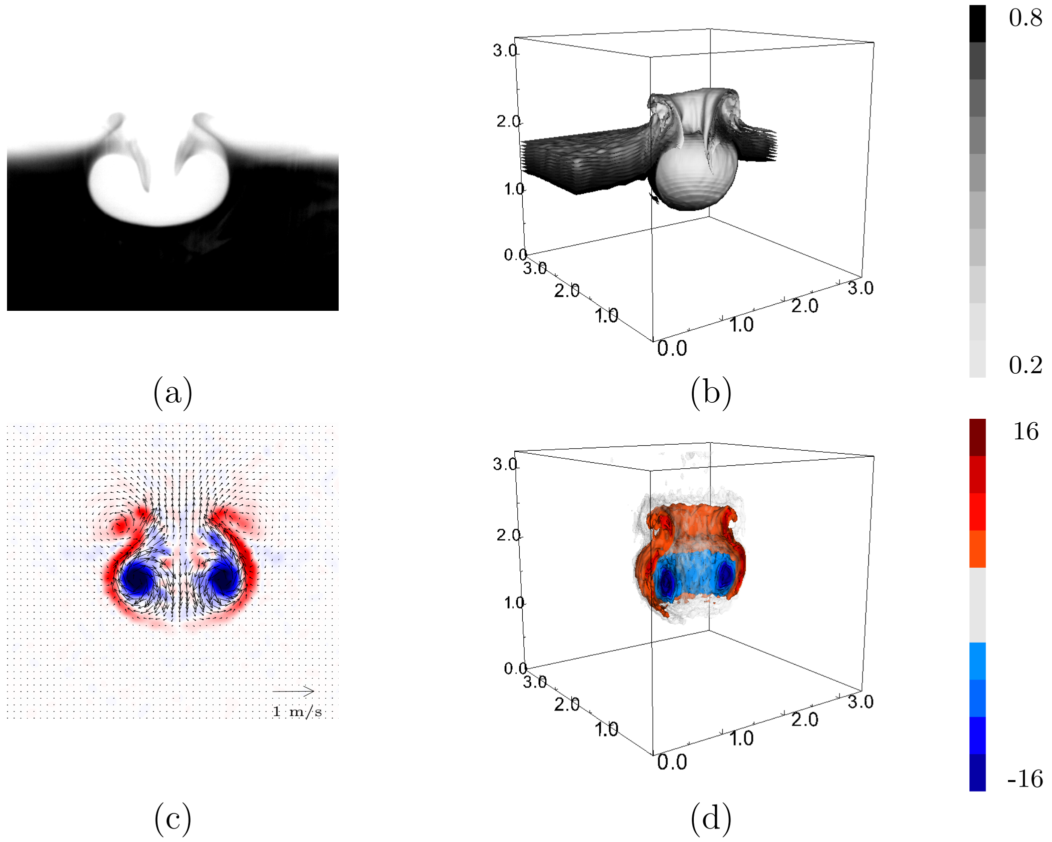

Fig. 5.5 Comparison of the density (panels (a)-(b)) and vorticity (panels (c)-(d)) measurements observed using two different light-sheet orientations. Panels (a),(c) are computed from a vertical light sheet, whereas panels (b),(d) are computed from a horizontal light sheet using the ensemble methodology. Note that the color scheme of (b) has been converted to grayscale for comparison with (a) and that the colour scheme of panel (c) was inverted across the vortex ring's central axis in order to make the comparison with panel (d) .

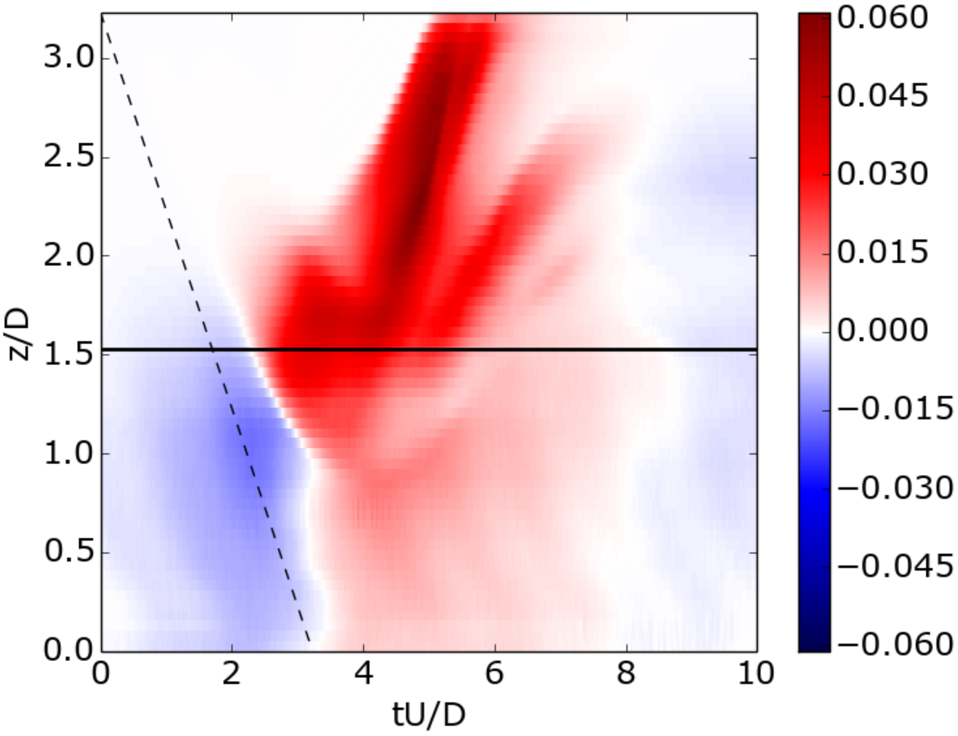

Fig. 5.6 Plot of the horizontally-averaged vertical buoyancy flux as a function of time. A horizontal line has been plotted at the estimated equilibrium height of the density interface. The dashed line plots a representative trajectory for the vortex ring in the absence of the stratification.

define

$$<F>_V=<F_+>_V+<F_->_V,$$

where $<\cdot>_V$ denotes the domain-volume average. The ± subscript denotes data that has been filtered by the sign of its buoyancy flux (positive or negative respectively). Figure 5.7(a) plots the mean vertical buoyancy flux as a function of time. As expected, the positive component of the vertical buoyancy flux is the dominant component of $<F>_V$ after the initial impact of the vortex ring onto the density interface. Note that there is a second peak in the negative buoyancy flux at $t \approx 4.5$, which is not visible in figure 5.6. This plot highlights the asymmetry in the vertical buoyancy flux, denoting a directional dependence to the mixing event. This directionality is an essential feature of the entrainment process. We return to this directionality in Chapter 8.

It is also of interest to quantify a length scale for the vertical transport of buoyancy. We can define a mean length scale based upon the gradient of the vertical buoyancy flux. That is, we define

$$L_F=\frac{<F>_V}{<|\nabla F|>_V}.$$

This provides an integral measure for the length scale associated with the vertical buoyancy flux. We can similarly define a length scale for the positive and negative components of the vertical buoyancy flux by suitably filtering F and its gradient. Figure 5.7(b) plots this integral length as a function of time. We see that the largest length scale is associated with the downward propagating vortex ring. However, as the density interface starts to rebound, we find the there is a lengthscale separation between the positive and negative buoyancy flux ($\frac{L_{F,+}}{L_{F,-}} \approx 2.5$). The length scale associated with the upwelling fluid is larger than the corresponding length scale of the downwelling fluid. This separation of length scales is similar to the results of Leclercq *et al.* (2016), who investigated the correlation between the density field and the vertical velocity, in a manner similar to Ivey *et al.* (1998). This analysis showed that the positive (negative) vertical mass transport in a turbulent Taylor-Couette flow was predominantly concentrated in the low (high) wavenumbers. Leclercq *et al.* (2016) argued then that the coherent motions of the flow were then the main mechanism for increasing the vertical flux in the system, and turbulent motions were responsible for transporting mass downward. This work suggests a similar conclusion, that the coherent BVT induced transport, and the large-scale buoyancy-driven recovery of the interface, are the primary mechanisms for vertical mass transport. The length scale of the negative buoyancy flux will be correlated with the size of the turbulent eddies, though admittedly, we do not resolve all of the scales of interest. As such, this length scale separation, found here, is significant as it suggests that the mechanism for buoyancy production of the vortex ring

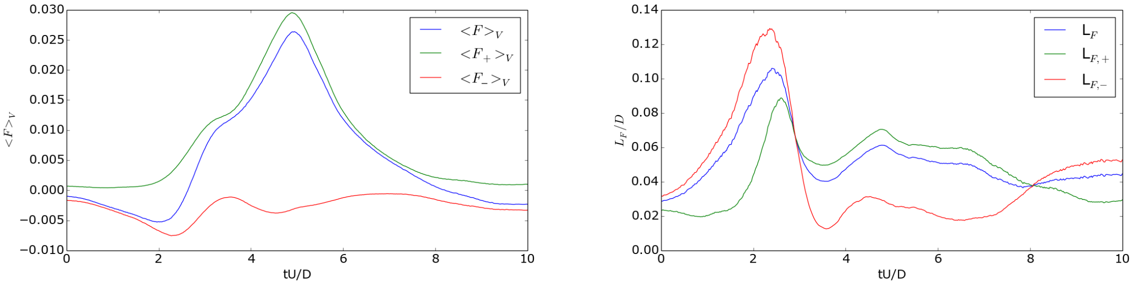

(a) (b)

Fig. 5.7 Plot (a) of the average vertical buoyancy flux (F) in addition to the mean positive and negative component of F. Similarly, (b) plots the integral length scale of F and the integral length scale associated with the positive and negative component of F.

will not be as significantly affected by dissipation as the turbulent production of buoyancy. With regards to a mixing efficiency, this uplift mechanism will be efficient precisely because viscous dissipation will not result in a significant loss of energy. We return to this in Chapter 8.

It is important to note that figure 5.7(a) cannot simply be integrated to get an accurate estimate of the total buoyancy flux of the vortex-ring interaction. That is, the ensemble methodology itself does not capture the non-reproducible (i.e. turbulent) feature of the flow that are typically of smaller scale. Also, the maximum resolution of the numerical grid does not resolve down to the Kolmogorav scale of the flow. As such, we did not attempt to estimate the total integrated buoyancy flux in this Chapter.

5.4 Summary

We numerically reconstruct the density field from experimentally measured velocity field data. In particular, we highlight how the density field evolves during this interaction. The results presented above provide a quantitative explanation of why the interaction of a vortex ring with a density stratification sharpens interfaces. We also demonstrate that there exists a length scale separation between the positive and negative components of the vertical buoyancy flux.

The numerical approach used in this chapter further highlights the repeatability of the ensemble experiments of Chapter 4. This would have been a useful exercise even if we had been able to measure the density field directly.

The buoyancy flux measurements described here do not provide a good estimate of the mixing efficiency (η) as the small scale turbulent motions are not captured by the velocity ensemble. In addition, the ensemble domain does not capture the entire region of interest (density advects out of the domain) for the vortex-ring interaction. In the next chapter, we will discuss a method of measuring the mixing efficiency of a vortex-ring interaction.

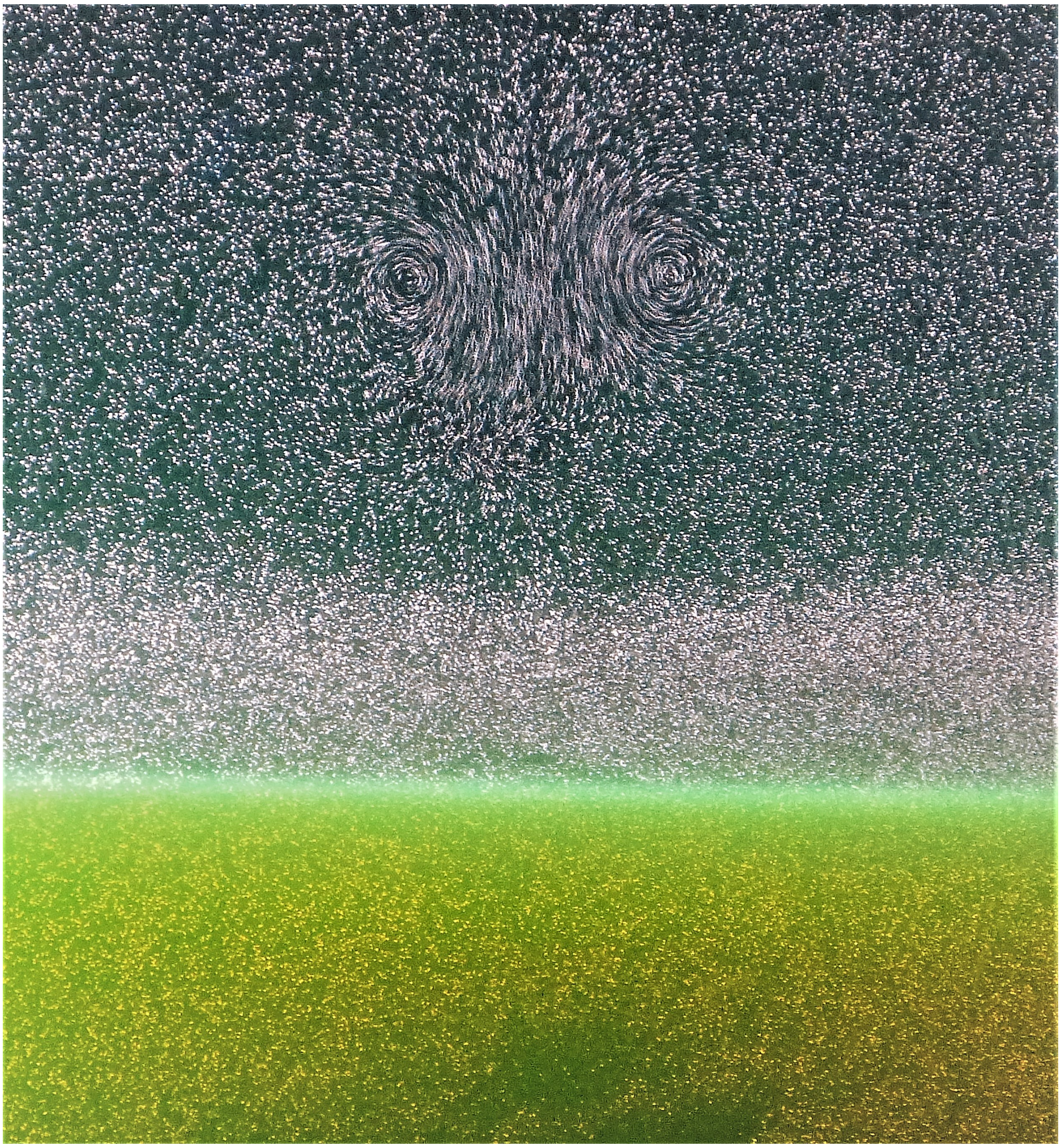

Plate 5: Picture of a vortex ring approaching a stratified interface.

Chapter 6

Vortex-ring-induced stratified mixing

> In this area of research, perhaps no other specific topic has been more controversial than the entrainment law.
>
> —Fernando, Ann. Rev. Fluid Mech., (1991)

In the previous chapters, we have investigated the mechanics associated with a vortex ring impacting a stratified interface. With this in mind, we want to understand the dynamics of the system over a large number of these vortex-ring interactions. In particular, we want to relate these dynamics with Turner's mixing box experiment. Stratified turbulence is characterized by its intermittent nature, its large range of scales, its highly vortical motion, and the role played by buoyancy forces. Often the vortical motions are contained within localized coherent structures, which are observed to play an important role in the mixing of a stratified fluid (Turner, 1986). We investigate the mixing induced by vortex rings as the ideal simplification for studying zero-mean-flow turbulent mixing without the complexity of fully developed turbulence.

This chapter focuses on the potential energy evolution of the system when it is repeatedly forced with independent mixing events, that is, vortex-ring interactions. Figure 6.1 provides a photograph of such an interaction. In this image, the more dense lower layer has been dyed green to highlight the density variation. This image clearly demonstrates the entrainment of the dense lower-layer fluid into the upper layer as a result of the vortex-ring interaction. While similar studies have focused on the mixing induced by a small number of vortex ring events (Dahm *et al.*, 1989; Linden, 1973), here we discuss the mixing observed in the limit of a large number of vortex ring events. Our results demonstrate a difference from the previous theory. As we have stated in Chapter 2, Linden (1973) proposed that for a vortex ring of diameter a and propagation speed U in a salt stratified fluid, the entrainment velocity u_e is

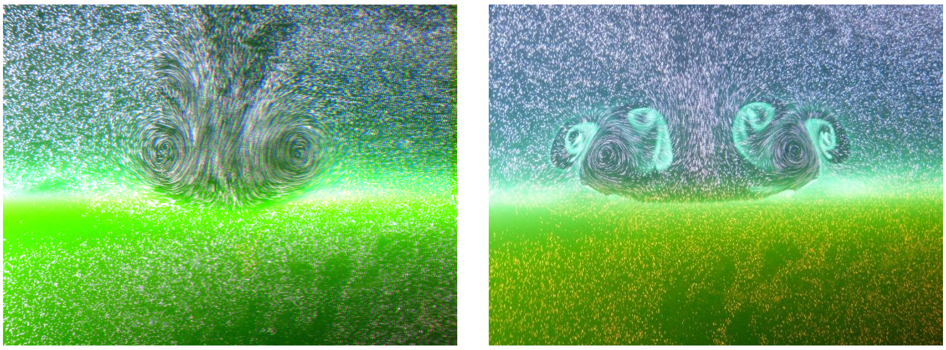

Fig. 6.1 Long exposure photographs of a vortex ring impinging on a sharp interface between an upper tracer particle-laden fresh water layer and a green-dyed salt water lower layer. Photographs display a vortex ring just prior to (left) and during (right) the vortex-ring interaction. Ri$\gg$ 1.

related to the bulk Richardson number (Ri) via the relationship

$$\frac{u_e}{U} \propto \mathrm{Ri}^{-\frac{3}{2}}, \text{ where } \mathrm{Ri} = g\frac{\rho_2 - \rho_1}{\rho_1}\frac{a}{U^2}. \tag{6.1}$$

Here, g is the acceleration due to gravity with densities of the homogeneous upper (ρ_1) and lower (ρ_2) layers. Note that this definition of the Richardson number is different from the one defined in Chapter 4 as a is necessarily quantified in order to measure the kinetic energy of the vortex ring. However, recall that $\frac{a}{D} \approx 1.25$ providing a convenient conversion between the two definitions. Linden's theory was then compared to the results of Turner's mixing box experiment (Turner, 1968), the measurements of which were somewhat ambiguous as to whether the entrainment velocity scales as Ri^{-1} or $\mathrm{Ri}^{-\frac{3}{2}}$. In contrast to the vortex ring idealization of Linden's theory, the experimental work of Moore & Long (1971) for shear induced mixing across a sharp interface suggested a Ri^{-1} scaling for the entrainment velocity of a turbulent shear flow. A more recent investigation by Oglethorpe *et al.* (2013) demonstrated a Ri^{-1} regime also occurs in stratified Taylor-Couette flow. In the following discussion, each vortex ring represents a discrete mixing event and provides a volume of entrained fluid, rather than an entrainment velocity, per se. We return to this issue below.

In this chapter, we demonstrate that in the limit of a large number of vortex-ring interactions, the system evolves to a Ri^{-1} regime, consistent with the fully turbulent mixing of Moore & Long (1971), Oglethorpe *et al.* (2013) and Park *et al.* (1994). In reference to the work of Linden (1979), the mixing efficiency is proportional to the product of the entrainment velocity and the Richardson number. As such, a Ri^{-1} scaling for the entrainment rate corresponds to a constant mixing efficiency. Here, we directly measure the mixing efficiency of independent vortex-ring interactions. Mixing efficiency measurements are complicated due to the large number of variables that must be measured in the system. A number of experimentally (Davies Wykes & Dalziel, 2014; Prastowo *et al.*, 2008, 2009) and numerically (Gayen *et al.*, 2013; Peltier & Caulfield, 2003; Scotti & White, 2011) measured mixing efficiencies have been reported. However, these results are typically measurements for internally mixed problems (Turner, 1979), where the mixing mechanism is generated near the mixing location. External mixing, in contrast to internal mixing, is where the source of the turbulence driving the mixing is not local to the site of the mixing (Turner, 1979). We extend this body of work with the mixing efficiency of external mixing produced by vortex rings. We continue the discussion of external versus internal mixing in Chapter 8

The remainder of this chapter is organized as follows. In §6.1 we introduce the experimental setup. We then develop, in §6.2, a new model of external mixing in a finite box and show that the model agrees with the experimental results of the many vortex ring interactions in §6.3. Finally, in §6.4, we summarize our results and provide avenues for future research.

6.1 Experimental methods

The experiments described here were performed by generating many neutrally buoyant vortex rings in the upper layer of a nominally two-layer salt-stratified fluid with a sharp density interface. The vortex rings were directed vertically downward into the more dense bottom layer. The interaction of the vortex ring with the stratification produced mixing of the density field. We focus on the potential energy evolution of the system in the limit of a large number of independent vortex ring mixing events.

We recall that the details of the experimental setup and generation procedure have been discussed in Chapter 3. Figure 6.2(a) sketches the tank setup where the tube is inserted into the center of the tank, far from the tank walls and normal to the base of the tank. In these experiments, the tube is submerged so that the base is 18 cm below the water surface and $L \approx 30$ cm above the maximum extension of the conductivity probe. It is worth noting that, for the generation mechanism described in section 3.3, the vortex rings are generated from fluid internal to the system, preserving the fluid volume. By digitally controlling the linear actuator, we are able to precisely control the propagation speed and timing of the generated vortex rings. Here, the actuation length ($\sim$15cm, corresponding to a fluid displacement of 8.3cm, provided the air is not compressed) and speed were varied, which produced variations in the vortex ring structure to ensure consistency over a range of parameter values. Two different tank sizes ($0.2 \times 0.4 \times 0.5$ m^3 and $0.45 \times 0.45 \times 0.6$ m^3) were used to ensure consistency of the results.

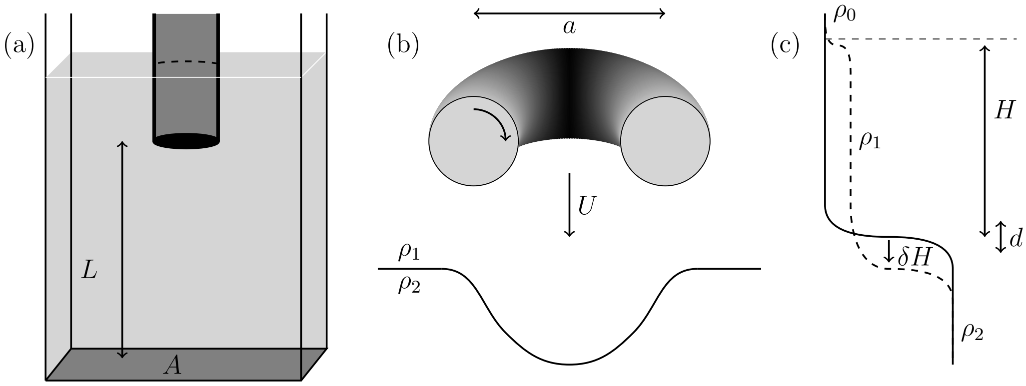

Fig. 6.2 Sketch of the (a) tank setup, the (b) physical parameters associated with the vortex ring and the (c) relevant parameters associated with the stratification.

Case	Diameter [a] (mm)	Propagation Speed [U] (mm/s)	Tank Area (m^2)	C_{KE}	Data Identifier
1	45.2 ± 1.6	37.1 ± 1.0	0.4×0.2	7.5	Black ❏
2	48.3 ± 1.5	39.0 ± 1.5	0.4×0.2	6.5	Red ▲
3	50.6 ± 0.5	54.2 ± 1.8	0.4×0.2	6.5	Blue ▼
4	49.9 ± 0.6	49.8 ± 3.3	0.45×0.45	6.5	Green ○

Table 6.1 Table of the relevant characteristic parameters of the four different vortex ring cases. Errors are reported as the average inter-generation difference in average diameter and propagation speed.

6.1.1 Velocity measurements

Using particle image velocimetry (PIV, see section 3.4), we reconstruct the vorticity field within a thin vertical light sheet generated by masking the illumination from a pair of xenon arc lamps (300W) with integrated paraboloidal dichroic reflectors producing ~35W of visible light. The light sheet was aligned with the centre of the vortex generation tube. Using this method, we are able to reconstruct the planar flow field generated by individual vortex rings. DigiFlow (Dalziel Research Partners, Cambridge, UK) was used to perform the analysis of the particles. A similar approach was taken by Bethke & Dalziel (2012). The video sequence was recorded with a Teledyne DALSA Falcon 2 (Teledyne DALSA Inc., Waterloo, Canada) camera (4M Pixel), here with a frame rate of 150 fps. It is worth noting that at the point that these experiments were performed, the laser system described in Chapter 4 was unavailable.

Both the vortex ring diameter a and propagation speed U were determined via the computed vorticity field. The diameter was defined as the distance between the centroids of positive and negative vorticity. Similarly, the propagation speed was computed by tracking the vertical position of maximum vorticity in time. The average values were taken over multiple such computations. Errors are reported as the average difference between the individual case values and the average value. Figure 6.2(b) plots a diagram of the vortex ring parameters.

Table 7.1 presents the relevant parameters for the four different vortex ring cases presented here. In the present work, the Reynolds number (Re=$\frac{Ua}{\nu}$, for molecular viscosity ν) was only varied by 50% (Re = 1700 - 2700). However, the change in vortex ring propagation velocity allows us to vary the Richardson number independently to the stratification. We necessarily restrict our current discussion to vortex rings at moderate Reynolds numbers.

6.1.2 Density profiles

In order to determine the density change through successive vortex ring generations, an aspirating conductivity probe (0.3 mm internal tip diameter) was used to measure density profiles through the tank. The conductivity of salt water is dependent on its salinity and temperature. By attaching a fast response thermistor (P25 NTC type, General Electric) to the conductivity probe, we measured both the conductivity and temperature of the water and, assuming no other solute in the fluid volume, we can back out the fluid density. See Appendix A for a complete description of the conductivity probe calibration. This methodology is similar to that preformed in Davies Wykes & Dalziel (2014). The relative error in the point density measurements in this method has been shown to be O(0.1%) of the density range with which it has been calibrated. Other sources of signal noise in this system were compensated for by oversampling then filtering the data with both a median and spectral filter. Unlike the work of Davies Wykes & Dalziel (2014), we have attached a computer controlled pinch valve to prevent fluid loss due to the aspiration while not measuring. In our experiments, the volume loss from aspiration can be shown to be O(0.1%) of the total volume in the tank.

The period between vortex ring generations was set to be $\tau \approx 75$ s. Doubling this period yielded no quantitative difference, demonstrating that this period was sufficient for the motion to decay and for successive collisions to be independent. For most experiments, a single density profile measurement was taken every 10 vortex rings. The choice of sampling interval had no measurable influence on the evolution of the density field. Experiments were run for 600 vortex rings (resulting in 61 density profile measurements).

6.2 Theory

As we are interested in a sequence of temporally discrete mixing events, it is convenient to consider time as a discrete quantity. If we consider a sequence of n vortex rings produced with a fixed inter-ring period τ, we can define a discrete time $t_n = n\tau$. The vortex ring events will be independent, (except through the resulting mixing of the density field) provided the time τ between successive vortex rings is such that the macroscopic motion within the fluid domain of interest has dissipated. We denote the time scale of this kinetic energy dissipation as τ_{dissip}. Thus, in order to ensure independence, we select $\tau > \tau_{dissip}$.

On the other extreme, as we are interested in the change in potential energy due to each vortex ring, and not due to background diffusion, we restrict ourselves to the case where

$$\tau_{dissip} < \tau \ll \tau_{diffusion}.$$

Here, $\tau_{diffusion} = \frac{1}{\kappa}\left(\frac{a^3}{A}\right)^2$ is the time scale of diffusion of the background density profile for molecular diffusivity κ ($\sim 1 \times 10^{-9}$ m^2/s) over the vortex ring equivalent-volume layer thickness $\frac{a^3}{A}$ for tank plan area A. With reference to table 7.1, we see that for case 4, the larger tank area decreases the diffusion timescale by a factor of four and the assumption of negligible background density diffusion begins to break down ($\tau \approx \tau_{diffusion}$). This case has been included to ensure that the results presented here are robust.

Under these assumptions, the change in potential energy over each vortex ring interaction (δPE) is produced by mixing the background density profile. The value of δPE was computed as the change in potential energy between conductivity probe measurements, divided by the inter-measurement number of vortex rings, corrected for the mass loss associated with the aspirating conductivity probe. The mixing efficiency is then defined as

$$\eta = \frac{\delta \mathrm{PE}}{\delta \mathrm{KE}}, \tag{6.2}$$

for the initial kinetic energy of an individual vortex ring (δKE). In this chapter, we will show that, under the conditions defined above and after an initial adjustment phase, η is independent of Ri and we recover the Ri^{-1} scaling for the entrainment as discussed above. This definition of the mixing efficiency is identical to the one given in Chapter 2.

6.2.1 Two-layer box model

Consider a stably stratified finite-volume fluid in a box of height L containing two homogeneous layers of densities ρ_1 and ρ_2, divided by a sharp density interface. The height of

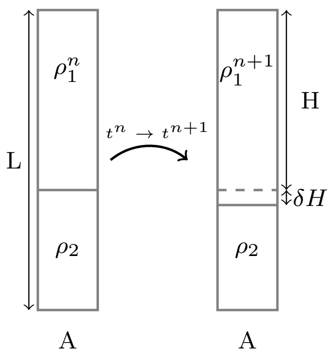

Fig. 6.3 Diagram of the change in density profiles between times t_n and t_{n+1} for the two-layer model.

the upper layer is H, with the lower layer of height $L-H$. Now, assume that the height of the density interface is lowered by a distance δH over a finite time $\tau = t_{n+1} - t_n$. For the present discussion, we assume that both layers remain homogeneous over τ, with the lower layer remaining at a constant density. Uniformly mixed layers are typical of external mixing processes, see Oglethorpe *et al.* (2013); Turner (1968). We will evaluate the effect of a non-homogeneously mixed upper layer later in this discussion. See figure 6.3 for a diagram of this two-layer box model.

The change in potential energy of this layered model ($\delta\mathrm{PE}_L$) is

$$\delta\mathrm{PE}_L = A\left(\int_0^L g\rho_L^{n+1} z dz - \int_0^L g\rho_L^n z dz\right).$$

Assuming a homogeneously mixed upper layer, the density is given

$$\rho_L^n = \begin{cases} \rho_1^n - \bar{\rho} & z > L-H \\ \rho_2 - \bar{\rho} & z < L-H \end{cases}, \qquad \rho_L^{n+1} = \begin{cases} \rho_1^{n+1} - \bar{\rho} & z > L-H-\delta H \\ \rho_2 - \bar{\rho} & z < L-H-\delta H \end{cases}.$$

Here, and elsewhere in this chapter, we remove the average density ($\bar{\rho}$) from our computation of the change in potential energy. Mass conservation requires that the density of the upper layer will increase as

$$\bar{\rho} = \frac{1}{L}\int_0^L \rho_L^{n+1} dz = \frac{1}{L}\int_0^L \rho_L^n dz, \qquad \rho_1^{n+1} = \frac{\rho_1^n H + \rho_2 \delta H}{H + \delta H}.$$

Integrating through and retaining the leading order term, assuming $\frac{\delta H}{H} \ll 1$, we find that

$$\frac{\delta \mathrm{PE}_L}{AH} = \left[\frac{\delta H}{a}\right]\left[\frac{1}{2}\rho_1 U^2\right]\mathrm{Ri}, \tag{6.3}$$

where Ri is given by (6.1).

As our experimental velocity measurements are on a single plane, they do not provide an independently rigorous estimate of the total kinetic energy of a single vortex ring (δKE) although they do provide a good measure of the propagation velocity and ring diameters. With reference to the theoretical results of Norbury (1973), δKE is computed as

$$\delta \mathrm{KE} = C_{KE}\left[\frac{1}{2}\rho_0 U^2\right]\left[\frac{4}{3}\pi\left(\frac{a}{2}\right)^3\right]. \tag{6.4}$$

The scaling coefficient C_{KE} is estimated through the theoretical prediction (for the relative core diameter of our rings) and was verified by computing the kinetic energy of the vortex ring from our 2D measurements assuming axisymmetry. Appendix C discusses this estimation in more details. We have determined $C_{KE} \approx 6.5 - 7.5$ depending on the vortex ring case, see table 7.1.

In our model, we are implicitly assuming that the effect of the diffusion of the background density profile is small. Indeed, under the assumptions of this model, there are only two relevant dimensionless parameters, η and $\gamma = \frac{\delta H}{H}$. In a given experiment, if $H \gg \delta H$ (i.e. $\gamma \ll 1$), the mixing efficiency is constant and, where H can be considered constant, δH (and hence the entrainment velocity, $u_e \approx \frac{\delta H}{\tau}$) scales as Ri^{-1}. Indeed, we will show below that after an initialization phase, these conditions hold in our experiment, and the mixing efficiency is indeed constant.

6.2.2 Density profile perturbation

As will be discussed in section §6.3, the experimental density profiles deviate from the two-layer idealization utilized in the previous subsection. In particular, the experiments exhibit a weakly-stable stratification in the upper layer and a finite interface thickness. In order to demonstrate the robustness of the results, we consider a simplified density profile that includes the contributions of an upper-layer gradient and a finite interface thickness, and compute the effect of these modifications on the potential energy change to the system. Figure 6.4 sketches, in an exaggerated manner, this decomposition of the simplified density profile (ρ_{total}) into a two-layer profile (ρ_L) as described previously, an upper-layer gradient perturbation (ρ_g), and a finite interface thickness perturbation (ρ_d). These profiles can be

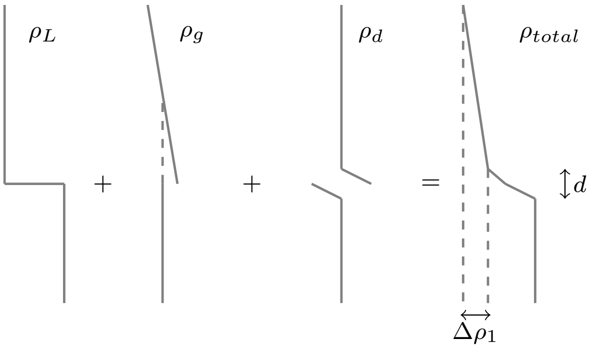

Fig. 6.4 Diagram of the decomposition of the simplified density profile (ρ_{total}).

modeled as perturbations to the two-layer profile, written here as

$$\rho_{total} = \rho_L + \rho_g + \rho_d,$$

$$\rho_g = \begin{cases} \frac{\Delta\rho_1^n}{H}\left(L - \frac{H}{2} - z\right) & z \geq L - H, \\ 0 & z < L - H, \end{cases}$$

$$\rho_d = \begin{cases} 0 & z \geq L - H + d, \\ -\frac{\Delta\rho}{2d}\left(z - (L - H + d)\right) & L - H \leq z < L - H + d, \\ -\frac{\Delta\rho}{2d}\left(z - (L - H - d)\right) & L - H - d < z < L - H, \\ 0 & z \leq L - H - d. \end{cases}$$

In this decomposition, we define the perturbations ρ_g and ρ_d to have net-zero mass. That is, both of these perturbations represent redistributions of the mass. We also assume that the density purtubations for not affect the kinetic energy of the vortex ring, δKE. These will change δPE as

$$\delta \mathrm{PE}_{total} = \delta \mathrm{PE}_L + \delta \mathrm{PE}_g + \delta \mathrm{PE}_d.$$

The same subscript convention as the density profiles is used here.

It is straight forward to show that for a linear upper-layer stratification $\partial_z \rho_1 = -\frac{\Delta\rho_1}{H}$, and a linear interface of thickness d, the relative contributions of δPE are given by:

$$\frac{\delta \mathrm{PE}_g}{\delta \mathrm{PE}_L} = -\frac{1}{6}\left[\frac{\Delta\rho_1}{\rho_2 - \rho_1}\right], \tag{6.5a}$$

$$\frac{\delta \mathrm{PE}_d}{\delta \mathrm{PE}_L} = \frac{1}{12}\left[\left(\frac{d_{n+1}^2 - d_n^2}{H\delta H}\right) - \left(\frac{d_{n+1}^2}{H^2}\right)\right]. \tag{6.5b}$$

Note that, for fixed interface thickness, both of these perturbations will reduce $\delta\mathrm{PE}_{total}$ (i.e. $\delta\mathrm{PE}_{total} < \delta\mathrm{PE}_{L}$).

6.3 Results

We now make a quantitative comparison between the two-layer model (6.3) and the experimental data. Figure 6.5(a) plots the density profiles of a single representative experiment after 10, 200, 400, and 600 vortex rings. These profiles demonstrate that there exists a mixing layer that develops above the density interface with some varying height H. We denote this region as the middle mixed layer.

We observe that the upward entrainment of each vortex ring is such that the interface moves downwards and the lower layer density remains constant. We can envisage a process in which the fluid volume contained within the vortex ring, mixed with the entrained fluid, forms a new band at the bottom of the middle mixed layer as the kinetic energy of the ring is dissipated. This process will continue with each subsequent vortex ring, transporting a volume of fluid from the base of the vortex generation tube to the bottom of the middle mixed layer. This is analogous to the classical “filling box" problem for a buoyant plume (Baines & Turner, 1969). Initially, the volume transport of the vortex rings will generate a middle mixed layer that will increase in height with each subsequent vortex ring interaction. We define the initial adjustment phase as the period before the top of the middle mixed layer reaches the base of the vortex tube. At the end of the initial adjustment phase, the initial vortex ring density will be determined by the density at the top of the middle mixed layer and almost no further fresh water is injected into the system (ignoring the fluid displacement from the conductivity probe aspiration). This effectively isolates the fluid above the vortex generation point from the system. After the initial adjustment phase, just as in the two-layer model, the domain of interest L (the sum of the lower layer height and the middle mixed layer height) is constant. Subsequent vortex ring generations continue the banding process, which results in the approximately linear stratification observed in the upper layer. The impact of this upper layer stratification will be discussed below.

The evolution of the potential energy over all vortex ring generations has been plotted (figure 6.5(b)) for six representative experiments at different initial Ri ranging from 4 to 12. The initial adjustment phase has been indicated by grey circles. After this adjustment period, all experiments demonstrate the same change in potential energy per vortex ring mixing event, within experimental error, over the range of Ri considered. That is, $\delta\mathrm{PE}$ is constant, in agreement with the dimensional analysis of the theoretical model. By varying the inter-vortex ring spacing (τ), we estimate that an upper bound of 10% of the potential energy increase

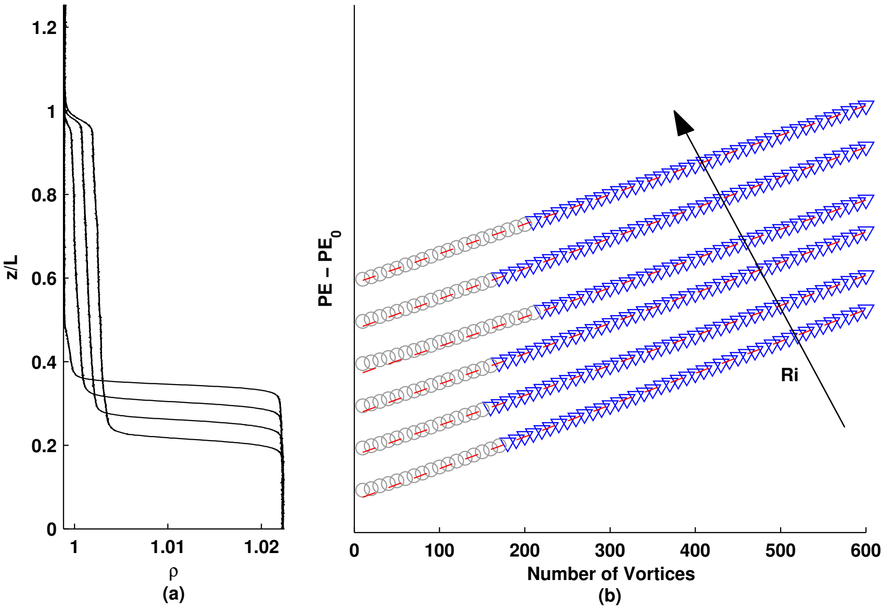

Fig. 6.5 Plot of the density profiles (a) every 200 vortex rings and (b) the potential energy of each measured density profile. Six experiments are shown, with Ri ranging between 4 (bottom curve) and 12 (top curve), increasing vertically. Note that a constant shift has been applied to the data in order to view the data sets individually. After an initial adjustment phase (grey circles), the change in potential energy becomes constant over the range of Richardson numbers.

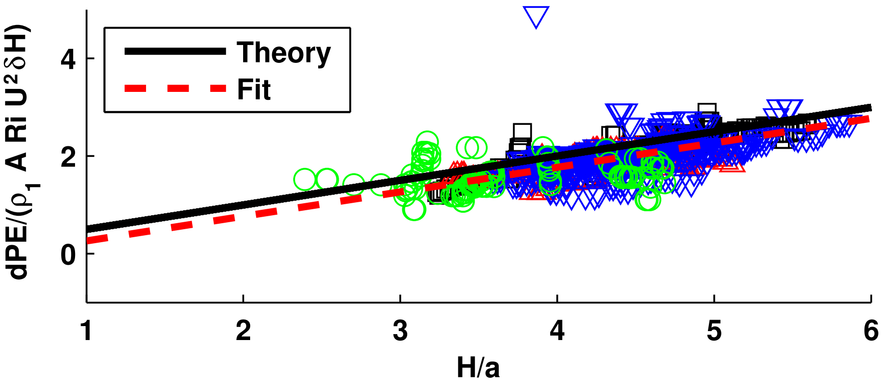

Fig. 6.6 Plot of the scaled δPE vs. normalized H. The theoretical curve is plotted in solid black and the fit to the data is displayed as a dashed line. Note that the fit scales very well with the theoretical fit (0.502 vs $\frac{1}{2}$).

is due to laminar diffusion of the background density stratification. However, δPE is not constant during the initial adjustment phase. This is due to a number of factors including the variations in the initial density profile, and the rapidly growing middle mixed layer.

Figure 6.6 plots, for all experiments, the scaled δPE versus the normalized middle mixed layer height H after the initial adjustment phase. As H is determined as the height of the maximum density gradient of the density profile, small fluctuations in the profile may result in significant errors in the measurement of the middle mixed layer height. As there are a large number O(1000) of density profiles measured, there exists a significant amount of noise in the plotted data. A five-point median filter was applied to each data set in order to smooth the data, and outliers were removed. The box-model (6.3) predicts a slope of $\frac{1}{2}$ and the least-squares linear fit through the data has a slope of 0.502±0.038. As will be discussed below, contrary to our two-layer model, the upper layer gradient and finite interface thickness are expected to cause the measured δPE to fall slightly below the model line, as observed. As noted in §6.1, identifiers of the data presented here, and in subsequent figures, correspond to the cases presented in table 7.1. Note that as the assumption of time scale separation between $\tau = 75s$ and $\tau_{diffusion} \approx 100s$ is no longer strictly justified for the larger tank (circles), we do not include these points in the discussion of the density profile perturbations presented below.

6.3.1 Density profile perturbations

In the present work, the interface thickness d is computed from the maximum density gradient $\partial_z \rho_{max}$ as $d = \frac{\rho_2 - \rho_1}{|\partial_z \rho_{max}|}$. This provides us with a relatively robust method of determining d. Figure 6.7(a) plots $\frac{d^2}{H^2}$ versus Ri, for comparison with the final term in (6.5b). As was suggested in Chapter 5, we observe that, regardless of the initial interface thickness, the vortex rings sharpen the interface and d rapidly collapses to some function of the Richardson number. For large Richardson numbers, the interface thickness is constant ($\frac{d^2}{H^2} \approx 2 \times 10^{-3}$, hence the last term in (6.5b) is dominant), consistent with the results of Shravat *et al.* (2012) for an entirely different external mixing mechanism. We expect the value of the constant interface thickness to depend on the other non-dimensional parameters of the problem. As the kinetic energy becomes dominant (low Richardson number), the vortex rings penetrate deeper into the lower layer and the vortex rings are no longer able to maintain an interface that is sharp.

Figure 6.7(b) plots $\frac{\delta \mathrm{PE}_g}{\delta \mathrm{PE}_L}$ versus Ri to demonstrate the role played by the middle mixed layer. The middle mixed layer density difference $\Delta\rho_1$ was computed using the average gradient within the middle mixed layer. As before, the data rapidly converges onto a single function of Ri. This figure demonstrates that for large Ri, the relative change in the potential energy, as a result of the middle mixed layer gradient, is small and increases in magnitude with decreasing Ri.

These results support the notion, through equations (6.5a)-(6.5b), that the variation in mixing rate as a result of the upper layer gradient and finite interface thickness are small compared with the mixing rate observed for the two-layer evolution at large Ri. As Ri$\rightarrow$ 0, the assumptions made in the two-layer model begin to break down and the impact of the density perturbations will increase. Thus, we argue that the mixing efficiency decreases as Ri$\rightarrow$ 0.

Referring back to Chapter 4, we noted a similar regime change for Ri=O(1). In particular, we found that as the timescale of the density interface rebound decreased, the three dimensional instability associated with the vortex ring interaction was effectively shut off. This is one possible explanation for the transition from the constant interface thickness regime and when the interface thickness is able to grow. This present work again supports the notion of a critical Richardson number (Ri$_c$) about which there will be a regime change.

6.3.2 Mixing rate

It is clear that the dynamics of the initial adjustment phase are different from the constant mixing-rate regime. As such, we introduce a transition Richardson number Ri$_T$, defined as the bulk Richardson number determined at the end of the initial adjustment phase. Figure 6.8(a) plots δH normalized by the vortex ring volume (V_R)-equivalent layer height after the initial adjustment phase versus Ri$_T$. This is plotted for all four cases obtained in table 7.1, three in one tank and the additional case of a tank with a larger plan area (circles). A

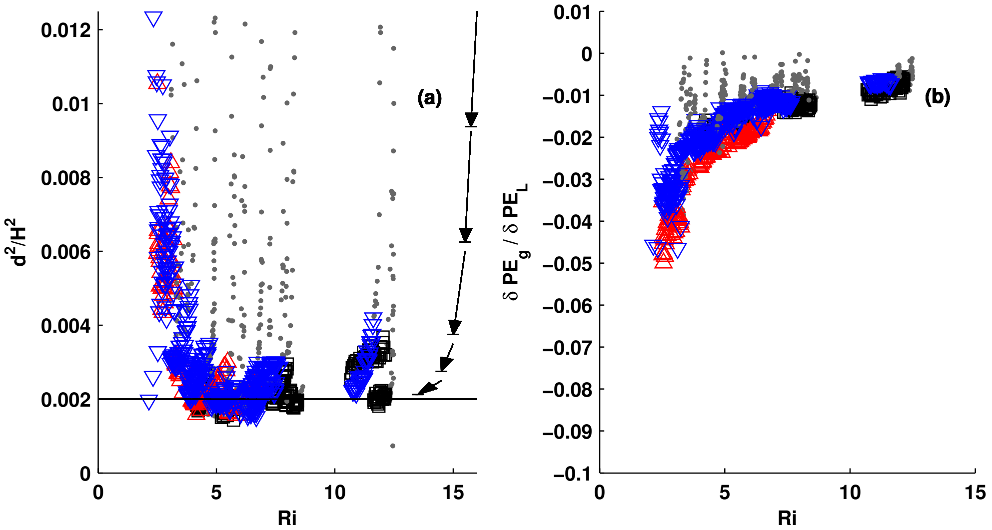

Fig. 6.7 Plot (a) of $\frac{d^2}{H^2}$ versus Ri. Note that for large Richardson numbers, this quotient tends to a constant. A constant line was plotted for comparison with a value of 2×10^{-3}. Diagramatic arrows have been plotted depicting the time evolution of the interface thickness. Plot (b) of $\frac{\delta \mathrm{PE}_g}{\delta \mathrm{PE}_L}$ versus Ri. Data points within the initial adjustment phase have been shaded grey.

Ri^{-1} fit (solid line) is provided for comparison. A least squares fit of the data produces the relationship

$$\frac{\delta HA}{V_R} = 0.695\mathrm{Ri}^{-0.95\pm0.13}.$$

Here, $V_R = \frac{4}{3}\pi\left(\frac{a}{2}\right)^3$ is the approximate vortex ring volume, only affecting the constant of proportionality. This power-law scaling is indistinguishable from the predicted Ri^{-1}, once the error bars of the measurements are taken into account. From (6.3), we expect the change in interface position (δH) to differ slightly from the Ri^{-1} relationship during the initial adjustment phase as H is also varying in time.

Using the Norbury scaling (6.4), figure 6.8(b) plots the mixing efficiency η normalized by a constant reference η_0 as a function of Ri_T. We see clearly that the mixing efficiency is constant over a range of vortex ring parameters and Ri. Since δKE is constant during an experiment, our use of the Norbury theory to estimate δKE does not affect our conclusion that η is constant. The method of estimating δKE does, however, affect the value of the mean mixing efficiency η_0. In particular, using this approach we estimate $\eta_0 = 0.42$, though the precision of this result is not clear. This value of the mixing efficiency is nearly double that of Linden (1979). The principal error in determining η_0 is in the estimate of the kinetic energy

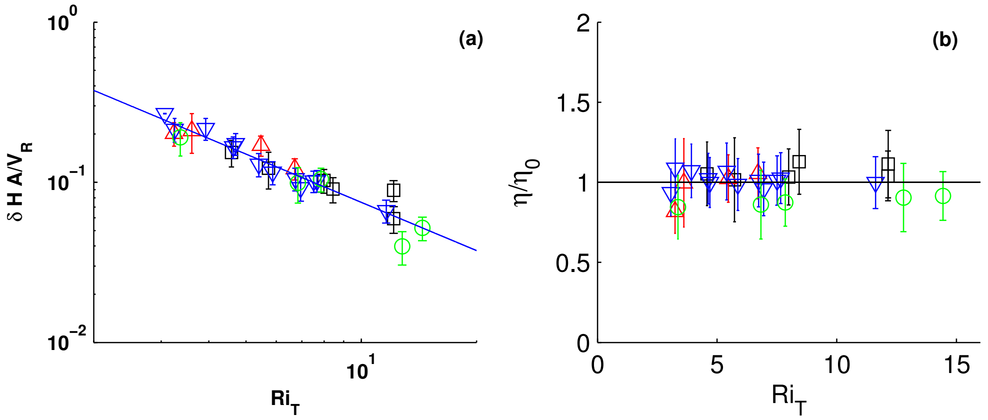

Fig. 6.8 Plot (a) of the normalized δH as a function of Ri_T. A Ri^{-1} line was plotted for comparison. Plot (b) of the normalized mixing efficiency as a fuction of Ri_T. Note that as $\mathrm{Ri}_T \to 0$, we expect that η will also tend to zero.

but the precise value of η_0 does not alter the conclusion of a constant mixing efficiency. As mentioned previously, at low Ri, we expect the mixing rate will decrease to zero.

6.4 Summary

By periodically generating temporally independent vortex rings that interact with a sharp interface, we externally mix the density stratification. The initial vortex rings evolve the stratification such that the density interface sharpens and a mixed fluid layer is generated above the density interface. This initial adjustment phase continues until the top of the mixed layer reaches the base of the vortex tube. After the initial adjustment phase, the system evolves such that the change in interface position is proportional to Ri^{-1}.

In this work, we have a clear indication that this externally mixed system will evolve such that the mixing efficiency becomes independent of Ri provided the following conditions hold. First, Ri must be large enough that the interface thickness and upper layer gradient remain small. Second, the system must be volumetrically constricted, in some sense, to restrict the height of the mixing layer H. Third, the entrainment rate is sufficiently high that the molecular diffusion is not dominant and that the density interface remains sharp. Note that this regime is only attainable provided that the time scale of diffusion is long enough (low molecular diffusivity) such that the increase in potential energy is dominated by the mixing induced by the vortex rings. In the present experiments this is ensured by restricting the temporal inter-vortex ring spacing, but it is our contention that this could have been equivalently performed by producing two spatially isolated vortex ring events with a longer time interval between subsequent vortex rings. These may appear to be very limiting constraints to the problem, however Oglethorpe *et al.* (2013) observe a similar set of mixing conditions and arrive at the same conclusion in a stratified Taylor-Couette flow. This mixing was driven by an entirely different mechanism of external mixing of the fluid. Similarly, Moore & Long (1971) observed an Ri^{-1} entrainment relationship in a stratified shear flow. Again, Park *et al.* (1994) identified a similar layering mechanism with a constant mixing efficiency when considering a horizontally moving vertical rod. The results presented in this chapter are consistent with observations made for a range of external mixing mechanisms. Chapter 7 will present a one-dimensional model of the vortex-ring-induced mixing, and extend these results to a larger range of Reynolds and Richardson numbers.

This work demonstrates a mixing efficiency dependence that is in direct contrast to the work of Linden (1973), and a significantly different maximum value of the mixing efficiency by a factor of 2 Linden (1979). The precise reason for this discrepancy is unknown, but there are several differences between our approach and that of Linden. First, the use of model experimental fluid mechanics equipment allows for a much more precise measurement of the mixing efficiency, which Linden (1973) would not have had access to. Second, Linden (1973) used a syringe to sharpen the density interface between subsequent vortex ring generations, where we do not. Third, the Reynolds number of the vortex rings differ by a factor of four. There are other differences between the experimental approaches but we view these as the largest differences. Future work will "pin-down" the precise reason for this discrepancy.

While other studies of internal mixing problems have reported mixing efficiency values higher than reported here (see Davies Wykes and Dalziel (2014)), the present value of η_0=0.42 is significantly higher than that reported for most other external mixing problems (see Linden (1979)). The largest source of uncertainty in these estimates is in the precise value of the kinetic energy through the parameter C_{KE}. It should be stressed again that our rings are highly reproducible (as shown in Chapters 4 and 5) and this error is in the quantification of the kinetic energy and not a random variation between experiments. We have estimated C_{KE} in four ways: (a) directly from our PIV data under the assumption of axisymmetry; (b) using the PIV data but projecting the flow outside the cores onto an irrotational field to minimise the influence of spurious noise at large radius; (c) the energy imparted to the fluid as it is displaced from the vortex tube; and (d) following Norbury's (1973) analysis using an estimate of the dimensionless core size[1]. These four measures produce broadly consistent results with differences of less than 20%. See Appendix C for details on these calculations. Although the cores do not have the constant ω/r assumed by

---

[1] We have subsequently compared the kinetic energy of the vortex ring as measure by the 3D ensemble of Chapter 4. The results are consistent with the Norbury estimate. See Appendix C for more details.

Norbury, we have elected to adopt the Norbury approximation throughout for simplicity and consistency. While this choice of quantification for the kinetic energy impacts the precise value of η_0, this does not alter our conclusion that the mixing efficiency η is independent of Ri.

We briefly return here to the distinction between the entrainment rate u_e and the discrete change in interface height δH. In this present work, the time-scale of mixing has been removed from the problem. If we write $u_e \approx \frac{\delta \mathrm{H}}{\tau_M}$ for some time scale τ_M, then that choice of mixing time scale affects the model for entrainment velocity (though not necessarily the mixing efficiency). This present work quantifies the increase in potential energy of the system for a given kinetic energy input (mixing efficiency). Future work will examine the time-scales associated with different external mixing problems.

This work agrees with the previous work in Chapter 4, which suggested a critical Richardson number Ri_c about which there will be a regime change. This work also supports the work of Chapter 5, where the asymmetric nature of the buoyancy flux suggests that there will be a sharpening of the density interface. In the next chapter, we will construct a one-dimensional turbulence model for these vortex-ring interactions in order to extend the parameter space dependence of the system on the mixing efficiency.

Note

The experimental data associated with this study is made available at
https://www.repository.cam.ac.uk/handle/1810/249285.

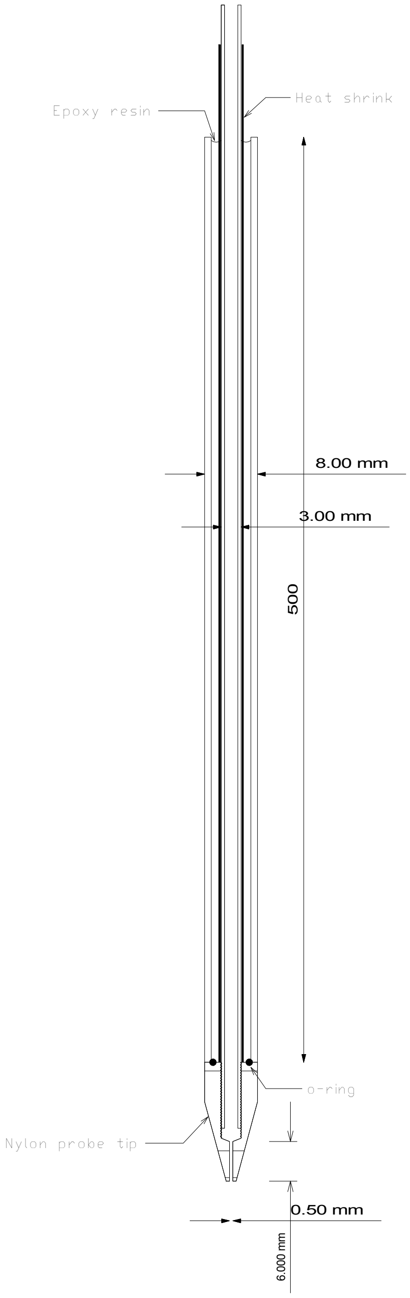

Plate 6: One of the original sketches of the conductivity probe circa 1997 courtesy of Prof. Stuart Dalziel. Design modifications, especially in regards to the probe tip, have been implemented.

Chapter 7

Vortex-ring-induced stratified mixing: mixing model

> I am an old man now, and when I die and go to Heaven there are two matters on which I hope for enlightenment. One is quantum electrodynamics, and the other is the turbulent motion of fluids. And about the former I am really rather optimistic.
> —Horace Lamb, as paraphrased by Goldstein (1969).
> (A similar quote has been attributed to Heisenberg.)

As we have seen in the previous chapter, when vortex rings are repetitively produced in a stratified environment, the density profile establishes a near self-similar form. The mixing efficiency of each subsequent vortex ring is constant. However, this work was limited to a moderate range of Richardson numbers and was only performed for a single stratifying agent (NaCl). This chapter presents a theoretical, one-dimensional model for the evolution of a stratified system in the context of isolated mixing events, based upon our understanding of the mechanics of the vortex-ring interaction (see Chapters 4 and 5). The model is then compared to both numerical simulations, and the physical experiments from Chapter 6. Qualitative agreement between the evolution of the density profiles is observed, along with close quantitative agreement of the mixing efficiency. This model highlights the key dynamical features of isolated mixing experiments and relates to the stratified turbulence experiments described in Chapter 2.

7.1 Introduction

Understanding the mixing produced by turbulent motion in a stratified environment remains elusive. This has been particularly relevant in an oceanographic context (Ivey *et al.*, 2008). The energy cascade found in turbulent flows results in a large range of length scales, which complicates the analysis. However, Turner (1968), while examining grid-generated stratified turbulence (with no mean flow), argued that the large scale eddies within the turbulent flow were the dominant mixing mechanism. Turner (1968) further demonstrated that when a stratified fluid is mixed by a second mixing grid, located at the opposite vertical end of the stratified tank, the buoyancy flux across the interface doubled, leading to the conclusion that the upper and lower mixing events are independent. These findings motivated Linden (1973) to study isolated vortex-ring mixing events, as an analogy to the intermittent large-eddy dynamics. Vortex rings provide a reproducible coherent structure of vorticity of a defined length scale, making them the ideal candidate for studying turbulent-eddy mixing events. The current chapter presents a one-dimensional (1D) model for the mixing induced by isolated mixing events driven by a large-scale source of coherent (non-turbulent) energy. Here, the term “large” refers to length scales greater than the thickness of the interface. Understanding the fluid mixing that occurs in this simplified context provides insight into the mixing produced by fully developed stratified turbulence.

Building on the work of Balmforth *et al.* (1998), we model the stratified vortex-ring experiments as a coupled system of equations for the coherent vortex ring energy density (T), turbulent kinetic energy density (e) and the background density field (ρ). The model does not explicitly include the available potential energy (APE) found in the physical experiments[1]. The absence of an independent APE reservoir prohibits a reversible buoyancy flux, and hence there is a one-way transfer of energy between e and the background density field ρ. However, as we are interested in the time-integrated mixing that results from a given energy input, we argue that this is not fundamental to our investigation. To ensure the validity of this approach, we compare the model results with both numerical simulations of the mixing events (presented here) and the experimental results of Chapter 6. The mixing efficiency, calculated for all three methodologies, is shown to be highly consistent.

The remainder of this discussion is organized as follows: §7.2 presents the setup and dynamics of the vortex-ring experiments. Section 7.3 describes the construction of a 1D mixing model. The model results are supplemented with numerical simulations as described in §7.4. Finally, §7.5 compares the mixing efficiency results for all three methodologies, and summarizes these findings.

---

[1] For clarity, the only form of potential energy we will consider in this problem is gravitational potential energy.

7.2 Experimental setup

In this study, we are interested in vortex-ring-induced mixing events in the limit of a large number of generated vortex rings. This topic has been previously investigated experimentally in Chapter 6. For each of those experiments, an individual vortex ring is generated within a stratified tank. The vortex rings will propagate along the direction of gravity. As it advects, the vortex ring will displace the isosurfaces of the density field, producing APE in the system. As we have seen in Chapter 4, the flow will also become unstable producing turbulent kinetic energy (TKE). The spatial overlap of turbulence with APE will mix the density field (see Winters *et al.* (1995) for more details), increasing the background potential energy of the system. Of course, as we have also seen in Chapter 4, vortex rings will produce both secondary vorticity and internal waves, which are not turbulent. For the purposes of this discussion, these additional sources of kinetic energy, which are not predicted to significantly mix the stratification, will be denoted as ordered kinetic energy (OKE). Figure 7.1 plots the generic energy pathway for the vortex ring experiments. The kinetic energy of the vortex rings (KE_{ring}) will produce APE at a rate $\mathbb{G}$ prior to the production of OKE and TKE, at some rate $\mathbb{I}$. The sum of APE, OKE, and TKE will be denoted as available energy, as it indicates the total amount of energy that is available to mix the stratification. There is a reversible buoyancy flux ($\mathbb{H}$) that enables APE to generate kinetic energy and vice versa. The available energy in the system will decrease both due to viscous dissipation (ε) and mixing ($\mathbb{M}$) of the background density profile, increasing the background potential energy (BPE) of the system. Internal energy will also slowly increase the BPE through background diffusion ($\mathbb{D}_\rho$). This schematic is consistent with the conceptualization of Winters *et al.* (1995), and a simplified view of mixing (assuming a Boussinesq fluid) as suggested by Tailleux (2009). Once the transient available energy in the system has sufficiently dissipated, another vortex ring is generated and the cycle repeats. This process continues until the desired number of vortex rings have been generated. The limitations imposed on the experiments of Chapter 6, and the opportunity provided by those results, prompted the development of a 1D turbulence model in order to further evaluate the dependence of the vortex-ring mixing on the stratification parameters.

In order to parameterize the vortex-ring-induced mixing, we require a velocity and length scale. In this setup, it is natural to select the vortex-ring propagation velocity U as the characteristic velocity, and the vortex-ring diameter a as the characteristic length scale. This work focuses on three dimensionless parameters: the Reynolds number (Re, the ratio of inertia to viscous forces), the Richardson number (Ri, the ratio of buoyancy to advective forces), and the Schmidt number (Sc, the ratio of viscous to molecular diffusion). These are

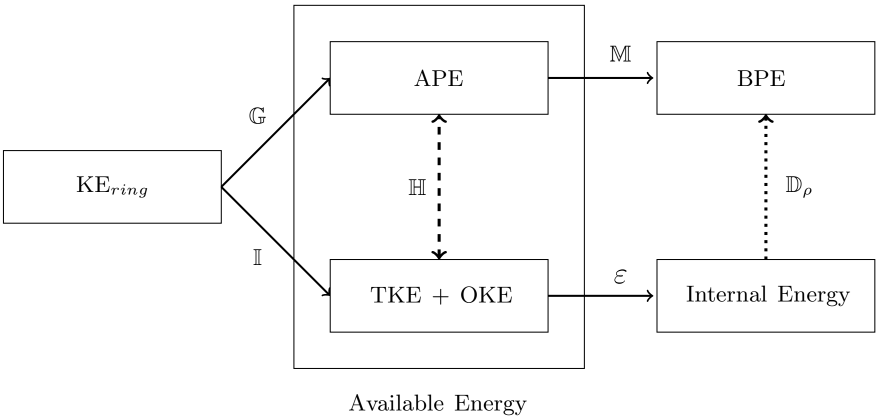

Fig. 7.1 Diagram of the energy cascade for each vortex ring experiment. The input of kinetic energy from the vortex ring (KE$_{ring}$) will lead to an increase in the gravitational potential energy (BPE) of the system.

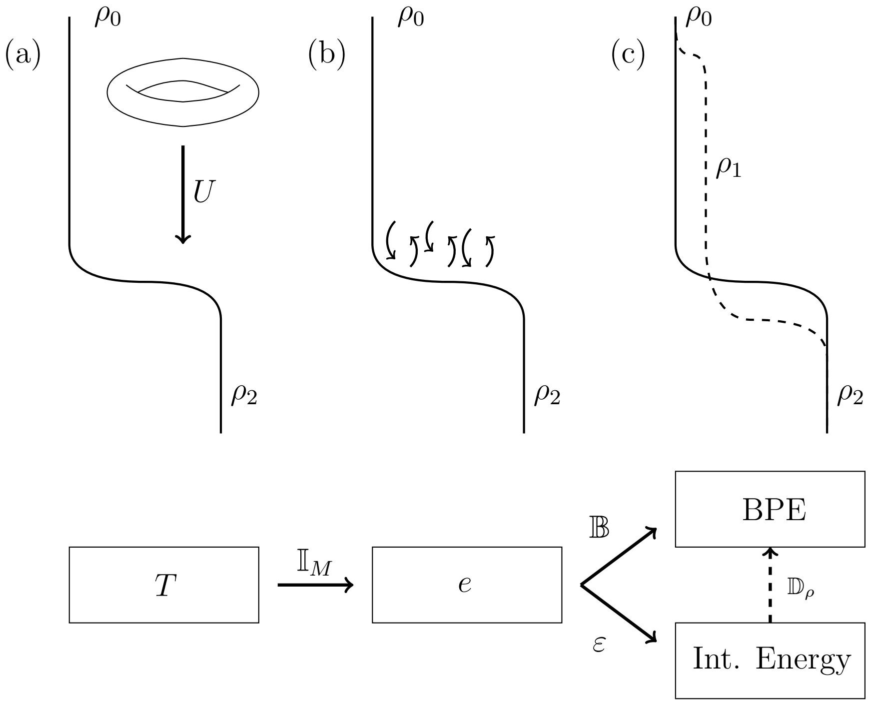

Fig. 7.2 Diagram of the energy cascade in the experimental setup. The kinetic energy of the vortex rings [T](a) breaks down into turbulent kinetic energy [e] (b), which subsequently mixes the density profile [ρ] (c) changing the background potential energy of the system [BPE].

defined as

$$\mathrm{Re} = \frac{Ua}{\nu}, \qquad \mathrm{Ri} = \frac{g\,(\rho_2 - \rho_1)}{\rho_1}\frac{a}{U^2}, \qquad \mathrm{Sc} = \frac{\nu}{\kappa}. \tag{7.1}$$

Here, g is the acceleration due to gravity, ρ_1, ρ_2 are densities associated with the stratification, ν is the kinematic viscosity (here, $\nu = 1 \times 10^{-6}$ m^2/s) and κ is the coefficient of mass diffusion. In this chapter, we will study the vortex-ring-induced mixing produced in physical, model and numerical experiments (presented below). In each of these experiments, we will ensure consistency by comparing the Reynolds, Richardson, and Schmidt numbers.

Another important parameter is the kinetic energy of each vortex ring (KE_{ring}). According to Norbury (1973), the kinetic energy of each vortex ring is given as

$$\mathrm{KE}_{ring} = C_{KE}\left(\frac{1}{2}\rho_1 U^2\right)\left(\frac{4}{3}\pi\left(\frac{a}{2}\right)^3\right).$$

The constant C_{KE} is a function of the vortex ring aspect ratio (the ratio of the core width to ring diameter). For the vortex rings used in Chapter 6, a value of $C_{KE} = 6.5$ has been estimated and thus, we use this value when discussing the model experiments below.

7.3 Model construction

The purpose of the present model is to predict the mixing produced by isolated vortex-ring-induced mixing events within a stratified fluid. In order to characterize this system, we model the non-turbulent vortex-ring energy density (T), the turbulent kinetic energy density (e) and the background density field (ρ). We consider horizontally averaged quantities such that each variable is only a function of a single spatial (vertical) dimension and time. This model builds upon the conceptualization introduced in figure 7.1. As a result of the 1D spatial structure of the model, we assume that the local mixing ($\mathbb{B}$) is an instantaneous sink of kinetic energy. Figure 7.2 presents a cartoon of the simplified model. Note that the evolution of e and T is dependent on the density field creating a coupled dynamical system for T, e and ρ. It is helpful to consider T as “coherent energy" that, in itself, does not mix the density field (ρ), but acts as a source for e and (in a transient way) allows for the creation of APE. With reference to figure 7.1, an alternative model formulation would consider e, not as the turbulent kinetic energy, but as the available energy in the system. The present model does not explicitly include a mechanism for the generation of APE in the system (i.e. no explicit inclusion of $\mathbb{G}$ as labeled in figure 7.1). However, the APE generation mechanism is important for the vortex-ring system, and in particular, for the Crow-like

		a (10^{-3} m)	U (10^{-3}m/s)	$\Delta\rho$ (10^{-5} kg/m^3)	A(m^2)	Re	Ri	Sc	Notes	
Phys. Exp.	E1	45.2 ± 1.6	37.1 ± 1.0	1.5 - 3.9	0.4 × 0.2	1700	4.8-12.3	700		
	E2	48.3 ± 1.5	39.0 ± 1.5	2.1 - 4.1	0.4 × 0.2	1900	3.1-6.5	700		
	E3	50.6 ± 0.5	54.2 ± 1.8	1.1 - 3.8	0.4 × 0.2	2700	3.1-11.7	700		
	E4	49.9 ± 0.6	49.8 ± 3.3	1.8 - 7.4	0.45 × 0.45	2500	3.5-14.6	700		
									Resolution	τ(s)
Num. Exp.	N1	(70)	25.0	0.5 - 2	0.1 × 0.1	1750	5.8-22.8	3	128x128x512	30
	N2	(70)	37.5	0.5 - 2	0.1 × 0.1	2625	2.5-10.2	3	128x128x512	30
	N3	(70)	50.0	0.5 - 4	0.1 × 0.1	3500	1.4-11.2	3	192x192x768	40
	N4	33.1	70.8	1-6	0.1 × 0.1	2343	1.3-3.9	3	128x128x512	40
Model Exp.	M1	40	40	1 - 8	0.4 × 0.2	1600	2.5-19.6	1000		
	M2	20	20	1 - 8	0.4 × 0.2	400	4.9-39.2	1000		
	M3	40	40	1 - 8	0.4 × 0.2	1600	2.5-19.6	3		
	M4	40	40	1 - 8	0.4 × 0.2	1600	2.5-19.6	1000	Linear Strat.	

Table 7.1 Table of the relevant characteristic parameters of the different VR cases. Data from the physical experiments was taken from Chapter 6. Note that the diameter of the Hill's VR (highlighted $(\cdot)$) is defined as $2R$.

instability discussed in Chapter 4. As such, the APE production will be implicitly modeled through the parameterization of the breakdown parameter $\mathbb{I}_M$. Similarly, while this model encapsulates the transfer of energy in the system, the flow evolution of the vortex ring was not explicitly modeled; see Chapter 4 for a study of the kinematics of the interaction between the vortex ring and the density stratification.

This model can then be written as a system of three couple differential equations:

$$\partial_t T = \mathbb{A} - \mathbb{I}_M + \mathbb{S}, \qquad \partial_t e = \mathbb{D}_e - \varepsilon + g\mathbb{B} + \mathbb{I}_M, \qquad \partial_t \rho = \partial_z \mathbb{B} + \mathbb{D}_\rho. \tag{7.2}$$

In this model, the non-turbulent kinetic energy density (T) is produced ($\mathbb{S}$), is advected ($\mathbb{A}$), and will break down in the presence of the stratification ($\mathbb{I}_M$). Then, e dissipates (ε), diffuses ($\mathbb{D}_e$) and produces BPE via an irreversible buoyancy flux ($\mathbb{B}$). This buoyancy flux $\mathbb{B}$ is irreversible as there is no mechanism for potential energy to generate kinetic energy in this system. That is, $\mathbb{B}$ is negative semi-definite. Finally, the density field also diffuses ($\mathbb{D}_\rho$). Each of the operators, described above, will vary with the vertical coordinate z.

Balmforth *et al.* (1998) constructed a turbulence model that coupled the horizontally-averaged turbulent kinetic energy and the density (buoyancy) field. That model depends critically on a mixing length scale l, over which the turbulent eddies are capable of mixing the surrounding fluid. We follow an approach similar to Balmforth *et al.* (1998) to model e and ρ. In this formulation, we write:

$$\mathbb{D}_e = \partial_z \left[(\nu_e + \nu)\, \partial_z e \right], \qquad \varepsilon = \beta \frac{e^{\frac{3}{2}}}{l}, \qquad \mathbb{B} = \alpha \nu_e \partial_z \rho, \tag{7.3}$$

$$\mathbb{D}_\rho = \kappa \partial_z^2 \rho. \tag{7.4}$$

Here, we have augmented the previous model with an explicit molecular viscosity and diffusivity. Both e and ρ are driven by eddy diffusion (turbulent viscosity), which, on dimensional grounds, is proportional to $\nu_e = l\sqrt{e}$. The turbulent dissipation, ε, is similarly constructed. The parameters α and β are model constants and will be discussed below. Finally, the non-dimensional turbulent length scale (l) will depend on the local density gradient. For a near uniform stratification, this length scale will be set by the vortex ring ($l = a$). However, where there is a strong stratification gradient, the vertical length scales are constrained. The experimental work of Park *et al.* (1994) suggested that, in a strongly stratified environment, the turbulent length scale will be proportional to $\frac{e}{\sqrt{g|\partial_z \rho|}}$. As such, Balmforth *et al.* (1998) proposed a simple model for the length scale that preserves these limits:

$$l = \frac{a\sqrt{e}}{\sqrt{e - \gamma g \partial_z \rho}}, \tag{7.5}$$

with the Ozmidov parameter γ, a scaling parameter in the limit of high stratification.

In order to model the vortex-ring system, we need to augment this turbulent model with the input of energy from the vortex rings, T. We define the advection $\mathbb{A}$ and breakdown $\mathbb{I}_M$ terms as:

$$\mathbb{A} = U \partial_z T, \qquad \mathbb{I}_M = \lambda g \left(\frac{\rho - \rho_1}{\rho_0} \right) \sqrt{T}. \tag{7.6}$$

The density $\rho_1 = \rho(z = z_0)$ is the density at the vortex ring initialization height z_0. The advection term ($\mathbb{A}$) prescribes that T is transported vertically downward at the propagation speed U. Based upon the work of Chapter 4, we know that there exists an instability in the vortex-ring system that is catalyzed by the stratification. The growth rate of this instability is proportional to the bulk Richardson number of the flow. The parameterization of $\mathbb{I}_M$, which is constructed on dimensional grounds, captures this dependence (see below) with constant λ, a free parameter that we will set to unity.

Finally, we must prescribe the production rate $\mathbb{S}$ of the vortex rings. In this model, T is forced periodically and instantaneously. That is, after a time $\Delta t = \tau_R$, a vortex ring is spontaneously introduced (no vortex-ring formation time) into the system. Mathematically, this is written as

$$\mathbb{S} = \sum_{n=0}^{N} f(z - z_0) \delta\left(t - n\tau_R\right). \tag{7.7}$$

Here, δ is a Dirac delta function. The system is periodically forced for a specified number of iterations N. The index n is the vortex-ring generation number, which identifies the number of vortex rings that have been input into the system. The functional form of f is defined below.

Now, the physical parameters in this problem are non-dimensionalized as

$$z' = \frac{z}{a}, \quad t' = \frac{U}{a} t, \quad T' = \frac{T}{U^2}, \quad e' = \frac{e}{U^2}, \quad \rho' = \frac{\rho - \rho_0}{\rho_2 - \rho_0}, \quad P' = \frac{a}{U} P, \quad \Delta\rho' = \frac{\rho_2 - \rho_0}{\rho_0},$$

	L (m)	z_0 (m)	σ_p (m)	H_0	τ_R (s)
Num. Exp.	0.5	0.375	0.02	0.15	30-40
Model Exp.	0.35	0.3	0.02	0.15	30

Table 7.2 Table of domain parameters for the model and numerical experiments.

where the reference density ρ_0 is selected to be the initial minimum density of the system. The model then reduces to the following, dropping the primes for convenience,

$$\partial_t T = \partial_z T - \lambda \mathrm{Ri}_0(\rho - \rho_1)\sqrt{T} + P, \tag{7.8}$$

$$\partial_t e = \partial_z \left[\left(\nu_e + \frac{1}{\mathrm{Re}}\right)\partial_z e\right] - \beta\frac{e^{\frac{3}{2}}}{l} + \alpha \mathrm{Ri}_0 \nu_e \partial_z \rho + \lambda \mathrm{Ri}_0(\rho - \rho_1)\sqrt{T}, \tag{7.9}$$

$$\partial_t \rho = \partial_z \left[\left(\alpha\nu_e + \frac{1}{\mathrm{Re\ Sc}}\right)\partial_z \rho\right]. \tag{7.10}$$

The initial Richardson number is denoted as Ri_0. The production term P is now written:

$$P = \sum_{n=0}^{N} \frac{1}{\rho_0 U^2} f(z - z_0)\delta(t - n\tau), \quad f(z) = \frac{\mathrm{KE}_{\mathrm{Ring}}}{Aa}\frac{1}{\sqrt{2\pi\sigma^2}}\exp\left[-\frac{z^2}{2\sigma^2}\right], \tag{7.11}$$

Here, A is the plan area of the stratified tank and $\sigma = \frac{1}{4}$ such that the width of the forcing is ≈ 1. The time between vortex ring generations is $\tau = \frac{U\tau_R}{a}$.

This model has four free parameters. The work of Tominaga & Stathopoulos (2007) has shown that the turbulent Schmidt (Prandtl) number α has a typical value of 0.2-1.3, depending on the flow structure. For the purposes of this model, we set $\alpha = 1$. As reported in Vassilicos (2015) for decaying turbulence, the dissipation parameter β, where it is constant, has a value near one, and thus we set $\beta = 1$. With reference to Park *et al.* (1994), the Ozmidov parameter γ is order one, and thus we set this parameter to unity. Based upon the work of Chapter 4, we suggest that the value of λ is also O(1). The vortex breakdown parameter λ is therefore also set to one. Thus, in this chapter we restrict ourselves to the case where the free parameters are all set to unity. We return to this later.

The model was implemented on an evenly spaced grid, using pseudospectral spatial derivatives and a first-order semi-implicit time stepping scheme. The computational domain was defined with 1024 grid points. Varying the grid resolution demonstrated that this resolution was sufficient for the parameter sets presented here. The code was verified to preserve mass within the system to near machine precision. Adaptive time stepping was used to ensure total energy conservation, which was typically within $O(10^{-4})$. A spectral filter was also used to limit the aliasing of the Fourier modes. See Appendix D for more details on the numerical implementation of the model.

We run a set of model experiments (runs) in a manner similar to that described in section 7.2. Four parameter cases were performed, which prescribe the functional form of the stratification and the vortex-ring parameters. We label these model cases M1-M4. For each of these cases, four different stratification strengths ($\Delta\rho = \{0.01, 0.02, 0.04, 0.08\}$) were set, resulting in a total of 16 runs. As described in section 7.2, each model run will comprise of sequentially generated vortex rings. We enumerate the number of generated vortex rings as $n = \{0, 1, 2, .., N\}$, for a total of $N = 500$ generated vortex rings in all cases, as prescribed by equation (7.11). The parameters associated with each of these cases are presented in table 7.1. In the first three model cases (M1-M3), similar to the experiments of Chapter 6, a two-layer density profile was specified using a tanh function, with an initial interface height of H_0 and an interface thickness of σ_ρ. The fourth case (M4) was initialized with a linear stratification. These density profiles are prescribed as

$$\rho_{M1-M3}(z, t=0) = \frac{1}{2}\left(1 - \tanh\left[\frac{z - H_0}{\sigma_\rho}\right]\right), \qquad \rho_{M4}(z, t=0) = (z - L). \tag{7.12}$$

Here, L is the height of the domain. The dimensionalized initial conditions are given in table 7.2 and were selected to approximate the physical experiments performed with salt-water in Chapter 6.

Figure 7.3 plots the evolution of the density profiles for one run ($\Delta\rho = 0.01$) from each of the model cases. Density profiles were plotted at vortex ring number $n = \{0, 125, 250, 375\}$. The results show excellent agreement with the physical experiments. We observe that, as in Chapter 6, the evolution of the density profiles is defined by three generic characteristics. First, the vortex rings sharpen the density interface. Second, the vortex rings generate a middle fluid layer that is near homogeneously mixed. Third, the growth of the middle fluid layer is limited by the vortex ring injection height.

Comparison of Figure 7.3(a)(Model Exp. M1) and Figure 7.3(b)(M2) demonstrates how the density field evolution changes for different vortex ring parameters (M1: Re=1600, Ri=2.5 vs. M2:Re=400, Ri=4.9). The same characteristic evolution of the density profiles is observed for M2, though only a small amount of scouring of the density interface has occurred due to the decrease in kinetic energy input. Figure 7.3(c)(M3) varies the molecular diffusivity (κ) of the stratification (Sc= 3 vs. Sc= 1000). Again, the same features of the density profiles are observable, except that the vortex rings are no longer able to effectively sharpen the lower interface as it diffuses. Molecular diffusion is significant as it reduces the maximum duration of the experiments due to the growth of the interface thickness combined

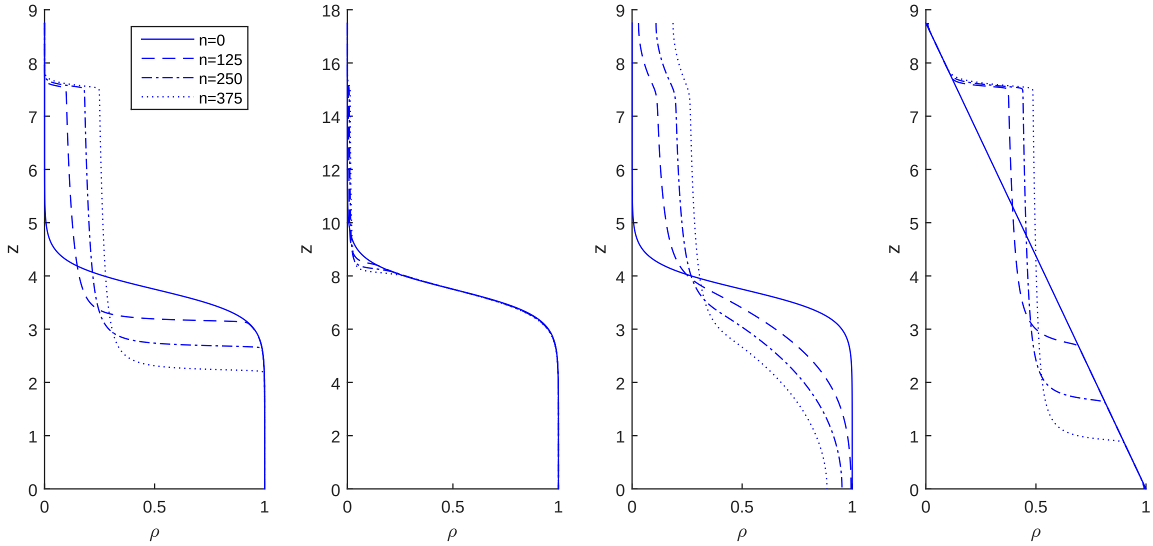

(a) (b) (c) (d)

Fig. 7.3 Plot of the evolution of the density profiles for one run ($\Delta\rho = 0.01$) from each of the model cases. Here, model experiments M1(a), M2(b), M3(c), and M4(d) are all presented. Density profiles are plotted at $n = \{0, 125, 250, 375\}$.

with the finite size of the domain. This will be important when discussing the numerical simulations below. Finally, figure 7.3(d)(M4) changes the initial background stratification to a linear profile demonstrating the same characteristic evolution, although we have no matching physical experiments against which to compare these runs.

Figure 7.4(a)-(c) plots the evolution of T, ρ, and e for a single mixing event of M1 ($\Delta\rho = 0.01$) at $\frac{t}{\tau} = \{250.00, 250.15, 250.30\}$. These snapshots demonstrate the advection of T and the production of e through $\mathbb{I}_M$. The associated partition of energy has been also plotted in Figure 7.4(d). This shows the integrated non-turbulent kinetic energy (NTKE) and integrated turbulent kinetic energy (TKE), along with the change in background potential energy (ΔBPE) of the system (correcting for the background diffusion $\mathbb{D}_\rho$). The integrated dissipation (D $= \int_{t_n}^{t} \int_V \varepsilon dt' dV'$) has also been plotted. We observe that the majority of the mixing is temporally confined near the peak in e. However, data on the time-dependent dissipation and mixing rates are not available for the physical experiments and thus comparison is limited to that of the density profiles $\rho(z,t)$.

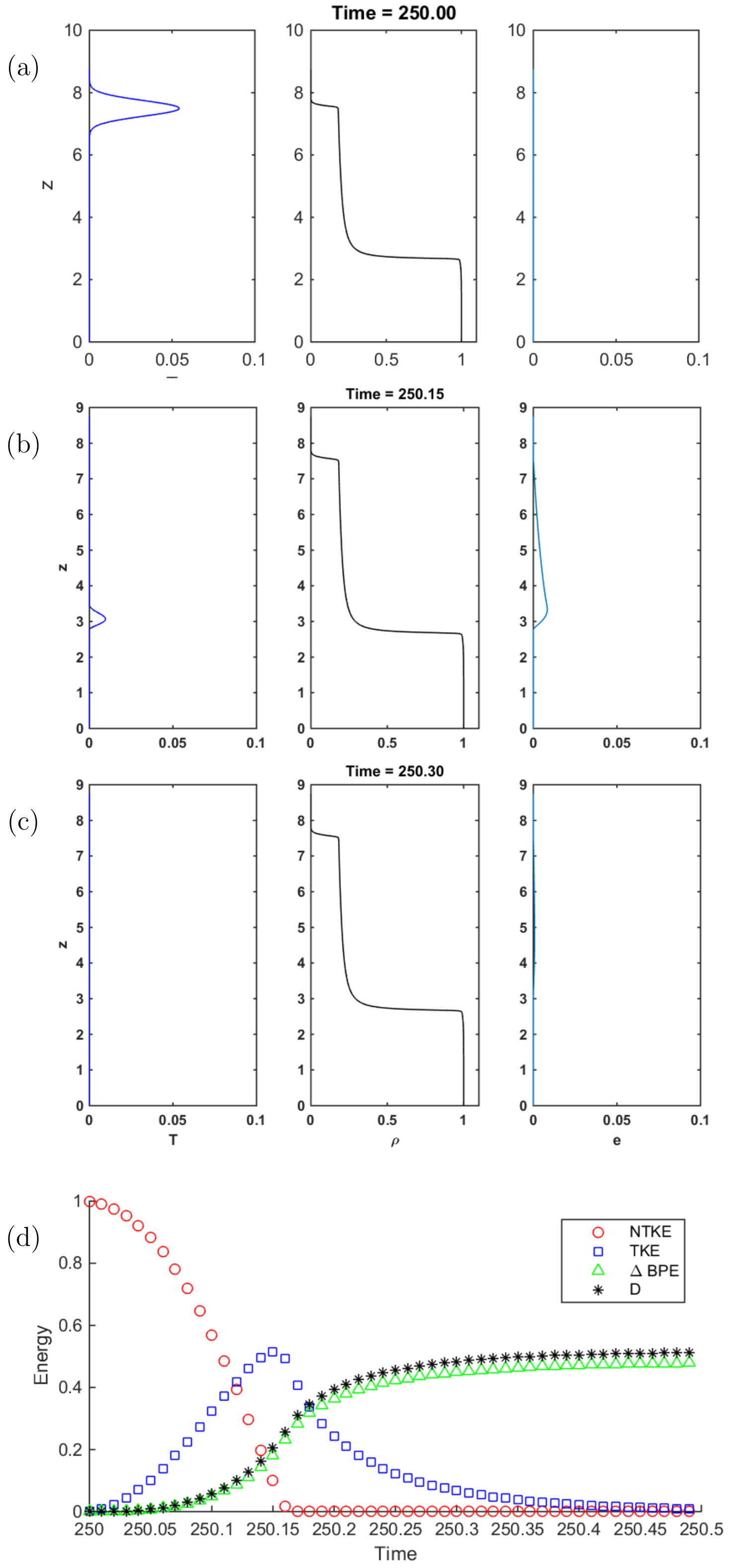

Fig. 7.4 Panels (a)-(c): Plot of the evolution of T, ρ and e for a single mixing event of M1 ($\Delta\rho = 0.01$) at $\frac{t}{\tau} = \{250.00, 250.15, 250.30\}$. Panel (d): Plot of the partition of energy between the integrated non-turbulent (NTKE) and turbulent (TKE) kinetic energy for n = 250. The change in potential energy (ΔBPE) and the integrated dissipation (D) are also plotted. Time has been normalized by the inter-VR spacing τ. Data has been plotted for M1 with $\Delta\rho = 0.01$.

.

7.4 Numerical simulation experiments

We validate the 1D model results using a 3D pseudospectral numerical solver (SPINS, see Subich *et al.* (2013)) to solve the incompressible Navier-Stokes equations under the Boussinesq approximation. These equations can be written as

$$(\partial_t + \mathbf{u}\cdot\nabla)\,\mathbf{u} = -\nabla p - \mathrm{Ri}\rho g\hat{\mathbf{z}} + \frac{1}{\mathrm{Re}}\nabla^2\mathbf{u}, \qquad (\partial_t + \mathbf{u}\cdot\nabla)\,\rho = \frac{1}{\mathrm{Re\ Sc}}\nabla^2\rho. \tag{7.13}$$

Here, $\mathbf{u}$ and p are the velocity and pressure fields respectively. Boldface variables denote vector quantities.

Experimental visualizations of the interaction of a vortex ring with a stratified interface (see Chapter 4) demonstrate that, where the vortex rings propagate parallel to the direction of gravity, the flow field remains predominantly axisymmetric about the vortex ring axis throughout the majority of the interaction, despite the formation of a three-dimensional instability. In order to facilitate the numerical computations, we take partial advantage of this symmetry by simulating a quarter ring in a triply periodic, free-slip (cosine transform) domain. The parameters associated with the numerical simulations can be found in table 7.1. Grid resolution studies determined that the resolution was sufficient to estimate the mixing efficiency, although we note that we do not resolve down to the Batchelor scale of the flow. As with the model results, a high molecular diffusivity results in a thick density interface, which will eventually violate the two-layer setup considered here, and will limit the run-time of each experiment. Thus, we desire the lowest diffusivity that is computationally viable. In these simulations, we select Sc = 3. Four sets of numerical simulations were performed. The initial density stratification for each case was defined via a tanh profile similar to (7.12). See table 7.2 for the dimensionalized initial conditions.

Three sets of simulations (Num. Exp. N1-N3) were initialized with a Hill's spherical vortex as a classical vortex ring solution. The Hill's vortex can be written as

$$u_r = \begin{cases} \frac{3}{2}U\frac{zr}{R^2}, & r \le R \\ \frac{3}{2}U\frac{zr}{R^2}\left(\frac{R^2}{z^2+r^2}\right)^{\frac{5}{2}}, & r > R \end{cases}, \qquad u_z = \begin{cases} \frac{3}{2}U\left(\frac{5}{3} - \frac{2r^2+z^2}{R^2}\right), & r \le R \\ U\left[\left(\frac{R^2}{r^2+z^2}\right)^{\frac{5}{2}}\left(\frac{2z^2-r^2}{2R^2}\right) - 1\right], & r > R \end{cases}.$$

In this chapter, R is the radius of the Hill's vortex, and $U < 0$ is its propagation speed. We note that there is a mismatch between the definition of the Hill's vortex diameter ($2R$) and the experimentally measured vortex-ring diameter that was defined as the distance between vorticity centroids (see Chapter 6). A random initial velocity perturbation of $\mathrm{O}(10^{-4})$, relative

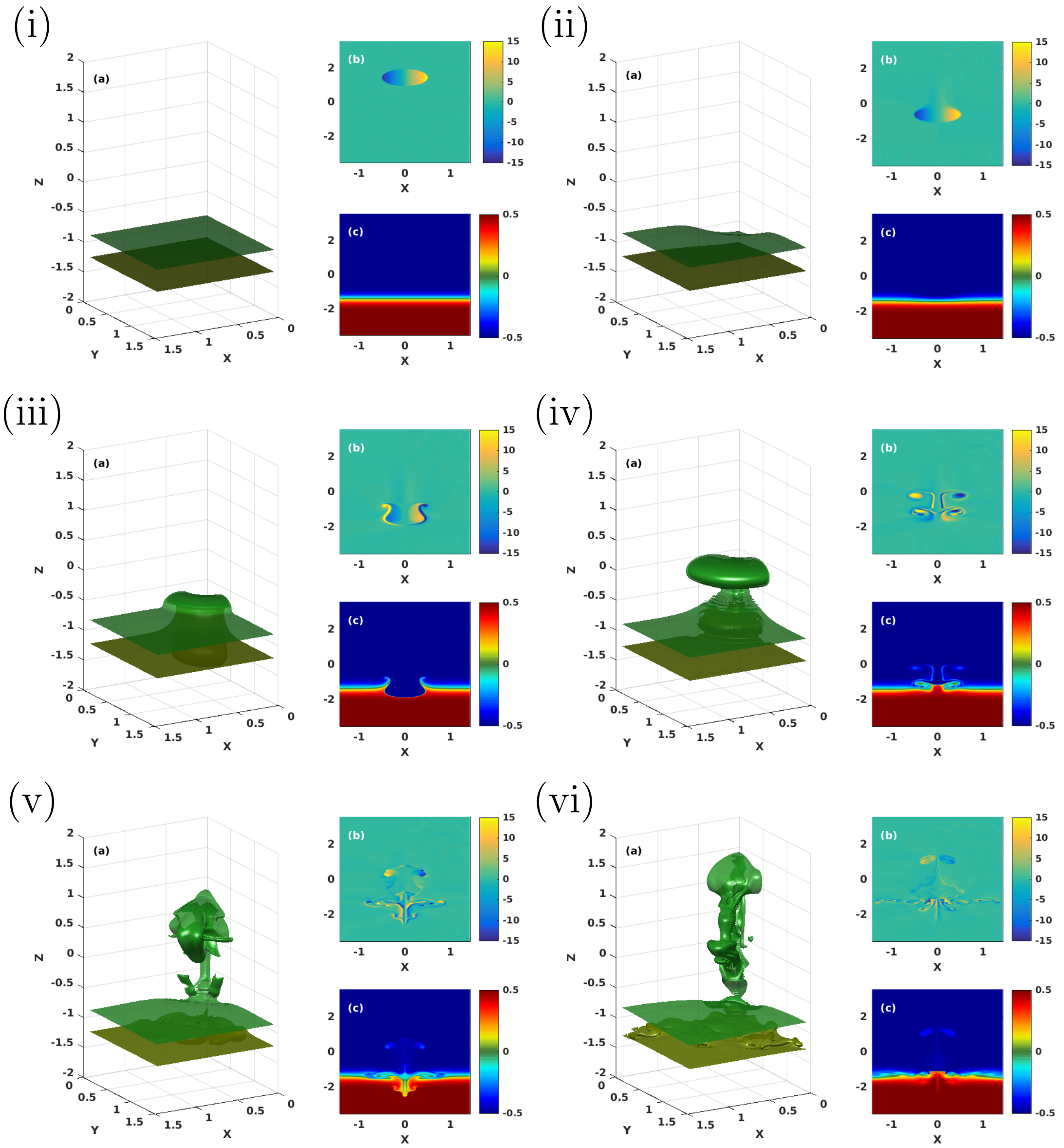

Fig. 7.5 Visualization of the evolution of the initial vortex-ring interaction for Num. Exp. N3 ($\Delta\rho = 0.01$). Panel (a) plots two isocontours of the density field ($\rho = \{-0.5, -0.95\}$). Panel (b) and (c) plot the (appropriately extended) vorticity and density fields, respectively, on the $y = 0$ plane. Plots have been provided for non-dimensional time $t/\tau_{advective} = 0$(i), 2.14(ii), 4.29(iii), 6.43(iv), 8.57(v), and 10.74(vi). Here, Re= 3500 and Ri= 2.75.

to the vortex-ring propagation speed, was added to the numerical simulations in order to trigger any instabilities in the velocity field.

Figure 7.5 plots the evolution of the initial Hill's vortex experiment in a stratified fluid (Num Sim. N3 ($\Delta\rho = 0.01$). Plots have been output at $\frac{t}{\tau_{adv}} = \{0, 2.14, 4.29, 6.43, 8.57, 10.74\}$ where, in this case only, the output time has been scaled by the advective timescale ($\tau_{adv} = \frac{a}{U}$) for comparison with the vortex-ring visualizations of Chapter 4. Here, two isocontours of density ($\rho = \{-0.5, -0.95\}$) have been plotted in each panel (a) of figure 7.5. Panels (b) and (c) of figure 7.5 plot the (appropriately extended) vorticity and density field, respectively, on the $y = 0$ plane. It is worth noting that the three-dimensional structure of the initial Hills-vortex interaction is not visually similar to the structure observed in Chapter 4. There are a number of potential reasons for this discrepancy. In particular, Hill's vortex rings do not have a small aspect ratio, which will affect the growth rate of the instability. We do not continue this discussion here.

For the fourth set of simulations (N4), a different initial condition was used to assess the dependence of the results on the ring aspect ratio (core size/ring diameter). Similar to Archer *et al.* (2009), a vorticity distribution was initialized into the numerical solver (we used an azimuthally rotated shielded dipole) that, when time evolved, produced a coherent vortex ring. This resultant non-spherical vortex ring was then used as the initial condition for the numerical mixing experiments. Fitting the vortex core to a Gaussian distribution, we estimate the aspect ratio of this vortex ring to be 0.17. In the physical experiments, the vortex rings had an aspect ratio of ≈ 0.1.

Similar to the model setup, the simulations were run by generating vortex rings that interact with the stratification. The flow was then evolved until the velocity field dissipated sufficiently. After a delay (τ), a new vortex was superimposed onto the residual velocity field. This cycle was repeated until the desired number of iterations was achieved. We set the end time to be 100 vortex rings. Thirteen different parameter cases (requiring 1300 simulations) were performed for various Reynolds and Richardson numbers, the details of which can be found in table 7.1. As with the experimental results of Chapter 6 and the model results above, there is an initial setup period, within which the functional form of the stratification varies. After this setup period, the stratification tends to a self-similar form and the mixing rate is nearly constant, which is the value reported.

Figure 7.6(a) plots the evolution of the distribution of energy into its various compartments for the first vortex ring of one numerical simulation (N3: Re = 3500, Ri = 2.75). This figure is reminiscent of figure 7.4 from the model results. In particular, note that the time dependence of the mixing (M) and the total dissipation (D) are similar to those found previously, though their relative values are different. Unlike the model work, the numerical simulations explicitly support the generation of APE. Associated with this APE is the generation of internal waves that manifest as oscillations between the APE and the kinetic energy (KE). Figure 7.6(b) plots the relative energy distribution prior to the generation of a new vortex ring, for all vortex ring generations. This plot quantifies the incremental change to the mixing rate of each subsequent vortex ring. Both panels (a)-(b) have been normalized by the vortex-ring energy (E) and the interval τ between vortex rings for comparison with the model results. Typical net total energy loss at time $t = \tau$ is 5×10^{-3}. Due to the late-time exponential decay of the internal waves generated, there will always be some residual energy ($\mathrm{RE} = \mathrm{KE} + \mathrm{APE}$ at $t = \tau$) in the system prior to subsequent vortex ring generations. As there is a practical limitation on the length of each numerical simulation, we terminated the simulations when $\frac{\mathrm{RE}}{\mathrm{KE}_{ring}} = O(10\%)$. The physical experiments also have RE, though it is much less than that of the numerical experiments, as we can wait longer between vortex ring generations at almost no cost. As this residual energy remains nearly constant with subsequent vortex ring generations, the RE will have a small, near constant, contribution to the increase in BPE of the system, when compared to the mean mixing rate of each vortex ring. As mentioned above, these simulations demonstrate an initialization period, after which the change in potential energy of the system is near constant. Figure 7.6(c) plots the sorted density profile every 20 vortex ring generations. Note the similarity between Figure 7.6(b) and Figure 7.3(c).

7.5 Discussion

For each experiment, we compute the ratio of the change in background potential energy (ΔBPE) between successive vortex rings ($\Delta t = \tau$) versus the energy of the input vortex ring (KE_{ring}). We define this ratio as the mixing efficiency (η), indicating the amount of background potential energy change for a given energy input. This definition of the mixing efficiency is unambiguous where RE=0. Where RE$\neq$ 0, provided that the RE is constant between vortex ring generations, the associated mixing will also be constant and the interpretation of the mixing efficiency remains well defined. The RE will have a small positive contribution to η. The mixing efficiency is then computed as

$$\eta = \frac{\Delta\mathrm{BPE} - \Delta\mathrm{PE}_\kappa}{\mathrm{KE}_{ring}}, \quad \text{where} \quad \Delta\mathrm{BPE} = gA\rho_0\Delta\rho a^2 \int \left[\rho_s^{n+1} - \rho_s^n\right] z dz. \tag{7.14}$$

Here, ρ_s^n is the sorted density profile after n vortex ring generations. The change in potential energy is corrected for the diffusive increase in potential energy ($\Delta\mathrm{PE}_\kappa = gA\kappa\tau\,(\rho(0) - \rho(L))$) as we are interested only in the contribution due to the vortex ring.

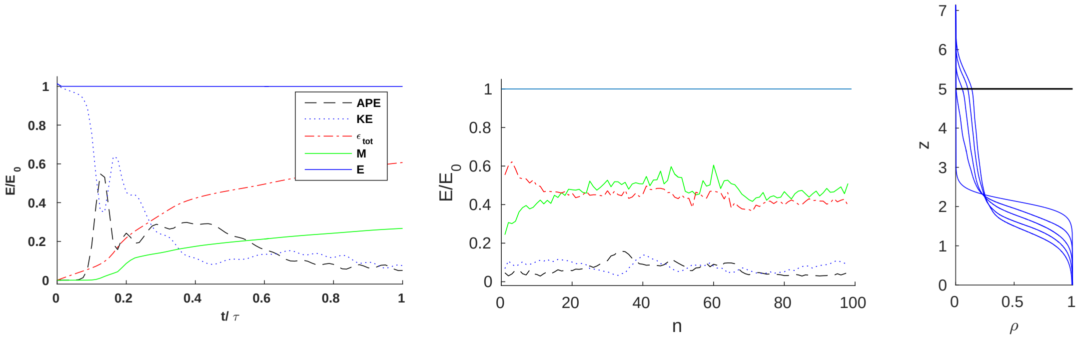

(a) (b) (c)

Fig. 7.6 (a) Plot of the energy partition for the first vortex ring interaction of Num. Exp. N3. Note that the KE is initially slightly above 1 as a result of the initial perturbation. (b) Plot of the energy partition at the end of each subsequent n vortex ring interactions. (c) Plot of the sorted density profile every twenty vortex ring generations. A solid line is drawn at $z = z_0$.

We briefly demonstrate the dependence of the mixing efficiency on the model parameters. Here, each parameter ($\{\alpha, \beta, \gamma, \lambda\}$) was independently varied from $0.5 - 1.5$ at an interval of 0.1. For each parameter value, simulations of Model Exp. M1 were run with $N = 100$ and $\Delta\rho = 0.01$. The final value of the mixing efficiency was plotted in the corresponding panel of figure 7.7. We observe that for the range of values considered here, α and λ do not affect the mixing efficiency, which does depend (nearly) quadratically on β and γ. This is consistent with Balmforth *et al.* (1998)'s analysis, who showed that, in that formulation, their three free parameters could be reduced such that the problem depends only on α and the product $\beta\gamma$. A more demanding parameter tuning is left for future work.

Comparing the model, numerical and physical experiments, figure 7.8 plots the mixing efficiency determined for all cases identified in table 7.1. In this plot, the mixing efficiency is near constant with Ri. Error bars are computed as the root mean squared error from the associated mean mixing efficiency value, once the system has completed its initial setup period. We observe that the mixing efficiency of the numerical experiments ($\eta_N \approx 0.45$) is slightly higher than the physical ($\eta_0 \approx 0.42$), salt-water experiments, as would be expected from the lower Sc. The mixing efficiencies found in the model work are consistently higher still ($\eta_M \approx 0.49$) than the numerical or physical experiments, though it is still within the experimental uncertainty of the physical experiments. As we have noted previously, this value of the mixing efficiency will be affected by our choice of parameters. With regards to figure 7.7, an increase in the parameter β by $\sim 15\%$ would account for the difference between the experimental value of the mixing efficiency and the model runs.

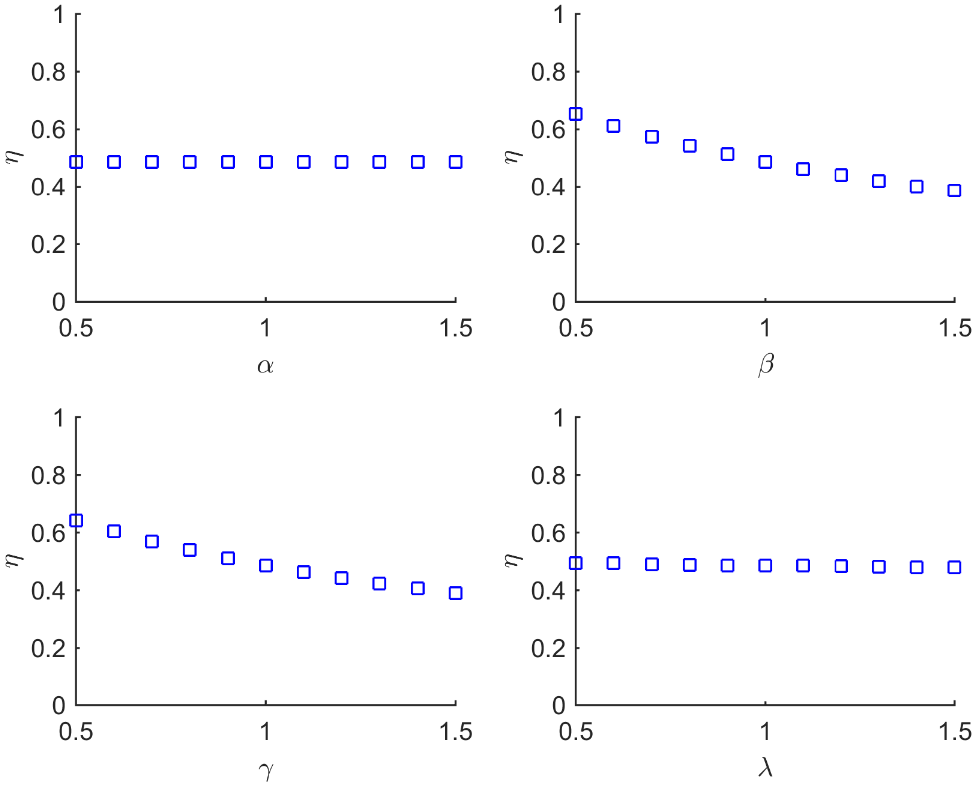

Fig. 7.7 The dependence of the mixing efficiency on the model parameters $\{\alpha, \beta, \gamma, \lambda\}$.

As the Richardson number decreases below O(1), the mixing efficiency dependence on Ri becomes more ambiguous. Indeed, recent work by Shrinivas & Hunt (2015) has indicated that the vertical confinement of turbulent mixing may change the mixing efficiency dependence on Ri. This confinement will be especially pronounced at low Ri due to the deep penetration of the vortex rings into the lower layer. The confinement is entirely omitted in the model work due to its 1D construction. As the effect of confinement will affect the three-dimensional structure of the flow, one might initially model it by modifying the propagation speed of the vortex rings U near the boundaries. We do not attempt this here.

Finally, the high mixing efficiency observed is partially a result of the definition. The mixing efficiency is defined as an aggregate, time-independent quantity. That is, the net fluid mixing that results from a given energy input. However, this definition does suggest that vortex rings are effective mixers as they are able to transport energy directly to the density interface, produce APE and subsequently create TKE. This series of events enables a vortex ring to create a near optimal mixing state such that nearly all of the vortex ring energy is transported directly to the location of peak mixing. The model work, which is a simplification of the vortex ring system, emphasizes this picture by generating TKE where the density field is not constant; where the TKE is able to mix the stratification.

This chapter presents a model for isolated vortex-ring-induced stratified mixing experiments. This work has been shown to provide qualitative and quantitative agreement with both physical experiments and numerical simulations. At moderate Ri, the mixing efficiency of the vortex rings has been shown, in all three methodologies, to be near constant after an initialization period with very similar asymptotic values. This simplified model highlights the essential features of the vortex-ring mixing experiments. Future work will investigate the application of this model to a mixing box experiment.

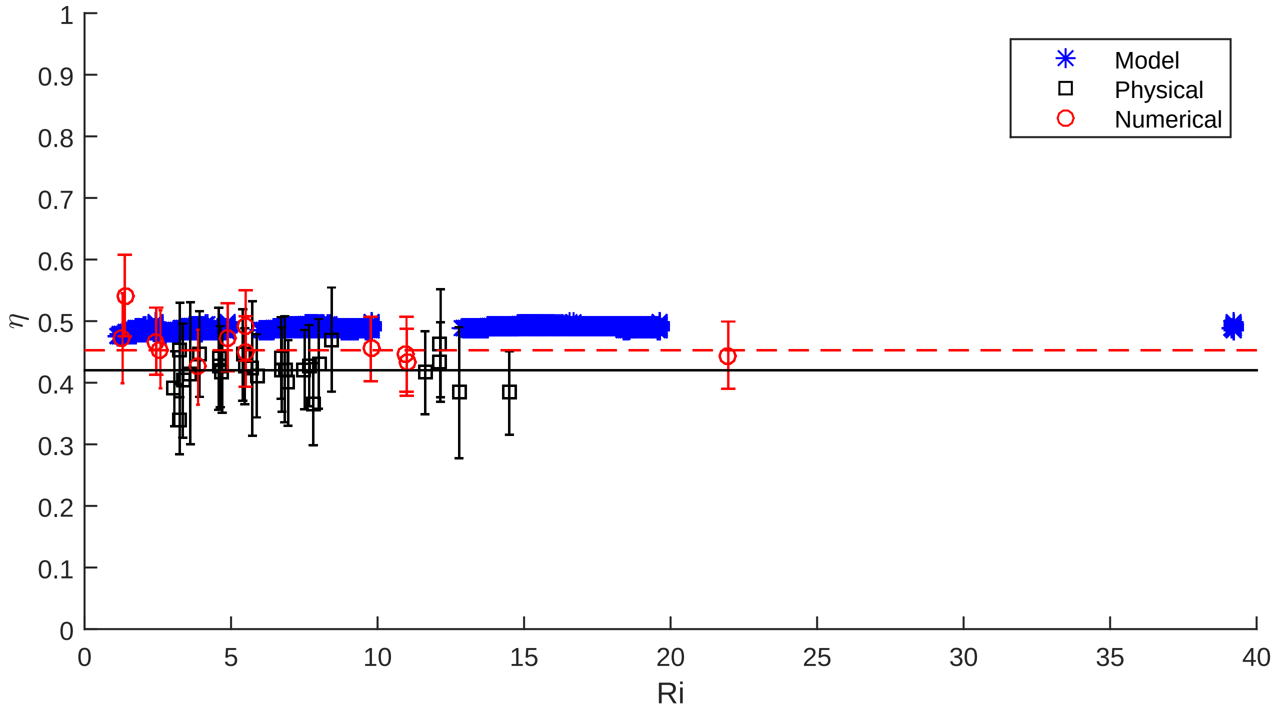

Fig. 7.8 Mixing efficiency as a function of Richardson number for the physical, numerical, and model experiments found in table 7.1. The black solid line corresponds to the mean mixing efficiency of the physical experiments ($\eta_0 = 0.42$). The dashed red line is the estimated mixing efficiency of the numerical experiments ($\eta_N = 0.45$).

Plate 7: Numerical simulation of the vortex-ring interaction initialized with the velocity ensemble of Chapter 4. Here, the vortex ring is highlighted in blue, the secondary vorticity is plotted in red, and isosurfaces of the density field are provided in green.

Chapter 8

Conclusions

> Never work on anything for longer than five years.
> Any progress you were going to make would have
> happened by then.
>
> —James Lighthill, as recounted by Paul Linden

Now that we have reached the end, we draw conclusions about this thesis as a whole. We will briefly summarize the major results found above, in §8.1. We will then interpret these results as a whole, in §8.2. Finally, in §8.3, we will make some final statements as we draw this thesis to a close.

8.1 Thesis summary

In this thesis, we have analyzed the dynamics and mechanics of vortex rings impacting onto a sharply stratified interface. We have used a combination of experimental, numerical and theoretical methodologies to analyze the key dynamical features of the vortex-ring interaction at moderate Richardson numbers. In particular, we have highlighted that the two-dimensional dynamics of the interaction are predominantly controlled by the bulk Richardson number of the flow. In contrast, the mode number of the dominant three-dimensional instability is controlled by the Reynolds number of the vortex ring. This three-dimensional azimuthal instability has been identified as a Crow-like instability. Further, by numerically evolving the density field, we have computed the associated vertical buoyancy flux and have argued, based upon its observed vertical asymmetry, that the vortex rings will sharpen density interfaces.

Azimuthal perturbations to an otherwise axisymmetric system will increase the total density gradient, and hence enhance the mixing of the stratification. We have shown that a three-dimensional instability does develop in the stratified vortex-ring system. As the vortex ring impacts the density interface, the baroclinic torque produces secondary vorticity through the baroclinic-vorticity-transfer (BVT) mechanism discussed in Chapter 4. At the early stages of the vortex-ring interaction (after the development of secondary vorticity, but prior to the development of the azimuthal instability), the flow has been shown to be largely two-dimensional, and little mixing is observed to have occurred. This is similar to the work of Patterson *et al.* (2006) who considered a Kelvin-Helmholtz instability, and noted that in one case (Experiment A), there existed a discernible delay between the production of APE and the initiation of mixing. In our system, we have identified the dominant instability, in Chapter 4, as a Crow-like instability, which grows more rapidly on the secondary vorticity field. As the fastest growing instability, it is reasonable to suggest that its growth mechanism will control the production rate of turbulent kinetic energy necessary to mix the background stratification. It is significant (see below) that the Crow-like instability has a growth-rate proportional to Ri. Note that, in this thesis, the vortex rings are generated sufficiently close to the density interface that the unstratified instability does not dominate the interaction. The Widnall instability, which will grow for an unstratified vortex ring, does not grow to large amplitude prior to impacting the stratified interface.

By generating many such vortex-ring interactions, we demonstrate that the density interface does indeed sharpen. In fact, the density profile tends to a nearly self-similar form. We have observed, in Chapter 6, that the mixing efficiency of such a system is constant and that the vortex-ring-induced mixing efficiency is very high. By developing a 1D turbulence model, we have shown that this constant mixing efficiency regime does not appear to be strongly dependent on the Schmidt number. Thus, the conceptualization of this work can be summarized in Figure 8.1. The incoming vortex ring impacts the density interface, which produces secondary vorticity through the BVT. The secondary vorticity is unstable to a Crow-like instability, allowing for the development of turbulent mixing, and the subsequent sharpening of the density interface. Many such vortex-ring interactions lead to the development of a (nearly) self-similar system.

8.2 ‘Big Picture’

Many of the observed features of the vortex-ring system are reminiscent of stratified turbulence. For example, the formation of layers has been observed in a variety of turbulent mixing contexts, from towed grids in a stratified environment (Holford & Linden, 1999) to stratified Taylor-Couette flow (Oglethorpe *et al.*, 2013). Associated with this layer formation is the possibility that the turbulent system will become, in some sense, self-similar in time. This self-similarity has been observed in Moore & Long (1971) for a stratified shearing flow, and,

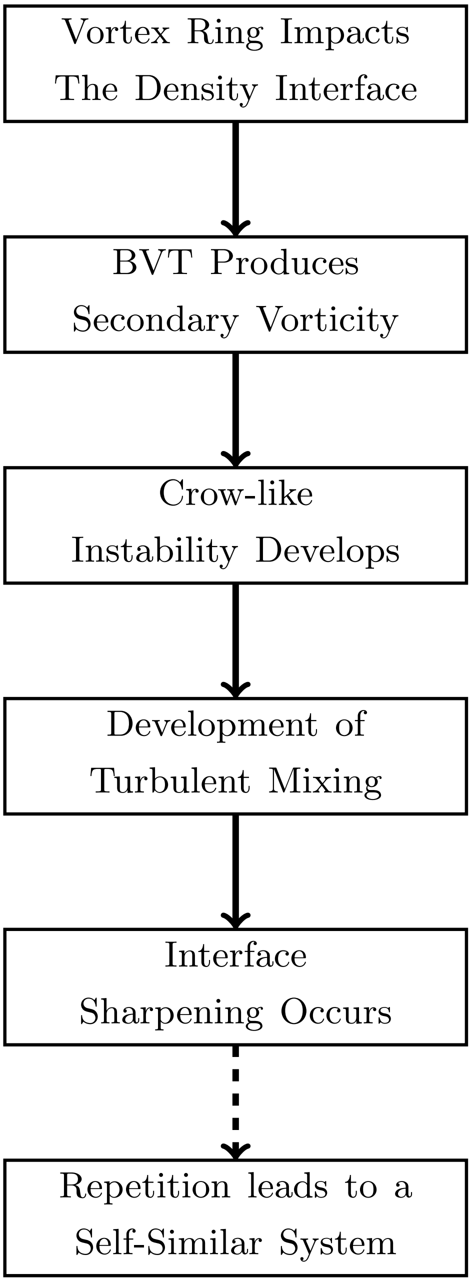

Fig. 8.1 Progression of the vortex-ring system

in Park *et al.* (1994) for a horizontally moving vertical rod in a stratified tank. Each of these experiments (Holford & Linden, 1999; Moore & Long, 1971; Oglethorpe *et al.*, 2013; Park *et al.*, 1994) and others (Higginson, 2001) have demonstrated a constant mixing efficiency regime for some range of Richardson numbers. These results suggest that the vortex-ring experiments discussed in this thesis are qualitatively similar to certain stratified-turbulence mixing experiments. Thus, where the vortex-ring/turbulent-eddy analogy is valid, we can make certain conjectures about the evolution of the density field in a stratified turbulent context, based upon the results found in this thesis.

To that end, figure 8.2(a) plots a representation, as suggested by the results found in this thesis, of the growth rates (σ) of three dominant instabilities for the vortex-ring system. The three instabilities listed are the unstratified Widnall instability, a stratified elliptic instability, and the Crow-like instability. The rate of interface recovery has also been plotted. This representative plot emphasizes when each instability is expected to be observed. In an unstratified tank, the unstratified Widnall instability will be the dominant instability for the vortex ring. In this thesis, we have demonstrated that a Crow-like instability will be the dominant instability mechanism above some critical Richardson number ($\mathrm{Ri} > \mathrm{Ri}_c$). For a stratified fluid with $\mathrm{Ri} < \mathrm{Ri}_c$, Nomura *et al.* (2006) and Ortiz *et al.* (2015) have, in the context of a vortex pair evolving in a linearly stratified fluid, predicted that the dominant instability will be Elliptic-like. Due to the close similarity between the instabilities observed for vortex filaments and vortex rings, we suggest that a similar instability will be observed for vortex rings. More work needs to be done to characterize the vortex-ring-induced mixing at low Richardson numbers. This conceptualization (Figure 8.2(a)) is not meant to suggest that these are the only instabilities that will develop in the system, but this highlights that for $\mathrm{Ri} < \mathrm{Ri}_c$, the Crow-like instability is predicted to be subdominant, and thus the associated buoyancy flux will diverge from that discussed in Chapter 5. This work suggests that, as the self-similarity of the system depends on the Crow-like instability (an instability that grows at a rate proportional to Ri), no stratified turbulence experiment, in which the vortex-ring/turbulent-eddy analogy is valid, can maintain a self-similar form for $\mathrm{Ri} \lesssim \mathrm{Ri}_c$ (assuming that the bulk Richardson number is appropriately defined). The previously cited papers (Higginson, 2001; Holford & Linden, 1999; Moore & Long, 1971; Park *et al.*, 1994) support this conclusion. The loss of self-similar form may result in an increase (Oglethorpe *et al.*, 2013) or decrease (Higginson, 2001) in the vertical buoyancy flux.

It is worth noting that the linear instabilities in a linear stratification (or highly diffuse interface) may be different from the ones observed here. However, as noted in Chapters 6 and 7, successive vortex ring generations will sharpen density interfaces and the system will become (provided that the density difference across the domain is large enough) sharply

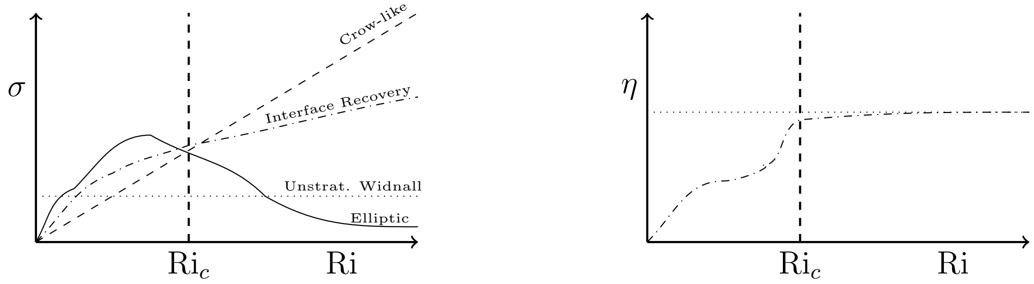

(a)

(b)

Fig. 8.2 Conjectured growth rates (a) and mixing efficiency (b) for the vortex-ring-induced mixing system.

stratified. Similarly, the orientation of the vortex rings relative to the density gradient may also modify the observed instability. The work of Atta & Hopfinger (1989) and Scase (2003) have studied vortex rings traveling transversely through a linear stratification and do not observe the Crow-like instability found in this thesis. This should not be surprising as the BVT mechanism, and hence the instability mechanism, does not occur in the same manner. A recent investigation by Benjamin Jackson (personal communication) has shown that a vortex ring impacting a sharp density interface at a small oblique angle to the density gradient is “self-correcting”. That is, the vortex ring will rotate such that its propagation axis aligns with the density gradient, as it approaches the interface. Certainly more work is required, but this suggests that the results found in this thesis are not sensitive to small perturbations to the angle of incidence of the vortex rings.

Figure 8.2(b) presents a simplification of the conjectured mixing efficiency as a function of the bulk Richardson number. That is, as we have shown in this thesis, for $\mathrm{Ri} > \mathrm{Ri}_c$ the mixing efficiency of the system is near constant. Below this critical Richardson number, other instability mechanisms will be dominant, and the mixing efficiency will drop (possibly non-monotonically) with Richardson number, as suggested in Chapter 6. As these other instabilities are not captured by the 1D turbulence model of Chapter 7, we do not expect the turbulence model to accurately predict the mixing efficiency below Ri_c. We note that at very high Richardson numbers, there may also be new physics at play. In this limit, the kinetic energy of the vortex ring is negligible compared to the potential energy of the stratification, implying that the isosurfaces of density will not be displaced, preventing the production of secondary vorticity. Thus, in this limit, the mixing efficiency is zero. It is not clear how this will manifest in physical vortex-ring experiments at high Richardson number, or whether this limit is singular.

In light of this mixing efficiency prediction, we briefly return to Turner's mixing box experiment. In this experiment, a vertically oscillating grid will mix a stratification. The resulting eddies within the turbulent flow will have an associated timescale, determined by the frequency of grid oscillations, and a length scale, associated with the grid spacing. A second length scale also exists related to the amplitude of the vertical grid motion. After the system has established a two-layer profile with an interface sufficiently far from the oscillating grid, the bulk Richardson number of the turbulent eddies within the flow will be greater than one. If the eddy analogy proposed by this thesis is valid, then this thesis suggests that, as the mixing efficiency is constant, then the distribution of parameters associated with these eddies will not affect the amount of mixing observed. That is, simply determining the total kinetic energy of all of the turbulent eddies impacting the density interface would be sufficient to predict the total amount of mixing observed. Now, this vortex-ring/turbulent-eddy analogy also assumes that each of these eddies will mix the fluid independently. More work needs to be done to understand how eddies impacting a stratified interface will interact.

The prediction of a constant mixing efficiency is in direct contrast to the work of Linden (1973). In Linden's theory, the entrainment rate (u_e) of the vortex ring should scale as

$$\frac{u_e}{U} \sim \frac{1}{\tau_{ND}} \frac{1}{\mathrm{Ri}^2}.$$

In this expression, τ_{ND} is the non-dimensionalized rate at which the turbulent kinetic energy is made available to mix the fluid. Linden suggested that if $\tau_{ND} = \tau_B$, where τ_B is the timescale of a purely buoyancy driven (wave-like) response to the interface deflection, then $\tau_{ND} \sim \mathrm{Ri}^{-\frac{1}{2}}$. Linden's theory suggests that

$$\frac{u_e}{U} \sim \mathrm{Ri}^{-\frac{3}{2}}.$$

We have shown in Chapter 4 that, at least for the timescale of secondary vorticity production, $\tau_D \sim \mathrm{Ri}^{-\frac{1}{3}}$, which (if $\tau_{ND} = \tau_D$) suggests a different scaling for the entrainment rate, but still a non-constant mixing efficiency. However, we have shown that the timescale of the Crow-like instability found in Chapter 4 is $\tau_{Crow-like} \sim \mathrm{Ri}^{-1}$. As this is arguably a better estimate for the rate at which the turbulent kinetic energy is produced, this suggests that

$$\frac{u_e}{U} \sim \mathrm{Ri}^{-1},$$

which implies that the modified Linden theory predicts a constant mixing efficiency. This instability timescale is built into the vortex-ring breakdown parameterization ($\mathbb{I}_M$) for the 1D model of Chapter 7, which also predicts a constant mixing efficiency regime.

The most surprising result from this thesis is the numerical value of the mixing efficiency for the vortex rings ($\eta_0 = 0.42$). This result was very surprising to the author, who verified this value of the mixing efficiency in a number of different ways (see Appendix C for an alternative estimate of the mixing efficiency from that of Chapter 6). However, this thesis also reveals why the mixing efficiency of these vortex rings is high. Vortex rings are capable of transporting kinetic energy directly to the interface with minimal dissipation, compared to a fully developed turbulent flow that relies on turbulent diffusion to propagate the turbulent kinetic energy (TKE). Once the vortex ring impacts the density interface, available potential energy (APE) is produced. Only after this APE is produced, does the system become unstable, producing turbulence directly at the point where it is capable of producing the most mixing. In addition, the BVT also deposits vorticity at the location of the density interface, where the mixing will occur. This is similar to the less efficient Kelvin-Helmholtz instability, in which coupled streamwise perturbations in a shear layer, roll-up producing a ‘billow’, stirring the surrounding fluid. However, the BVT mechanism is suggested to be more efficient at generating vorticity as it relies on a baroclinic torque, rather than a linear instability of the system. The overlap of vorticity with the density interface, along with the generation of APE and TKE, will result in an effective mixing mechanism. This view is supported by Leclercq *et al.* (2016), who argue that purely chaotic motion will decrease the mixing efficiency of a stratified Taylor-Couette flow, suggesting instead that spiral coherent structures were the most effective mixers. This conclusion agrees with the observations, found here, that the coherent vortex ring will induce more mixing than purely chaotic motion. Indeed, Chapter 5 has argued that the positive component of the vertical buoyancy flux is associated with the larger length scales in the flow. This suggests that the efficiency of generating APE in the system may play a role in determining the total mixing efficiency of the system, in combination to the turbulent induced mixing. More work needs to be done to study the optimal APE/TKE mixing mechanism.

In Chapter 1, we introduced Turner’s concept of internal versus external mixing. We return to this distinction in light of the results of this thesis (particularly Chapter 4). It is true that the vortex rings are produced external to the density interface, where mixing will occur. However, the majority of the mixing will only occur once the Crow-like instability develops and the system becomes turbulent. The generation of this instability occurs at the location of the density interface. Thus, defining this mixing mechanism as internal or external is ambiguous. However, what is clear is that the input energy is kinetic energy, as opposed to available potential energy. The distinction of mixing experiments according to their input of kinetic or available potential energy was proposed by Tailleux (2009). This may prove to be a more interesting distinction as it does clarify the present experiments. This definition also avoids the ambiguity of the mixing “location.” Yet, this definition does not account for the asymmetry of the mixing mechanism. That is, the vortex rings propagate towards one side the density interface, and the interface deflection is not symmetric with respect to the generation point of the vortex rings. A new categorization of stratified mixing experiments must encompass this directionality. Thus, the work of this thesis relates to asymmetric (relative to the density interface) kinetic energy produced turbulent mixing. Turner’s mixing box fits well into this definition. Conversely, a Rayleigh-Taylor experiment would be an example of symmetric APE produced mixing.

8.3 Final word

The objective of this thesis was to study vortex rings as they impact a stratified interface, in order to estimate the mixing efficiency of fully-developed stratified-turbulence experiments. As we have highlighted here, we have developed a solid understanding of the vortex-ring system. However, we have not yet drawn a direct application of this work to a stratified turbulent flow. Preliminary work (not shown in this thesis) has begun to study an experiment, similar to Turner’s mixing box experiment, in light of these new developments. The extent to which the conclusions drawn in this thesis apply to the stratified turbulent context remains to be seen. However, as we have argued above, many similarities exist between the vortex-ring system studied here and stratified-turbulent mixing experiments.

In terms of the vortex-ring system itself, more work needs to be done to expand upon the study of the stratification induced instabilities. Using a data-assimilation method, future work will expand the experimental analysis of Chapter 4 in both Richardson number range, and in the details of the instability development. Similarly, it would be worth comparing the Crow-like instability found here and the linear optimal instability of the system (see Kaminski *et al.* (2014)). Finally, it remains to be seen how the aspect ratio of the vortex rings (the ratio of the vortex-ring diameter to its core-width), affects the vortex ring instabilities.

The stratified vortex-ring system remains a largely unexplored area of study. Clearly more research needs to be performed to fully characterize this system. We choose to end this discussion here, as it presents both a mechanical and dynamical description of the vortex-ring system at moderate Richardson number.

> Maybe for someone like Lighthill you can do that.
> For the rest of us mortals, it takes a lot longer than five years.
>
> —Paul Linden

Appendix A

Conductivity probe calibration

In this appendix, we describe the calibration procedure used for the conductivity probe. The conductivity probe itself is described in Chapter 3. The calibration relied on a set of density samples with different salinity and temperature values. By measuring the temperature through a thermistor, and the voltage from the conductivity probe, we use an inversion method to determine the density of the fluid surrounding the tip of the conductivity probe.

A.1 Conductivity probe calibration proceedure

By mixing salt and fresh water, we created a calibration fluid (CF) of a given density. We measured the density of this CF using a density meter (Anton Paar DMA 5000) with an error of $\pm 1 \times 10^{-6}$ g cm^{-3}. This CF was then divided into two containers, one to be cooled, and one to be heated. We then filled two water baths, one with cold water and one with hot water. We placed one of the CF containers into each bath. As the cooling/heating time was short ($\sim$ 1 hour), we assumed that the salinity change due to evaporation of the CF was negligible.

In order to measure the temperature of the fluid near the probe tip, a thermistor was attached to the conductivity probe. The thermistor was set to output a 0-10V signal corresponding to a temperature range of approximately 15 °C and 25 °C. The density calibration was performed using the output thermistor voltage. As such, it was unnecessary to calibrate the thermistor in Celsius (i.e. temperature units).

Once the cold CF was lowered to a temperature below 15 °C, it was placed beneath the probe and the measurements began. The hot CF was then slowly dripped into the cold CF to slowly raise its temperature until the thermistor output measured 10V. This process was repeated for several density samples. Physical perturbations (hand mixing of the fluid) of the CF ensured a well-mixed, homogeneous temperature fluid.

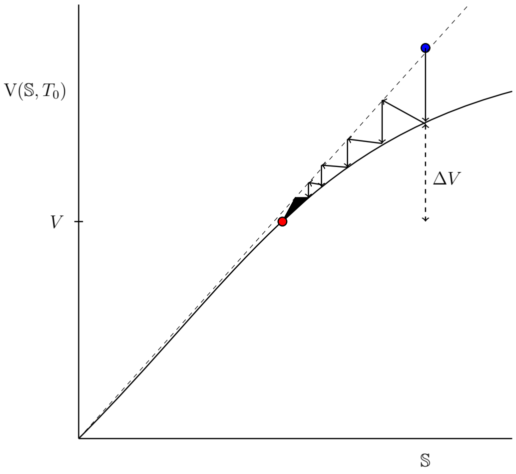

Fig. A.1 Diagram of the iterative solving process for initial density guess (blue) to the solution(red) for a fixed temperature T_0. The value of the measured voltage (V) is indicated along with a representative calibration (solid line).

The conductivity probe was sampled at a rate of 5000Hz. Each Voltage measurement was recorded over a period of 2s. The probe and temperature Voltages were then sorted and the top and bottom forty percent of the data was discarded. The remaining fortieth to sixtieth percentiles were averaged and the measurement was recorded. This oversampling methodology was used to attempt to reduce the noise of the calibration signal by removing any spurious measurement values.

Once a sufficient number of temperature curves had been recorded, near constant temperature (point) density samples were then measured. Each sample was placed under the probe and approximately 50 point measurements were recorded.

A.2 Calibration fit

If we assume that the Voltage (V) of the conductivity probe depends on the salinity ($\mathbb{S}$) of the surrounding fluid and the fluid temperature (T), then we can Taylor series expand the voltage function as

$$\begin{aligned} V(\mathbb{S},T) =& V(\mathbb{S}_0,T_0) + \partial_{\mathbb{S}} V(\mathbb{S}_0,T_0)(\mathbb{S}-\mathbb{S}_0) \\ & + \partial_T V(\mathbb{S}_0,T_0)(T-T_0) + \ldots \end{aligned}$$

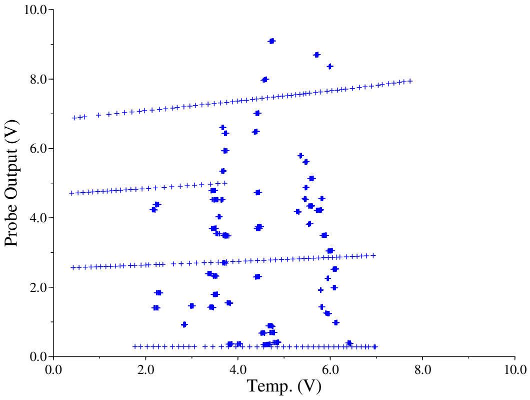

Fig. A.2 Plot of the various probe measurements vs thermistor output for density samples of a known salinity. All data was collected in voltage.

We truncate this series to fourth order. However, we are interested in the salinity as a function of voltage and temperature and hence we need to invert this function for $\mathbb{S}$. We do this using an iterative method for salinity by making an initial salinity estimate and then correcting until the error between iterations is arbitrarily small.

Given known quantities V_M, T, we assume an initial salinity estimate $\mathbb{S}'_0$. Given this, we find the associated voltage

$$V' = V(\mathbb{S}', T).$$

We assume a refinement criterion where V depends linearly on $\mathbb{S}$. In such a case,

$$\mathbb{S}'_{n+1} - \mathbb{S}'_n = a\frac{\Delta V}{2},$$

where $\Delta V = V' - V_M$. Based upon previous work, and experimental evidence, we know that V is monotonic in $\mathbb{S}$. Hence, the choice of a is arbitrary up to the correct sign, and that

$$\frac{\text{Range of } \mathbb{S}}{\text{Range of } V} < \frac{a}{2},$$

to ensure that the linear curve spans the Range of $\mathbb{S}$. A better choice of a will potentially help the iteration process converge faster. In our case, as the probe output has a range of 10V, over a density difference of ≈ 0.1 g/cm^3, here we pick $a = 0.01$ g/cm^3/V. Figure A.1 plots a schematic of the iteration process. We end the iteration process when the difference between successive iterations is less than 1×10^{-9} g/cm^3.

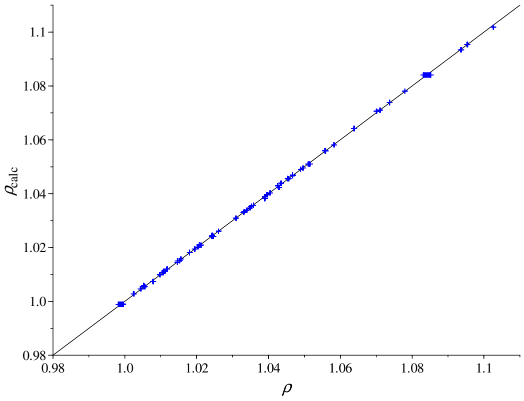

Fig. A.3 Plot of the computed vs measured density values. Standard deviations of the computed values from the measured is 2.88×10^{-4} g cm^{-3}.

A.3 Calibration results

The calibration curves that were deemed fit for use are plotted in figure A.2 along with many point density measurements. All of these data points were used in the calibration fit.

In order to evaluate how well the calibration curve is fitting the data, figure A.3 plots the computed density of each calibration point versus its measured density. A linear line (solid line plotted) represents perfect agreement. This graph demonstrates a reasonable agreement between computed and measured density values with a standard deviation of 2.9×10^{-4} g cm^{-3}. This represents a error of 0.26% of the density range. However, this error is substantially greater than the error reported by Davies Wykes & Dalziel (2014) (which was 2×10^{-5} g/cm^3 over a smaller density range) for a similar device. Evaluation of a similar methodology to their work did not show a significant improvement in the error.

Appendix B

Numerical methods used to compute the evolution of the density field

B.1 Lagrangian particle advector

As a first attempt to understand how vortex rings mix the stratification, we simulate the advection of Lagrangian particles. Lagrangian particles are massless tracer particles that simply advect with the flow. The position of each particle ($\mathbf{p}_i$, $i = \{1...N_p\}$) is given:

$$\frac{d}{dt}\mathbf{p}_i = \mathbf{u_p}, \qquad \mathbf{p}_i(t) = \mathbf{p}_i(t = t_0) + \int_{t_0}^{t} \mathbf{u_p} dt, \tag{B.1}$$

where $\mathbf{u_p} = \mathbf{u}(\mathbf{x} = \mathbf{p}(t), t)$ is the fluid velocity at the location of the particle. Boldfaced variables denote vector quantities. Unlike the velocity field measurements of Chapter 4, the Lagrangian particles are not confined to a spatial grid (lattice). As such, we need to overcome the limitations of the spatial and temporal discretization of the velocity ensemble.

B.1.1 Spatial discretization

In general, the location of each Lagrangian particle ($\mathbf{p}_i$) will not coincide with the location of the ensemble's velocity field nodes. Thus, it is necessary to spatially interpolate the velocity field in order to accurately estimate $\mathbf{u_p}$. We do this using a simple linear interpolation based upon the eight velocity node points that encompass the particle. Each particle position, relative to these nodal coordinates, is given $\tilde{\mathbf{p}}_i = (x_{p,i}, y_{p,i}, z_{p,i})$. Figure B.1 plots a diagram of the particle position relative to the enclosing velocity nodes. The interpolation scheme first linearly interpolates along the z-axis, then along the y-axis before interpolating along the

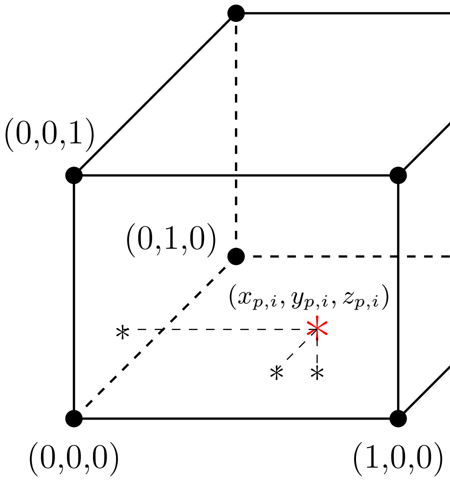

Fig. B.1 Diagram of the particle position within the enclosing velocity nodes. Axes have been normalized for convenience.

x-axis (the order is insignificant). That is,

$$\mathbf{u}_z^1 = \mathbf{u}(0,0,0)z_{p,i} + \mathbf{u}(0,0,1)(1-z_{p,i}), \qquad \mathbf{u}_z^2 = \mathbf{u}(0,1,0)z_{p,i} + \mathbf{u}(0,1,1)(1-z_{p,i}), \tag{B.2}$$

$$\mathbf{u}_z^3 = \mathbf{u}(1,0,1)z_{p,i} + \mathbf{u}(1,0,1)(1-z_{p,i}), \qquad \mathbf{u}_z^4 = \mathbf{u}(1,1,0)z_{p,i} + \mathbf{u}(1,1,1)(1-z_{p,i}), \tag{B.3}$$

$$\mathbf{u}_y^1 = \mathbf{u}_z^1 y_{p,i} + \mathbf{u}_z^2(1-y_{p,i}), \qquad \mathbf{u}_y^2 = \mathbf{u}_z^3 y_{p,i} + \mathbf{u}_z^4(1-y_{p,i}), \tag{B.4}$$

$$\mathbf{u_p} = \mathbf{u}_y^1 x_{p,i} + \mathbf{u}_y^2(1-x_{p,i}). \tag{B.5}$$

Note that in this description, the nodal coordinates of the grid points have been normalized. This linear interpolation will result in a first-order method. For the ensembles presented in this thesis, the error ($O(dx^2+dy^2+dz^2)$) will be dominated by dz, as it is the largest grid spacing. This method is also known as trilinear interpolation.

B.1.2 Temporal discretization

The time resolution of the velocity-field ensemble is also discrete. We will denote the velocity at time step n as $\mathbf{u}^n$. It is important to note that the discrete time step of the ensemble, $\Delta t = t^{n+1} - t^n$, will not necessarily satisfy the Courant-Friedrichs-Lewy (CFL) condition[1]. As such, each time interval Δt is divided into a series of non-uniform substeps $\{\varepsilon_i\}$. At each substep, a predictor-corrector method was used to temporally update the particle positions.

---

[1] $\frac{u\Delta t}{dx} < 1$.

Case	Ri	Re	μ (m)	σ (m)
1	0.98	1600	0.081	0.015
2	1.7	2400	0.060	0.0084
3	2.4	1600	0.036	0.0075

Table B.1 Table of the estimated interface parameters associated with the three ensemble cases.

Thus, at time step $n+\varepsilon_i$ (for i^{th} substep ε_i) the particle position $\mathbf{p}_i$ is predicted to be:

$$\hat{\mathbf{u}}_{\mathbf{p}}^{n+\varepsilon_i} = \mathbf{u_p}^n \varepsilon_i + \mathbf{u_p}^{n+1}(1-\varepsilon_i), \tag{B.6}$$

$$\mathbf{p}_i^* = \mathbf{p}_i^{n+\varepsilon_i} + \hat{\mathbf{u}}_{\mathbf{p}}^{n+\varepsilon_i} dt_\varepsilon, \tag{B.7}$$

$$\mathbf{p}_i^{n+\varepsilon_{i+1}} = \mathbf{p}_i^* + \hat{\mathbf{u}}_{\mathbf{p}}^{n+\varepsilon_{i+1}} dt_\varepsilon. \tag{B.8}$$

Here, dt_ε is the temporal spacing between substeps. The predictor-corrector (Improved Euler) method is second-order.

B.1.3 Interface parameter estimate

As described in Chapter 5, we use the Lagrangian particle advector to estimate the position and thickness of the density interface. We duplicate Table 5.1 here (see table B.1). We will use these estimates to define initial conditions for the density field solver described below.

B.2 Density field solver

Now that we have an estimate for the initial conditions associated with the density field, we can attempt to compute its evolution. In this section we describe the numerical implementation of the density field solver for the equation

$$\partial_t \rho + \mathbf{u} \cdot \nabla \rho = \kappa \nabla^2 \rho. \tag{B.9}$$

This equation will use the ensemble velocity field $\mathbf{u} = \mathbf{u}_E$ to integrate the evolution of the density field ρ. The constant κ is the coefficient of molecular diffusivity. As mentioned when discussing the particle advector, the time step of the ensemble will not be sufficient to meet the stability requirements of a numerical solver. Thus, temporal interpolation was required to ensure accuracy. A third-order pseudospectral advection-diffusion solver is

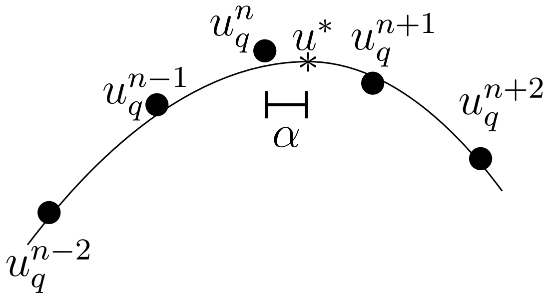

Fig. B.2 Diagram of the parabolic fit to the ensemble time steps u_q^n.

then implemented, incorporating the velocity field measurements from the temporally and spatially interpolated ensemble.

B.2.1 Temporal interpolation

For the density solver, we make the stringent time-stepping criterion (based upon the three-dimensional CFL condition) to be

$$\frac{\max\sqrt{u^2+v^2+w^2}}{\min\left(dx,dy,dz\right)}dt < \frac{1}{10}. \tag{B.10}$$

Here, u, v, w are the velocity components of the ensemble and dx, dy, dz are the physical grid spacings. The time spacing (Δt) of the ensemble is fixed and thus, in order to satisfy condition (B.10), this work will use a least-squares method to interpolate between ensemble time steps.

We begin the temporal interpolation by defining a vector $\vec{u}_q = \left(\ldots, u_q^{n-1}, u_q^n, u_q^{n+1}, \ldots\right)^T$ that is comprised of ensemble velocity data u^n at time-step n. The (^{T}) symbol denotes the transpose, and the index q refers to one specific data element (grid point) of u^n. In this implementation, we select $\vec{u}_q$ to comprise of five time steps. A quadratic fit was used between the elements of the vector $\vec{u}_q$. This fit allows us to estimate the velocity field at time steps between those of the ensemble. Figure B.2 plots a diagram of the fit to the ensemble time step u_q^n. We define the time matrix T and fit coefficients vector $\vec{c}$ as

$$T^n = \begin{pmatrix} 1 & t^{n-2} & \left(t^{n-2}\right)^2 \\ & \vdots & \\ 1 & t^{n+2} & \left(t^{n+2}\right)^2 \end{pmatrix}, \qquad \vec{c} = \begin{pmatrix} a \\ b \\ c \end{pmatrix}. \tag{B.11}$$

The elements of T^n depend on the ensemble output times t^n.

We want to interpolate the velocity field to a time t^*. We define the weight $\alpha = \frac{t^*-t^n}{t^{n+1}-t^n}$ such that $\alpha \in [0,1]$. This allows us to define the weighted inner product for the difference between the quadratic fit and ensemble time steps $\vec{u}_q$,

$$< (T^n\vec{c} - \vec{u}_p) \left| W \right| \left(T^n\vec{c} - \vec{u}_q \right) >, \qquad W = \begin{pmatrix} \alpha & 1 & 1 & 1 & (1-\alpha) \\ & & \vdots & & \\ \alpha & 1 & 1 & 1 & (1-\alpha) \end{pmatrix}$$

in bra-ket notation. This weighting function ensures that the interpolation function will be continuously defined as $t^* \to t_n$. Thus, the interpolated ensemble (u_p^*) at time $t = t^*$, which minimizes the least squares error, is computed as

$$u_p^* = T^* \left[(T^{n*} W T^n)^{-1} T^{n*} W \vec{u}_q \right]. \tag{B.12}$$

B.2.2 Spatial interpolation and differentiation

Spatial derivatives were computed using Fourier transforms. As a one-dimensional example, the Fourier transform along the x-axis is given:

$$\tilde{u}(k) = \mathrm{F}[u] = \frac{1}{\sqrt{2\pi}} \int_{x=-\infty}^{\infty} u(x) \exp[-ikx]\, dx, \tag{B.13}$$

$$u(x) = \mathrm{F}^{-1}[\tilde{u}] = \frac{1}{\sqrt{2\pi}} \int_{k=-\infty}^{\infty} \tilde{u}(k) \exp[ikx]\, dk. \tag{B.14}$$

As such, the derivatives can be computed as :

$$u_x = \mathrm{F}^{-1}[ik\mathrm{F}[u]]. \tag{B.15}$$

A direct extension applies for the y- and z-axes. In practice, Fast Fourier Transforms (FFTs) were used to compute the Fourier transforms on the discrete computational domain. Fourier methods are an example of the more generic category of spectral methods. Spectral methods are desirable as their associated discretization error decreases exponentially with the number of grid points. Fourier methods, in particular, assume a periodic grid. See Trefethen (2000) for more details.

As this numerical solver is envisioned to solve for the evolution of the density field within the domain of the ensemble, the periodicity of the Fourier transforms presents a challenge. We overcome this issue by reflecting the domain in the vertical direction. This enforces that the vertical derivative at the top and bottom boundary is zero. While technically incorrect boundary conditions, we argue that this is sufficient for the work presented here. The draw-back to this methodology is that it requires twice the number of vertical grid points ($2n_z$). A cosine transform would be more efficient at accomplishing the same transformation, but the Python packages used (the language in which the code was implemented) did not have the appropriate cosine transformations.

FFT methods also have the potential for spectral aliasing. We can limit this error by implementing a spectral filter (Subich *et al.*, 2013), written

$$\text{filter} = \begin{cases} 1 & K \leq K_M, \\ \exp\left[-\alpha\left(\frac{K-K_M}{1-K_M}\right)^{\beta}\right] & K > K_M. \end{cases} \tag{B.16}$$

The constants $\alpha = 20, \beta = 6$, and $K_M = 0.6$ are parameters of the filter. Here, the wavenumber K has been normalized.

For practical reasons, the vertical grid was interpolated, using a third-order spline, onto a $n_z = 64$ grid such that each dimensional of the ensemble grid ($n_x \times n_y \times n_z = 256 \times 256 \times 64$) is a power of 2. This is important for the efficiency of the Fourier transforms.

B.2.3 Time stepping and Startup

We now describe the time-stepping scheme used to evolve the density field. In this work, we implement a third-order implicit time-stepping method. This methodology is similar to the approach taken by Subich *et al.* (2013). The generic form of this method is written out as

$$\sum_{j=0}^{k} \alpha_j \rho^{n+1-j} = \mathbf{L}\{\rho^{n+1}\} + \sum_{j=0}^{k-1} \beta_j \mathbf{N}\{\rho^{n-j}\}. \tag{B.17}$$

The factor k is the order of the time stepping scheme. The terms **L** and **N** are the linear and nonlinear terms in equation (B.9), respectively. As a result of the time step condition (B.10), the time step between subsequent density outputs ρ^n, ρ^{n+1} will not be constant. Hence the values of α_j and β_j will vary at each time-step. The coefficients are given in compact form:

$$\alpha_0 = \sum_{i=1}^{k} \left(t^{n+1} - t^{n+1-i}\right)^{-1}, \tag{B.18}$$

$$\alpha_{i,i\neq 0} = \frac{1}{t^{n+1-1} - t^{n+1}} \prod_{j\neq\{i,0\}} \frac{t^{n+1} - t^{n+1-j}}{t^{n+1-i} - t^{n+1-j}}, \tag{B.19}$$

$$\beta_i = \prod_{j\neq i} \frac{t^{n+1} - t^{n-j}}{t^{n-i} - t^{n-j}}. \tag{B.20}$$

It can be shown (see Subich *et al.* (2013)) that the first- and second-order methods produced in this way are unstable for purely advective flow. The third-order method is conditionally stable. Thus, we use the third-order time-stepping scheme.

The third-order time-stepping scheme requires access to the two previous time-steps in order to evolve the current state. At startup, when no previous time-steps are available, an initialization methodology must be employed. One might naively set these past time-steps to be zero and proceed forward. This disjoint approach produces an unquantified error within the flow, which will be especially significant when initializing a case with a nontrivial velocity field. We use the next simplest implementation, which is to bootstrap the first two time-steps using the first, and then second-order methods. For time-step dt^* estimated from equation (B.10), we minimize the error of the startup by decreasing the initial time-steps such that each step is roughly third order in the CFL determined time-step, without decreasing to arbitrarily small time steps. Here,

$$dt^i = \begin{cases} \max\{\frac{(dt^*)^3}{4}, 1\times 10^{-8}\} & i \leq 2, \\ dt^*, & i > 2. \end{cases} \tag{B.21}$$

B.2.4 Accuracy check

We verify the order of accuracy of the numerical scheme by initializing the density field with a bi-Gaussian function in the xz-plane. The time-step dt^* was fixed (after startup). A constant uniform horizontal (x-axis) velocity field was specified within the domain. Thus,

$$\rho\bigg|_{t=0} = \exp\left[-\frac{\left(x-\frac{1}{2}\right)^2 + \left(z-\frac{1}{2}\right)^2}{0.01}\right], \quad u\bigg|_{t=0} = -0.01, \quad v\bigg|_{t=0} = 0, \quad w\bigg|_{t=0} = 0.$$

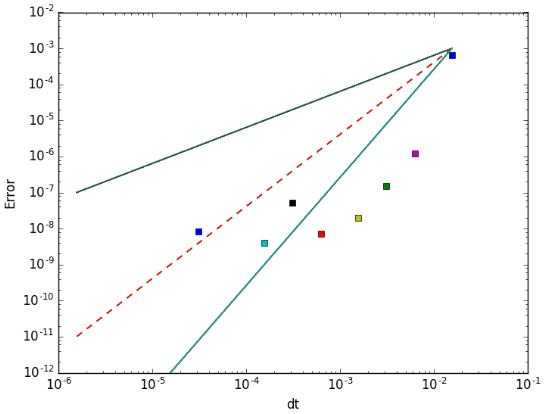

Fig. B.3 The error in the position of peak density as a function of the fixed time step dt. Lines plot a first (solid black), second (dashed red) and third (solid teal) -order convergence rate.

All physical dimensions are normalized to unity. We track the position of the maximum of ρ as a function of time. Figure B.3 plots the error of this position from its analytic value at time $t = 25$, for different time-steps $dt*$. Lines corresponding to a first-, second- and third-order convergence rate are also plotted in black, dashed red and teal, respectively. We see that there is indeed a third order convergence in the error with time-step, saturating at a value of 1×10^{-8}, which is coincidentally the minimum time step in the startup methodology. At these values of $dt*$, the error in the startup appears to be saturating the error of the simulation. As we are satisfied with this level of error, we do not pursue an alternative startup scheme.

Appendix C

Experimental Mixing Efficiency

Due to the surprisingly high mixing efficiency observed in Chapter 6, we have verified the value of η_0 in several different ways. In this appendix, we highlight one way of quantifying the mixing efficiency, being explicit in how we compute both the kinetic energy of the vortex ring and the change in potential energy of the system.

C.1 Kinetic energy estimate

The generation of each vortex ring will inject a certain amount of kinetic energy into the system. We will estimate the kinetic energy density of these vortex rings in three ways: using the prediction of a Norbury vortex ring, using the PIV[1] computed velocity field discussed in Chapter 6, and using the three-dimensional ensemble discussed in Chapter 4. We will start with the kinetic energy density of Norbury rings.

Recall from Chapter 2 that Norbury rings are a class of inviscid vortex rings with $\frac{\omega}{r}$ constant[2] inside of the vortex ring core. Norbury (1973) predicted that the kinetic energy density of the vortex rings can be computed

$$\mathrm{KE}_{Nor} = C_{KE}(\alpha)\left(\frac{1}{2}U^2\right)\left(\frac{4}{3}\pi\left(\frac{a}{2}\right)^3\right).$$

The coefficient $C_{KE}(\alpha)$ depends on $\alpha \in [0, \sqrt{2}]$, parameterizing the size of the vortex core relative to its radius. For the vortex rings produced here, we estimate $\alpha \approx 0.3$. According to Norbury (1973), $C_{KE}(\alpha = 0.3) \approx 6.5$, which was the value used in Chapter 6. For the

---

[1] Particle Image Velocimetry.

[2] Here, ω is the fluid vorticity and r is the radius from the centre of the vortex ring.

remainder of this appendix, we will define

$$\mathrm{KE}_{ref} = \left(\frac{1}{2}U^2\right)\left(\frac{4}{3}\pi\left(\frac{a}{2}\right)^3\right),$$

such that

$$\frac{\mathrm{KE}_{Nor}}{\mathrm{KE}_{ref}} = C_{KE}.$$

As an alternative to the Norbury estimate, we can estimate the kinetic energy density of the vortex rings using a vertical light sheet aligned with the centre of the vortex tube. For the estimates found here, we will use the PIV results of Chapter 6, which relied on a pair of 300W arc lamps. In order to estimate the kinetic energy of the rings from the planar measurements, we assume axisymmetry of the rings. As we have shown in Chapter 4, this is a reasonable assumption at early times. However, this estimate will be significantly affected by a misalignment of the light sheet with the axis of the vortex ring. Consistent with Chapter 6, we define the vortex ring diameter of the i^{th} PIV experiment $\{a_i\}$ as the distance between vorticity centroids. The estimated ring diameter $\bar{a}$ is then given as the average of $\{a_i\}$. Thus, we compute the kinetic energy of the vortex rings from the PIV determined components of velocity (u, v) within the light sheet:

$$\mathrm{KE}_0 = \frac{1}{2}\left(u^2 + v^2\right), \qquad \mathrm{KE}_{2D} = \pi\bar{a}\int_z\int_{r=-\infty}^{\infty} \mathrm{KE}_0\, H\left(\frac{\mathrm{KE}_0}{\max \mathrm{KE}_0} - 0.01\right)\frac{r}{a_i}\, drdz. \tag{C.1}$$

By normalizing the radial coordinate r by the ring diameter, we reduce the error induced by variations in the position of the vertical light sheet. Note that, as we compute the velocity field within a vertical sheet, we define $r = (-\infty..\infty)$. In practice, r is limited by the camera window used for the PIV. As supported by the measurements of Chapter 4, we assume here that the vortex rings are swirl-free (the azimuthal velocity $u_\theta = 0$). Due to the assumption of axisymmetry, small velocity fluctuations (whether from noise in the PIV computations or small thermal fluctuations visible within the light sheet) that are far from the centre of the vortex ring will have a large impact on the computation of the kinetic energy KE_{2D}. In order to correct for these fluctuations, we introduce a Heaviside filter (H) to remove the kinetic energy contributions from noise in the PIV determined velocity field. A reduction in the cutoff value 0.01 shows a weak $(\pm 10\%)$ dependence on the estimate of KE_{2D}. Figure C.1 plots the estimated kinetic energy density of the vortex rings, normalized by KE_{ref}, as a function of time. This estimate of the kinetic energy of the vortex rings, assuming axisymmetry, is consistent with the Norbury approximation. For the case presented here,

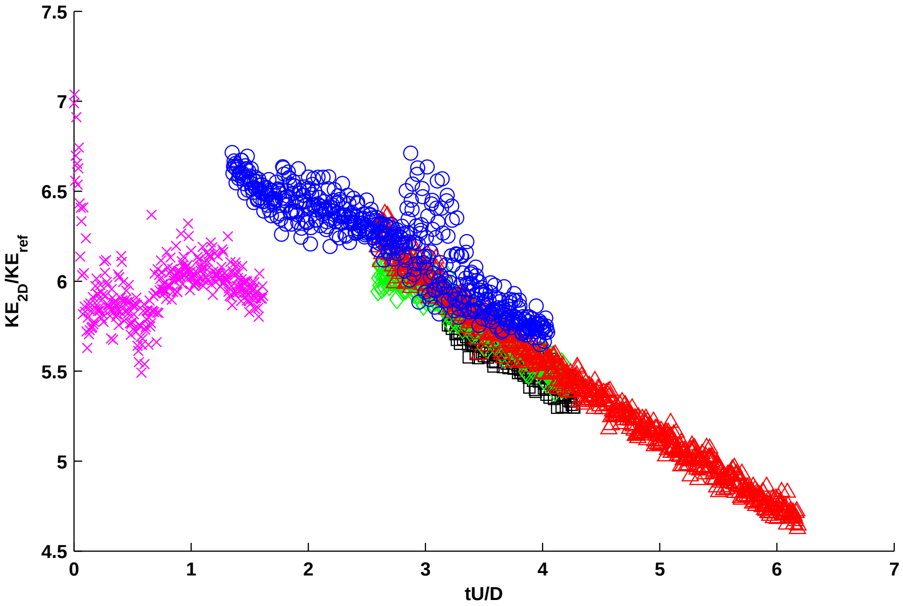

Fig. C.1 Computation of the kinetic energy density of the vortex rings assuming axisymmetry. Here, data have been taken from Case 2 of Chapter 6 ($a = 0.048$m, $U = 0.039$ m/s). Different coloured symbols correspond to different PIV experiments.

the kinetic energy density is estimated to be $\approx 2.9 \times 10^{-7}$ [m^5 / s^2]. Similar estimates are achieved through a projection of the flow external to the ring onto a potential flow field.

Finally, we can estimate the kinetic energy density of the vortex rings produced by the three-dimensional velocity ensemble from Chapter 4. Here, we can directly integrate to find that

$$\mathrm{KE}_{3D} = \int_D \frac{1}{2} |\mathbf{u}_E|^2 \, dxdydz.$$

It is important to note that the volume of the ensemble domain D is small compared to the volume of the vortex ring itself. Also, once the vortex ring enters the ensemble domain, it has already started to interact with the density stratification. As such, the kinetic energy within the ensemble domain will be less than the kinetic energy of the full vortex ring induced flow. Figure C.2 plots the kinetic energy of the ensemble velocity field as a function of time. Again, we find reasonable agreement with the prediction of the Norbury rings. For reference, we estimate the Norbury parameter of these rings to be approximately $\alpha \approx 0.3$. According to the numerical results of Norbury (1973), we have that $\alpha = (0.2, 0.4)$ gives $C_{KE} = (3.1, 7.5)$ in agreement with Figure C.1.

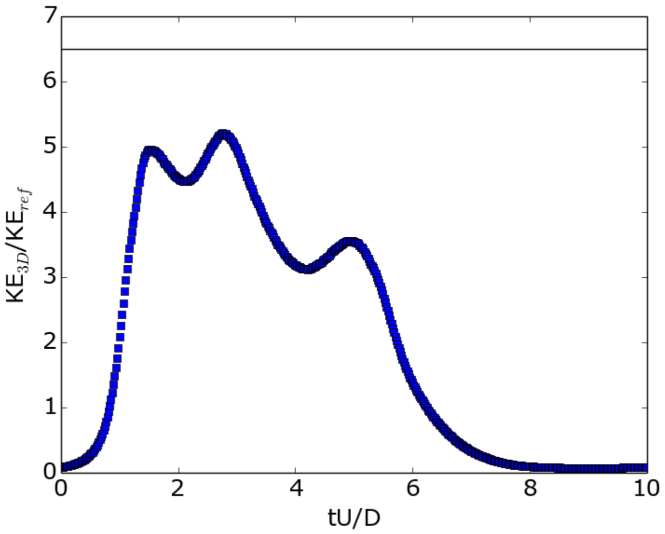

Fig. C.2 Computation of the normalized kinetic energy density within the ensemble domain. Data points were computed from Case 2 of Chapter 4. For comparison, a solid line has been plotted for $\mathrm{KE}_{3D}/\mathrm{KE}_{ref} = 6.5$.

We observe that the Norbury estimate provides a good measure of the kinetic energy of the vortex ring. As this estimate is a very convenient measure, and is much more consistent than the other two estimates, we will use the Norbury estimate.

C.2 Potential energy estimate

In the experiments of Chapter 6, vertical density profiles have been collected every 10 vortex rings. These density profiles allow us to compute the inter-ring change in potential energy of the system. We define the change in potential energy between subsequent density measurements ρ^{n+1}, ρ^n as

$$\frac{d\mathrm{PE}}{\rho_0} = \int_V g\left(\frac{\rho^{n+1} - \bar{\rho}^{n+1}}{\rho_0}\right) z dV - \int_V g\left(\frac{\rho^n - \bar{\rho}^n}{\rho_0}\right) z dV, \tag{C.2}$$

where $\bar{\rho}$ is the average density of the profile. In principle, with no mass loss to the system, $\bar{\rho}^{n+1} = \bar{\rho}^n$. In practice, the variation in mean mass from the conductivity probe fluid extraction, in conjunction with measurement error, will have an effect on the potential energy estimate. The error in the potential energy measurement is reduced by subtracting the mean mass.

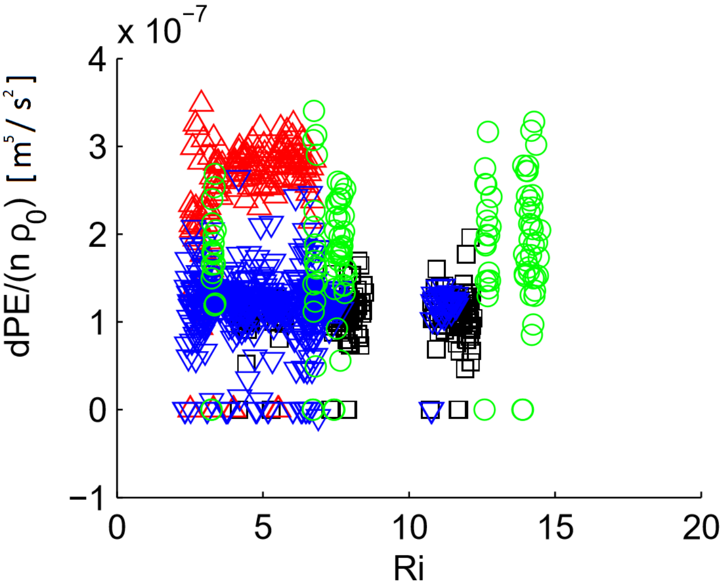

Fig. C.3 Plot of the change in potential energy between density profile measurements divided by the number of vortex rings created between measurements.

Figure C.3 plots the change in potential energy between density profile measurements for each of the physical vortex-ring experiments, divided by the number of vortex rings between measurements ($n = 10$ vortex rings between measurements). In Chapter 6, the potential energy change was computed by fitting a linear function to the potential energy of the system versus the number of vortex ring generations. Here, we plot the point-wise change in potential energy to display the spread in the data. The symbol and colour of the data points is consistent with the identifiers of Chapter 6. We see here that the change in potential energy of the system will depend on the kinetic energy of the injected vortex ring. For Case 2 (as defined in Chapter 6 (blue dots), consistent with the kinetic energy estimate KE$_{2D}$), the change in potential energy is $\sim 1.25 \times 10^{-7}$ [m^5 /s^2]

C.3 Mixing efficiency estimate

By comparing the kinetic energy of each vortex ring with the associated change in the potential energy, we can estimate the mixing efficiency as

$$\eta = \frac{d\mathrm{PE}}{n\mathrm{KE}} \approx \frac{1.25 \times 10^{-7}}{2.9 \times 10^{-7}} \approx 0.43.$$

This number is surprisingly high. Chapter 6 presented a more precise estimate to the mixing efficiency η, using the Norbury kinetic energy estimate, and a linear fit through the potential energy data. This appendix was added to provide an alternate estimate of the mixing efficiency.

Appendix D

Numerical implementation of the 1D model

This appendix provides a detailed description of the numerical implementation of the model presented in Chapter 7. As we will see, the numerical method uses pseudospectral spatial derivatives and a semi-implicit time-stepping scheme. Here, we make explicit the update methodology for T, e, and ρ.

A pseudocode for the model implementation can be written out as follows:

```
Initialize
While $t <$ N
    Force
    Update $T$
    Update $\rho$
    Update $e$
    Update Time Step
end
```

This appendix will discuss each update step in turn. We will provide a validation of the numerical convergence rate, and demonstrate that the numerical method adequately preserves energy and mass.

D.1 Numerical method

We begin by describing two extension schemes that allow us to use FFTs to compute the spatial derivatives. We then describe the forcing function for T. We continue with the update methods for T, ρ, and e. We end this section by describing the time step update.

D.1.1 Extension schemes

In order to use FFTs with the current variables, two extension operators are defined to periodically extend the variables on a domain of size N onto an extended domain of size $2N-1$. These extensions enforce the desired symmetry about the problem boundaries. The operators are given:

$$R_E(A) = \begin{cases} A_i, \; i \in [1,N] \\ A_{N-i}, \; i \in [N+1, 2N-1] \end{cases}, \qquad R_0(A) = \begin{cases} A_i, \; i \in [1,N] \\ 0, \; i \in [N+1, 2N-1] \end{cases}.$$

We can similarly define a truncation operator R_T such that

$$R_T(\, R_E(A)\,) = R_T(\, R_0(A)\,) = A.$$

Each variable is implicitly truncated back to its native domain size at the end of each update step.

D.1.2 Forcing

Recall from Chapter 7 that the model is forced with the function

$$P = \sum_{n=0}^{N} \frac{1}{\rho_0 U^2} f(z-z_0)\delta(t-n\tau), \quad f(z) = \frac{\mathrm{KE}_{\mathrm{Ring}}}{Aa} \frac{1}{\sqrt{2\pi\sigma^2}} \exp\left[-\frac{z^2}{2\sigma^2}\right].$$

The various physical parameters are defined in the initialization step, prior to the evolution of the problem variables. We define the energy input of a single vortex ring

$$K = \frac{1}{\rho_0 U^2} f(z-z_0).$$

As the time-stepping scheme used for this model does not depend on the previous time step, a spontaneous input of energy is imposed via the condition:

```
% Force
if(t > n);
    T = T + K
end;
```

Note that while no kinetic energy should advect out of the domain, the initialization of the Gaussian onto a finite domain will crop the vertical extent of K. This energy loss due to the finite domain size is negligible compared to the total energy loss within the system, as we will discuss below.

D.1.3 Numerical scheme for T

The numerical scheme for T is the most complicated due to the square root dependence of $\mathbb{I}$. In order to surmount this issue, we first make the substitution

$$w = \sqrt{2T}. \tag{D.1}$$

The evolution equation for w then becomes

$$\partial_t w = \partial_z w - \frac{\lambda}{\sqrt{2}}\mathrm{Ri}_0\ (\rho - \rho_1).$$

We implement a splitting method for w^n, where n is the iteration step of the simulation with time step dt. The pseudocode for the update step is:

```
% Update T
UpdateT();
    Solve: $\left[I - \frac{dt}{4}(D)\right] w^* = \left[I + \frac{dt}{4}(D)\right] R_0(w^n)$;
    $w^{**} = R_T(\ \max(w^* - dt\mathbb{I}_w^n, 0)\ )$;
    Solve: $\left[I - \frac{dt}{4}(D)\right] w^{n+1} = \left[I + \frac{dt}{4}(D)\right] R_E(w^{**})$;
end;
```

The spatial derivative operator is denoted as D. The pointwise maximum operator (denoted $\max()$) enforces the positivity of w. The breakdown term ($\mathbb{I}_w$) is defined as

$$\rho_1 = \rho\,(z = z_0), \qquad \mathbb{I}_w = \frac{\lambda}{\sqrt{2}}\mathrm{Ri}\,(R_E(\rho) - \rho_1), \tag{D.2}$$

Any spurious negative values are eliminated, and a spectral filter is applied to smooth the resulting solution.

D.1.4 Numerical scheme for e and ρ

The model equations for e and ρ are written:

$$\partial_t e = \partial_z \left[\left(\nu_e + \frac{1}{\mathrm{Re}} \right) \partial_z e \right] - \beta \frac{e^{\frac{3}{2}}}{l} + \alpha \mathrm{Ri}_0 \nu_e \partial_z \rho + \lambda \mathrm{Ri}_0 (\rho - \rho_1) \sqrt{T}, \tag{D.3}$$

$$\partial_t \rho = \partial_z \left[\left(\alpha \nu_e + \frac{1}{\mathrm{Re\ Sc}} \right) \partial_z \rho \right]. \tag{D.4}$$

In the numerical code, we *a priori* define

$$B^n = \nu_e^n D \rho^n, \qquad \nu_e^n = l^n \sqrt{e^n}.$$

Both ρ and e are solved using a semi-implicit time-stepping scheme. These are written:

```
% Update $\rho$
UpdateRho();
    Solve: $\left[1 - \frac{dt}{Re\ Sc} D^2\right] \rho^{n+1} = R_E(\rho^n) + a_2 dt D\left[R_E\left(B^n\right)\right]$;
end;

% Update $e$
UpdateE();
    $e^i = e^n - \beta\ dt \left(\frac{e^{\frac{3}{2}}}{l}\right)$;
    $e^{ii} = e^i + \alpha\ dt \left(\nu_e^n D^2 e + D\left(\nu_e^n\right) D e^n\right)$;
    $e^{iii} = e^{ii} + Ri_0\ dt B^n$;
    $e^{iv} = e^{iii} + dt \mathbb{I}_w\ w$;
    Solve: $\left[1 - \frac{1}{Re} dt D^2\right] e^{n+1} = R_E(e^{iv})$;
end;
```

Solving the linear diffusion operator implicitly increases the stability of the numerical solver.

D.1.5 Time-stepping

Finally, we define an adaptive time-stepping scheme. Time is scaled by τ, the inter-vortex ring generation time. We ensure that each time step dt is below the stability criterion of the system. As such,

```
% Update $t$
Update_dt();
    $dt_{max} = 1 \times 10^{-3}$;
```

```
    $dt_{cfl} = \frac{1}{2}\frac{dz}{\tau}$;
    $dt_{diff} = 0.9\frac{1}{2}\frac{dz^2}{\tau \frac{1}{Re}}$;
    $dt_{diff,\nu} = 0.5\frac{1}{2}\frac{dz^2}{\tau \max \nu_e}$;
    $dt_{CLF,\nu} = \frac{1}{2\tau}\frac{dz}{\tau \max \partial_z \nu_e}$;
    $dt = \min\left(dt_{max}, dt_{cfl}, dt_{diff}, dt_{diff,\nu}, dt_{CLF,\nu}\right)$;
end;
```

These conditions enforce both the Courant-Friedrichs-Lewy (CFL) condition and the diffusion stability criterion.

Now that each update step of the code is defined, we validate the numerical methodology to ensure that the code conserves energy and mass.

D.2 Code validation

We evaluate the numerical scheme presented above. First, we verify that the numerical scheme is first-order in the time step dt. Second, we then verify that the system preserves total mass of the density field. Last, we demonstrate the numerical inter-generational energy loss over many vortex ring events.

D.2.1 Convergence rate

As the numerical scheme used for this model is not explicitly designed to conserve energy, the energy balance in the system provides a good metric to evaluate the convergence rate of the numerical implementation. Over a range of grid resolutions N_z, we compute the energy balance at the end of a single vortex ring interaction (Model Exp. M1, $\Delta\rho = 0.01$, $\lambda = \sqrt{2}$). Figure D.1 plots the energy deficit at the end of each simulation versus the fixed time step dt. Two linear lines are superimposed on the graph corresponding to an O(Δt) convergence. We see that for better resolved simulations ($N_z > 128$), we achieve slightly better than first order convergence. Now that we have verified the order of accuracy of the numerical method, we evaluate the mass and energy loss of over many vortex-ring interactions using a variable time-step. As with Chapter 7, we fix $N_z = 1024$.

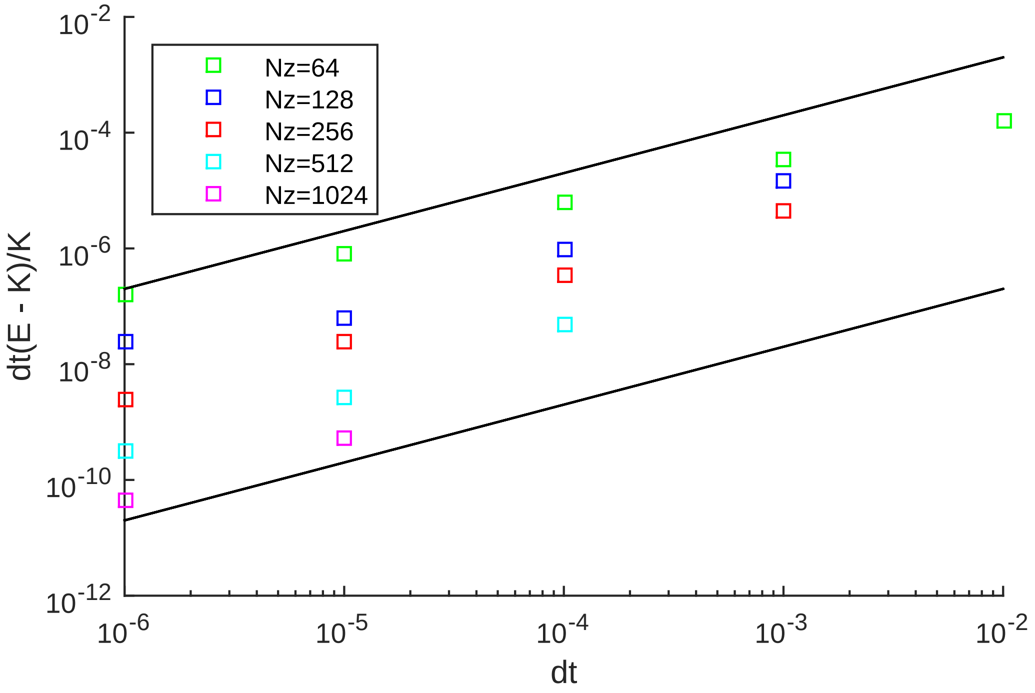

Fig. D.1 Convergence rate of the energy conservation at the end of a single vortex ring interaction (Model Exp. M1, $\Delta\rho = 0.01$). Note that here, for historical reasons, $\lambda = \sqrt{2}$.

D.2.2 Mass and Energy loss

We verify that the mass in our system is conserved. We define the mass

$$M = A \int \rho dz.$$

Figure D.2 plots the mass loss of four different experimental runs ($\Delta\rho = \{0.01, 0.02, 0.04, 0.08\}$) for Model Exp. M1 of Chapter 7. Here, M_0 is the initial mass of the system. The time step was allowed to vary according to the adaptive time stepping scheme. We find that the mass loss in our system is near MatLab^{tm}'s machine precision. Our methodology adequately preserves the mass in our system.

Similarly, we measure the energy loss over a large number of vortex ring interactions. Figure D.3 plots the energy deficit between outputs of Model Exp. M1 of Chapter 7. All four experimental runs ($\Delta\rho = \{0.01, 0.02, 0.04, 0.08\}$) are plotted. We see that, for all the runs presented, the energy loss in our system converges to O(10^{-4}) which is deemed sufficient for our present discussion.

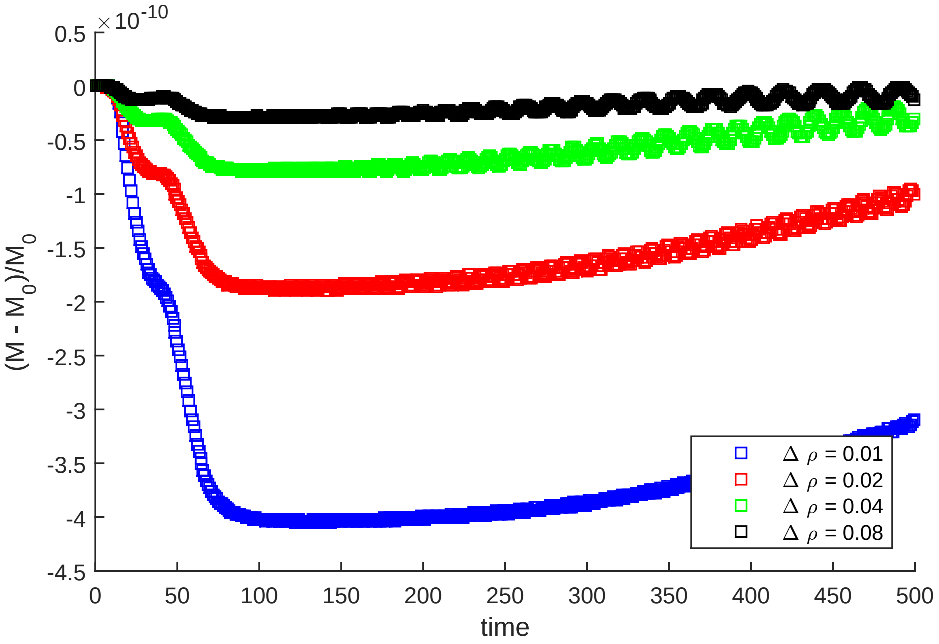

Fig. D.2 Mass loss over time for four model simulations (Model Exp. M1).

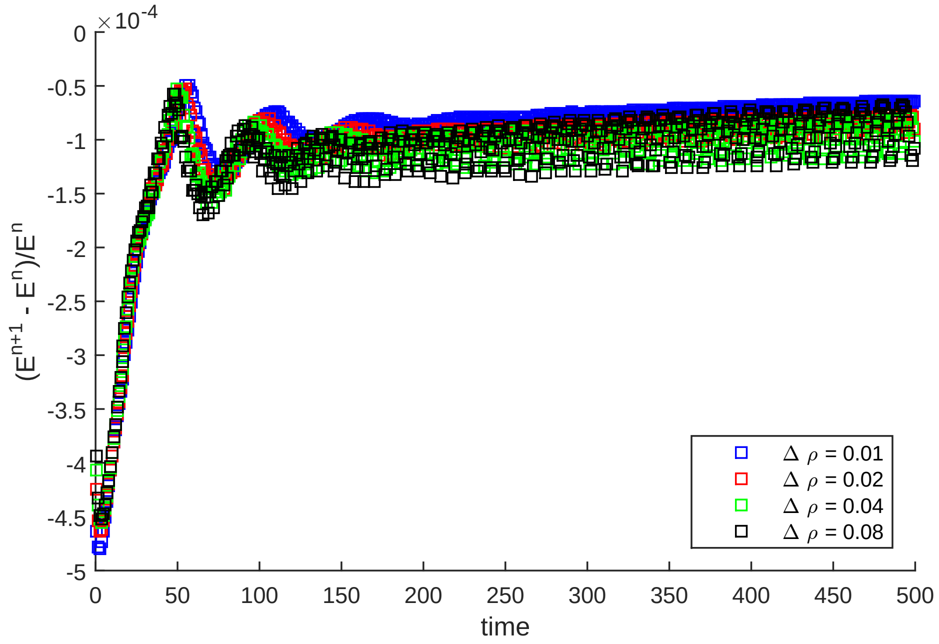

Fig. D.3 Energy loss over time for four model simulations (Model Exp. M1).

References

AKHMETOV, D. G. 2009 *Motion of Turbulent Vortex Rings*, pp. 105–119. Berlin, Heidelberg: Springer Berlin Heidelberg.

ALAHYARI, A. & LONGMIRE, E. K. 1994 Particle image velocimetry in a variable density flow: application to a dynamically evolving microburst. *Experiments in Fluids* **17** (6), 434–440.

ARCHER, P. J., THOMAS, T. G. & COLEMAN, G. N. 2008 Direct numerical simulation of vortex ring evolution from the laminar to the early turbulent regime. *Journal of Fluid Mechanics* **598**, 201–226.

ARCHER, P. J., THOMAS, T. G. & COLEMAN, G. N. 2009 The instability of a vortex ring impinging on a free surface. *Journal of Fluid Mechanics* **642**, 79–94.

ATTA, C. W. & HOPFINGER, E. J. 1989 Vortex ring instability and collapse in a stably stratified fluid. *Experiments in Fluids* **7** (3), 197–200.

BAINES, W. D. & TURNER, J. S. 1969 Turbulent buoyant convection from a source in a confined region. *Journal of Fluid Mechanics* **37** (1), 51–80.

BALMFORTH, N. J., LLEWELLYN SMITH, S. G. & YOUNG, W. R. 1998 Dynamics of interfaces and layers in a stratified turbulent fluid. *Journal of Fluid Mechanics* **355**, 329–358.

BARTELLO, P. & TOBIAS, S. M. 2013 Sensitivity of stratified turbulence to the buoyancy reynolds number. *Journal of Fluid Mechanics* **725**, 1–22.

BATCHELOR, G.K. 2000 *An Introduction to Fluid Dynamics. Cambridge Mathematical Library* . Cambridge University Press.

BAYLY, B. J. 1986 Three-dimensional instability of elliptical flow. *Phys. Rev. Lett.* **57**, 2160–2163.

BETHKE, N. 2009 Vortex ring interaction with a particle layer : implications for sediment transport. PhD thesis, University of Cambridge.

BETHKE, N. & DALZIEL, S.B. 2012 Resuspension onset and crater erosion by a vortex ring interacting with a particle layer. *Phys. Fluids* **24**, 063301.

BRISTOL, R. L., ORTEGA, J. M., MARCUS, P. S. & SAVAŞ, Ö 2004 On cooperative instabilities of parallel vortex pairs. *Journal of Fluid Mechanics* **517**, 331–358.

CAMASSA, R., KHATRI, S., MCLAUGHLIN, R., MERTENS, K., NENON, D., SMITH, C. & VIOTTI, C. 2013 Numerical simulations and experimental measurements of dense-core vortex rings in a sharply stratified environment. *Computational Science and Discovery* **6** (1), 014001.

CROW, S. C. 1970 Stability theory for a pair of trailing vortices. *AIAA Journal* **8**, 2172–2179.

DAHM, W. J. A., SCHEIL, C. M. & TRYGGVASON, G. 1989 Dynamics of vortex interaction with a density interface. *Journal of Fluid Mechanics* **205**, 1–43.

DALZIEL, S. B. 1993 Rayleigh-Taylor instability: experiments with image analysis. *Dynamics of Atmospheres and Oceans* **20**, 127–153.

DALZIEL, STUART B. 2012 *DigiFlow User Guide*. Dalziel Research Partners.

DAVIES WYKES, M. S. 2014 Efficient mixing in stratified flows :rayleigh-taylor instability within an otherwise stable stratification. PhD thesis, University of Cambridge.

DAVIES WYKES, M. S. & DALZIEL, S. B. 2014 Efficient mixing in stratified flows: experimental study of a rayleigh–taylor unstable interface within an otherwise stable stratification. *Journal of Fluid Mechanics* **756**, 1027–1057.

DENG, JIAN, TENG, LUBAO, CAULFIELD, C. P. & MAO, XUERUI 2016 Instabilities of interacting vortex rings generated by an oscillating disk. *Phys. Rev. E* **94**, 033107.

DENG, JIAN, XUE, JINGYU, MAO, XUERUI & CAULFIELD, C. P. 2017 Coherent structures in interacting vortex rings. *Phys. Rev. Fluids* **2**, 022701.

FENG, H., KAGANOVSKIY, L. & KRASNY, R. 2009 Azimuthal instability of a vortex ring computed by a vortex sheet panel method. *Fluid Dynamics Research* **41** (5), 051405.

FERNANDO, H.J.S. 1991 Turbulent mixing in stratified fluids. *Annual review of fluid mechanics* **23** (1), 455–493.

FRAENKEL, L. E. 1969 On the method of matched asymptotic expansions. *Proceedings of the Cambridge Philosophical Society* **65**, 263.

GAYEN, B., HUGHES, G. O. & GRIFFITHS, R. W. 2013 Completing the mechanical energy pathways in turbulent rayleigh-bénard convection. *Phys. Rev. Lett.* **111**, 124301.

GHARIB, MORTEZE, RAMBOD, EDMOND & SHARIFF, KARIM 1998 A universal time scale for vortex ring formation. *Journal of Fluid Mechanics* **360**, 121–140.

GOLDSTEIN, S. 1969 Fluid Mechanics in the First Half of this Century. *Annual Review of Fluid Mechanics* **1**, 1–29.

GOTO, S. & VASSILICOS, J.C. 2015 Energy dissipation and flux laws for unsteady turbulence. *Physics Letters A* **379**, 1144–1148.

HARRIS, D. M. & WILLIAMSON, C. H. K. 2012 Instability of secondary vortices generated by a vortex pair in ground effect. *Journal of Fluid Mechanics* **700**, 148–186.

HAYNES, W.M. 2012 *CRC Handbook of Chemistry and Physics, 93rd Edition*. *CRC Handbook of Chemistry and Physics* 93. Taylor & Francis.

HELMHOLTZ, H. VON 1858 Über integrale der hydrodynamischen gleichungen, welche der wirbelbewegung entsprechen. *J. für die reine und angewandte Mathematik* **55**, 25–55.

HIGGINSON, R. C. 2001 Turbulence and mixing in a stratified fluid. PhD thesis, University of Cambridge.

HOLFORD, J. M. & LINDEN, P.F. 1999 Turbulent mixing in a stratified fluid. *Dynamics of Atmospheres and Oceans* **30**, 173 – 198.

IVEY, G.N., WINTERS, K.B. & KOSEFF, J.R. 2008 Density stratification, turbulence, but how much mixing? *Annual Review of Fluid Mechanics* **40** (1), 169–184.

IVEY, G. N., IMBERGER, J. & KOSEFF, J. R. 1998 *Buoyancy Fluxes in a Stratified Fluid*, pp. 377–388. American Geophysical Union.

KAMINSKI, A. K., CAULFIELD, C. P. & TAYLOR, J. R. 2014 Transient growth in strongly stratified shear layers. *Journal of Fluid Mechanics* **758**.

KERSWELL, R. R. 2002 Elliptical instability. *Annual Review of Fluid Mechanics* **34** (1), 83–113.

KLECKNER, D. & IRVINE, W. T. M. 2013 Creation and dynamics of knotted vortices. *Nature Physics* **9**, 253–258.

KRAUS, E. B. & TURNER, J. S. 1967 A one-dimensional model of the seasonal thermocline ii. the general theory and its consequences. *Tellus* **19** (1), 98–106.

KRUTZSCH, C.-H., BOLSTER, D., HERSHBERGER, R. & DONNELLY, R.J. 1939 On an experimentally observed phenomenon on vortex rings during their translational movement in a real liquid. *Annalen der Physik* **523** (5), 360–379.

LAMB, H. 1945 *Hydrodynamics*. *Dover Books on Physics* . Dover publications.

LECLERCQ, C., PARTRIDGE, J. L., CAULFIELD, C. P., DALZIEL, S. B. & LINDEN, P. F. 2016 Nonlinear waves in stratified Taylor–Couette flow. Part 2. Buoyancy flux. *ArXiv e-prints* .

LEWEKE, T., DIZÈS, S. LE & WILLIAMSON, C. H.K. 2016 Dynamics and instabilities of vortex pairs. *Annual Review of Fluid Mechanics* **48** (1), 507–541.

LINDEN, P. F. 1973 The interaction of a vortex ring with a sharp density interface: a model for turbulent entrainment. *Journal of Fluid Mechanics* **60**, 467–480.

LINDEN, P. F. 1975 The deepening of a mixed layer in a stratified fluid. *Journal of Fluid Mechanics* **71**, 385–405.

LINDEN, P. F. 1979 Mixing in stratified fluids. *Geophysical & Astrophysical Fluid Dynamics* **13** (1), 3–23.

MAXWORTHY, T. 1972 The structure and stability of vortex rings. *Journal of Fluid Mechanics* **51** (1), 15–32.

MAXWORTHY, T. 1977 Some experimental studies of vortex rings. *Journal of Fluid Mechanics* **81**, 465–495.

MCDOUGALL, TREVOR J. 1979 Measurements of turbulence in a zero-mean-shear mixed layer. *Journal of Fluid Mechanics* **94** (3), 409–431.

MCDOUGALL, T. J. 1979 On the elimination of refractive-index variations in turbulent density-stratified liquid flows. *Journal of Fluid Mechanics* **93**, 83–96.

MOORE, D. W. & SAFFMAN, P. G. 1975 The instability of a straight vortex filament in a strain field. *Proceedings of the Royal Society of London A: Mathematical, Physical and Engineering Sciences* **346** (1646), 413–425.

MOORE, M. J. & LONG, R. R. 1971 An experimental investigation of turbulent stratified shearing flow. *Journal of Fluid Mechanics* **49**, 635–655.

MORTON, B. R., TAYLOR, G. & TURNER, J. S. 1956 Turbulent gravitational convection from maintained and instantaneous sources. *Proceedings of the Royal Society of London. Series A, Mathematical and Physical Sciences* **234** (1196), pp. 1–23.

MUNRO, R. J., BETHKE, N. & DALZIEL, S. B. 2009 Sediment resuspension and erosion by vortex rings. *Physics of Fluids* **21** (4), 046601.

NOMURA, K. K., TSUTSUI, H., MAHONEY, D. & ROTTMAN, J. W. 2006 Short-wavelength instability and decay of a vortex pair in a stratified fluid. *Journal of Fluid Mechanics* **553**, 283–322.

NORBURY, J. 1973 A family of steady vortex rings. *Journal of Fluid Mechanics* **57**, 417–431.

OGLETHORPE, R. L. F., CAULFIELD, C. P. & WOODS, A. W. 2013 Spontaneous layering in stratified turbulent taylor–couette flow. *Journal of Fluid Mechanics* **721**, R3, 1–12.

OLSTHOORN, J. & DALZIEL, S. B. 2015 Vortex-ring-induced stratified mixing. *Journal of Fluid Mechanics* **781**, 113–126.

OLSTHOORN, J. & DALZIEL, S. B. 2016 Three-dimensional visualization of the interaction between a vortex ring and a stratified interface: The evolution of the density field. *Proceedings of the* VIII$^{\text{th}}$ *Int. Symp. on Stratified Flows* .

OLSTHOORN, J. & DALZIEL, S. B. 2017*a* Three-dimensional visualization of the interaction of a vortex ring with a stratified interface. *Journal of Fluid Mechanics, Accepted* .

OLSTHOORN, J. & DALZIEL, S. B. 2017*b* Vortex-ring-induced stratified mixing: Mixing model. *Journal of Fluid Mechanics, Under Review* .

ORLANDI, P. & VERZICCO, R. 1993 Vortex rings impinging on walls: axisymmetric and three-dimensional simulations. *Journal of Fluid Mechanics* **256**, 615–646.

ORTIZ, S., DONNADIEU, C. & CHOMAZ, J.-M. 2015 Three-dimensional instabilities and optimal perturbations of a counter-rotating vortex pair in stratified flows. *Physics of Fluids* **27** (10).

PARK, Y.-G., WHITEHEAD, J. A. & GNANADESKIAN, A. 1994 Turbulent mixing in stratified fluids: layer formation and energetics. *Journal of Fluid Mechanics* **279**, 279–311.

PATTERSON, M. D., CAULFIELD, C. P., MCELWAINE, J. N. & DALZIEL, S. B. 2006 Time-dependent mixing in stratified Kelvin-Helmholtz billows: Experimental observations. *Geophysical Research Letters* **33** (15), l15608.

PELTIER, W. R. & CAULFIELD, C. P. 2003 Mixing efficiency in stratified shear flows. *Annual Review of Fluid Mechanics* **35** (1), 135–167.

PHILLIPS, O.M. 1972 Turbulence in a strongly stratified fluid—is it unstable? *Deep Sea Research and Oceanographic Abstracts* **19** (1), 79 – 81.

PIERREHUMBERT, R. T. 1986 Universal short-wave instability of two-dimensional eddies in an inviscid fluid. *Phys. Rev. Lett.* **57**, 2157–2159.

PONITZ, B., SASTUBA, M. & BRÜCKER, C. 2015 4d visualization study of a vortex ring life cycle using modal analyses. *Journal of Visualization* pp. 1–23.

POSMENTIER, ERIC S. 1977 The generation of salinity finestructure by vertical diffusion. *Journal of Physical Oceanography* **7** (2), 298–300.

PRASTOWO, T., GRIFFITHS, R. W., HUGHES, G. O. & HOGG, A. MCC. 2008 Mixing efficiency in controlled exchange flows. *Journal of Fluid Mechanics* **600**, 235–244.

PRASTOWO, T., GRIFFITHS, R. W., HUGHES, G. O. & HOGG, A. M. 2009 Effects of topography on the cumulative mixing efficiency in exchange flows. *Journal of Geophysical Research: Oceans* **114** (C8).

SAFFMAN, P.G. 1995 *Vortex Dynamics. Cambridge Monographs on Mechanics* . Cambridge University Press.

SAFFMAN, P. G. 1978 The number of waves on unstable vortex rings. *Journal of Fluid Mechanics* **84**, 625–639.

SCASE, M.M. & DALZIEL, S.B. 2006 An experimental study of the bulk properties of vortex rings translating through a stratified fluid. *European Journal of Mechanics - B/Fluids* **25** (3), 302 – 320.

SCASE, M. M. 2003 Vortex rings in a stratified fluid. PhD thesis, University of Cambridge.

SCOTTI, A. & WHITE, B. 2011 Is horizontal convection really "non-turbulent?". *Geophysical Research Letters* **38** (21), l21609.

SHARIFF, K. & LEONARD, A. 1992 Vortex rings. *Annual Review of Fluid Mechanics* **24** (1), 235–279.

SHRAVAT, A., CENEDESE, C. & CAULFIELD, C. P. 2012 Entrainment and mixing dynamics of surface-stress-driven stratified flow in a cylinder. *Journal of Fluid Mechanics* **691**, 498–517.

SHRINIVAS, A. B. & HUNT, G. R. 2015 Confined turbulent entrainment across density interfaces. *Journal of Fluid Mechanics* **779**, 116–143.

STOCK, M. J., DAHM, W. J. A. & TRYGGVASON, G. 2008 Impact of a vortex ring on a density interface using a regularized inviscid vortex sheet method. *J. Comput. Phys.* **227** (21), 9021–9043.

SUBICH, C. J., LAMB, K. G. & STASTNA, M. 2013 Simulation of the Navier–Stokes equations in three dimensions with a spectral collocation method. *International Journal for Numerical Methods in Fluids* **73** (2), 103–129.

SULLIVAN, I. S., J., NIEMELA J., HERSHBERGER, R. E., BOLSTER, D. & DONNELLY, R. J. 2008 Dynamics of thin vortex rings. *Journal of Fluid Mechanics* **609**, 319–347.

SWEARINGEN, J. D., CROUCH, J. D. & HANDLER, R. A. 1995 Dynamics and stability of a vortex ring impacting a solid boundary. *Journal of Fluid Mechanics* **297**, 1–28.

TAILLEUX, R. 2009 On the energetics of stratified turbulent mixing, irreversible thermodynamics, boussinesq models and the ocean heat engine controversy. *Journal of Fluid Mechanics* **638**, 339–382.

THOMPSON, M. C., LEWEKE, T. & HOURIGAN, K. 2007 Sphere–wall collisions: vortex dynamics and stability. *Journal of Fluid Mechanics* **575**, 121–148.

THOMSON, J.J. 1883 *A treatise on the motion of vortex rings: An essay to which the Adams prize was adjudged in 1882, in the University of Cambridge*. Macmillan.

TOMINAGA, Y. & STATHOPOULOS, T. 2007 Turbulent Schmidt numbers for CFD analysis with various types of flowfield. *Atmospheric Environment* **41** (37), 8091 – 8099.

TREFETHEN, L. N. 2000 *Spectral methods in Matlab*. Philadelphia, PA, USA: Society for Industrial and Applied Mathematics.

TSAI, C.-Y 1976 The short wave instability of vortex rings and filaments. PhD thesis, massachusetts institute of technology.

TSAI, C.-Y. & WIDNALL, S. E. 1976 The stability of short waves on a straight vortex filament in a weak externally imposed strain field. *Journal of Fluid Mechanics* **73** (4), 721–733.

TSENG, Y.-H. & FERZIGER, J. H. 2001 Mixing and available potential energy in stratified flows. *Physics of Fluids* **13** (5), 1281–1293.

TURNER, J.S. 1979 *Buoyancy Effects in Fluids*. *Cambridge Monographs on Mechanics* . Cambridge University Press.

TURNER, J. S. 1957 Buoyant vortex rings. *Proceedings of the Royal Society of London. Series A, Mathematical and Physical Sciences* **239** (1216), 61–75.

TURNER, J. S. 1968 The influence of molecular diffusivity on turbulent entrainment across a density interface. *Journal of Fluid Mechanics* **33**, 639–656.

TURNER, J. S. 1986 Turbulent entrainment: the development of the entrainment assumption, and its application to geophysical flows. *Journal of Fluid Mechanics* **173**, 431–471.

VASSILICOS, J. C. 2015 Dissipation in turbulent flows. *Annual Review of Fluid Mechanics* **47** (1), 95–114.

VENAILLE, A., GOSTIAUX, L. & SOMMERIA, J. 2014 The role of fluctuations across a density interface. *ArXiv e-prints* .

WALKER, J. D. A., SMITH, C. R., CERRA, A. W. & DOLIGALSKI, T. L. 1987 The impact of a vortex ring on a wall. *Journal of Fluid Mechanics* **181**, 99–140.

WIDNALL, S. E., BLISS, D. B. & TSAI, C.-Y. 1974 The instability of short waves on a vortex ring. *Journal of Fluid Mechanics* **66**, 35–47.

WIDNALL, S. E. & SULLIVAN, J. P. 1973 On the stability of vortex rings. *Proceedings of the Royal Society of London A: Mathematical, Physical and Engineering Sciences* **332** (1590), 335–353.

WIDNALL, S. E. & TSAI, C.-Y. 1977 The instability of the thin vortex ring of constant vorticity. *Philosophical Transactions of the Royal Society of London A: Mathematical, Physical and Engineering Sciences* **287** (1344), 273–305.

WINTERS, K. B., LOMBARD, P. N., RILEY, J. J. & D'ASARO, E. A. 1995 Available potential energy and mixing in density-stratified fluids. *Journal of Fluid Mechanics* **289**, 115–128.

WORSTER, M. G. & HUPPERT, H. E. 1983 Time-dependent density profiles in a filling box. *Journal of Fluid Mechanics* **132**, 457–466.